DISCLAIMER

NATURAL CONVECTION HEAT TRANSFER FOR A STAGGERED ARRAY OF HEATED, HORIZONTAL CYLINDERS WITHIN A RECTANGULAR ENCLOSURE

by

CHRISTOPHER ERIC TRIPLETT, B.S.

THESIS

Presented to the Faculty of the Graduate School
of The University of Texas at Austin
in Partial Fulfillment
of the Requirements
for the Degree of

MASTER OF SCIENCE IN ENGINEERING

THE UNIVERSITY OF TEXAS AT AUSTIN

December, 1996

DISCLAIMER

Portions of this document may be illegible electronic image products. Images are produced from the best available original document.

NATURAL CONVECTION HEAT TRANSFER FOR A STAGGERED ARRAY OF HEATED, HORIZONTAL CYLINDERS WITHIN A RECTANGULAR ENCLOSURE

APPROVED BY
SUPERVISING COMMITTEE:

Dale E. Klein

Bernard W. Wehring

Acknowledgments

This thesis was performed under appointment to the Office of Civilian Radioactive Waste Management (OCRWM) Fellowship program administered by the Oak Ridge Institute for Science and Education. I would also like to thank Marcia Prewitt, Sandra Johnson, and Craig Williamson for their administrative assistance and support.

This research was also supported through the Chris M. Shaughnessey Thrust 2000 Fellowship awarded by the College of Engineering at The University of Texas at Austin. I would like to thank Sonja Swanson, Glen Masada, and Chris Shaughnessey for their administrative and financial support.

To my mother, Donna Triplett, I thank for your love and for "raisin' me right!" I love you, and God bless you.

To Dr. Dale Klein, I thank you bringing me on board for this project. My graduate school experience has been wonderful, and I am deeply grateful to you for your support, your technical and career advice, your signature on the cover of this thesis, and your gifts from various ends of the world.

To Robert "I have some rods. . .they are hot" Canaan, I have enjoyed your friendship greatly and have learned a great deal from your technical guidance. Thanks for introducing me to good cigars, Lyle Lovett, big water (or at least San Marcos water), Big Bend, and noodle bowls. I hope you'll let me stay for free at your bed and breakfast in Ouray someday! I wish you and Linda a long and wonderful life together.

To Steve "Satan Boy" Manson, I'll never forget the first taste of Guinness, the first bed of bulls, the volleyball, the sick stomachs at the Frontier and the

Arkansas River, the pain of Mt. Elbert, the prime rib in Leadville, the dip in Lake Katherine, and the mexican steak special. I've enjoyed my grad school experiences with you very much, and I'll always consider you one of my best friends. Here's to many more good times!

I would also like to thank Jaime Moya, Walt Gill, David Schulze, and Kim Haulenbeek, who made my practicum at Sandia Labs an enjoyable learning experience. I wish you all the very best.

I'd like to thank Shawn Burns, whose work on the RADERA code helped me to finish this research. I owe you another mexican dinner!

Finally, I'd like to thank Sandy Taylor, who kept the entire ship running smoothly and helped to make my life much easier. I can't thank you enough for all your help.

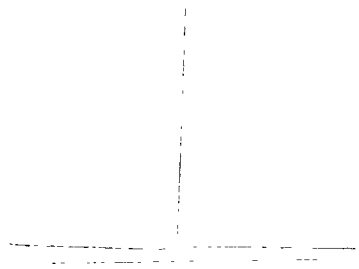

NATURAL CONVECTION HEAT TRANSFER FOR A STAGGERED ARRAY OF HEATED, HORIZONTAL CYLINDERS WITHIN A RECTANGULAR ENCLOSURE

by

Christopher Eric Triplett, M.S.E.
The University of Texas at Austin, 1996
SUPERVISOR: Dale E. Klein

This thesis presents the results of an experimental investigation of natural convection heat transfer in a staggered array of heated cylinders, oriented horizontally within a rectangular enclosure. The main purpose of this research was to extend the knowledge of heat transfer within enclosed bundles of spent nuclear fuel rods sealed within a shipping or storage container. This research extends Canaan's investigation of an aligned array of heated cylinders that thermally simulated a boiling water reactor (BWR) spent fuel assembly sealed within a shipping or storage cask.

The heated rod array was comprised of 60 tubular stainless steel heater rods with a nickel-chromium resistance heating element running through the center of each rod. The heater rods were supplied with uniform power generation per unit length. A rectangular, copper, water-cooled box provided an isothermal enclosure for the heater rods. The rod ends were insulated to minimize axial temperature variations, which allowed a two-dimensional heat transfer analysis to accurately characterize the thermal characteristics of the rod bundle. The temperature variations throughout the rod bundle were measured with embedded thermocouples placed just beneath the outer surface of each rod. Extensive thermal characterization

of the staggered rod array was performed by varying three parameters independently. Placing the test assembly within a sealed pressure vessel allowed variations both of the type of backfill fluid and of the fluid pressure. The two types of gas used were helium and nitrogen, and the pressure was varied from 0 to 60 psig. The third parameter varied was the total power input to the assembly, which was varied uniformly from 1 to 5 watts per rod.

The results are presented in terms of piecewise Nusselt-Rayleigh number correlations of the form $Nu = C(Ra)^n$, where C and n are constants. Correlations are presented both for individual rods within the array and for the array as a whole. The correlations are based only on the convective component of the heat transfer. The radiative component was calculated with a finite-element code that used measured surface temperatures, rod array geometry, and measured surface emissivities as inputs. The correlation results are compared to Canaan's aligned array results and to other studies of natural convection in horizontal tube arrays.

For the rod bundle as a whole, the data show a distinct two-regime trend that is reminiscent of the Rayleigh-Benard problem, which describes a conduction regime and a convection regime. In the conduction regime, the bundle-averaged Nusselt numbers are lower for the staggered array than for Canaan's aligned array. However, in the convection regime, the staggered array has higher bundle-averaged Nusselt numbers than the aligned array. Also, the slope of the Nusselt-Rayleigh curve in the convection regime indicates that turbulent flow is present within the rod bundle.

For individual rods, the research shows that fluid rising from the rods in the lower half of the array tend to preheat rods in the upper half, resulting in lower Nusselt numbers for the upper row rods. Rods in the lower half of the array exhibit two-regime Nusselt number behavior, similar to the bundle-averaged Nusselt numbers. However, rods in the upper half of the array do not display this trend. Comparing this enclosed staggered array to a non-enclosed staggered array shows that the reduction in Nusselt number as one goes up a given column of rods is more dramatic for the enclosed array than for the non-enclosed array.

Table of Contents

List of Tables

List of Figures

List of Symbols

symbols

C	constant multiplier in Nusselt-Rayleigh number correlations
c_p	fluid specific heat at constant pressure
d, D	heater rod diameter
da_i, da_j	differential area element at points i or j
ds_i, ds_j	differential arc length at points i or j
g	gravitational acceleration at sea level (9.81 m / s^2)
Gr, Gr_x	Grashof number, Grashof number based on length scale "x"
h	convection heat transfer coefficient
h_{bund}	full array convection coefficient based on ΔT_{bund}
h_{max}	full array convection coefficient based on ΔT_{max}
h_r	convection heat transfer coefficient at specific circumferential angle on rod surface
$h_{r,avg}$	rod-averaged convection heat transfer coefficient
H	CuBE height
i	current
k	fluid thermal conductivity
L	rod heated length
n	constant exponent in Nusselt-Rayleigh number correlations
$\hat{n}$	unit outward pointing normal vector
N	counting integer (such as i = 1, 2, . . ., N)
Nu	Nusselt number
Nu_r	rod-averaged Nusselt number
Nu_{bund}	full array Nusselt number based on ΔT_{bund}
Nu_{max}	full array Nusselt number based on ΔT_{max}
Nu_{cond}	full array "conduction" Nusselt number
p	pressure
P	rod pitch or spacing
Pr	Prandtl number

q''	heat flux
q'	heat rate per unit length
q	heat rate
q'_r	net heat rate per unit length for a single rod
q'_{conv}	net convective heat rate per unit length for a single rod
q'_{rad}	net radiative heat rate per unit length for a single rod
Q'	heat rate per unit length for the entire rod bundle
Q'_{conv}	convective heat rate per unit length for the entire rod bundle
$\mathbf{q}''_{i,inc}$	incident radiative flux vector at point i
$\mathbf{q}''_{j,inc}$	incident radiative flux vector at point j
$q''_{emitted}$	emitted radiative flux at point i
$q''_{i,net}$	net radiative flux at point i
q''_{inner}	heat flux on inner surface of rod cladding
$\mathbf{r}_i$ or $\mathbf{r}_j$	position vector for points i or j
$\mathbf{r}_{ij}$	difference vector $\mathbf{r}_i - \mathbf{r}_j$
$\hat{\mathbf{r}}_{ij}$	unit vector in direction of $\mathbf{r}_{ij}$
R	electrical resistance
Ra	Rayleigh number
Ra_x	Rayleigh number based on length scale "x"
Ra_{bund}	bundle-averaged Rayleigh number based on ΔT_{bund}
$Ra_{critical}$	critical or transition Rayleigh number
Ra_{max}	bundle-averaged Rayleigh number based on ΔT_{max}
Ra_{mod}	modified Rayleigh number
$Ra_{Q'}$	bundle-averaged Rayleigh number based on Q'_{conv}
Re	Reynolds number
Re_x	Reynolds number based on length scale "x"
T_C	mean CuBE, or enclosure, temperature
ΔT	Individual rod temperature difference $\Delta T = T_r - T_C$
T_{bund}	average bundle rod temperature
ΔT_{bund}	bundle averaged temperature difference $\Delta T_{bund} = T_{bund} - T_C$
T_f	average, or film, temperature

$T_{f,bund}$	bundle-averaged film temperature
T_{max}	maximum rod surface temperature
ΔT_{max}	maximum rod temperature difference $\Delta T_{max} = T_{max} - T_c$
T_r	mean temperature of a given rod
T_s	surface temperature
T_{surr}	temperature of the surroundings
T_∞	ambient fluid temperature
x	length scale, coordinate direction
y, z	coordinate directions
α	thermal diffusivity, absorptivity
β	fluid expansion coefficient
ε	surface emissivity
ν	kinematic viscosity
π	pi, ratio of circumference to diameter of a circle
θ	angle
ρ	fluid density
σ	Stefan-Boltzmann constant (5.67 e -8 $W / m^2 - K^4$)
Ω	solid angle
$\partial\Omega$	differential solid angle, Ω

subscripts

avg	average value
b	general bundle-averaged quantity
branch	related to one of four power supply branches
bund	bundle-averaged quantity based on average rod temperature, T_{bund}
c	enclosure, or CuBE, value
cond	conduction-related quantity
conv	quantity based convective portion of heat transfer
critical	critical or transition value
d, D	based on diameter
emitted	related to radiation emission

f	film temperature quantity
i	index of rod numbers, relating to point i
inc	incident quantity
inner	relating to inner surface of the rod cladding
j	relating to point j
mod	modified quantity
Q'	based on total convective heat rate per unit length, Q'_{conv}
r	rod-averaged value
rad	quantity based radiative portion of heat transfer
s	surface quantity
surr	related to surroundings
x	related to length scale x
∞	ambient value

List of Acronyms

A/D	Analog-to-Digital
ADAS	Automated Data Acqisition System
ASME	American Society of Mechanical Engineers
BWR	Boiling Water Reactor
B&W	Babcock and Wilcox Company
CuBE	Copper (Cu) Boundary Enclosure
DC	Direct Current
DOE	Department of Energy
GPIB	General Purpose Interface Bus
MIMS	Mineral-Insulated / Metal-Sheathed
NASA	National Aeronautics and Space Administration
NIST	National Institute for Standards and Technology
PWR	Pressurized Water Reactor
RADERA II	RADiation in Enclosed Rod Arrays, version II
SNF	Spent Nuclear Fuel
TC	Thermocouple
UT	The University of Texas at Austin

Chapter 1 -- Introduction

1.1 Applications of the Study of Natural Convection of Heated Tube Arrays Within Enclosures

The study of natural convection from horizontally-oriented heated cylinder arrays within an enclosure has three primary applications of interest to current industry. The first application is electronics packaging, where electronic components generate heat within a computer or other packaging and are cooled primarily through natural convection. As computer components become smaller and faster, heat generated by these components must be rejected more effectively to prevent thermally-induced changes in material properties that could cause malfunctions. The smaller the product, the more difficult it becomes to use forced convection to provide cooling within the product housing. Thus, an understanding of natural convection for complex shapes within an enclosure allows product designers to geometrically arrange the components in a way that maximizes natural convection.

The second application is immersion heating, where a heated tube bank is used to heat a fluid in a container, such as oil in a large tank. The tube bank may be electrically heated, or it could be a heat exchanger in which hot fluid passes through the hollow tubes to heat the surrounding liquid. The effectiveness of the heat transfer can be changed, depending on the spacing of the tubes and the orientation of the tube bundle within the fluid. Thus, an understanding of the relationship between these factors and the overall heat transfer can aid the design of a tube bundle that heats the fluid in an optimal manner.

The third common application in which natural convection from a tube bank within an enclosure is important is in the thermal study of the transportation and storage of spent nuclear fuel (SNF) rods. Approximately half of the commercial nuclear power plants in the U.S. are boiling water reactors (BWRs) [Todreas and Kazimi, 1990]. In a BWR, water boils as it flows over nuclear fuel rods in which heat is generated through nuclear fission. This steam is directly used to drive the

turbine-generator. The other half of U.S. commercial reactors are pressurized water reactors (PWRs), which heat water at high pressure, but do not cause the water to boil in the reactor. A secondary heat transfer loop using heat exchangers creates the steam used to drive the turbine-generator. For both BWRs and PWRs, the construction of the fuel rods, fuel assemblies, and reactor cores are very similar. However, since PWR fuel assemblies contain about 4 times as many rods as a BWR fuel assembly, let us focus on the less complex construction of the BWR fuel assembly.

Figure 1.1 shows a typical nuclear fuel rod used in a boiling water reactor. It is made up of cylindrical pellets of uranium oxide (UO_2) that are stacked within a zircalloy cladding to form a fuel rod that is a little over 4 meters in length. The individual fuel pellets are about 1 cm in diameter and about 1 cm in length [Todreas and Kazimi, 1990]. As shown in Figure 1.2, these rods are grouped into an 8x8 square array housed within a rectangular casing to form a single fuel assembly that is about 4.4 meters long [Todreas and Kazimi, 1990]. A PWR fuel assembly contains either a 15x15, a 16x16, or a 17x17 square array of fuel rods. A typical BWR core contains several hundred fuel assemblies, oriented vertically and arranged in a roughly cylindrical pattern. Figure 1.3 shows the arrangement of fuel assemblies within a typical BWR core.

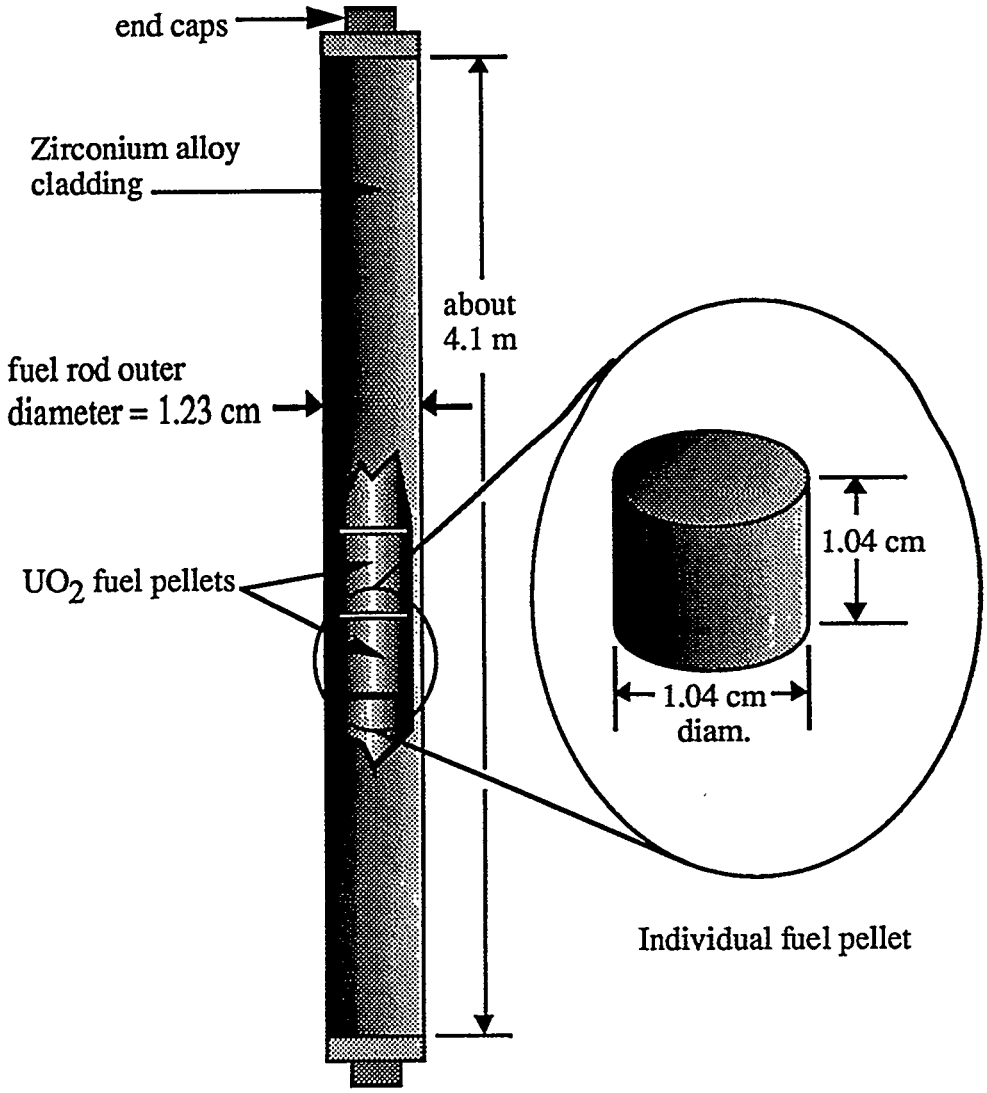

Figure 1.1 Diagram of a BWR fuel rod, showing UO_2 pellets. (drawing not to scale)

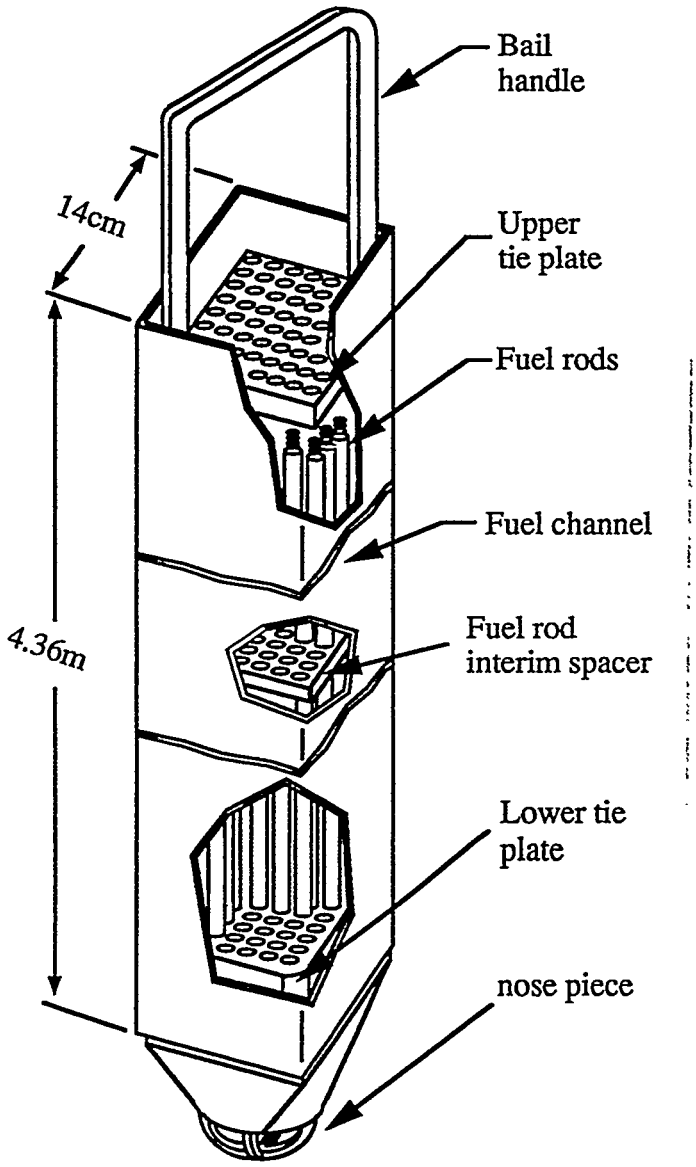

Figure 1.2 Diagram of a typical BWR fuel assembly. [Canaan, 1995] (drawing not to scale).

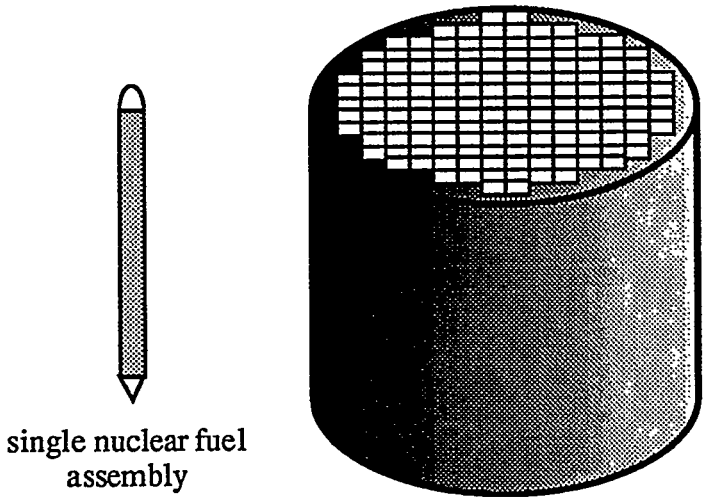

Figure 1.3 Arrangement of BWR fuel assemblies in a reactor core.

In the BWR core, water flows vertically through the spaces between the fuel rods, removing the heat generated by the fission process and turning into steam. As the fission process continues, the amount of useful UO_2 within the rods gradually is used up, being converted to lighter elements such as barium, cesium, niobium, and zirconium. When the amount of UO_2 reaches a certain low level, the fuel assemblies are removed from the reactor and are referred to as spent nuclear fuel (SNF) assemblies. These SNF assemblies are currently stored on-site at the plant until a permanent storage facility for spent fuel can be approved and constructed.

When this permanent facility is built, the SNF will be transported to the permanent disposal site in specially designed casks. These casks must isolate the SNF—which remains highly radioactive—from the outside environment. The casks must be tough enough to remain sealed even if a severe accident were to occur during transport. Since the rods continue to generate heat for many years after they are removed from the reactor, the cask must also be able to withstand the elevated temperatures generated by this decay heat within the cask. As shown in Figure 1.4, a typical transport cask would be carried on a rail car or large truck, and would carry many fuel assemblies. Since the fuel assemblies are very long, they are stored in a horizontal configuration within the cask. Each assembly is separated from the others by a rectangular stainless steel sleeve. In this geometry, an individual fuel assembly can be modeled thermally as an aligned array of 64 very long cylinders with internal heat generation, enclosed by a rectangular, isothermal box. Understanding the heat transfer mechanisms within the fuel assembly allows cask designers to predict and design for the maximum temperatures that will occur within the cask as a result of the SNF decay heat.

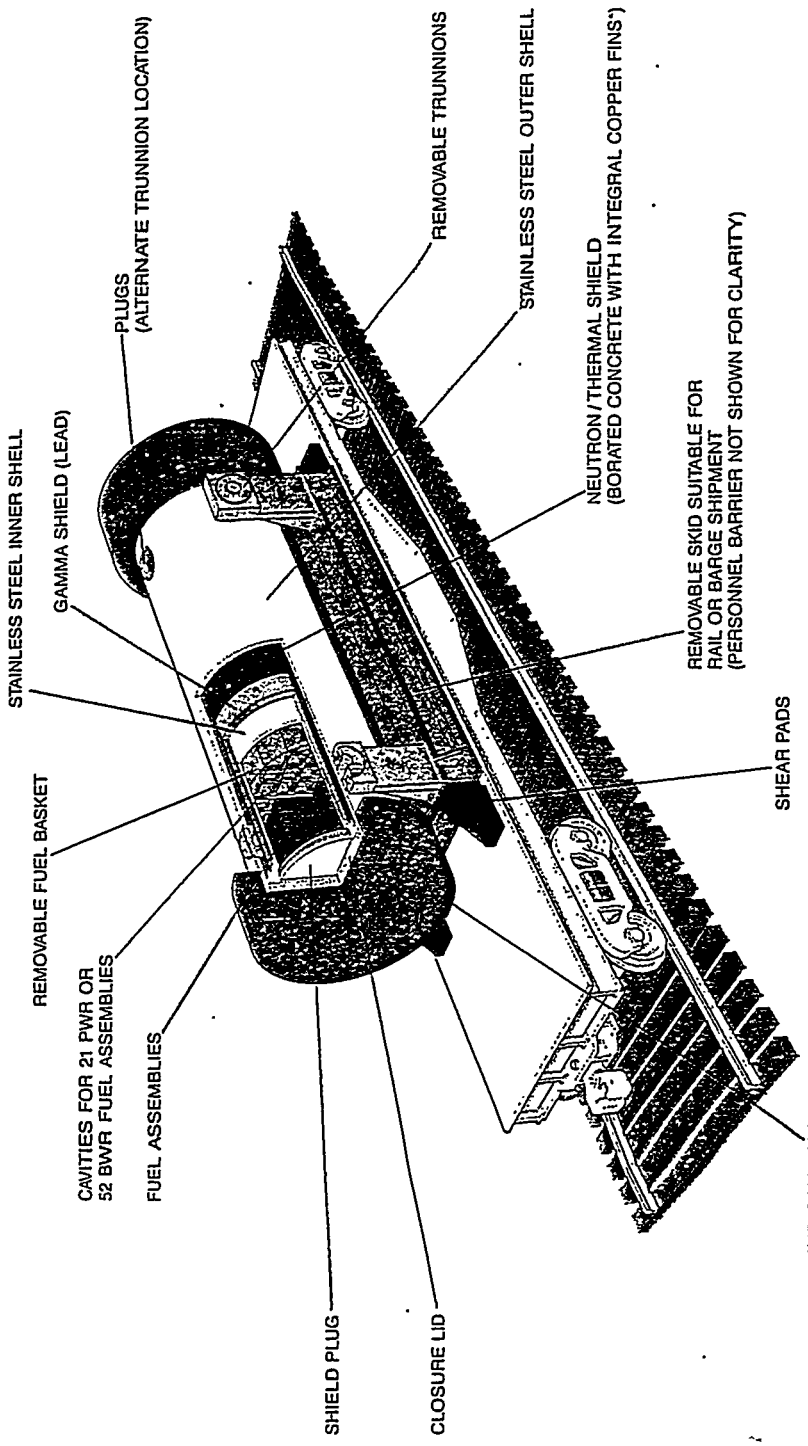

Figure 1.4 A Babcock and Wilcox spent fuel shipping cask. It holds 52 BWR spent fuel assemblies [DOE/ID/12701-1, 1990].

1.2 THE UT / CANAAN EXPERIMENTS ON SIMULATED SNF BUNDLES

Of the three applications described above, the thermal analysis of spent fuel rods is the one that is driving the current research. The author's current project is an extension of Canaan's investigation into the thermal behavior of enclosed SNF rods begun in 1991 at The University of Texas at Austin (UT).

Canaan's doctoral research experimentally modeled a single, horizontally-oriented BWR spent fuel assembly within an isothermal enclosure. The individual spent nuclear fuel rods were modeled with tubular stainless steel heater rods, each with an electric resistance heating element that ran through the rod centerline. The rods were made to the same diameter as BWR spent fuel rods and arranged in an aligned array of the same spacing as rods within a BWR fuel assembly. The rods were made of materials which are thermally similar to actual BWR rod materials. By making the rods long enough, and by thermally insulating the ends of each rod, the axial flow and heat transfer effects were minimized, and a 2-D analysis was possible.

The electric heater rod bundle was surrounded with a rectangular, water-cooled copper enclosure that was maintained at constant temperature on all sides. The entire rod bundle and enclosure was placed within a pressure vessel, which allowed experiments with different types of gas at varying pressures. By independently varying the vessel pressure, the type of gas, and the rod power, a wide range of natural convection flow regimes could be investigated. Two types of backfill gas were used, helium and nitrogen. The heater rod power input, which was approximately the same for each rod, was set to levels that simulated the range of decay heats likely to be generated in actual spent fuel assemblies of various ages stored within a transportation cask. The surface temperature of each rod within the array was measured with thermocouples placed just beneath the rod surfaces. The rod surfaces were assumed to be isothermal around their circumference. The validity of this assumption was confirmed both with experimentation and numerical analysis [Canaan, 1995].

By measuring the temperatures of all rod surfaces, the enclosure temperature, the heater rod input power, and the thermal radiation properties of the rod and enclosure surfaces, Canaan was able to produce dimensionless heat transfer correlations not only for the overall rod bundle, but for each individual rod as well. These results were published in his Ph.D. dissertation [1995].

1.3 Objectives of the Current Research

To extend the fundamental knowledge gained from Canaan's experiments, the 8 by 8 aligned array of heater rods was modified to form a staggered array. Most studies and experimental heat transfer correlations for flow across tube bundles give results for both aligned and staggered array configurations. While a staggered array using heater rods of the size and spacing used in this experiment does not directly relate to a specific spent fuel assembly, it is important to compare Canaan's results to a staggered array and to other enclosed tube arrays to learn more about the fundamental characteristics of natural convection in this configuration.

For example, consider the fact that many published results for overall heat transfer coefficients of a tube array show that a staggered array transfers heat more effectively from the tubes to the fluid, both in forced and in natural convection situations [Choi and Cha, 1990; Incropera and DeWitt, 1990]. If it could be shown that heat transfer could be improved significantly within a BWR spent fuel assembly simply by shifting the rods to a staggered array spacing, this reconfiguration might be warranted in order to reduce the cost of the cask by simplifying its thermal design. This would make the cask safer, and could possibly reduce the cost of the cask by reducing the amount of thermal engineering needed to handle the cask's lowered maximum temperature.

A diagram of the cross-section of Canaan's array and the current staggered array is shown in Figure 1.5. This staggered array was made by removing one heater rod from the first, third, fifth, and seventh rows (the top row of rods is considered the first row), and then shifting these rows horizontally. Thus, Canaan's array contained 64 rods, and the current staggered array contains 60 rods.

Figure 1.5 also shows the outer diameters of the heater rods, the "pitch", or spacing between each rod, and the dimensions of the inner walls of the enclosure. Other details of the experimental setup, such as the heater rod construction, the pressure vessel, thermocouples, enclosure cooling system, rod power supply, and the data acquisition system are described in Chapter 3 -- Experimental Apparatus and Setup.

There are two basic objectives of this experimental work. The first is to produce non-dimensional Nusselt-Rayleigh number heat transfer correlations for this staggered array and compare the results to the Canaan aligned array. The vessel pressure and rod powers are independently varied over a similar range as in the Canaan experiment. The comparison between the staggered and Canaan's aligned array investigates whether or not overall heat transfer is improved or hindered by changing the array geometry. Also, correlations are compared for individual rods to see how the fundamental natural convection behavior changes for specific rods between aligned and staggered arrays.

The second objective is to compare the results from the staggered array experiment to other experiments done on natural convection from heated tube arrays. Other research has experimentally investigated natural convection from both aligned and staggered arrays, both in enclosed and non-enclosed arrays. Hopefully, some useful information about the fundamental nature of natural convection from enclosed tube arrays can be obtained by comparing the current staggered array results to these previous experimental works. However, not much experimental research has been performed on enclosed tube arrays. In fact, the UT research begun in 1991 by Canaan and continued in this thesis is the first experimental investigation of enclosed, heated tube arrays that both fully describes the temperature variation for all of the rods within the array and that produces radiation-corrected Nusselt and Rayleigh number correlations.

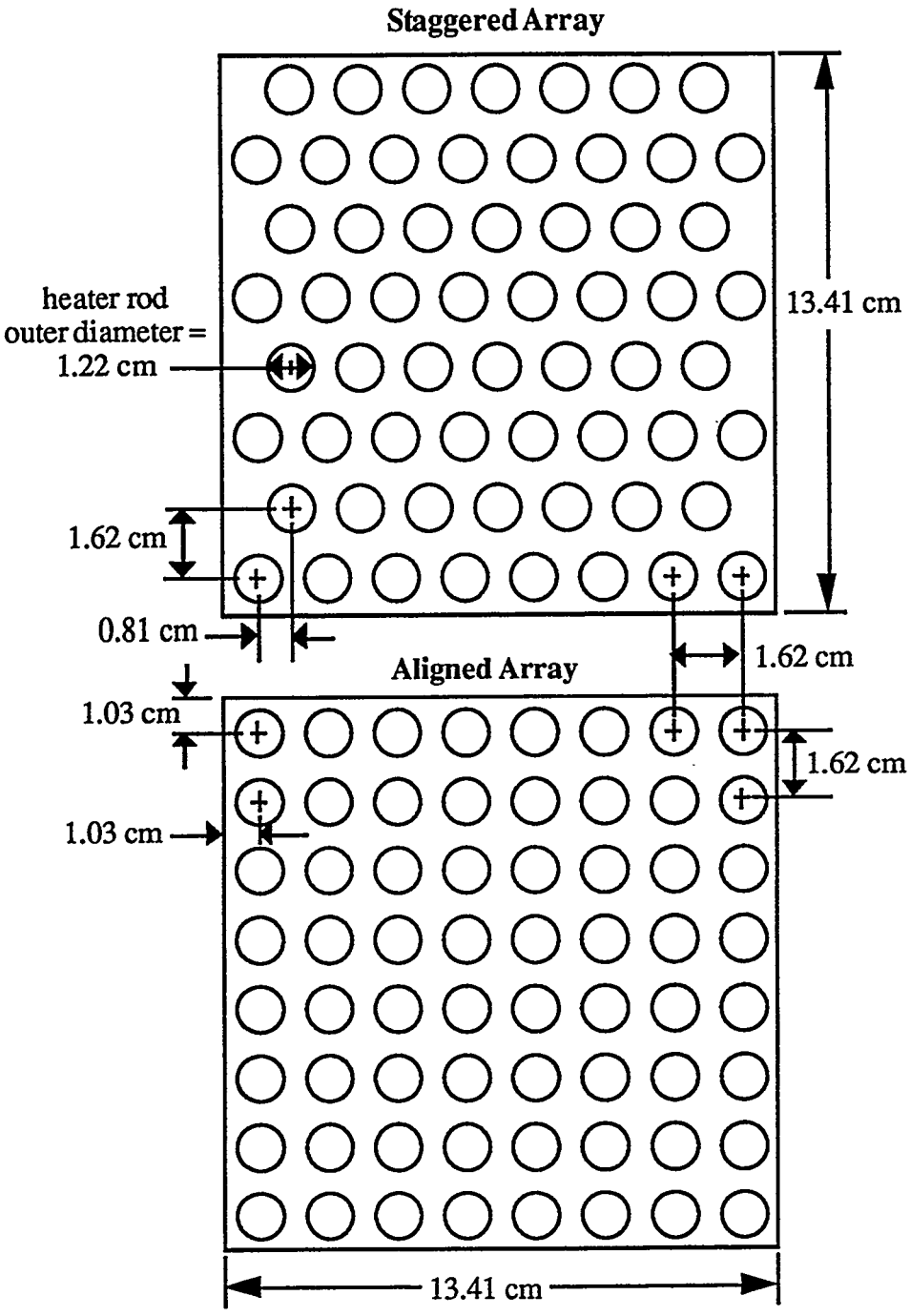

Figure 1.5 Cross-sectional views of the geometry of Canaan's aligned array and the current staggered array.

Furthermore, this experimental investigation of natural convection within an enclosed tube array is important because numerical techniques have difficulty modeling the full, multi-mode heat transfer and flow behavior within the array. Numerical techniques can model laminar natural convection in this geometry relatively easily; however, it is much more difficult to solve the necessary equations when natural convection is coupled with thermal radiation between the rod surfaces and the enclosure. The modeling task becomes even more difficult when one realizes that for higher rod powers, the natural convection flow is probably turbulent within the array, and that an even more sophisticated model is needed.

1.4 LITERATURE SURVEY

While the available literature regarding natural convection within enclosed, horizontally-oriented tube arrays is limited, particularly for the staggered array configuration, there are some studies that are important and that relate closely to this research. One main reference used for this work is Canaan's 1995 Ph.D. dissertation, *Natural Convection Heat Transfer Within Horizontal Spent Nuclear Fuel Assemblies*.

One of the best studies of natural convection from a heated, staggered cylinder array comes from a 1990 report from Choi and Cha. They published results from a flow visualization study of natural convection from a horizontally-oriented array of heated cylinders. These cylinders were hollow, stainless steel tubes about 10 cm in length. These tubes were arranged in a rectangular, aligned array of 12 rows and 7 columns. A DC current passed through the walls of the tubes was used to heat the rods, and a Mach-Zehnder interferometer was used to record visual images of the temperature contours around each rod. The tube bundle could be rotated about one corner of the rectangle to produce a staggered array. They used two different tube diameters, 3.2 and 6.4 mm, at a spacing of about 13 mm, yielding an approximate pitch-to-diameter ratio of 4 and 2, respectively. Their array was open to the quiescent room air and was not enclosed. Figure 1.6 gives a diagram of the rod array used by Choi and Cha. Notice that the staggered array

produced by rotating the aligned array is different geometrically from a staggered array produced by horizontally shifting alternate rows of rods.

Choi and Cha used the temperature contour and temperature gradients measured directly from the interferometric images to calculate Nusselt number as a function of circumferential angle around each rod. They also calculated rod-averaged Nusselt numbers for several rods in the array, and compared results for a staggered versus an aligned array. However, since they did not calculate an array-averaged Nusselt number, their array was not enclosed, and their staggered array had a different configuration, their quantitiative results are not directly comparable. Also, because they did not include a correction for radiation, the correlations they produced are the result of multi-mode heat transfer, not just convection. This means that the total heat transfer is counted as all convection, which tends to inflate the Nusselt number. But since they did compare an aligned array to a staggered array, their results have some bearing on the current research. The results of the current UT research are compared to Choi and Cha's work in Chapter 5 -- Results and Discussion.

In 1984, Warrington and Weaver presented their results of an investigation of both aligned and staggered arrays of heated, horizontally-oriented rods within a water cooled, rectangular enclosure. They studied a 4 by 4 and a 3 by 3 aligned array, and a 14-rod and an 8-rod staggered array. The hollow copper tubes were 19.5 cm in length and 4.2 cm in diameter, with a wall thickness of 0.4 cm. Heat was supplied to the inner surface of the tubes with DC-powered heat tape applied to the inner tube surface. Since their rods were fairly short, conduction losses were significant, but they were corrected for using a 1-D fin conduction analysis.

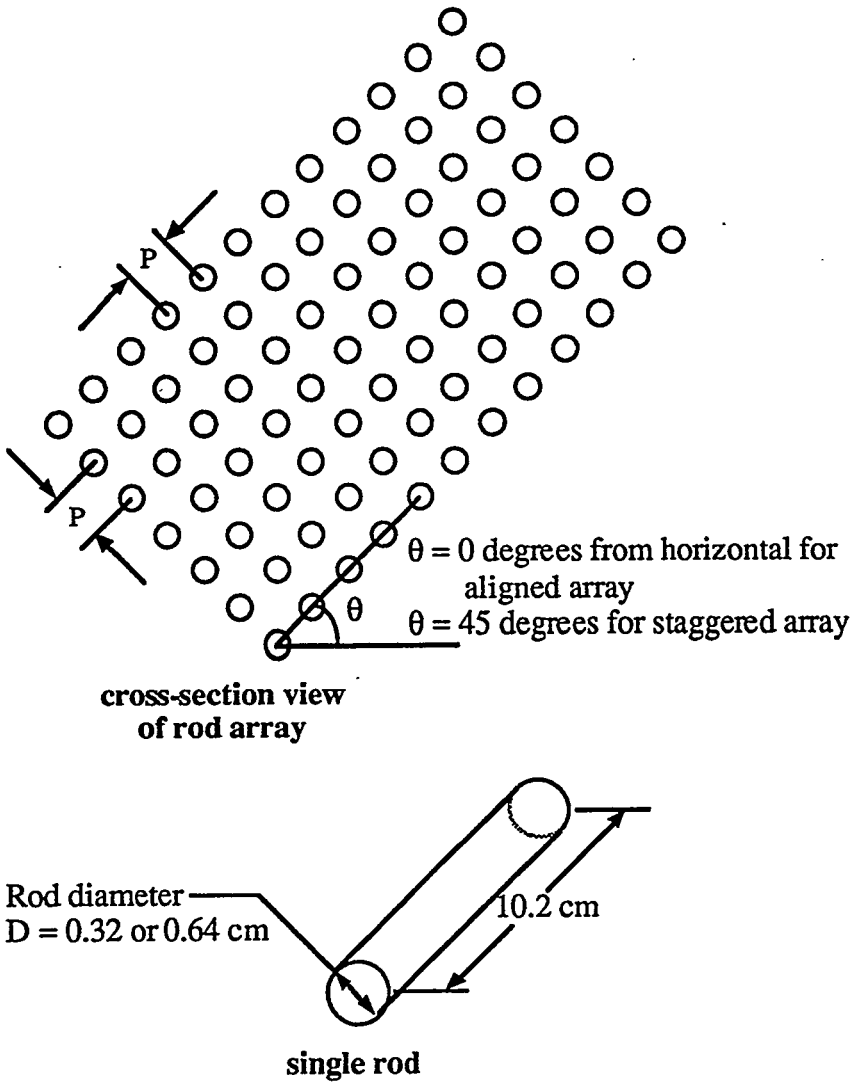

Figure 1.6 Diagram of Choi and Cha's tube array.

Warrington and Weaver accounted for radiation by evacuating the enclosure to a very low pressure, then adjusting the rod power levels independently in order to produce the same rod temperature field as when the enclosure was filled with fluid. The rod power used to produce this temperature field within the evacuated enclosure was the radiation heat transfer. However, the authors did not state the error of this method. The problem with this form of radiation correction is that independently varying each rod power to produce the same temperature field as the multi-mode heat transfer case is like trying to solve a set of N linear equations (where N is the number of rods--14 or 16 in this case) simply by guessing values independently for all the coefficients--it is not very accurate. However, it is possible that the error of this method may be within the overall experimental error caused by the uncertainty of the other measurements.

The enclosure was tested with four different fluids--air, water, glycerine, and silicone oil. The rod and enclosure surface temperatures were measured with embedded type T thermocouples. A diagram of their geometry is shown below in Figure 1.7.

Warrington and Weaver calculated only bundle-averaged Nusselt numbers for the four arrays. That is, they did not calculate Nusselt numbers for individual rods. They report that "the enclosure reduced the expected increase in both the average and the local heat transfer coefficients caused by changing the inner body [cylinder array] from an in-line arrangement to a staggered arrangement of comparable spacing." It is not clear exactly how much of an increase the authors were expecting based on their report; however, it is clear that they expected a larger difference in average Nusselt number between an aligned and a staggered array. They report that at lower Rayleigh numbers, a staggered array had a bundle-averaged Nusselt number that was about 10 percent higher than a comparable aligned array. However, at higher Rayleigh numbers, the bundle-averaged Nusselt number was about the same. These results are compared to the UT aligned and staggered results in Chapter 5.

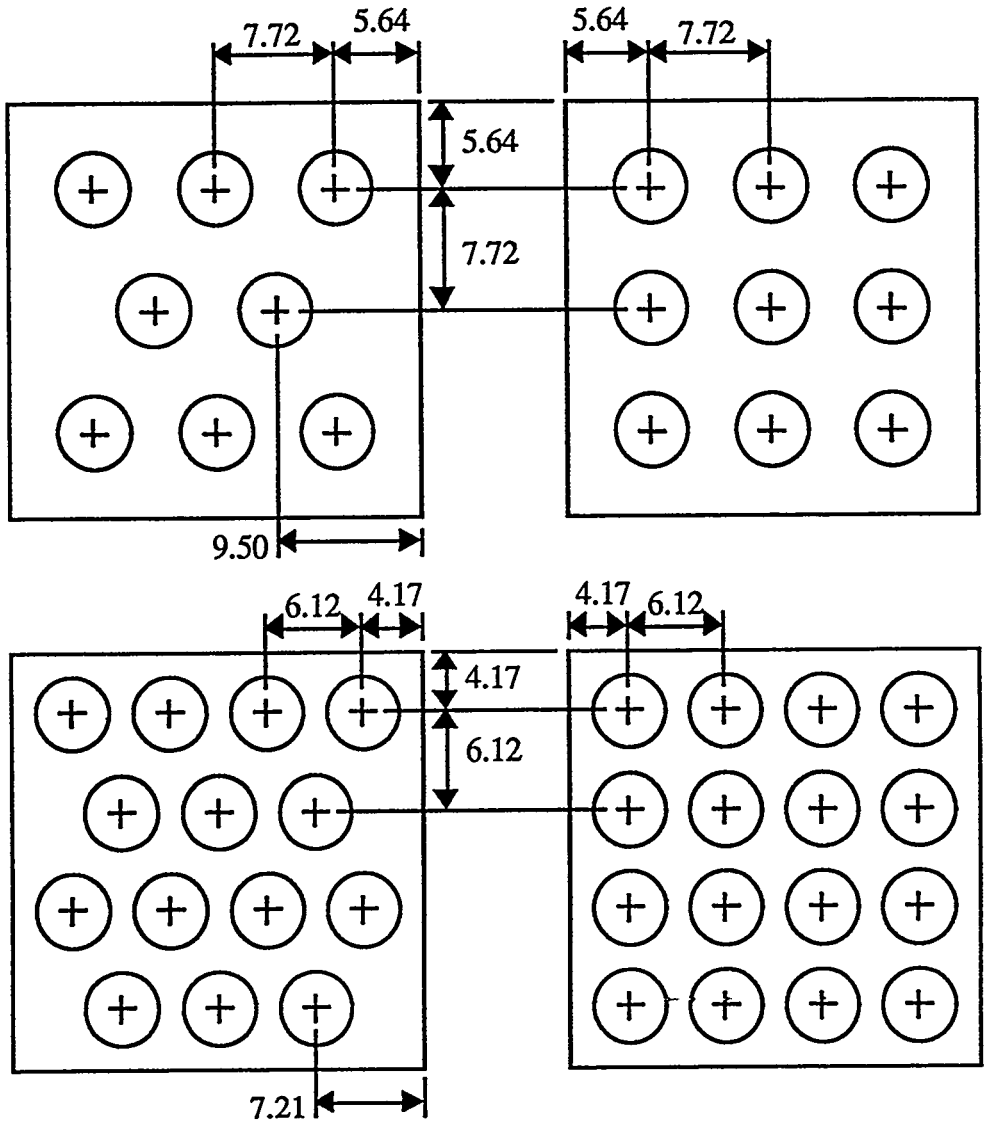

-- All dimensions are in centimeters

-- All rods are 4.22 cm in diameter

-- Enclosure is cubical in cross-section and is 26.67 cm on a side

Figure 1.7 Diagram of Warrington and Weaver's 4 enclosed tube array geometries.

In 1979, Tilman reported results for a non-enclosed array of aligned and staggered cylinders that were surrounded by room air at atmospheric pressure. The two arrays were a 4 by 4 and a 14-rod staggered array. The rods were 1.3 cm in diameter and 10.2 cm long. Tilman neglects conduction end losses; however, the short length of the rods makes this assumption questionable. Power was supplied using resistance heaters in the centerline of the rods, and rod surface temperatures were measured with a single thermocouple soldered to the rod surface at the midpoint. Tilman reports that rods above the bottom row had lower Nusselt numbers than that of a single, isolated cylinder, due to the heating of the fluid that surrounded the upper rods by the buoyant plume from the lower rods. Also, Tilman reports that the staggered configuration had an average Nusselt number that was about 17 percent higher than the aligned array. However, since Tilman made no correction either for conduction end losses or for radiation losses, his Nusselt numbers are likely inflated due to counting all of the heat loss from the rods as leaving through convection only.

Sparrow and Niethammer [1981] provide an interesting study of the interaction between two heated, horizontal cylinders located directly above one another in a vertical plane. They supplied the same internal electric heat generation to both rods, and then varied the vertical rod center-to-center separation distance, P, between the rods. Both radiation and conduction end losses were taken into account. First, for a given rod power, they calculated the rod-averaged Nusselt number for a single cylinder. They then compared the Nusselt numbers for the two interacting cylinders. As they varied the distance of the upper rod from the lower rod, they describe 4 different spacing regimes and the effect on the Nusselt number of each rod. At very small spacings ($P \leq 1.2D$, where D is the cylinder diameter), the upper rod was heated by the plume from the lower rod, and had a lower Nusselt number than the lower rod. Also, because a stagnation region formed between the two rods, the lower cylinder had a lower Nusselt number than the single, isolated cylinder. At larger spacings ($P \geq 2D$), the lower rod had a Nusselt number that was about the same as the isolated cylinder. For $P = 2D$ to $3D$, the upper rod was still heated by the plume from the lower rod, and had a lower Nusselt number than the

bottom rod. However, at higher separation distances (P = 7D to 9D), the Nusselt number of the upper rod actually became higher than that of the lower rod. This effect is caused by the upper rod being in a forced convection situation caused by the plume from the lower rod. Even though the plume does tend to preheat the upper rod, at these higher separation distances the increased flow velocity on the upper rod is a more dominant effect. At very high separation distances ($P \geq 10D$), both the upper and lower cylinders behaved like single, isolated cylinders. The above results are pertinent to the discussion of the Nusselt numbers of rods of different positions within the UT staggered and aligned arrays, and this comparison is also discussed in Chapter 5.

One of the oldest studies of natural convection from horizontal, heated cylinders comes from an Air Force report by Eckert and Soehngen released in 1948. They used interferometric techniques to produce very sharp pictures of the temperature contours around three heated, horizontal copper cylinders that were 2.2 cm in diameter . They used the temperature gradient from the interferograms to find the Nusselt number of the three rods for two different geometric arrangements. The first arrangement had all three cylinders lined up in a vertical column with each other, while the second arrangement shifted the middle rod over to the right by one half of a rod diameter. The separation distance between each of the cylinders when they were all in line was about 1.9 rod diameters. For the in-line arrangement, they found that the bottom rod Nusselt number was about the same as an isolated cylinder, and that the middle and upper rods had Nusselt numbers that were 83% and 65% of the Nusselt number for the bottom rod, respectively. When the middle rod was shifted over, it's Nusselt number became 103% of the lower rod, and the upper rod's Nusselt number was 86% of the Nusselt number for the lower rod. Thus, the overall heat transfer coefficient was higher in the staggered arrangement than for the in-line arrangement. The increase in Nusselt number for the shifted middle rod was due to the increased flow velocity past the middle cylinder due to the plume from the lower cylinder. Figure 1.8 shows the temperature contours from the staggered arrangement of their experiment.

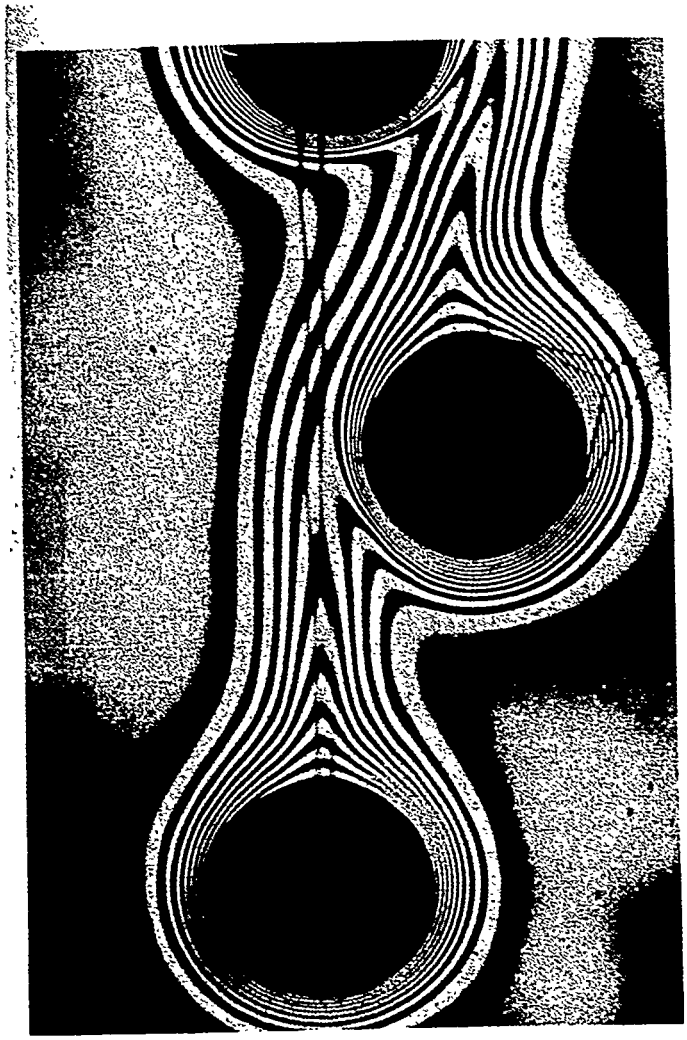

Figure 1.8 Temperature contours from an interferogram of three heated horizontal cylinders [Eckert and Soehngen, 1948].

1.5 THESIS OVERVIEW

This chapter has briefly introduced the topic of natural convection from heated tube arrays oriented horizontally within an enclosure. Some applications of the research were given, most notably the thermal characterization of spent nuclear fuel assemblies within a storage cask. The objectives of the research were given, and a brief survey of some pertinent related research was provided.

Chapter 2 derives or simply states some of the important equations needed for this research. It defines the important non-dimensional quantities both for the bundle-averaged correlations and for the individual rod correlations. Also, Chapter 2 discusses the calculation of the radiation heat transfer component, which is important in making sure that the correlations presented are system independent and can be used for other rod bundles.

Chapter 3 describes the equipment and experimental apparatus used in this experiment. Major features include discussion of the heater rods and their construction, the placement of thermocouples just beneath the rod surfaces, the copper boundary enclosure (CuBE) and it's water cooling system, the pressure vessel, the power supply system, and the automated data acquisition system used to measure thermocouple temperatures and rod power levels. Diagrams and figures are used to show the layout of the overall system.

Chapter 4 describes the procedure used to run the experiments, take data, and reduce the data to produce the heat transfer correlations. The quantities that were independently varied are discussed, and examples of calculations performed to obtain bundle-averaged and individual rod heat transfer correlations are given. Also, the procedure for using the numerical radiation code described in Chapter 2 is given. Finally, this chapter discusses the overall experimental uncertainty of the heat transfer results and correlations presented in Chapter 5.

Chapter 5 is the heart of the thesis. It presents the results of the experiment in the form of non-dimensional heat transfer correlations, both for the average bundle and for individual rods. These results are discussed in three ways. First, the results are examined for interesting trends within the staggered array. Second,

the results are compared to Canaan's aligned array. Finally, the results are compared to other experiments on natural convection from horizontal tube bundles. The most important trends and results are summarized at the end of the chapter.

Chapter 6 concludes the thesis and describes some interesting possibilities for future work on this subject.

Chapter 2 -- Theory

This chapter briefly discusses some basic theory behind the equations used to calculate the Nusselt and Rayleigh numbers, both for the individual rods and for the tube array as a whole. The first section discusses the heat transfer behavior for a single heater rod. The heat transfer mechanisms are diagrammed, and the Nusselt and Rayleigh numbers are defined for the individual rod. Some simplifying assumptions are made and discussed. The second section discusses the heat transfer behavior for an enclosed rod bundle, and derives the Nusselt and Rayleigh numbers averaged over the entire rod bundle. The final section discusses the calculation of the radiation component of the heat transfer, which is necessary to ensure that the dimensionless correlations produced are independent of the surface radiation properties of the rods. Keep in mind that this analysis is for a rod or a rod array that is at steady state; that is, no transient heat transfer is considered in this thesis.

2.1 Heat Transfer for a Single Heater Rod

Figure 2.1 shows a simplified cross-sectional view of one of the heater rods used in this experiment. The exact dimensions and construction of these rods is given in Chapter 3. The rod is heated by a nichrome wire coil that runs down the center of the rod and dissipates DC current to generate heat. Since the magnesium oxide ceramic that fills the inside of the rod has a relatively low thermal conductivity, the heat dissipated from the wire and conducted through the ceramic imposes a uniform heat flux on the inside surface of the cladding, q''_{inner}. However, this does not mean that the heat flux on the outside of the cladding is uniform. In fact Canaan demonstrated, using both numerical techniques and experimental measurements, that the outside surface of the cladding is *isothermal* to within 0.5 degrees C over the entire range of experimental parameters [Canaan, 1995]. The basic explanation for this is that the high-conductivity stainless steel

cladding conducts heat very easily in the circumferential direction, and thus the circumferential temperature variation is very small.

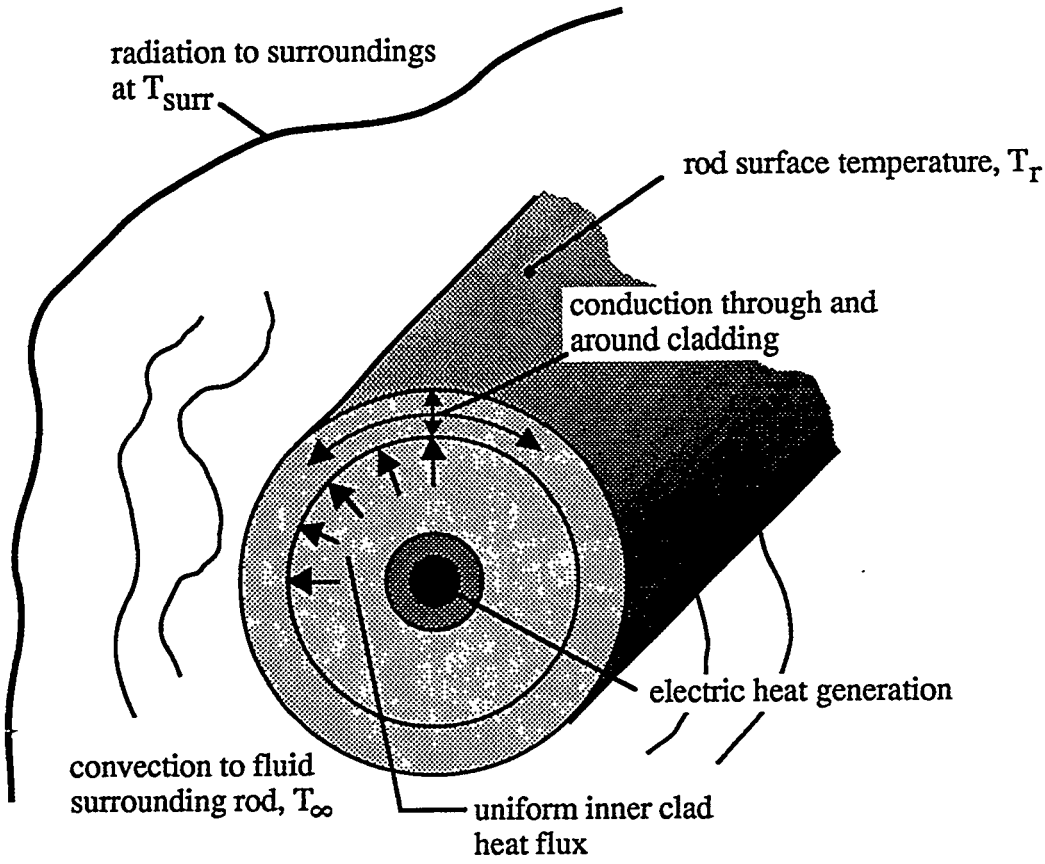

Figure 2.1 Diagram of heat transfer modes for a single heater rod.

The heat is then removed from the rod surface by convection to the fluid surrounding the rod and by radiation to other surfaces surrounding the rod. Heat can also flow by conduction in the axial direction (into or out of the page in Figure 2.1). However, since the length of the rods is about 65 times the rod diameter, and since the ends of the rods are insulated quite well, axial conduction is minimal. Canaan showed that for these heater rods, the axial temperature variation along the heated length of the rod is much less than 1 percent of the temperature at the rod's midpoint [Canaan, 1995]. There may, however, be some 3-D convection occurring near the ends of the rod. For this analysis, only a 2-D convection model is considered.

2.1.1 Nusselt Number for an Individual Heater Rod

Natural convection from the rod surface to the surrounding fluid is characterized by the Nusselt and Rayleigh numbers. The Nusselt number is the dimensionless temperature gradient at the surface, and the Rayleigh number defines the strength of the buoyant forces that drive natural convection flow from the rod surface. In general, the Nusselt number is given by

$$Nu = \frac{hx}{k} \tag{2.1}$$

where h is the convection coefficient, x is some characteristic length, and k is the thermal conductivity of the fluid surrounding the body or surface of interest. For a single heater rod, this characteristic distance is the rod diameter, d. The fluid thermal conductivity is evaluated at the "film temperature," T_f, which is the average of the rod surface temperature, T_r, and the bulk temperature of the fluid to which the rod is transferring heat, T_∞. The convection coefficient, h_r, at a given point on the rod surface is given by

$$h_r = \frac{q_r''}{\Delta T} \tag{2.2}$$

where q_r'' is the heat flux at a point on the rod surface, and ΔT is the temperature difference $T_r - T_\infty$, where T_r is the surface temperature on the rod at the same point.

While the characteristic rod temperature difference, ΔT, is uniform around the rod surface, the local heat flux, q_r'', is not. Since there is no simple way in this experiment to determine the local heat flux on the rod surface as a function of circumferential angle, a rod-averaged convection coefficient is used. This coefficient is defined as

$$h_{r,avg} = \frac{q''_{r,avg}}{\Delta T} = \frac{q'_r}{(\Delta T)\pi d} = \frac{q_r}{L(\Delta T)\pi d} \qquad (2.3)$$

where $q''_{r,avg}$ is the average heat flux on the rod surface, calculated by dividing the heat flow per unit rod length at the rod surface, q_r', divided by the circumference of the rod, πd. The heat flow per unit rod length is the total rod power input, q_r, divided by the heated length of the rod, L. By using this convection coefficient, one can calculate a rod-averaged Nusselt number using equation 2.1.

However, the above convection coefficient has assumed that all of the heat input to the rod was removed by convection only. This is not actually true, since some of the heat was removed by radiation as well. A convection coefficient based only on the heat removed through convection is required to accurately characterize the convection behavior from the rod. The heat balance at the rod surface, on a per-unit-length basis shows that

$$q'_r = q'_{rad} + q'_{conv} \qquad (2.4)$$

where q_r' is the heat input to the rod per unit length, q'_{rad} is the net radiation heat transfer from the rod to the surroundings per unit rod length, and q'_{conv} is the net heat transferred from the rod by convection per unit length. The total power input to the rod per unit length is given by

$$q'_r = \frac{i^2 R}{L} \tag{2.5}$$

where i is the current flowing through the nichrome coil running along the rod centerline, and R is the total electric resistance of the wire. If a single heater rod was surrounded by a very large enclosure that was at a constant temperature, T_{surr}, and if the surface emissivity over the entire rod surface was a constant, ε, then the net radiation from the rod per unit length would be given by

$$q'_{rad} = (\pi d) q''_{rad} = (\pi d) \varepsilon \sigma (T_r^4 - T_{surr}^4) \tag{2.6}$$

where T_r is the rod surface temperature in Kelvin, σ is the Stefan-Boltzmann constant (5.67×10^{-8} W / m^2 - K^4), and d is the rod diameter. The convective heat transfer per unit length could be calculated from equation 2.4, and then the rod-averaged heat transfer coefficient would be given as

$$h_{r,avg} = \frac{q'_{conv}}{(\Delta T)\pi d} \tag{2.7}$$

The Nusselt number would then be given by

$$Nu_{r,avg} = \frac{h_{r,avg} d}{k} = \frac{(q'_r - q'_{rad})\cancel{d}}{(\Delta T)\pi \cancel{d} k} = \frac{\left(\frac{i^2 R}{L} - \pi d \varepsilon \sigma \left(T_r^4 - T_{surr}^4 \right) \right)}{(\Delta T)\pi k} \tag{2.8}$$

However, in general, the surroundings of the rod are not at a constant temperature. In this thesis experiment, a given heater rod is surrounded by many other rods that are at varying temperatures. Some rods also exhange thermal radiation with the cool enclosure wall. Thus, the Nusselt number that is properly corrected for radiation must take the complexity of the surroundings into account. In general, the net radiation heat rate per unit length for each rod, q'_{rad}, is not given by equation 2.6. The correct calculation for q'_{rad} will be discussed later in this

chapter. Once the correct method of calculating q'_{rad} is known, the final form for the Nusselt number of an individual rod will be given by

$$Nu_{r,avg} = \frac{(q'_r - q'_{rad})}{(\Delta T)\pi k} = \frac{\left(\frac{i^2 R}{L} - q'_{rad}\right)}{(\Delta T)\pi k} \tag{2.9}$$

2.1.2 Rayleigh Number for an Individual Heater Rod

There are two dimensionless quantities that describe the strength of the flow field in a natural convection situation. These two numbers are the Grashof number and the Rayleigh number. The Grashof number is similar to the Reynolds number for forced convection flow. While the Reynolds number characterizes the ratio of the inertial forces to the viscous forces acting on a fluid particle, the Grashof number describes the ratio of the buoyant forces to the viscous forces on a fluid particle. The Grashof number is given by

$$Gr_x = \frac{g\beta(\Delta T)x^3}{\nu^2} \tag{2.10}$$

where g is the gravitational acceleration (9.81 m/s^2 at sea level), β is the coefficient of thermal expansion, ΔT is the temperature difference between the surface and the ambient surrounding fluid, x is some characteristic length scale, and ν is the kinematic viscosity of the fluid. The subscript x indicates that the Grashof number is based on the length scale defined by x. If one assumes an ideal gas, the thermal expansion coefficient is given by

$$\beta = \frac{1}{T_f} = \left[\frac{T_s + T_\infty}{2}\right]^{-1} \tag{2.11}$$

where T_f is the mean film temperature, which is the average of the surface temperature, T_S, and the ambient fluid temperature, T_∞. All of the fluid properties

for natural convection correlations, such as fluid thermal conductivity and kinematic viscosity, are evaluated at this mean film temperature.

In natural convection, heat transfer correlations are often given in the form Nu = f(Gr, Pr), where Pr is the Prandtl number, a dimensionless quantity that describes the ratio of viscous diffusivity to thermal diffusivity of a fluid. The Prandtl number is given by

$$Pr = \frac{\nu}{\alpha} \tag{2.12}$$

where α is the thermal diffusivity, given by

$$\alpha = \frac{k}{\rho c_p} \tag{2.13}$$

The variable k is the fluid thermal conductivity, ρ is the fluid density, and c_p is the specific heat at constant pressure. All of these properties are evaluated at the mean film temperature, T_f.

If a heat transfer correlation is given that involves one or several fluids that span a very narrow Prandtl number range, the correlation is often given in the form of Nu = f(Ra), where Ra is the Rayleigh number, which is the product of the Grashof and Prandtl numbers. For this experiment, the working fluids are nitrogen, which has a Prandtl number of 0.716 at 350 K, and helium, which has a Prandtl number of 0.678 at 350 K. Since these Prandtl numbers are not very different, the Prandtl number is not correlated separately in this thesis. The Rayleigh number can be written as

$$Ra_x = \frac{g\beta(\Delta T)x^3}{\nu\alpha} \tag{2.14}$$

where again, the subscript x indicates that the Rayleigh number is based on the length scale x. For an individual heater rod, the length scale is the rod diameter, d, and ΔT is the temperature difference between the rod surface and the surrounding

fluid, $T_r - T_\infty$. Thus, for an individual heater rod with an ideal gas surrounding the rod, the Rayleigh number is given by

$$Ra_d = \frac{g\beta(T_r - T_\infty)d^3}{\nu\alpha} \tag{2.15}$$

where the expansion coefficient, β, is given by equation 2.11, substituting the subscript r for "rod" instead of s for "surface."

The final results for the Nusselt-Rayleigh number correlations of the individual rods of the UT staggered array are given in Chapter 5, section 4. However, there is one major difference between the Nusselt and Rayleigh numbers used for those correlations and the Nusselt and Rayleigh numbers presented in above equations. The equations presented above are for a single heater rod that is open to an ambient, quiescent fluid. But in the UT staggered array, a given individual rod is surrounded by a cooled enclosure and by 59 other rods in a fairly tight spacing. In this situation, it is difficult to define the ambient fluid temperature, T_∞, around each rod. In this enclosed rod array experiment, a simpler and easier-to-measure choice of the characteristic temperature difference, ΔT, is between the rod surface and the enclosure temperature, T_c. The subscript "c" refers to the Copper (Cu) Boundary Enclosure, or CuBE. Thus, the Nusselt and Rayleigh numbers used for the individual rod correlations of section 5.4 are given below in equations 2.16 and 2.17. Since this thesis never calculates Nusselt numbers as a function of rod circumferential angle, the subscript "avg" will be dropped from the rod-averaged Nusselt number.

$$Nu_r = \frac{(q'_r - q'_{rad})}{(\Delta T)\pi k} = \frac{\left(\frac{i^2R}{L} - q'_{rad}\right)}{(T_r - T_c)\pi k} \tag{2.16}$$

$$Ra_d = \frac{g\beta(T_r - T_c)d^3}{\nu\alpha} \tag{2.17}$$

$$T_f = \left[\frac{T_r + T_c}{2}\right] \tag{2.18}$$

2.2 Heat Transfer for an Enclosed Rod Array

The above section has discussed the heat transfer mechanisms for a single horizontal heater rod at steady state in an unbounded, quiescent fluid medium. Let us now consider an array of rods within an enclosure. Heat generation occurs within each rod, and this heat leaves the rod by convection and conduction through the fluid surrounding each rod. Each rod also exchanges radiation with the other rods and with the enclosure surface. Ultimately, the heat generated within all of the rods is conducted, convected, and radiated to the cooled enclosure wall, which is maintained at a constant temperature through a water cooling system. The experimental apparatus and layout is described in Chapter 3.

2.2.1 Nusselt Numbers for the UT Staggered Array

The previous section described the Nusselt and Rayleigh numbers for an individual heater rod. One can also define Nusselt and Rayleigh numbers for the entire tube bundle. The full array Nusselt number is defined as

$$Nu = \frac{hx}{k} \tag{2.19}$$

where x is now some characteristic length for entire bundle, and h is defined as the total *convective* heat transfer from the rod bundle to the enclosure wall, divided by a characteristic temperature difference for the full array. This overall heat transfer coefficient is given by

$$h = \frac{\sum_{i=1}^{N} q'_{conv,i}}{4H(\Delta T)} = \frac{Q'_{conv}}{4H(\Delta T)} \tag{2.20}$$

where $q'_{conv,i}$ is the convective heat transfer per unit length for an individual rod, i, and ΔT is some characteristic temperature difference between the rod bundle and the enclosure. "H" is the height of the CuBE side wall. The convective heat rate per unit length for each rod can be calculated by subtracting the radiative heat rate per unit length for each rod, q'_{rad}, from the total heat input for each rod, given by equation 2.5. The calculation of q'_{rad} for each rod is given in section 2.3 of this chapter.

The characteristic temperature difference for the rod bundle can be defined in one of two ways. The first way defines a characteristic temperature difference based on the *average* surface temperature of all of the rods, T_{bund}, minus the CuBE temperature, T_C. The second way defines the characteristic temperature difference based on the surface temperature of the hottest rod in the array, T_{max}, minus the CuBE temperature, T_C. This thesis will refer to the characteristic temperature difference based on the bundle-averaged rod temperature as ΔT_{bund}, and the characteristic temperature difference based on the maximum rod temperature as ΔT_{max}.

These two definitions for the bundle characteristic temperature difference can be used in equation 2.20 to define the full array convection coefficient, and then in equation 2.19 for the full array Nusselt number. The characteristic length used for the full array correlations is the CuBE height, H. Thus, the two Nusselt numbers used for the full array heat transfer correlations are given as

$$Nu_{bund} = \frac{h_{bund}H}{k} \tag{2.21}$$

$$Nu_{max} = \frac{h_{max}H}{k} \tag{2.22}$$

For both definitions of the Nusselt numbers, the thermal conductivity is based on the bundle-averaged film temperature, $T_{f,bund}$, which is defined as

$$T_{f,bund} = \frac{T_{bund} + T_C}{2} \tag{2.23}$$

where T_{bund} is the average of all of the rod surface temperatures. The above definitions of the Nusselt number are used to calculate the results for the rod bundle that are presented in Chapter 5, section 3.

2.2.2 Rayleigh Numbers for the UT Staggered Array

As with the Nusselt number, one can use two different definitions of the bundle Rayleigh number based on the two different definitions of the bundle characteristic temperature difference described above. These two Rayleigh numbers are defined as

$$Ra_{bund} = \frac{g\beta(\Delta T_{bund})H^3}{\nu\alpha} \tag{2.24}$$

$$Ra_{max} = \frac{g\beta(\Delta T_{max})H^3}{\nu\alpha} \tag{2.25}$$

As with the above full array Nusselt numbers, the expansion coefficient β, the kinematic viscosity ν, and the thermal diffusivity α are evaluated at the mean bundle film temperature defined in equation 2.23. These two Rayleigh numbers are used in conjuction with the Nusselt numbers of equations 2.22 and 2.23 to correlate the bundle heat transfer data.

There is an alternate definition of the Rayleigh number that uses a heat flux, rather than a temperature difference. In general, this modified Rayleigh number is given by

$$Ra_{mod} = \frac{g\beta q'' x^4}{\nu\alpha k} \tag{2.26}$$

where q" is the heat flux at the surface of interest. For the enclosed rod bundle, this modified Rayleigh number is given as

$$Ra_{Q'} = \frac{g\beta Q'_{conv} H^4}{4H\nu\alpha k} = \frac{g\beta Q'_{conv} H^3}{4\nu\alpha k} \tag{2.27}$$

This modified Rayleigh number is used along with the bundle-averaged Nusselt number defined in Equation 2.21 to produce the third type of correlation for the bundle heat transfer data presented in Chapter 5.

Morgan (1975) has recommended a power curve correlation for Nusselt and Rayleigh number data for a single, smooth, horizontal cylinder in natural convection. It has the form $Nu = C(Ra)^n$, where C and n are constants. Piecewise correlations for the individual rod heat transfer data and the full bundle data are correlated in this form, using a least-squares curve fit analysis. All of these correlations for the UT staggered array are presented in Chapter 5.

2.3 Calculation of the Radiation Component, q'_{rad}

In order to produce dimensionless heat transfer coefficients that are not dependent on the specific radiative properties of the apparatus used in this particular experiment, the Nusselt and Rayleigh numbers must be based on the net *convective* heat rate per unit length, q'_{conv}, and not the total heat rate per unit length, q'_r. As shown in the energy balance of equation 2.4, the net radiative heat flux per unit length, q'_{rad}, is needed to obtain the net convective heat rate.

2.3.1 Experimental vs. Numerical Determination of q'_{rad}

There are two ways to obtain this radiative heat transfer component. The first way involves an experimental approach. Assume that one has measured a complete set of rod and enclosure surface temperatures for a certain rod input power and pressure. The heat input to each rod leaves through radiation and convection, neglecting axial conduction losses. If the pressure vessel were then totally evacuated, then the only way heat would be exchanged would be through radiation. If the power to each rod were then changed independently so that the surface temperatures of all of the rods and the enclosure matched the "at pressure" temperature field, then the power input to each rod for the evacuated vessel would be equivalent to the net radiative heat rate for each rod for the "at pressure" case.

While this method is the most direct way to obtain the radiative heat transfer component, there are two difficulties with this technique. First, it is very difficult to produce a "hard" enough vacuum with the current UT equipment to reduce the thermal conductivity of the gas low enough to where all heat transfer is essentially radiation. Second, this method requires independently adjusting the power to all rods of the array to reproduce the temperature field, which is a problem similar in complexity to solving a set of N equations in N unknowns, where N is the number of rods in the array. Since the UT staggered array has 60 rods, and since the dependence of radiation on temperature is a fourth-power relationship, not a linear relationship, this is a very complex problem that would require a sophisticated power control system.

The second way to calculate the radiative heat transfer component is by using the experimentally measured surface temperatures to calculate the radiative heat flux numerically. Because the UT equipment could not produce a low enough vacuum, and because of the difficulties associated with properly controlling the power independently for each rod, the numerical calculation method was chosen.

2.3.2 Numerical Determination of the Radiation Component, q'_{rad}

For the geometry of this problem, a typical first analysis of the radiation exchange between the rods might focus on calculating the view factors (also called

configuration factors) between each cylinder and the other cylinders and between each cylinder and the CuBE wall. In other words, one might calculate a view factor between the lower corner cylinder and the cylinder next to it. At first, this seems like a reasonable thing to do, since each rod is approximately isothermal around its circumference. This means that the emitted heat flux at the rod surface, $q''_{emitted} = \varepsilon\sigma T_r^4$, is constant around each rod circumference. Unfortunately, the use of view factors between the entire cylinder surfaces requires that the entire surface have uniform *radiosity*, not just uniform emitted heat flux [Seigel and Howell, 1992]. The radiosity is the emitted heat flux plus the radiation from other sources that is reflected from the rod surface. Since the rods and walls that surround a given rod are not all at the same temperature, the radiation that is reflected from a given rod surface varies around the rod circumference. Thus, the rod surfaces must be broken up into smaller areas, and then the assumption of uniform radiosity made over the surface of the smaller area element.

This thesis uses a finite element method developed by Burns [1995] to solve for the net radiative heat flux for each rod. The code works by using input files that describe the geometry and temperature boundary conditions of the enclosed rod array, and then calculating the radiation exchange between small area elements on the rod surfaces. The details of radiation heat transfer and the operation of the code that Burns developed to calculate the radiation for each rod of an enclosed array are very complex and are described in detail by Canaan [1995]. The code used to calculate the radiation heat transfer for each rod is essentially the same as that of Canaan, except that in the current work the rods are in a different configuration. However, it is helpful to briefly mention the basics of how the code operates.

In the analysis of radiation in this experiment, several assumptions are made regarding the radiation heat transfer and the radiation properties of the interior surfaces of the rod bundle. These assumptions are:

Nonparticipating media within the enclosure. It is assumed that the gas or fluid that fills the enclosure and surrounds the rods is transparent to thermal radiation. Seigel and Howell [1992] state that helium and nitrogen gas are transparent to thermal radiation, thus this approximation is likely valid.

Diffuse, gray, opaque surfaces. For the UT aligned and staggered array experiments, the outer surfaces of all rods and the inner CuBE wall were coated with Pyromark 2500 flat black paint, manufactured by Big Three Industries. Experiments conducted at NASA [Wade and Slemp, 1962], at Sandia National Laboratories [Longenbaugh, et al, 1990], and at UT [Canaan, 1995], have shown that the surface emissivity, ε, is relatively constant over all of the radiation wavelengths of interest, and that the paint obeys Lambert's cosine Law for diffusely emitting surfaces.

Surface emissivity is invariant with changing surface temperature. The Sandia Labs study of Pyromark 2500 paint on a smooth, mild steel surface showed that the emissivity values for this paint over the temperature range of this experiment (approximately 20 to 150 degrees C) ranged from 0.81 to 0.83, with an experimental error of about 0.02. The NASA study gave an emissivity for this same paint on 304 stainless steel of 0.78 ± 0.02, and this value did not vary over a similar temperature range. An experimental investigation of the emissivity of Pyromark 2500 was also conducted at the UT facilities, using an Inframetrics thermal imaging camera. This investigation, which is thoroughly described in Canaan's dissertation, yielded an emissivity value of 0.8. Aliaga [1992] reports an experimental uncertainty of about 0.02 in emissivity values using this method. Thus, for this experiment, the emissivity of all interior surfaces within the rod bundle was taken to be 0.8 ± 0.02, and was assumed to be independent of surface temperature for the experimental conditions encountered.

Figure 2.2 defines some of the important quantities used to calculate the net radiation component from each rod. Consider two points, designated nodes i and j, which are on the surfaces of two bodies. The positions of these two points are denoted by vectors $\mathbf{r}_i$ and $\mathbf{r}_j$. The vector between the two points is defined as $\mathbf{r}_{ij}$, which is equal to the vector difference $\mathbf{r}_i - \mathbf{r}_j$. Node i is in the center of an infinitesmal area element on the surface of the first body, denoted by da_i, while

node j is also at the center of an infinitesmal area element, called da_j. Both nodes i and j have outward pointing unit normal vectors, $\hat{n}_i$ and $\hat{n}_j$.

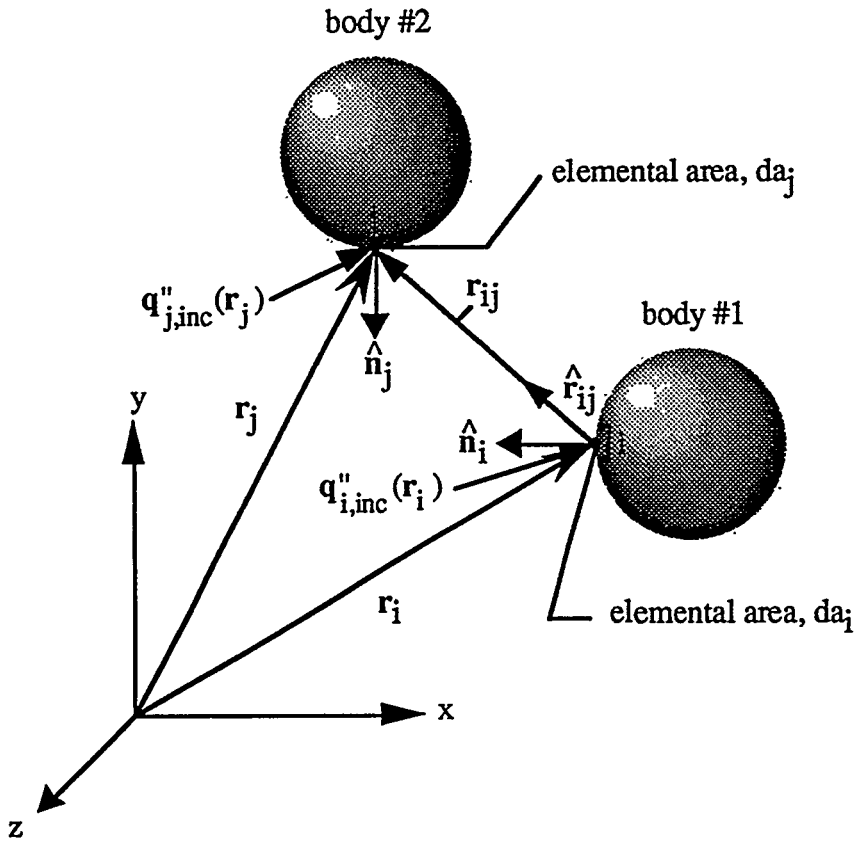

Figure 2.2 Radiation exchange between nodes on two surfaces.

We are interested in obtaining the net heat radiative flux at point i. This consists of two parts, the radiative heat flux emitted from point i due to the temperature of point i, and the flux that is incident on point i from all other sources in the domain of interest. The emitted radiative heat flux is given by $q''_{emitted} = \varepsilon\sigma T_i^4$, where ε is the emissivity of surface i and T_i is the absolute temperature of surface i. This is a relatively straightforward calculation. The second component, however, is much more complex, because it must account for the radiation incident on node i from all other points j in the computational domain, not just a single point. The mathematical expression that describes the incident radiative flux,

$q''_{i,inc}$, on point i from all other points is stated, without proof, below in equation 2.28. This equation defines the vector $\mathbf{r}_{ij}$ as the product of a unit vector $\hat{\mathbf{r}}_{ij}$ and its magnitude, $|\mathbf{r}_{ij}|$.

$$q''_{i,inc}(\mathbf{r}_i) = \frac{1}{\pi}\oint_{\partial\Omega}\left[\varepsilon_j \sigma T_j^4(\mathbf{r}_j)\right]\left(\hat{\mathbf{n}}_j \bullet \hat{\mathbf{r}}_{ij}\right)\frac{\hat{\mathbf{r}}_{ij}}{|\mathbf{r}_{ij}|^2}da_j$$
$$+\frac{1}{\pi}\oint_{\partial\Omega}\left[q''_{j,inc}(\mathbf{r}_j)\right]\left(1-\varepsilon_j\right)\left(\hat{\mathbf{n}}_j \bullet \hat{\mathbf{r}}_{ij}\right)\frac{\hat{\mathbf{r}}_{ij}}{|\mathbf{r}_{ij}|^2}da_j \qquad (2.28)$$

This expression is derived for radiation exchange for diffuse, gray bodies within an enclosure in Siegel and Howell, and is discussed more thoroughly in Canaan's dissertation. The first term on the right hand side solves for the radiant flux incident on node i from direct emission from all nodes j. The second term describes the radiant flux on node i coming from the surface of all nodes j via reflection.

Burns' finite element code, RADERA II (RADiation in Enclosed Rod Arrays, version II) solves for this incident radiant flux vector on node i, for all nodes i. For the three-dimensional geometry described in Figure 2.2, the integrals of equation 2.28 are surface integrals. However, in the two-dimensional analysis of the current UT experiment, the integrals are only line integrals. Figure 2.3 describes the geometry that is more appropriate for the radiation analysis of the UT experiment. The rods and the CuBE interior wall are broken up into small elements over which uniform radiosity is assumed. The radiant flux incident on each node i is found by integrating the emitted and reflected flux coming from all other nodes j. The finite element formulation used to solve equation 2.28 for all nodes i is also thoroughly discussed in Canaan's dissertation.

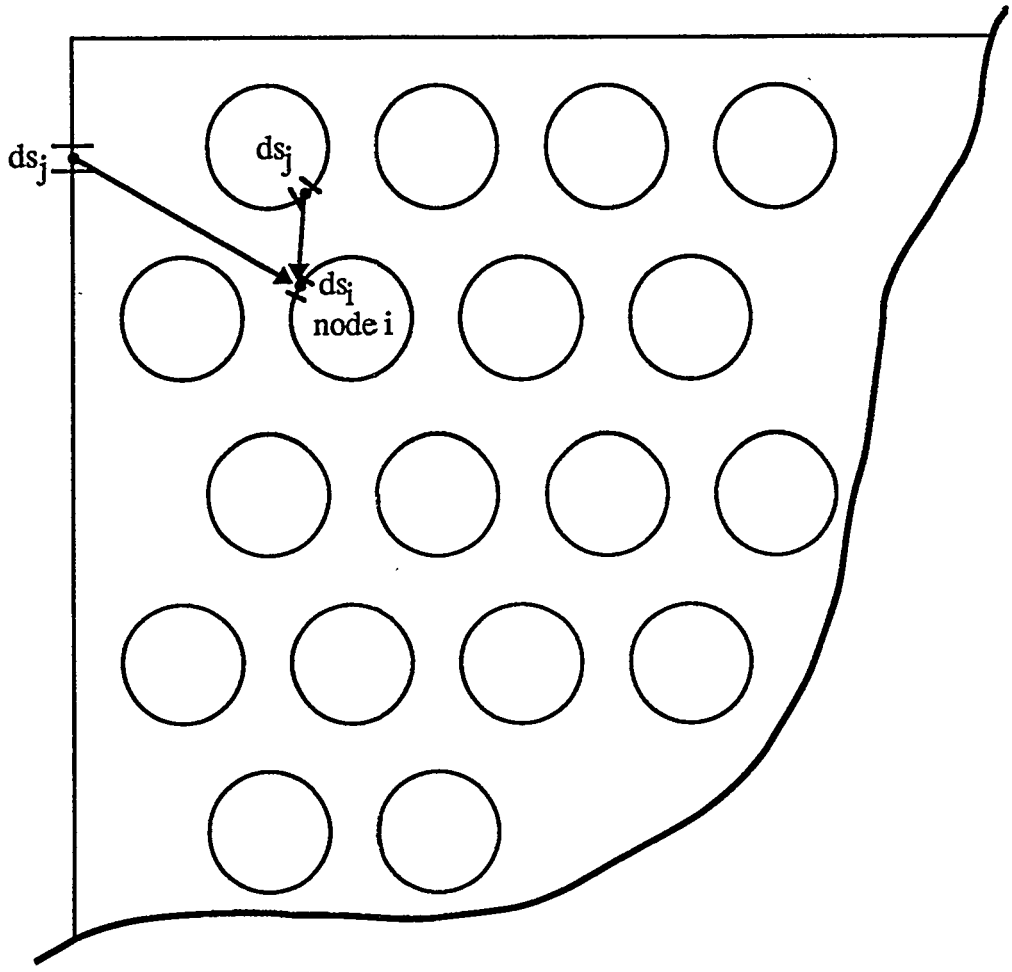

Figure 2.3 2-D radiation exchange between nodes of the UT enclosed rod array.

The radiation code is simplified by performing visibility checks. As shown in Figure 2.4, many of the nodes within the rod bundle cannot "see" an particular node i because they are either on the same rod, which is a convex surface (case 1), or they are blocked by nodes on other rods (cases 2 and 3). The code simplifies the calculation of the incident radiative flux on a particular node by calculating the radiant exchange only between nodes that can "see" each other, such as cases 4 and 5 in Figure 2.4. Also, the middle line of the array was assumed to be a symmetry boundary, with no radiant heat flux across this boundary. The specifics of how these checks and simplifications were implemented in the code are described in Canaan's dissertation [1995].

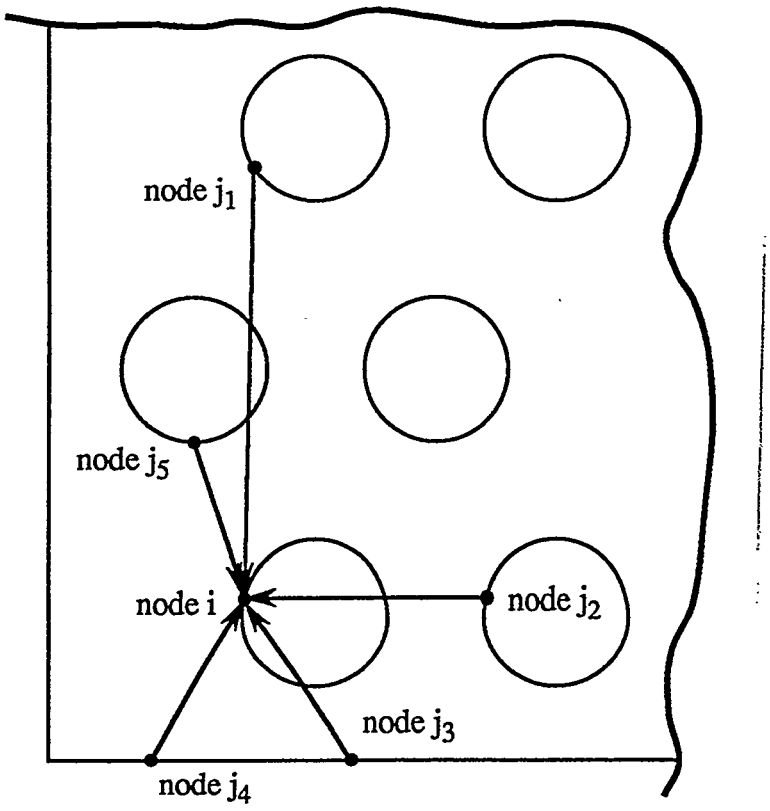

Figure 2.4 Different visibility situations for different nodes within the enclosed rod array.

Once the *incident* flux on a particular node is calculated, the *net* radiative flux from a particular node can be calculated from equation 2.29 as

$$q''_{i,net} = \varepsilon_i \sigma T_i^4 - \alpha_i \left(q''_{inc}(\mathbf{r}_i) \bullet \hat{\mathbf{n}}_i \right) \tag{2.29}$$

where $\hat{\mathbf{n}}_i$ is the outward unit normal vector from the surface of node i, $\mathbf{q}''_{i,inc}(\mathbf{r}_i)$ is the radiative flux vector incident on node i, and a is the surface absorptivity at node i. This equation results from a radiative energy balance at node i that is diagrammed in Figure 2.5.

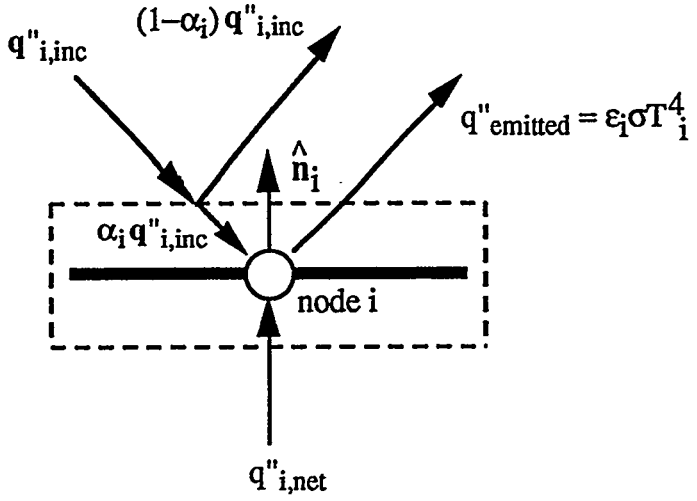

Figure 2.5 Energy balance for radiation at node i.

Since, for a diffuse, gray, opaque surface, the absorptivity is equal to the surface emissivity, we can rewrite the net radiant flux at the rod surface node as

$$q''_{i,net} = \varepsilon_i \left[\sigma T_i^4 - \left(q''_{i,inc}(\mathbf{r}_i) \bullet \hat{\mathbf{n}}_i \right) \right] \tag{2.30}$$

The final quantity that remains to be calculated is to integrate the heat flux around the surface of each rod to find the actual quantity we desire, the net radiant heat rate for the rod, per unit length of the rod, q'_{rad}. This quantity is given by

$$q'_{rad} = \oint_{\text{rod surface}} q''_{i,net} ds_i \qquad (2.31)$$

where ds_i is the arc length of the individual node on the rod surface. Equation 2.31 gives the quantity that is needed in equations 2.9 and 2.16 to calculate the convective heat transfer per unit length from each rod.

The code was benchmarked by comparing the code results to analytical results for some simple geometric cases, and a heat balance error was also calculated that compared the sum of all the radiant heat leaving the rods to the total heat rate to the CuBE wall [Canaan, 1995]. For all cases, this heat balance error was less than 1 percent. The listing of the RADERA II code is given in the Appendix. The Appendix also gives examples of input and output files used and produced by the code. Chapter 4 shows how the radiation code fits into the overall data reduction procedure used to obtain the final heat transfer correlations.

This chapter has presented the theory and equations needed to calculate the Nusselt and Rayleigh numbers for the individual heater rods and for the entire rod bundle. The next chapter describes the complete experimental apparatus and layout of the system used to investigate natural convection within an enclosed, staggered rod bundle.

Chapter 3 -- Experimental Apparatus and Setup

This chapter presents a concise look at the equipment used in this experiment, how this equipment was set up, and how the components fit together. It should be mentioned that much of Canaan's 4-year research effort focused on the design and construction of the equipment described in this chapter. Since the only major change in experimental setup between this thesis research and his research is the change in rod array geometry, this chapter will not go into the same level of detail as Canaan's dissertation. While this thesis gives the reader an overall view of the experimental equipment and setup used, Canaan's dissertation provides such a fine level of detail of most components (including part serial numbers and manufacturers) that the entire experimental setup could be reconstructed by using his dissertation as a reference.

The experimental equipment and apparatus is discussed in the following order. First, the geometry and construction of the individual heater rods are discussed, and the location and construction of the thermocouples used to measure each rod's surface temperature are described. Next, the copper boundary enclosure (CuBE) is discussed, showing how the rods are supported within the enclosure and how the enclosure is water-cooled to provide an isothermal heat sink. The pressure vessel is described next, followed by a description of the power supply system that heats the rods. The final section describes the automated data acquisition system used to take measurements of the surface temperature of each rod and the power being dissipated by each rod. As each component is described, an effort is made to show how each component fits into the overall experimental apparatus.

3.1 The Electric Heater Rods

Figures 3.1 and 3.2 diagram the construction of an individual heater rod. Table 3.1 also lists some important specifications for the rods. The rods are 1.224 cm in outer diameter and are 92.1 cm in overall length. They were made by the

Watlow Electric Mfg. Co. of St. Louis, MO. The heater rods feature a nichrome coil that runs along the centerline of the rod. This coil dissipates electricity from a DC power supply to generate heat within the rod. The inside of the rod is filled with compacted magnesium oxide ceramic, and the rod is sheathed with a 304 stainless steel cladding. The ends of the rod are thermally insulated with cylindrical mica endpieces to minimize axial conduction effects. Each end of the rod provides a threaded pin and some hexagonal nuts, which allow secure attachment of electrical leads. Note that Figure 3.1 is not a scale drawing, in that the insulated end of the rod is shown as being right next to the rod's midpoint, where the thermocouple junctions are located just under the rod sheath. In reality, the end of the rod is a little over 40 cm from the rod midpoint, and this drawing simply shows most of the major features of the heater rod in one schematic.

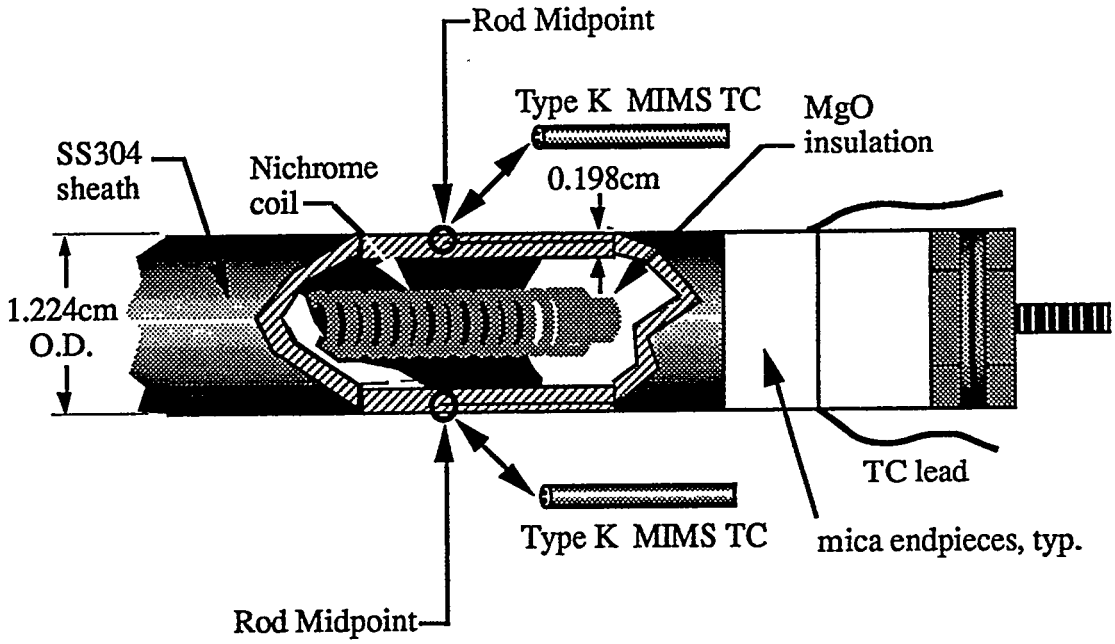

Figure 3.1 Schematic of a single instrumented heater rod.
[Canaan, 1995]

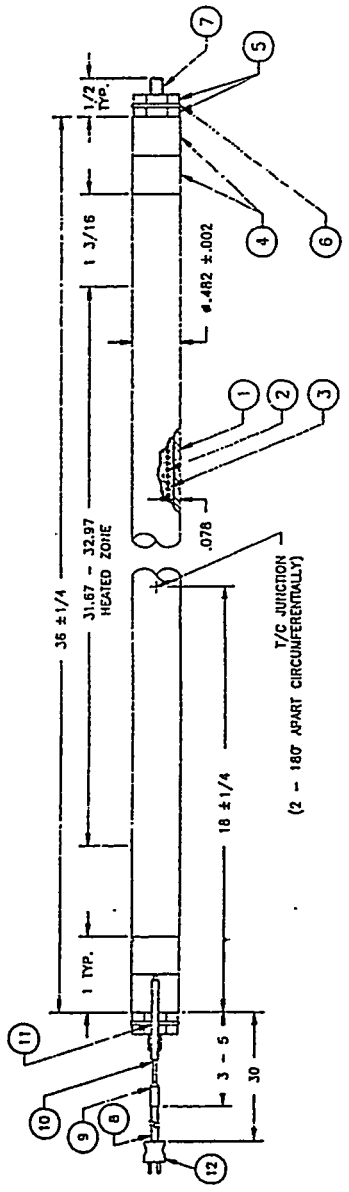

Item	Bill of Material
1	Sheath - Type 304 stainless steel
2	Resistance elemcnt - 80%Ni/20%Cr
3	Insulation - Magnesium oxide
4	Terminal insulator - mica
5	6-32 Hex nut - stainless steel
6	#6 Flat washer - stainless steel
7	6-32 Terminal - stainless steel
8	TC lead - 24 Ga. Type K insulated wire
9	TC adapter - Type 304 stainless steel
10	TC - ϕ0.032" Type K MIMS TC
11	TC insulator - rubber coated fiberglass
12	TC connector - Gordon pt. 850-K

Figure 3.2 Watlow Co. design diagram of a heater rod with 2 embedded thermocouples [from Canaan, 1995].

Table 3.1 UT Heater Rod Specifications
[from Canaan, 1995]

Sheath material	stainless steel, SS304
Resistance element	nichrome wire (80% Ni / 20% Cr)
Insulation	magnesium oxide (MgO)
Terminal insulator	mica
Heater coil resistance	$6.0 \pm 0.3\ \Omega$
Coil to sheath insulation resistance	$> 25\ M\Omega$
Rod outer diameter	1.224 ± 0.0051 cm
Sheath thickness	0.198 cm
Heated length	82.1 ± 1.65 cm
Thermocouples	Type K metal-insulated metal sheathed (MIMS)
TC junction location	0.051 cm below rod surface
TC metal sheath diameter	0.081 cm
TC individual wire diameter	0.013 cm
TC wire resistance	$39.5 \pm 1.0\ \Omega$

The individual heater rods were designed to thermally simulate individual BWR fuel rods. Thus, the dimensions of the heater rods are similar to a BWR, as are the thermal characteristics. As listed in Table 3.2, the dimensions and thermal conductivities of the materials used for the electric heater rods are very similar to those of an individual spent fuel rod.

Table 3.2 Comparison of the Thermal Properties of Spent Fuel and a UT Heater Rod (averaged from 200°C to 1000°C)

Material	k, W/m-K
MgO	2.07
SS304 clad	15.2
UO_2	3.60
Zircalloy clad	13.0

There are three types of Watlow heater rods used in the UT staggered array. The first type is an uninstrumented heater rod, which contains no thermocouples. Since the natural convection flow and the temperature distribution within the rod bundle is symmetric about the vertical centerline of the array, the experimental setup was simplified by only measuring the temperature of the rods on one side of the array. By only using rods with thermocouples on one side of the array, the number of thermocouple wires and the size of the data acquisition system was significantly reduced.

The second type of heater rod is the one diagrammed in Figures 3.1 and 3.2. This rod contains 2 type K, mineral insulated, metal sheathed (MIMS) thermocouples whose junctions are located at the axial midpoint of the heater rod. The two thermocouples are located within the stainless steel cladding, 0.05 cm from the rod surface. These two thermocouples are circumferentially separated by 180 degrees. The reason the thermocouples are placed within the cladding is as follows. If thermocouples were attached directly to the outer rod surface, then the

lead wires that run to the data acquisition system would likely interfere with the convection flow patterns and the radiation exchange between the rods. Having the thermocouples run just underneath the rod surface allows the study of heat transfer within an uncluttered rod array, while still giving an accurate measurement of the rod surface temperature. Also, embedding the TCs reduces the conduction errors that would result from having exposed TC wires. Although the rod surfaces were assumed to be isothermal, having two thermocouples 180 degrees apart allows an experimental verification of this assumption.

The third type of heater rod is instrumented with the same two thermocouples as the heater rod in Figures 3.1 and 3.2, but also has a third thermocouple whose junction is located about halfway between the rod's axial midpoint and the end of the rod. This thermocouple allows an experimental check of the temperature variation with axial position along the rod. Recall that this analysis assumes no axial temperature variation along the rod, and thus no conduction losses.

Figure 3.3 shows a cross-sectional view of the heater rods within the array. This diagram shows which rods are uninstrumented, which rods have two TCs, and which rods have three TCs. While the rod temperatures on most of one side of the array are not measured because of the symmetry assumption, there are two rods with thermocouples on that side. These two temperature measurements allow confirmation of the symmetry assumption by allowing comparisons of the surface temperatures of two rods that are in the same "mirrored" positions about the array vertical centerline. For example, the rod on the fourth row from the top on the far left side of the array should have the same temperature as the rod from the same row on the far right side of the array, if the symmetry assumption is valid. These temperature symmetry and axial temperature variation checks are performed on the fifth row from the bottom because it is this row that is expected to have the highest temperatures. Thus it is likely that any symmetry or axial variation errors would be greatest on this row.

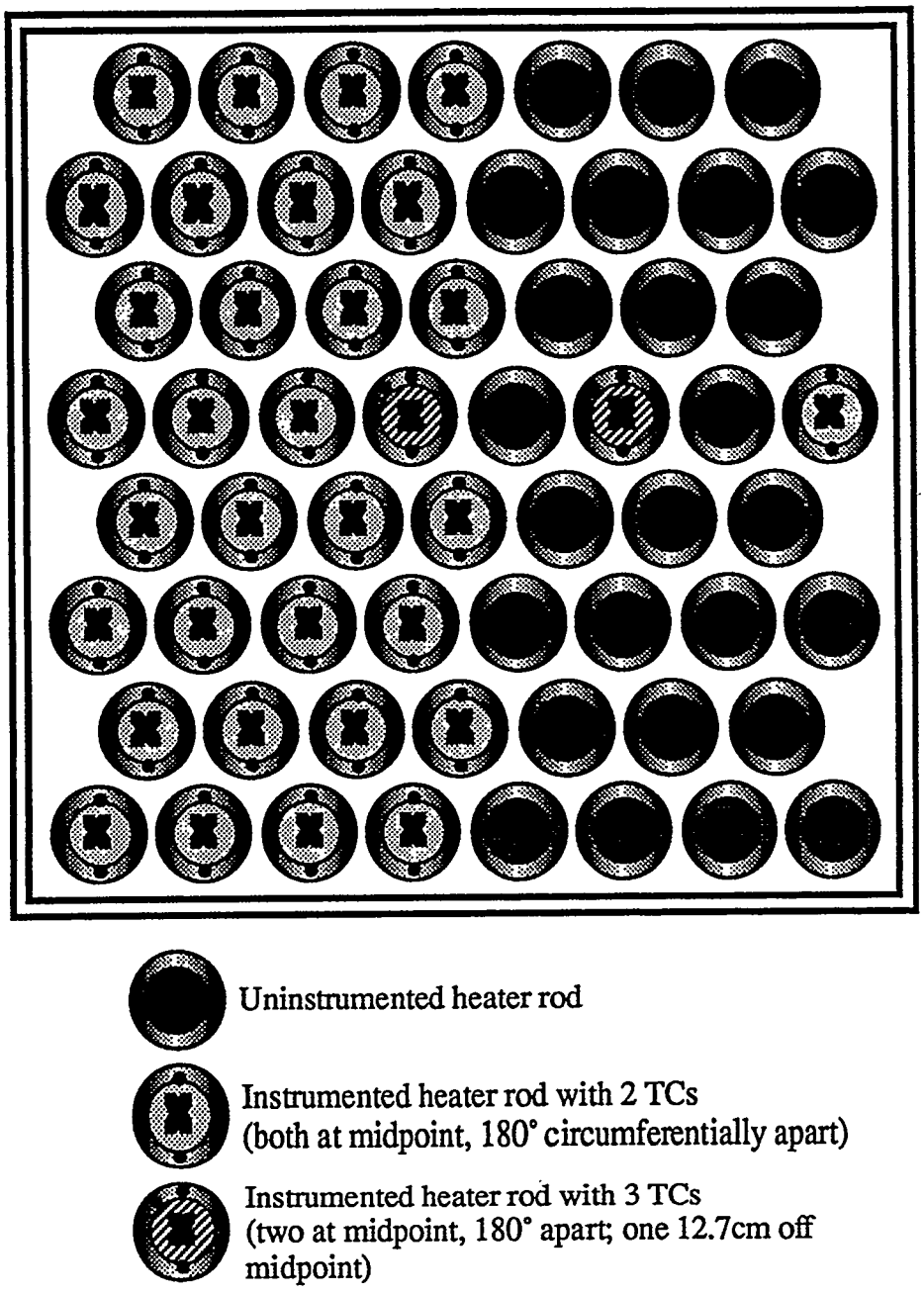

Figure 3.3 Diagram showing positions of uninstrumented and instrumented heater rods.

3.2 THE COPPER BOUNDARY ENCLOSURE (CUBE)

3.2.1 CuBE Construction

The purpose of the Copper Boundary Enclosure (CuBE) is twofold. First, the endplates of the CuBE support the heater rods in the array geometry. Second, the CuBE provides a constant temperature heat sink that surrounds the rod bundle. Figures 3.4 through 3.8 show the CuBE construction. The CuBE is a rectangular box that is square in cross-section. The walls of the CuBE are 1.27 cm (1/2") thick, and the CuBE is 87.3 cm (34.4") in length. Copper tubing (0.64 cm, or 1/4", O.D.) is soldered in an "S" pattern over the outer surface of the 4 long sides of the CuBE. The water tubes that provide the cooling water that keeps the box at a constant temperature are attached to the ends of the copper tubing with Swagelok tube fittings, which provide a tight seal between the copper tubing and the flexible plastic tubing through which the supplied cooling water flows. Small ceramic feet are attached to the bottom surface of the CuBE, which allows the CuBE to sit on its support plate within the pressure vessel without crushing the ductile copper tubing on the bottom face of the CuBE.

Figure 3.4 shows an end, cross-sectional view of the CuBE, while Figures 3.5 and 3.6 show the top / bottom and left side / right side views of the outside of the CuBE. Figure 3.7 shows one of the two endplates that support the heater rods in the current staggered configuration. The brass endplates are 1/16" thick, and provide essentially a point contact between the CuBE and the rod end, which limits axial conduction losses. Figure 3.8 shows a top, oblique, cutaway view of how the rods sit in the CuBE. Except for the endplates, all of the inner surfaces of the CuBE and the outer rod surfaces are painted with Pyromark 2500 flat black paint, which provides a consistent, high emissivity surface that allows for less complex radiation analysis. Small, thin foil TCs (not shown) are attached to the inside surfaces of the CuBE walls at various locations. These temperature measurements are critical not only in the heat transfer analysis of the rod bundle, but they also ensure that the inner surface of the CuBE is indeed isothermal, as assumed.

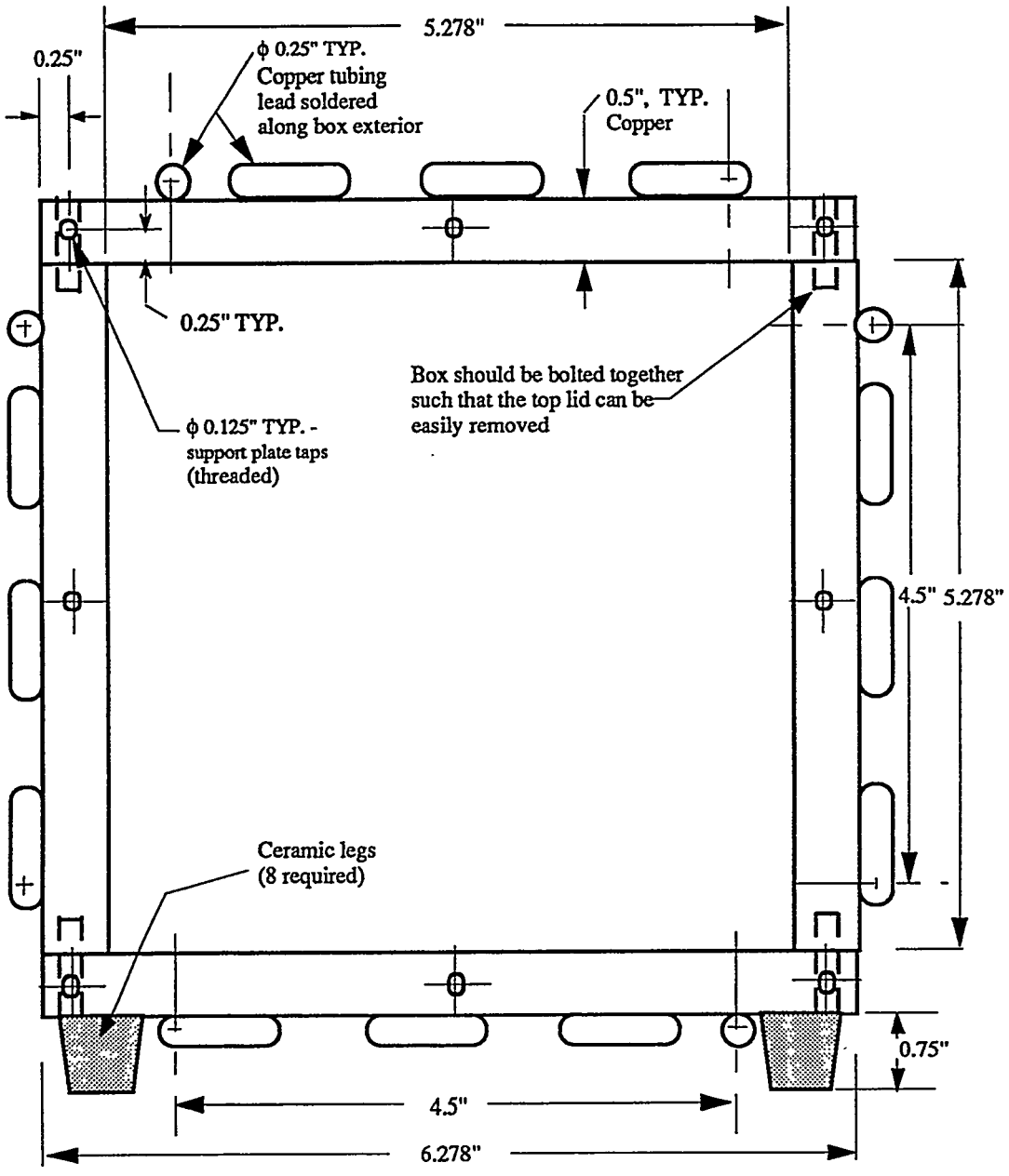

Figure 3.4 End view of the CuBE (units in inches).
[Canaan, 1995].

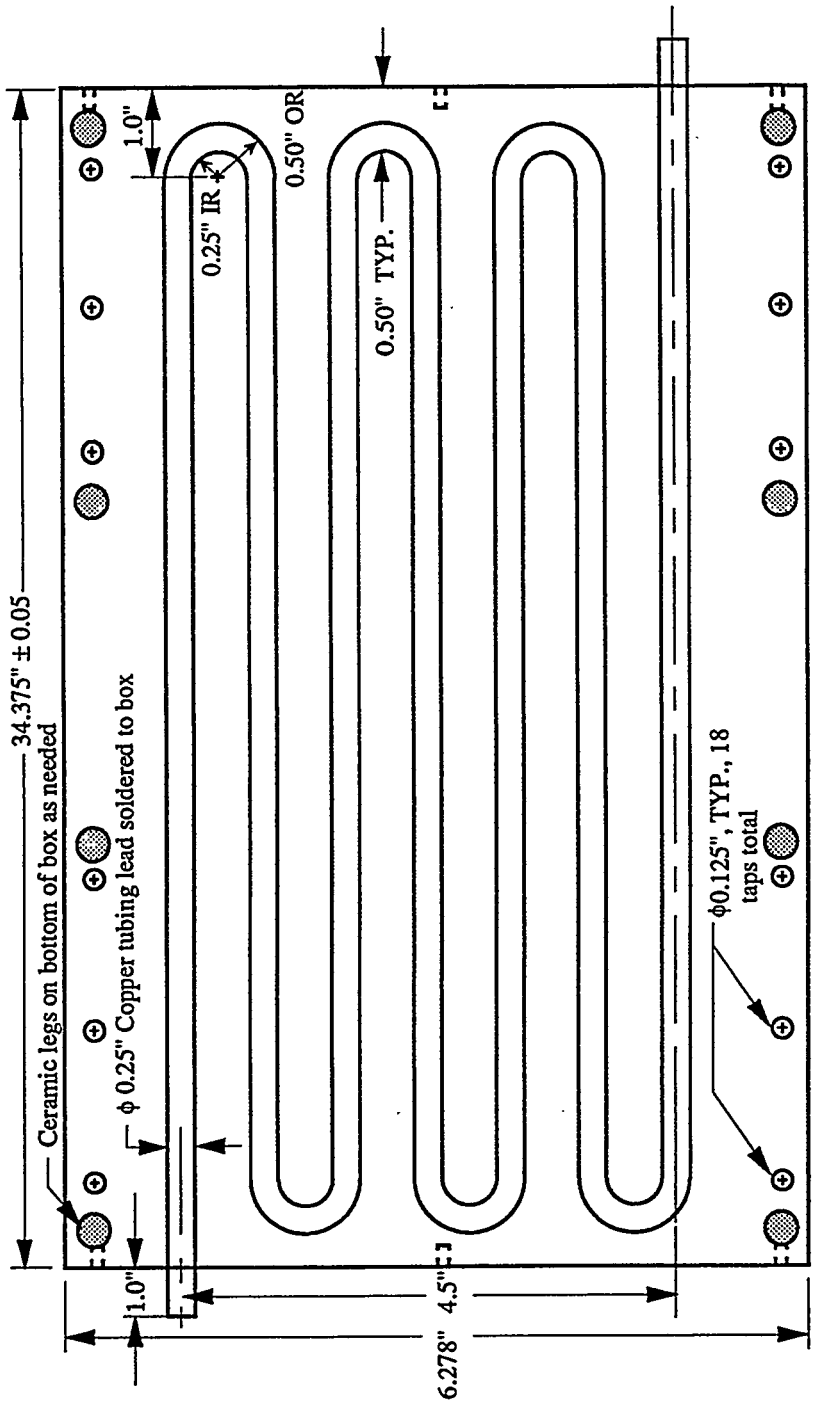

Figure 3.5 Top / bottom view of CuBE (units in inches).
[Canaan, 1995].

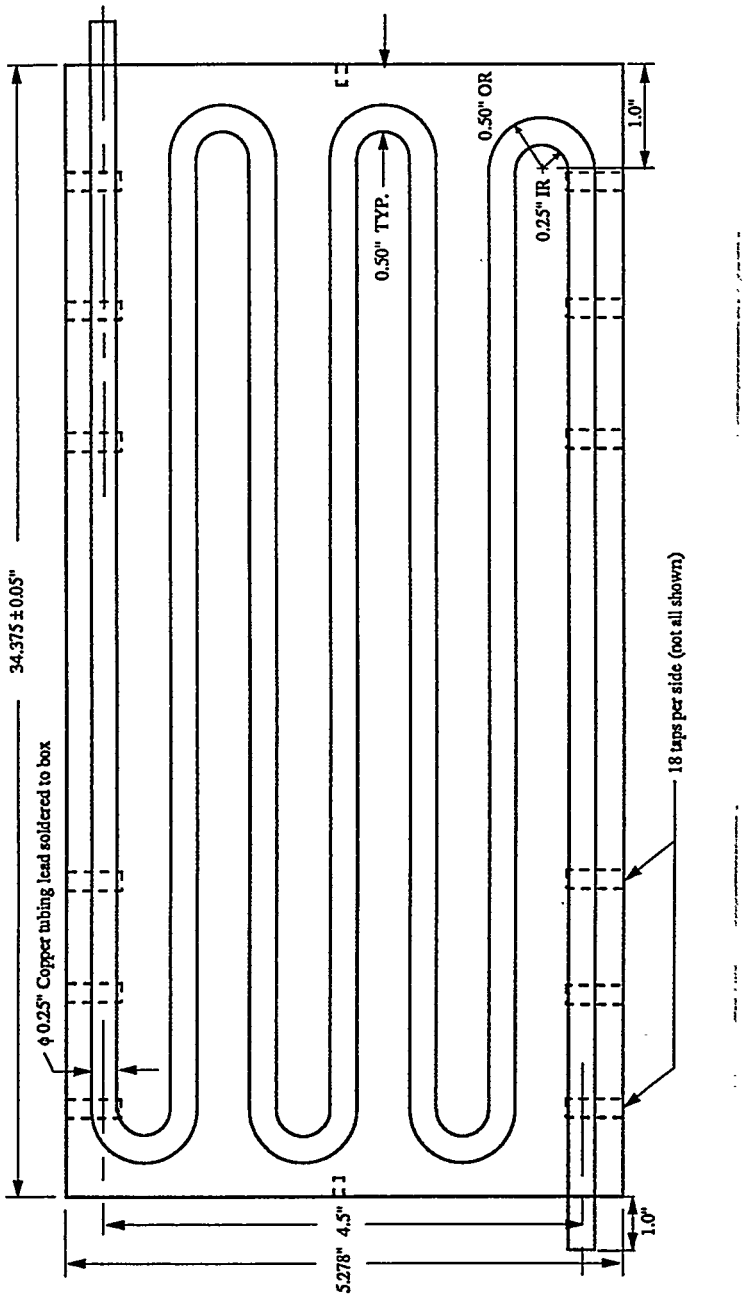

Figure 3.6 Side view of CuBE (units in inches).
[Canaan, 1995].

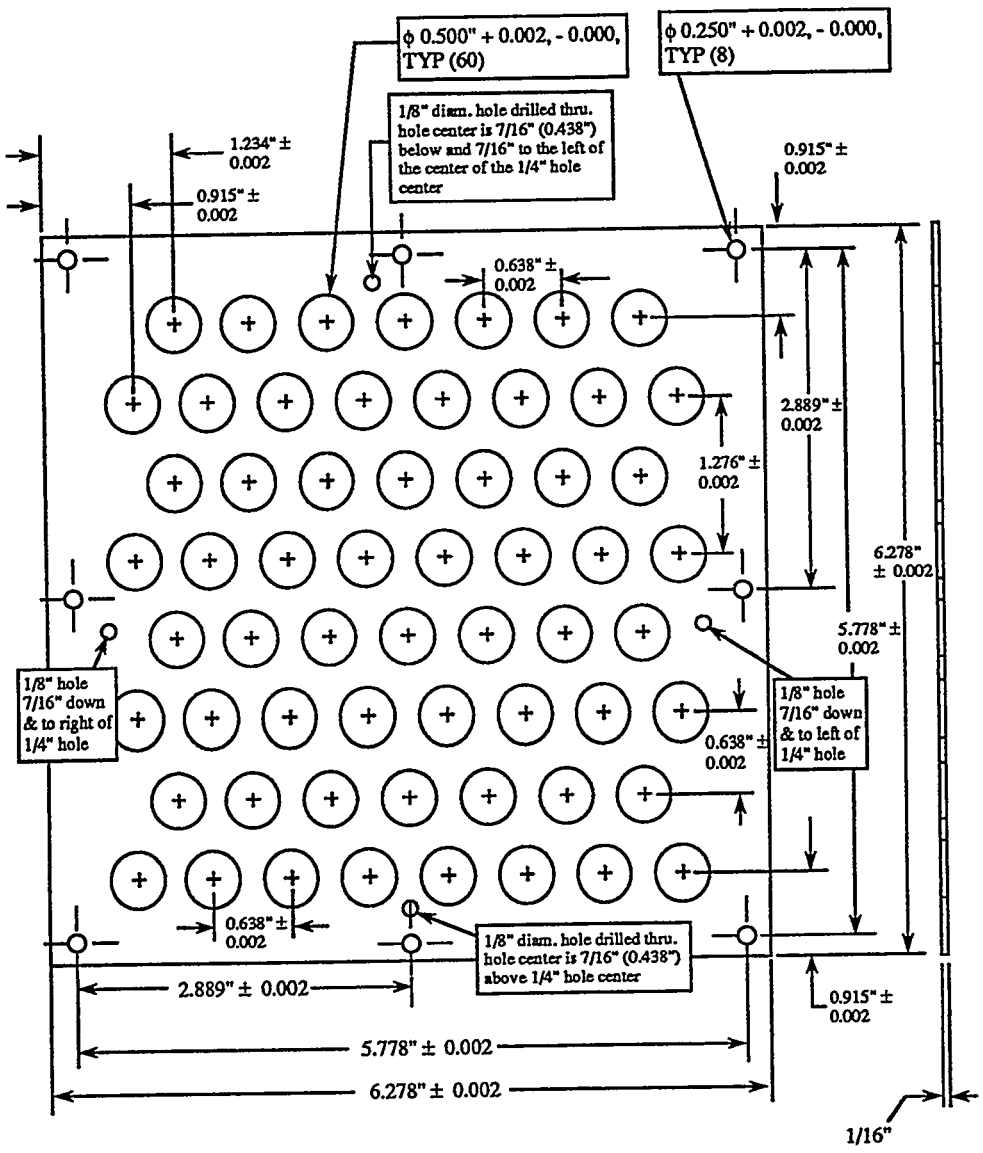

Figure 3.7 End support plates for the heater rods (units in inches).

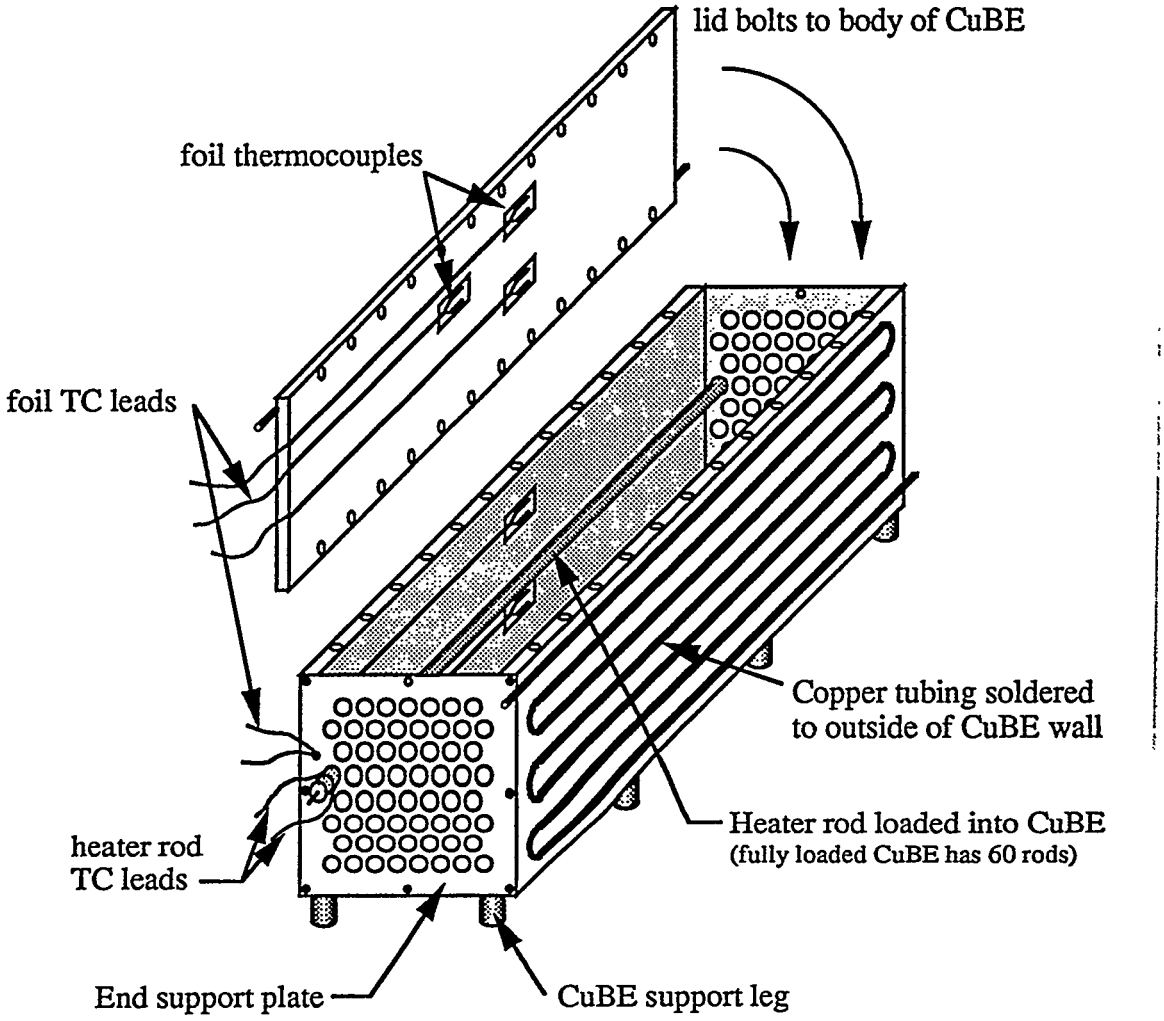

Figure 3.8 Top oblique view of CuBE loaded with a single heater rod.

3.2.2 CuBE Cooling Water System

Figure 3.9 gives a simple diagram of the cooling water system. Water from the UT Pickle Research Center chilled water supply flows first through a filter, next through tee junctions, then through 4 separate valves to each of the four plastic tubing lines that attach to the CuBE copper tubing with Swagelok 1/4" tube fittings. Four visual flowmeters on each of the four tubing branches ensure that the water flow rate is the same for each face of the CuBE. The water flows through the copper tubing, then drains out through four more plastic tubes to a sink drain.

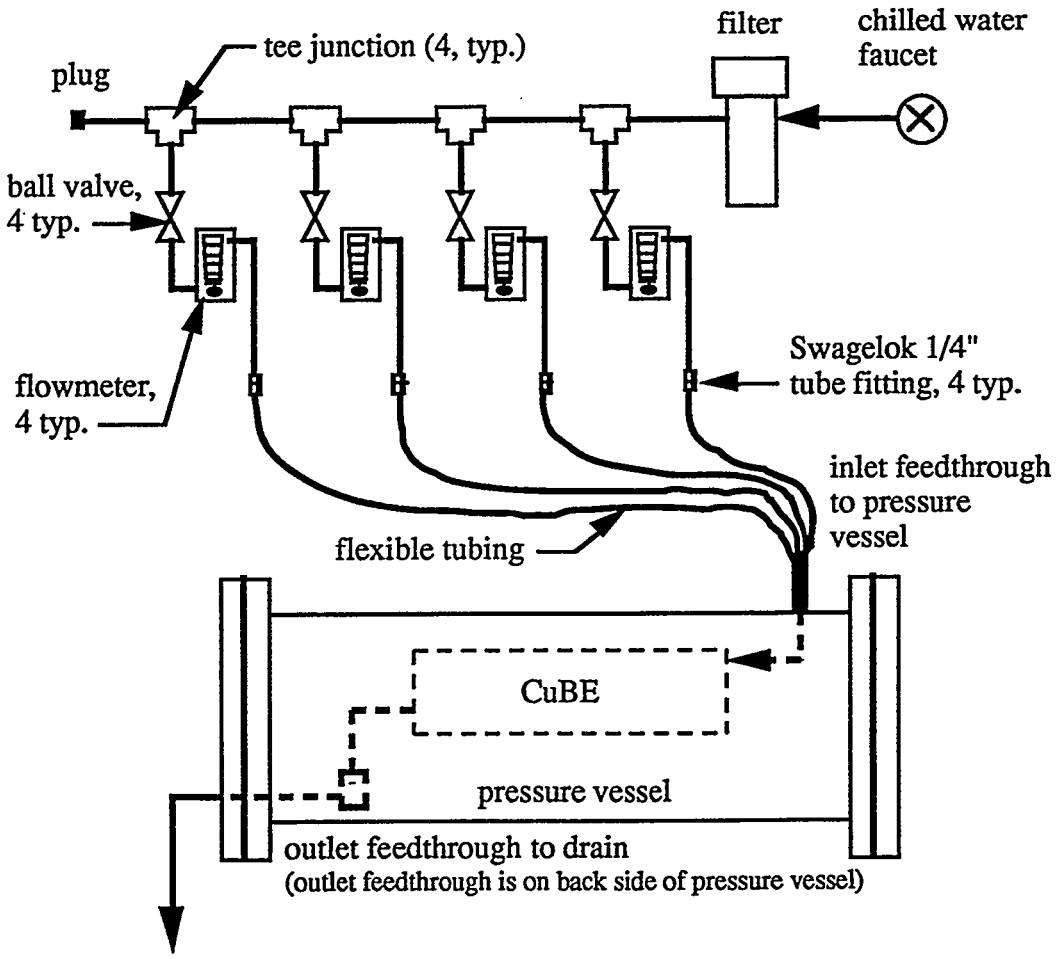

Figure 3.9 Diagram of water cooling system.

3.3 THE PRESSURE VESSEL

Figure 3.10 gives a side cutaway view of the cylindrical pressure vessel used in the UT experiments. The vessel is made of low carbon steel and is 47.2 cm (18.6") in outer diameter and is about 1.3 cm (1/2") thick. It is sealed on each end with a hinged door that shuts on a gasket that is trapped between the door and a flange. The door is sealed shut by sixteen 1.91 cm (3/4") bolts on each end. The vessel's maximum pressure is 618 kPa (75 psig), but this experiment ran at pressures ranging only from 101.3 to 514.8 kPa (0 to 60 psig). A safety relief valve ensures that the maximum pressure is not exceeded. Three Conax feedthrough connections allow the thermocouple leads, the heater rod electrical power leads, and the inlet and outlet cooling water lines to be passed into and out of the pressure vessel, while allowing the vessel to remain tightly sealed. A ball valve was connected to a supply gas canister, which allowed the vessel to be filled to a desired pressure either with helium or nitrogen. Another ball valve attached to a Sargent-Welch vacuum pump that can depressurize the tank down to about 1 torr. The vessel pressure was measured with an analog Omega type-T Bourdon tube pressure gauge that gives a visual readout of the tank pressure to a resolution of $\pm$ 0.2 psig.

Inside the pressure vessel, a steel support table slides in and out to allow the placement of the CuBE within the vessel. The leads from all of the heater rod TCs, as well as from all of the CuBE foil TCs plug into a TC jack panel at one end of the pressure vessel. Attached to the bottom of the jack panel are the wires that are fed out of the pressure vessel through Conax feedthroughs to the automated data acquisition system.

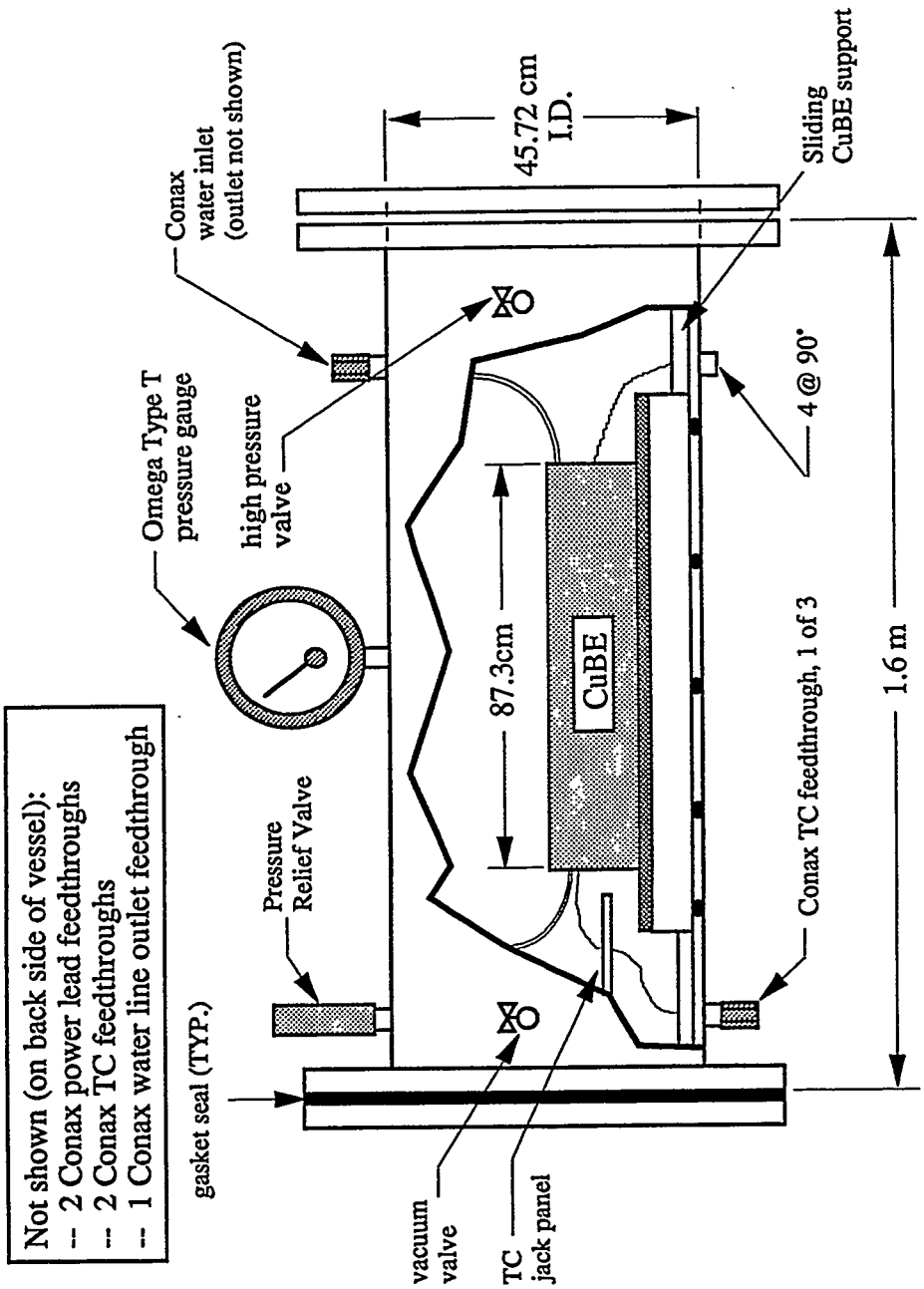

Figure 3.10 Side cutaway view of the pressure vessel.
[adapted from Canaan, 1995].

3.4 THE DC POWER SUPPLY SYSTEM

The heater rods were heated internally by dissipating DC current in the nichrome coil that runs through the center of each rod. The power was supplied to the heater rods with a Hewlett-Packard model 6030A DC power supply. This power supply has a GPIB board that allows direct control and monitoring of the heater rod power from the automated data acquisition system. As shown in Figure 3.11, power was supplied to the rod bundle through one of 4 parallel branches. Each branch consisted of 15 individual heater rods connected in series. The power leads were passed into and out of the pressure vessel through Conax feedthrough valves.

The most accurate way to measure the heater rod power for each rod would be to individually measure the current and voltage drop across each rod. However, since there was limited space in the data acquisition system, only 4 branches could be used. The voltage drop across 4 small shunt resistors was used to determine the current in each branch. The resistance of the shunt resistors and of each rod was measured very accurately with an HP multimeter. Canaan determined that the resistance change of the heater rods over the temperature range of this experiment was less than 1 percent, so the resistance of each rod was assumed constant [Canaan, 1995]. Given these quantities, the heat dissipated by each rod is given by

$$q_r = i_{branch}^2 R_r \tag{3.1}$$

where R_r is the measured resistance of each rod, which is 6 ± 0.3 ohms, at room temperature. The heat dissipated per unit rod length is found by dividing q_r by the heated length of the rod, L, which is 82.1 cm (32.3 in).

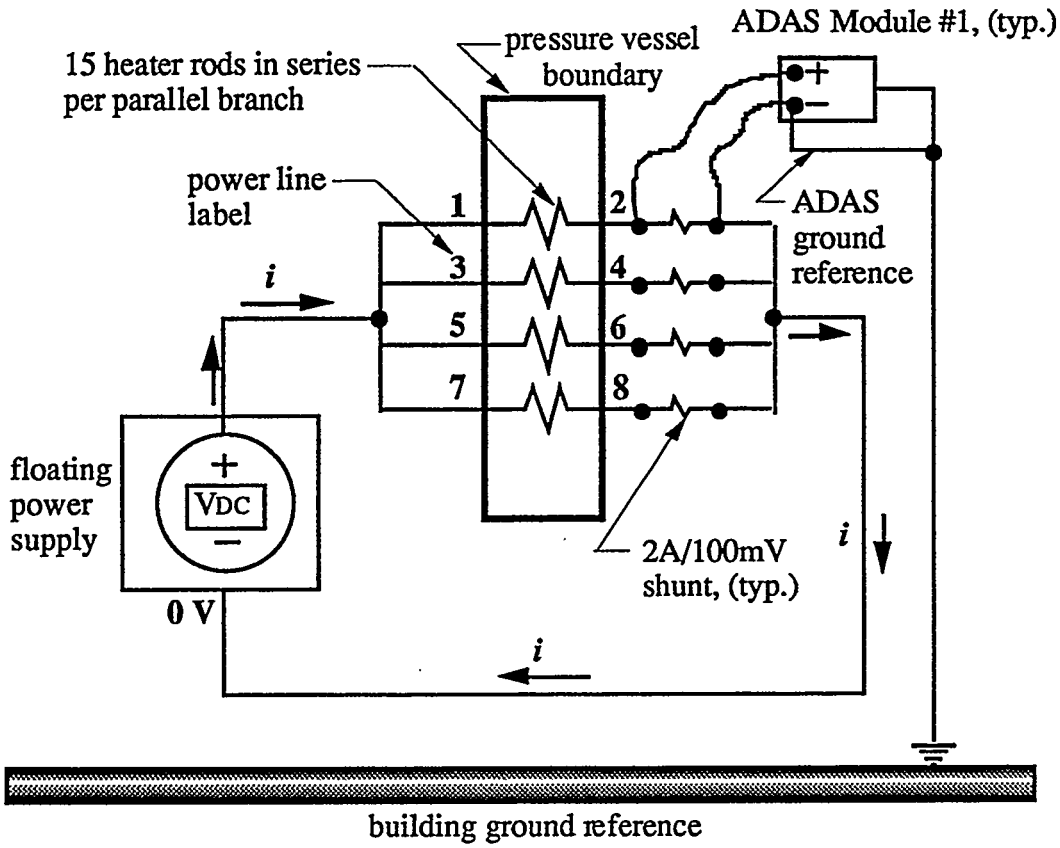

Figure 3.11 Diagram of DC power supply system for the heater rods.

3.5 THE AUTOMATED DATA ACQUISITION SYSTEM

This experiment requires the acquisition of millivolt signals from 78 thermocouples and the monitoring of individual heater rod powers. To acquire all of this data quickly and accurately requires an automated data acquisition system (ADAS), particularly if one is interested in performing multiple sample passes very quickly. The ADAS used in this experiment features LabVIEW software running on a Macintosh IIx personal computer. The Macintosh had two National Instruments NuBus cards installed. The first card is the 16-bit A/D board that converts analog voltage signals into digital signals that can be processed by the LabVIEW software. The second card is a general purpose instrument bus (GPIB) card that both controls and reads data from the HP 6030A DC power supply. National Instruments hardware was used first to multiplex the analog voltages from the TCs and the shunt resistors, and then to amplify and condition the signals to increase the resolution of the voltage measurements and reduce the effects of environmental noise. The ADAS is diagrammed in Figure 3.12.

The LabVIEW software controls all aspects of the data acquisition process, such as sampling rate, the order in which individual multiplexer channels are read, the total number of samples read, and amplifier gains. Also, the software performs the mathematical conversions from voltages to temperature, and the conversions from shunt resistor voltages to DC current in each of the 4 heater rod power branches. The software then displays the temperature and power readings, and stores the results in a spreadsheet format. Once the data are in a spreadsheet format, the temperature and rod power data can be analyzed and reduced to produce heat transfer correlations.

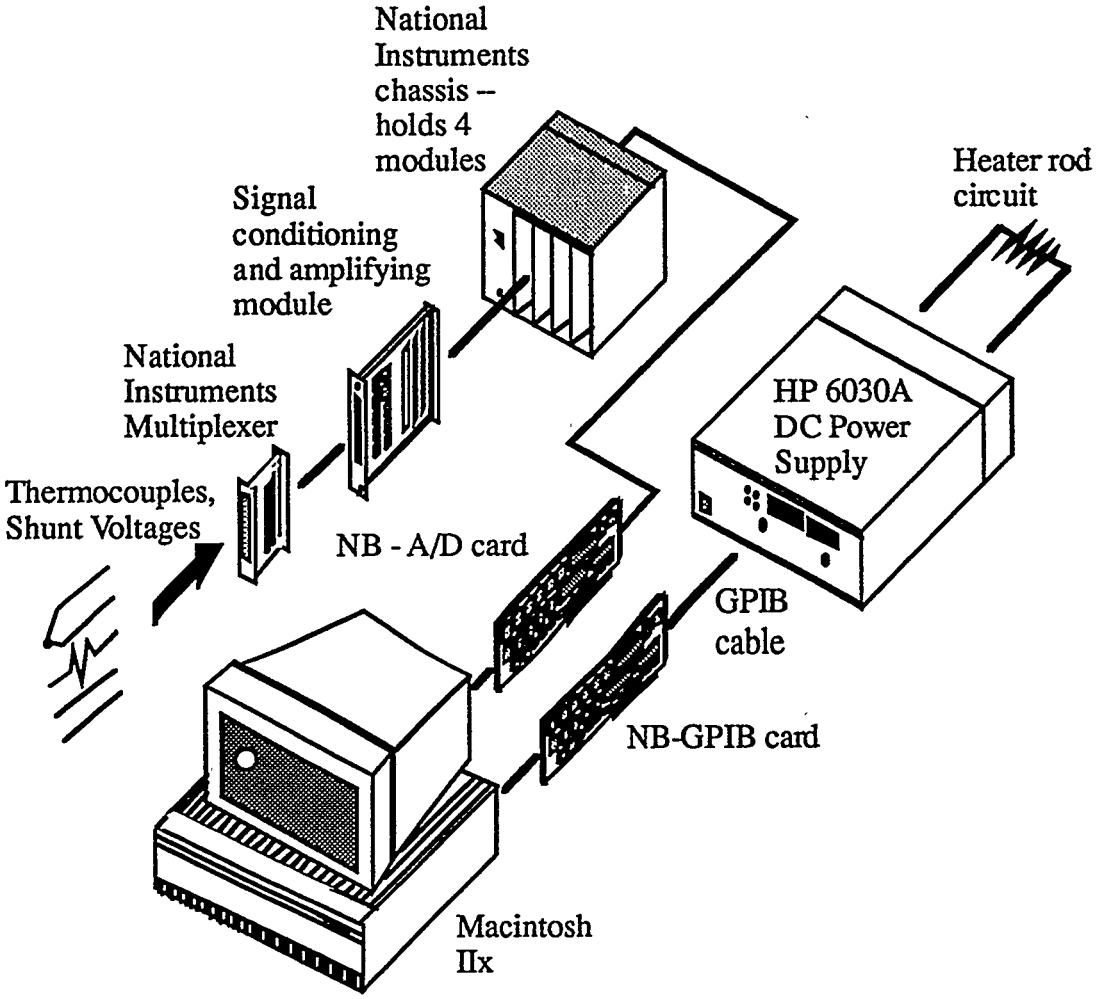

Figure 3.12 Diagram of the automated data acquisition system.

This chapter has given a concise look at the experimental apparatus and setup used for this experiment. The next chapter looks at the steps involved in running an experiment, as well as the steps involved in reducing the data into useful heat transfer correlations.

Chapter 4 -- Experimental Procedure and Data Reduction

This chapter presents the steps involved in preparing the experimental apparatus for taking data, the procedure for running an experiment, and the steps needed to reduce the data into the final results that are presented in Chapter 5. This chapter is divided into five sections. Section 4.1 describes the initial steps involved in setting up the apparatus. Section 4.2 describes the range over which the independent parameters of this experiment--rod power, backfill fluid type, and vessel pressure--were varied to thoroughly characterize the heat transfer behavior within the enclosed, staggered rod array. The test procedure used for taking each data set is described in section 4.3, followed by a description of the steps involved in reducing the data, given in section 4.4. Section 4.5 summarizes the main sources of experimental error for this research and gives error estimates for the Nusselt and Rayleigh numbers that are presented in Chapter 5.

4.1 Initial Setup

This section describes the steps involved in setting up the experiment prior to acquiring all of the data sets. Individual tasks are listed below.

- Disassemble Canaan's experiment. The first step in getting this experiment set up was to take apart Canaan's rod bundle. This involved opening the pressure vessel, disconnecting all of the heater rod TC leads from the jack panel, disconnecting the water and power leads from the CuBE, and removing the CuBE from the pressure vessel. The CuBE was placed on a workbench, the lid was removed, and the heater rods were disengaged from the end support plates. Finally, the aligned configuration end support plates were removed.

- Reload CuBE with heater rods in staggered configuration. New end support plates (recall Figure 3.7) were fabricated by the UT mechanical engineering machine shop. After the aligned rod support plates were removed, the staggered array support plates were attached to the ends of the CuBE. Each heater rod was loaded into the CuBE, and the CuBE top was then replaced.

- Test ADAS; calibrate TC channels. Before the CuBE was placed back into the pressure vessel, the thermocouples and the data acquisition system were checked out to ensure proper operation. Each channel of the ADAS was tested with an Omega hand-held TC calibrator. This calibrator sent DC millivolt signals into each ADAS channel that corresponded to the voltages for a type K thermocouple at specified temperatures. The TC measurement error was determined by noting the difference between the set calibration temperature and the temperature read by the ADAS. This error is discussed in section 4.5.

- Load CuBE into pressure vessel. After testing the ADAS, an engine hoist crane was used to lift the 200+ pound CuBE onto the support table inside the vessel. This support table can slide in and out to allow easy removal and insertion of the CuBE.

- Connect water lines to CuBE; leak test. After placing the CuBE in the vessel, the flexible water lines used to cool the CuBE were inserted into the vessel feedthroughs, then connected to the ends of the copper tubing with Swagelok 1/4" tube fittings. The water valves were turned on and water allowed to flow for several minutes to ensure that no water would leak into the pressure vessel and damage the electronic equipment.

- Plug in all TCs to plug board. Next, the TC connectors from each rod and from the foil TCs inside the CuBE wall were connected to the outlets on the ADAS plug board. Room temperature readings were then taken from all of

the TCs through the ADAS, and these readings were compared to the room temperature measured by the TC calibrator. From this comparison, an initial estimate of the TC bias error could be found.

- Connect power leads; test connectivity. Next, the power leads from the DC power supply were run into the pressure vessel and connected to the heater rods. As shown in Figure 3.11, the 60 heater rods were connected in 4 parallel branches, each of which have 15 heater rods connected in series using small copper clips. The connectivity of each branch was thoroughly checked to ensure that current was actually flowing through each rod.

- Turn on power, check TCs. The next step involved turning on the power to the heater rods, then observing the TC readings from the ADAS to ensure that the temperature trends were qualitatively reasonable and that the DC current to the rods did not influence the millivolt signals from the TCs to the ADAS. If a heater rod TC was not properly grounded, the DC current in the coil would influence the TC voltage signals and give erroneous temperature readings. The debugging of this system and the grounding procedures required are discussed in Chapter 6 of Canaan's dissertation [1995].

- Ensure proper CuBE cooling. This step involved turning on the water cooling system with the heater rods powered up to ensure that the cooling system maintains a constant temperature on all walls. For all test cases, the CuBE wall temperature was found to be constant to within 0.5 degrees C.

- Seal pressure vessel; leak test. After all of the system components were tested and found to operate satisfactorily, the vessel was sealed. The vessel was then purged of room air by shutting the valve to the gas canister, opening the vacuum valve, and then reducing the pressure within the vessel to 1 torr with the vacuum pump. The vacuum valve was then shut, and high-purity (99.999%) nitrogen was introduced from the gas canister to

bring the vessel pressure back up to approximately atmospheric. This process was repeated twice to ensure a reasonably pure nitrogen backfill. The vessel was then pressurized to 60 psig and leak-tested both by checking to ensure that the tank pressure did not fall over time and by applying a soap-bubble liquid to the vessel penetrations. No leaks were found at the penetrations, and the pressure remained constant over 8 hours, which is the typical length of time between data sets. Thus, the vessel was assumed to be sealed satisfactorily.

4.2 TEST PARAMETERS

To ensure that the heat transfer behavior of the rod bundle could be characterized over a wide range of flow regimes, three parameters were varied independently in this experiment. First, two different gases were used to fill the vessel--nitrogen and helium. Both gases are inert and are transparent to thermal radiation. For a given temperature and pressure, nitrogen has a Rayleigh number that is about 65 times higher than helium [Canaan, 1995]; thus, using both helium and nitrogen allows the investigation of a wide range of Rayleigh numbers. Second, the power to the rods was varied between 1, 3, and 5 watts per rod. These rod powers are similar to the settings Canaan used in his experiment, and are comparable to the typical range of decay heat produced by SNF rods stored in transportation casks [Canaan, 1995]. Finally, the pressure of the gas in the vessel was set to seven different pressure settings between 0 and 60 psig, in 10-psi increments (0, 10, 20, ... , 60 psig). Since the Rayleigh number is approximately proportional to the square of the absolute pressure [Canaan, 1995], varying the vessel pressure was a good way to obtain a large Rayleigh number variation. The combination of taking data at three power levels, at seven pressures, and with two different gases led to a total of 42 data runs for the staggered array. Each run produced Nusselt-Rayleigh information both for the overall rod array and for each rod.

4.3 EXPERIMENTAL PROCEDURE

Once all of the initial setup steps were completed, the experimental runs were begun. To start the experimental runs, the pressure vessel was again purged with nitrogen. After a couple of purgings to ensure that the gas in the vessel was relatively pure, the pressure was adjusted to 0 psig, and the rod power was set to about 1 watt / rod. The cooling water was turned on, and then the system was left to equilibrate for several hours.

The first step involved in taking a data set was to turn on the ADAS equipment and open the appropriate LabVIEW software files. Next, the vessel pressure and cooling water flow rates were recorded. After about 15 or 20 minutes to allow the ADAS hardware to warm up, the temperatures of selected thermocouples within the assembly were plotted versus time to ensure that the entire assembly was at steady state. Also, the assembly power was checked to make sure that the data were being taken at the intended power state point.

Next, the data sets were recorded. At each state point, two data sets were taken to ensure repeatability and to reduce environmental noise effects. The data taken consisted of readings of all of the heater rod and CuBE thermocouples, along with the 4 branch current readings. Each temperature and branch current reading was actually an average of 3250 samples. Fifty data samples were collected every 5 seconds, and each of these 50 readings was actually an average of 65 samples taken over a span of approximately 0.02 seconds. This multiple averaging scheme reduced the effects of environmental electronic noise. The variation of sample readings from this average value gave a measure of the noise error in the samples. The temperature and branch current data was stored in a text file, and then later converted to an Excel spreadsheet to perform data reduction calculations.

Once the data were recorded, the ADAS hardware was turned off. The vessel pressure was then increased to 10 psig by adding nitrogen from the cylinder. Once the pressure reading had settled, slight pressure adjustments were made either by cracking the vacuum valve or by introducing more nitrogen from the canister. When the guage read 10 psig ($\pm$ 0.1 psig), the entire system was left alone for 6-8

hours to settle into the new equilibrium state point. Later, the next data set was taken, the pressure was increased to 20 psig, and so on up to 60 psig.

Next, the rod power was changed to 3 watts per rod, and the data sets were again taken for the seven pressure settings. Finally, the rod power was changed to 5 watts per rod, and again data was taken over the seven pressure settings. When these data sets were completed, certain state points were repeated to determine a repeatability error. When the nitrogen data sets were completed, the vessel was purged with helium, and the entire procedure was repeated for the three different power settings and the seven different pressure settings. Certain state points were also repeated with helium backfill to further characterize the repeatability error.

4.4 DATA REDUCTION

The next step in this experiment involved analyzing the raw data from the test results and calculating the Nusselt and Rayleigh numbers both for the individual rods and for the rod array as a whole. Figure 4.1 gives a diagram that describes the data reduction methodology. The data were reduced by converting the raw data text files into an Excel spreadsheet, on which all of the calculations were performed.

The first step in the data reduction process was to average the multiple TC readings and determine their standard deviation from the average. This standard deviation gives an estimate of the noise and repeatability error in the TC readings. The two TC readings from each rod and the ten CuBE TC readings were then averaged to give a single surface temperature for each rod (T_r) and for the CuBE (T_c). The film temperature for each rod was calculated next, followed by the average rod temperature and the bundle-averaged film temperature.

This temperature data, the bundle geometry, and the measured surface emissivities formed the inputs to the RADERA II code, listed in the Appendix. As described briefly in Chapter 2, this code solves a finite-element form of the radiation transport equation for discrete elements of each rod and of the CuBE wall. This solution yields the net radiative heat flux for each element. The code then integrates this heat flux around the each rod's surface to calculate the net radiative

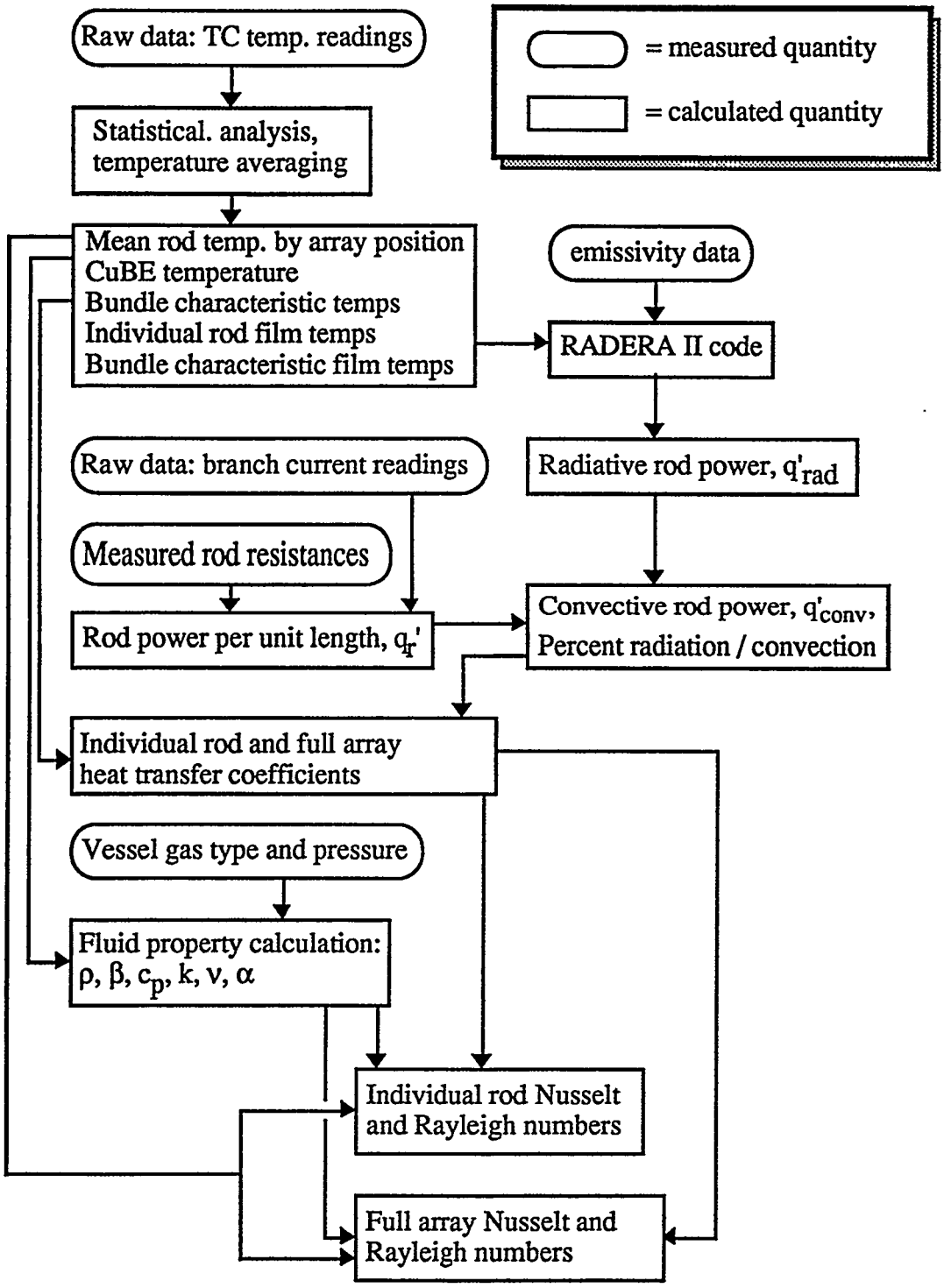

Figure 4.1 Diagram of data reduction sequence.

heat rate per unit length for each rod, q'_{rad}. Examples of an input file to and an output file from this code are also given in the Appendix.

The branch current readings were, like the temperature readings, also averaged over many samples. The averaged current readings, the measured resistances of each rod (about 6 ohms), and the known heated length of each rod (about 82 cm) allowed the calculation of the total rod input power per unit length, q'_r (see equation 2.5). Next, the net radiative heat rate per unit length was subtracted from the total input power per unit length to yield the net convective heat rate per unit length, q'_{conv} (see equation 2.4). This quantity was summed for each rod to yield the total convective heat rate for the bundle, Q'_{conv} (see equation 2.20). A fraction of the total bundle heat rate that is transferred by radiation and convection was also calculated and is discussed in Chapter 5.

Next, the individual rod and the full array heat transfer coefficients are calculated from the temperature results and the net convective heat rate results. The individual rod heat transfer coefficient is given in equation 2.7, and the full array heat transfer coefficient is given in equation 2.20.

Almost all of the relevant fluid properties were calculated using semi-empirical correlations obtained from *The Properties of Liquids and Gases* [Reid, Prausnitz, and Poling, 1987]. These correlations used the backfill gas identity (either nitrogen or helium), the vessel pressure, and the appropriate film temperature as inputs. For the individual rod correlations, these fluid properties were evaluated at the individual rod film temperature, given in equation 2.18. For the full array correlations, the fluid properties were evaluated at the mean bundle film temperature, given in equation 2.23. The one exception to this was the thermal expansion coefficient, β (eqn. 2.11), which was calculated theoretically based on the ideal gas law.

Next, the heat transfer coefficients, the temperature data, and the fluid properties were used to calculate the individual rod Nusselt and Rayleigh numbers (equations 2.16 and 2.17), as well as the full array Nusselt (eqns. 2.21 & 2.22) and Rayleigh numbers (eqns. 2.24, 2.25, & 2.27). Finally, the Nusselt and Rayleigh number data were plotted and piecewise curve-fits for the data were calculated using the logarithmic correlation form recommended by Morgan [1975],

$Nu = C(Ra)^n$. Chapter 5 presents all of the Nusselt and Rayleigh number data, along with tabulations of the correlations.

4.5 EXPERIMENTAL UNCERTAINTY

As with any experimental procedure, there is uncertainty both in each measurement taken and subsequent calculations based on those measurements. This section describes some of the major sources of experimental error and gives the overall uncertainty of the individual rod and full array Nusselt and Rayleigh numbers. However, this thesis will not discuss the propagation of each individual error source throughout all of the data reduction. This topic is thoroughly discussed in Chapter 9 of Canaan's dissertation. Canaan's analysis used the method of sequential perturbation [Moffatt, 1988] to propagate uncertainties in directly measured quantities (such as temperature and pressure) through to the derived quantities (such as Nusselt and Rayleigh numbers) that are based on these measured variables. This section will simply describe the major error sources and state the approximate uncertainty from each source, then present the final uncertainty in the Nusselt and Rayleigh numbers.

4.5.1 Surface Temperature Uncertainty

There are many potential sources of error influencing the temperature values recorded by the automated data acquisition system (ADAS). There are two general types of temperature measurement error. The first type of errors are errors resulting either from thermal effects or from experimental assumptions--errors in which the temperature measured at the TC junction is not the same as the true temperature of interest. The second error type results from errors in the TCs and the ADAS--the components that translate a temperature into a measured voltage signal.

One contributor to the first type of error is thermocouple (TC) mounting error, which results from the fact that the TC junction may not be at exactly the same temperature as the rod or the CuBE surface. For example, the foil TCs

mounted on the CuBE walls have a thin layer of epoxy that separates the TC junction from the actual surface. Also, the junctions of the rod TCs are mounted about 0.5 mm below the rod surface. However, a radial thermal conduction analysis has shown that the temperature difference between the rod surface and the TC junctions is less than 0.01°C [Canaan, 1995].

Another contributor to the first type of error arises from the symmetry and isothermal assumptions made in this experiment. First, it was assumed that the entire CuBE surface was isothermal. Ten different TCs were used to measure the CuBE temperature, and the final CuBE temperature used was an average of these 10 readings. For the most extreme case, which was a nitrogen backfill at 0 psig and 5 watts / rod, the variation in all the CuBE readings was ± 0.3°C. Second, the rod surface temperatures were assumed to be symmetric about the vertical plane of the array. A couple of instrumented rods were used on the "non-instrumented" side (the right side in Figure 3.3) to check this assumption, and the worst error case showed an error of about ± 0.4°C in the symmetry assumption. A final temperature assumption is that the rod surface is isothermal around its circumference. Each rod surface temperature is an average of two TC readings at different points on the rod circumference. The maximum variability between TC readings on the same rod was ± 0.2°C.

The main source of error in the surface temperature comes from using thermocouples and the ADAS to measure the temperature. The thermocouples produce a small voltage that is proportional to the temperature at its junction, and the ADAS multiplexes these signals, amplifies them and converts them to digital signals. There are errors associated both with the TCs themselves and with the signal processing and conditioning within the ADAS.

There are two ways to determine the overall uncertainty associated with the ADAS. The indirect method involves adding up all of the stated individual manufacturer error specifications for the TCs and the ADAS hardware. Canaan's analysis yields an overall uncertainty of ± 2.3°C from the overall TC and ADAS hardware [Canaan, 1995].

The direct calibration method involves comparing the readings from the ADAS at various temperatures to a known standard. For the UT experimental error

analysis, the "known standard" took the form of an Omega hand-held TC calibrator. First, a given temperature is set on the calibrator and a small TC connector is run between the calibrator and the plug board of the ADAS. The calibrator sends out a DC voltage signal that is equal to the voltage that the National Institute for Standards and Technology (NIST) has established for that temperature as the standard for a Type K thermocouple. The difference between the temperature read by the ADAS and the set temperature on the calibrator gives a measure of the ADAS error. For this experiment, the maximum deviation between the Omega calibrator setting and the ADAS reading was ± 1.5°C [Canaan, 1995].

When this direct calibration error of ± 1.5°C was combined with the uncertainty of the calibrator of 1.0°C and the additional temperature uncertainties from the mounting errors and the symmetry assumptions described above, the overall surface temperature uncertainty was taken to be ± 2.0°C [Canaan, 1995]. This is the error for a single TC measurement. The uncertainty in the rod surface temperature, T_r, which is the *average* of 2 TC readings, is only ± 1.5°C. This is because the process of averaging measured values reduces the uncertainty in the *averaged* result. The final uncertainties in all of the temperature variables used in this analysis are summarized below in Table 4.1.

Table 4.1 Uncertainties of Temperature Variables
[Canaan, 1995]

Temperature variable	Uncertainty, ± °C
Individual TC measurement	2.0
Rod surface temp., T_r	1.5
CuBE surface temp., T_c	0.71
Ind. rod film temp., T_f	0.79
Bundle-averaged rod temp., T_{bund}	0.25
Mean bundle film temp., $T_{f,bund}$	0.38

4.5.2 Rod Power Uncertainty

The rod input power per unit length, q'_r, is an essential quantity in determining the heat transfer coefficients used to calculate the Nusselt numbers. This quantity, given by equation 2.5, depends on knowing the current in the nichrome coil, the resistance of the coil, and the heated length of the rod. The heated length of each rod is 82.1 ± 1.5 cm, and the uncertainty in the measured resistance of each rod *at room temperature* is about 0.001 Ω [Canaan, 1995]. This very small uncertainty comes from the measurement error of the multimeter used to measure the rod's resistance. However, since the rod resistance varies from its room temperature value (about 6 Ω) by about 1% over the temperature range of this experiment, a value of ± 0.05 Ω is more appropriate to use for the uncertainty analysis [Canaan, 1995].

The error in the measured current in each rod is more complicated, because the ADAS is used to measure current. Thus, this measurement is subject to the same types of ADAS errors as the temperature measurements. Canaan's analysis asserts that the overall error in branch current measurement is about 3.5 mA. At the lowest experimental power setting of 1 W / rod, the current is about 0.4 A; thus, the current measurement error corresponds to an uncertainty of about 0.9 percent. Propagating these error values through the calculation for rod power per unit length results in an uncertainty in q'_r of ± 0.067 W/m for the most extreme case, and an uncertainty of ± 0.030 W/m on the average [Canaan, 1995].

4.5.3 Uncertainty of Pressure

Recall from Chapter 3 that the vessel pressure was measured with an Omega type T Bourdon tube pressure gauge with a visual analog readout. The resolution of this gauge was 0.5 psig; thus, the gauge uncertainty was taken to be ± 0.2 / 2 psig, or ± 0.1 psig.

4.5.4 Uncertainty of the Net Radiative Heat Rate, q'_{rad}

There are three main sources of error in the numerical calculation of the net radiative heat rate per unit length of each rod, q'_{rad}. The first error source is the error that is propagated through the code due to the uncertainties in the surface temperatures, which form one of the code's main inputs. The uncertainty in the mean temperature of each rod is $\pm$ 1.5°C. The second error source is the uncertainty in the surface emissivities of each rod and of the CuBE surface. The emissivity of all interior surfaces within the bundle was taken to be $\varepsilon = 0.80 \pm 0.02$. The final error source is the error that comes from discretizing the continuous surfaces into finite elements. The first two errors are arise from uncertainties in measured variables or properties, while the third error comes from the uncertainties in the RADERA II code's solution.

Canaan performed a systematic investigation of the effect of each error source on the final net radiative heat rate for each rod. This investigation was performed on the state point of nitrogen at 0 psig, with a rod power input of 5 W/rod, which corresponds to a rod power input per unit length of $q'_r = 6.1$ W/m. The results of this calculation yielded both a maximum and an average uncertainty in q'_{rad} due to each of the above three factors. These errors were then combined using the appropriate root-sum-square method recommended by Moffatt to combine uncertainties. The final results of this investigation showed that the *maximum* uncertainty in q'_{rad} for any given rod was 0.76 W/m, and the average uncertainty in q'_{rad} for a given rod was 0.12 W/m. Thus, the maximum radiative heat rate uncertainty for any rod was about 12 percent of the rod input power, and the average radiative heat rate uncertainty for all of the rods was about 2 percent of the rod input power.

4.5.5 Uncertainty of Calculated Fluid Properties

As mentioned in section 4.4, semi-empirical correlations from Reid et al. [1987] were used to calculate the fluid properties needed to calculate Nusselt and

Rayleigh numbers. When these correlations were compared to experimentally measured values for nitrogen and helium [Vargaftik, 1975] over the range of temperature and pressure in this experiment, the maximum percentage error for any property was less than 1 percent, and the average deviation was about 0.7 percent. These errors are much smaller than the uncertainty introduced into the fluid properties due to uncertainties in the temperature and pressure used as calculation inputs. Thus, this error was deemed negligible [Canaan, 1995].

4.5.6 Other Uncertainties

Some other uncertainties in this experiment included uncertainties in the length scales involved, as well as experimental repeatability errors. The heater rod length, L, the rod outer diameter, d, and the height of the inside wall of the CuBE, H, are all quantities needed to calculate the Nusselt and Rayleigh numbers. As mentioned earlier, the heated length of the rods is 82.1 ± 1.65 cm. The rod diameter is 1.224 ± 0.005 cm, and the CuBE height is 13.406 ± 0.003 cm. These uncertainties were incorporated into the uncertainty analysis of the Nusselt and Rayleigh numbers.

One variable factor that one might think would be an experimental error but is actually not is the variability in the CuBE temperature, T_C. This variability results from day-to-day changes in the UT cooling water supply at the J.J. Pickle Research Campus. Over the course of this series of experiments, this temperature varied by about 1.5°C. However, the Nusselt and Rayleigh numbers are based on the temperature *difference* between the rods and the CuBE. Thus, while the CuBE temperature may have varied from experiment to experiment, the actual temperature difference between data sets for rods at the same power and pressure settings varied less than 0.5°C. Since this error is well within the 2.0°C experimental uncertainty of a temperature measurement, this error was neglected.

Another possible factor that could increase the overall experimental error is the fact that the uncertainty in the surface emissivities of the rods and the CuBE could be higher than the 0.02 value used in this uncertainty analysis. This 0.02

value comes from testing done both at NASA and at Sandia for the Pyromark 2500 coating on steel. Further experimental testing at UT with a thermal imaging camera supported the emissivity measurement [Canaan, 1995], and Aliaga [1992] asserts that the uncertainty of emissivity measurements with the thermal camera are about 0.02. However, since it was not feasible to make direct emissivity measurements inside the rod bundle, it is possible that the emissivity could be slightly lower than 0.78 or higher than 0.82.

An additional possible error source arises from the definition of the bundle averaged film temperature (eqn. 2.23). This temperature may not be the best definition of the average temperature of the fluid in the bundle. Thus, the calculated fluid properties based on this bundle averaged film temperature may not accurately represent the average fluid properties of the fluid in the entire bundle.

4.5.7 Uncertainties in Nusselt and Rayleigh Numbers

Table 4.2 presents the results of the uncertainty propagation to the final Nusselt and Rayleigh numbers. Notice that the uncertainties in the full bundle numbers are lower than the uncertainties for the individual rod Nu and Ra numbers. This is because the bundle-averaged Nu and Ra numbers are based on upon averages of many more quantities, which reduces the experimental uncertainty.

These figures represent the overall experimental uncertainty in the Nusselt and Rayleigh number data. They do not include the deviation of the data from the logarithmic curve fits given in the following chapter. Because this thesis may not consider all possible types of error (such as the possibility of higher emissivity error), a conservative error estimate would be to assume 15 to 20 percent error for the individual rod Nusselt and Rayleigh number data and 10 percent error for the bundle-averaged Nusselt and Rayleigh number data.

Table 4.2 Summary of Nusselt and Rayleigh Number Uncertainties
[Canaan, 1995]

Dimensionless number	Uncertainty, ± %
Ind. rod Rayleigh number, Ra	5 %
Ind. rod Nusselt number, Nu	13 %
Bundle Nusselt number, Nu_{bund}	2 %
Bundle Nusselt number, Nu_{max}	2 %
Bundle Rayleigh number, Ra_{bund}	4 %
Bundle Rayleigh number, Ra_{max}	4 %
Bundle Rayleigh number, $Ra_{Q'}$	4 %

This chapter has presented the experimental procedure and data reduction methodology for this research, as well as briefly summarized the major contributors to experimental error and uncertainty. The following chapter presents the results of the research, and Chapter 6 summarizes the thesis' main points and recommends some possible future research work.

Chapter 5 -- Results and Discussion

5.1 Overview

This chapter presents the final results of the measurements and calculations described in the previous chapter. The results are presented in three sections.

The first section discusses variations of temperature and heat transfer within the rod bundle as the system state points are varied. The variation of maximum rod temperature difference with respect to changes in vessel pressure and rod input power is discussed first, along with a discussion of the location of the maximum rod temperature. Next, the change in the contribution of radiation and convection to the overall heat transferred within the bundle is discussed. As these trends are discussed, comparisons are made to trends observed in the aligned rod bundle experiment.

The second section discusses the dimensionless Nusselt-Rayleigh number correlations for the entire rod bundle. These trends in these full array correlations are discussed and compared to similar correlations for the aligned bundle. The experimental results for these two arrays are also compared to results of a numerical conduction study in order to investigate differences between the aligned and staggered arrays in the low Rayleigh number regime. The results are also compared to known results from forced convection in aligned and staggered tube bundles, and to known results from natural convection in non-enclosed and enclosed tube bundles.

The third section presents Nusselt-Rayleigh number correlations for individual rods. This section discusses trends in heat transfer for different rods, and points out some unexpected results for certain rod locations. Next, this section compares the results for individual rods to results for individual rods in similar positions in Canaan's aligned array. Also, the results are compared to individual rods in other natural convection experiments, such as the results of Choi and Cha [1990].

5.2 Temperature and Heat Transfer Trends

5.2.1 Maximum Rod Temperature Variation

Figure 5.1 shows the steady state maximum rod temperature difference for each of the 42 equilibrium states. The maximum temperature difference, rather than the absolute maximum temperature, is presented because it is the temperature difference which drives heat transfer from the rods to the CuBE. For all of these experiments, the CuBE temperature varied between 21 and 23 degrees C. Recall that the maximum rod temperature difference is defined as the maximum rod temperature minus the CuBE temperature ($\Delta T_{max} = T_{max} - T_C$). The maximum temperature difference is plotted for seven different pressures (0 to 60 psig), for 3 different power levels (1, 3 and 5 watts per rod), and for the two backfill gases, nitrogen and helium.

Two main trends should be observed immediately from these curves. First, notice that for both a nitrogen and a helium backfill at any fixed pressure, the maximum temperature difference increases as the rod input power is increased. Since temperature difference is the driving force for heat flow, this rise in temperature difference with increased heat input is expected.

Second, notice that for a given power input, the temperature difference decreases as the system pressure is increased. This decrease in temperature is due to increased natural convection between the heated rods and the cooled enclosure wall. Increasing the system pressure increases the system Rayleigh number, which increases the strength of the buoyancy forces within the rod array. For an ideal gas, the Rayleigh number is proportional to the square of the absolute pressure [Canaan, 1995].

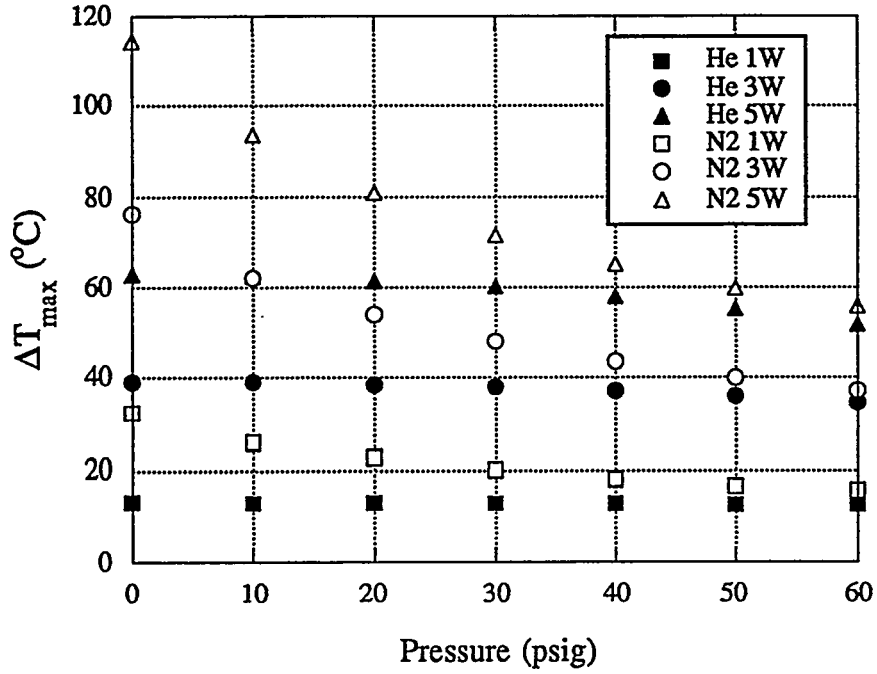

Figure 5.1 Maximum rod temperature difference (ΔT_{max}) versus vessel pressure. $T_C = 22° \pm 1°$ C.

However, the increase in Rayleigh number only causes a significant temperature decrease for the nitrogen backfill. For the nitrogen backfill at 5 W / rod, the maximum temperature difference drops by about 60° C (from 114°C to 54°C) from a pressure of 0 psig to 60 psig, a drop of a little over 50%. For the helium at 5 W / rod, the maximum temperature is much lower, and the temperature drops by only about 10° C over the same 0-to-60 psig pressure range. For the case of helium at 1 W / rod, the maximum temperature changes less than one degree over the entire pressure range.

Since, for the helium backfill, the temperature difference is approximately constant while the driving force for natural convection is increasing, this indicates that conduction and not convection is the primary mode of heat transfer from the rods to the enclosure. For a given bulk gas temperature and pressure, nitrogen has

a Rayleigh number that is about 65 times greater than helium [Canaan, 1995]. Thus, for a given state, the buoyancy forces that drive natural convection are much stronger in a nitrogen backfill than in a helium backfill. However, since helium's thermal conductivity is about 7 times higher than that of nitrogen, the helium transfers heat more easily from the rods to the wall.

5.2.2 Comparison of Maximum Rod Temperature for Aligned and Staggered Arrays

Figure 5.2 shows maximum rod temperature difference data for the aligned array experiment. This data shows many of the same trends as the staggered array. However, while this data may look exactly like the staggered array data, a couple of points should be noted.

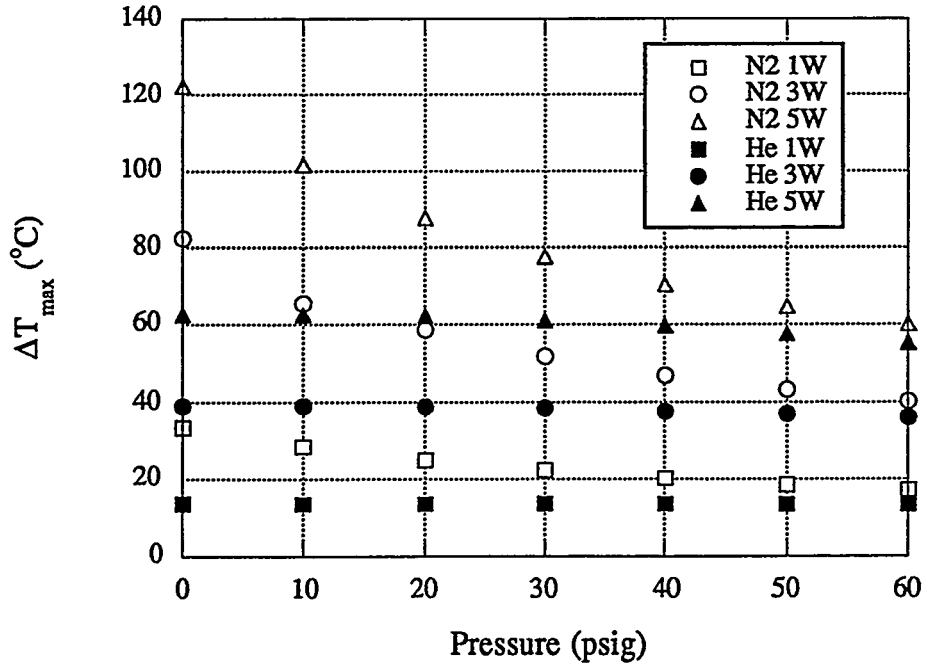

Figure 5.2 Maximum temperature difference vs. pressure for aligned array. $T_C = 22° \pm 1°$ C [Canaan, 1995].

For the nitrogen data, the aligned array has a slightly higher maximum temperature at a given pressure and rod power. This is an expected result, because while both array configuration experiments used the same heat input per rod, the aligned array has 4 more rods than the staggered array. Thus, the total heat input for the aligned array is greater for a given rod power setpoint, resulting in a slightly higher maximum temperature.

However, for the helium data, the maximum temperature difference is about the same between the two geometries, even though the total heat input is higher for the aligned array. This suggests that, for the helium backfill, the aligned array may be transferring heat more effectively from the rod bundle to the walls than the staggered array. This topic will be discussed in more detail in section 5.3 of this chapter.

5.2.3 Location of Maximum Rod Temperature

Figure 5.3 gives the location of the rod with the maximum surface temperature in the staggered array. The maximum rod temperature was always on a rod in column D, the column closest to the vertical centerline of the bundle. Since the vertical centerline is farthest from the cooled side walls of the enclosure, this result is expected. The plot gives the column D row number of the rod versus the bundle averaged Rayleigh number, defined in equation 2.24 (refer to Figure 5.4 for a diagram of the rod locations).

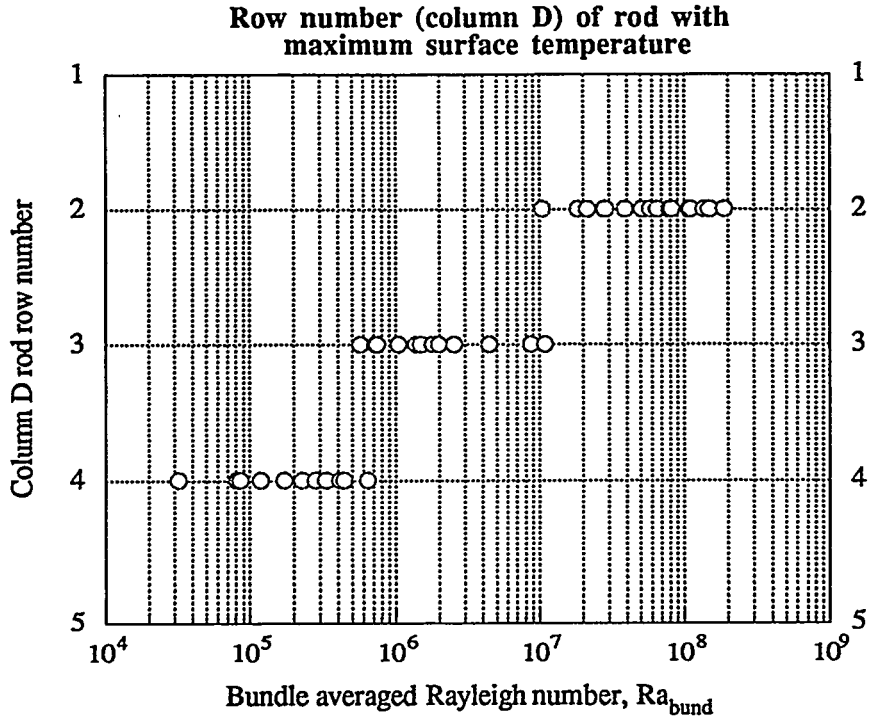

Figure 5.3 Location of maximum rod surface temperature for the staggered array versus bundle-averaged Rayleigh number.

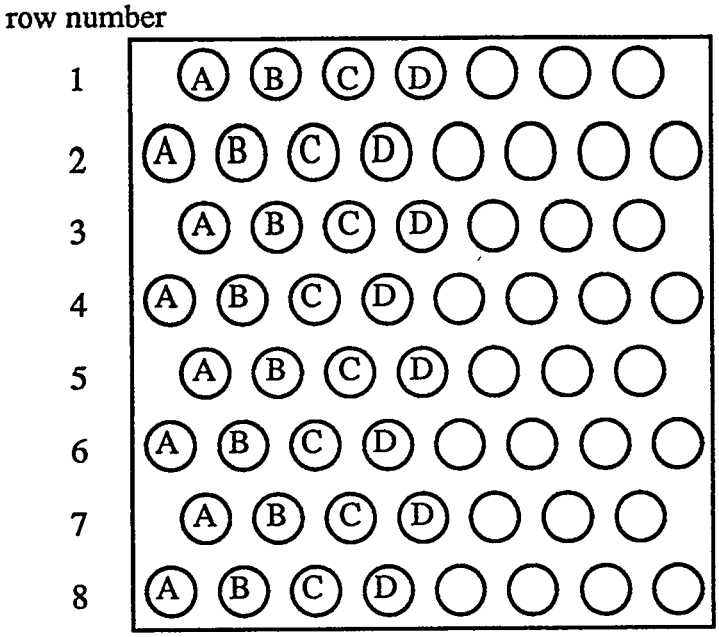

Figure 5.4 Diagram of rod locations within the UT staggered array.

The bundle average Rayleigh number defines the strength of the buoyant flow in the entire enclosed rod bundle. As the Rayleigh number increases, one would expect to see the location of the maximum temperature move upward within the enclosure as the natural convection velocities increase. For a non-enclosed rod bundle, the maximum rod temperature could be located as high as the top row of rods. However, since the enclosure "ceiling" is maintained at a constant cool temperature by the water flow, the maximum temperature location is kept within the interior of the rod bundle. Also, note that because of the geometry of the staggered rods and the symmetry of the flow about the vertical centerline, the maximum temperature is shared by two rods on rows 2 and 4—rods D2/E2 and D4/E4, respectively. The Rayleigh number where the maximum rod temperature moves from rod D4 to D3 is about $7.0*10^5$. For transition from D3 to D2, the Rayleigh number is about $1.5*10^7$. This transition is not a perfectly "sharp" transition but is slightly blurred. This is evidenced by the "jumps" of maximum temperature location back and forth between rods in the vicinity of these transition Rayleigh numbers.

5.2.4 Contribution of Radiation to Overall Heat Transfer

Figure 5.5 (next page) shows the percent contribution of radiation heat transfer to the total heat dissipated in the rod bundle, for the same experimental data. Recall that the heat input to each rod is dissipated as both radiation and convection. The percent radiation contribution is the sum of the radiative power per unit length (q'_{rad}) summed over all rods, divided by total input power per unit length to all rods (Q'), multiplied by 100. The remaining percentage of heat input is removed through convection.

There are two main trends that should be observed from this data. First, notice that for a given rod power and pressure, radiation heat transfer is greater for the nitrogen gas than for the helium. This is because the average temperature of the rod bundle is much lower in the helium backfill than in the nitrogen backfill, due to helium's high thermal conductivity. As the average bundle temperature increases, the amount of heat transferred through radiation increases because of the fourth-power dependence of radiation on surface temperatures.

Second, notice that in the nitrogen backfill, the percent radiation decreases significantly as the system pressure is increased, but for the helium backfill, the percent radiation changes very little as the pressure is increased. These trends support the assertion that the helium backfill is primarily in a conduction heat transfer mode, while the nitrogen backfill is more in a convection mode. As the system pressure, and thus the Rayleigh number, is increased, the percent convection increases significantly for the nitrogen backfill, but not for the helium backfill. Since an increasing Rayleigh number implies increasing buoyant forces and local fluid velocities, the fact that convection doesn't change appreciably with Rayleigh number indicates that conduction is the dominant heat transfer mechanism.

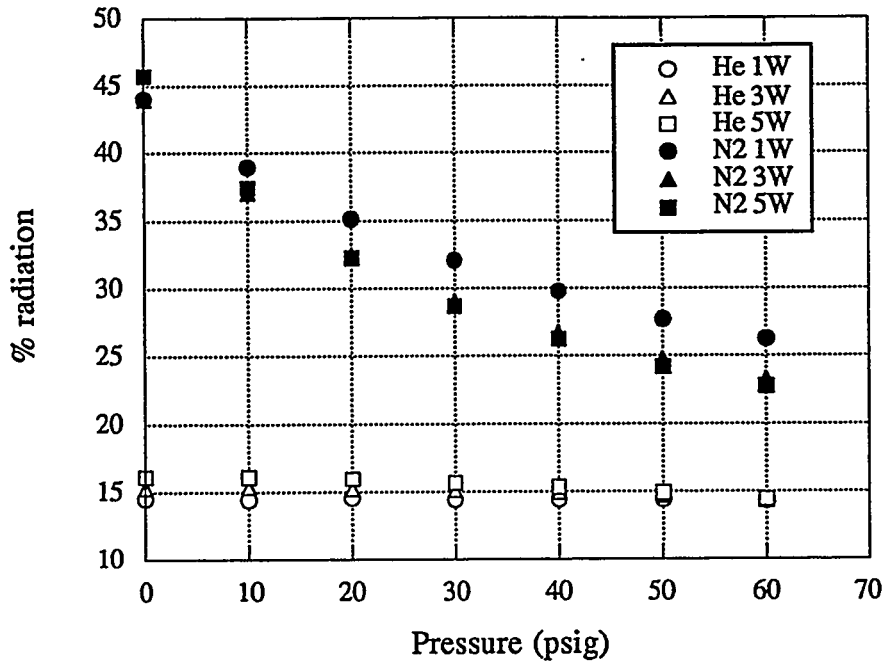

Figure 5.5 Percent contribution of radiation versus system pressure. $T_C = 22 \pm 1°C$.

Figure 5.6 shows the percent contribution of radiation versus system pressure for Canaan's aligned experiment. Again, the trends are very similar to those of the staggered array. However, a couple of interesting contrasts should be noted.

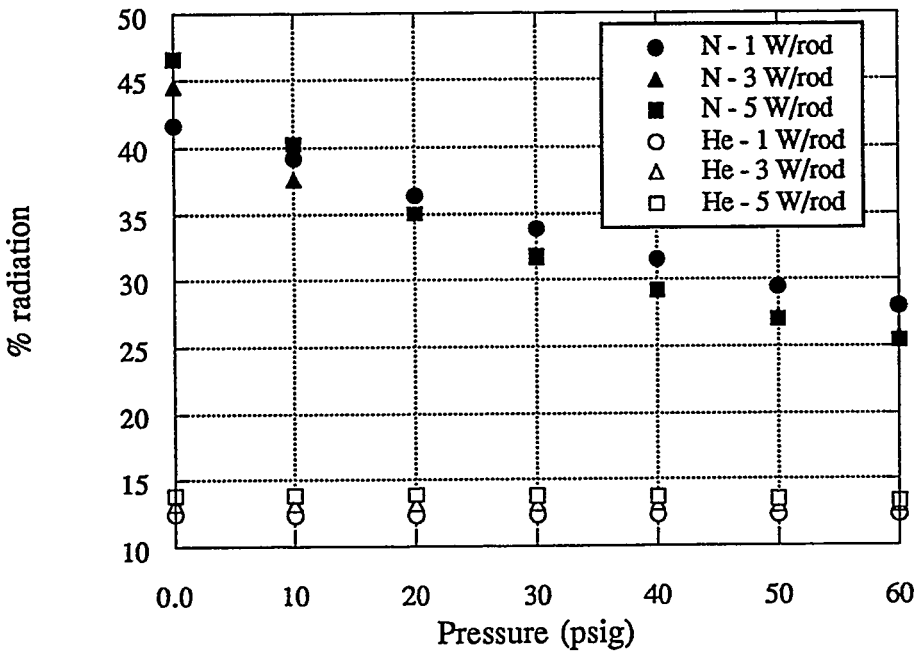

Figure 5.6 Percent radiation contribution vs. pressure for Canaan's aligned array. $T_C = 22 \pm 1°C$ [Canaan, 1995].

For the nitrogen data, the percent radiation is slightly higher for the aligned array than the staggered array. This is probably because the average temperature difference between the rods and the enclosure is higher in the aligned array due to the additional 4 heated rods. However, for the helium data, the percent radiation is higher in the staggered array, which means that the percent contribution of

convection / conduction is lower in the staggered array than in the aligned array. This is a bit surprising, because one normally thinks of convection and heat transfer being enhanced in a staggered array versus an aligned array. However, since the helium data is in more of a conduction regime, factors other than flow conditions around the rods are influencing the overall heat transfer. This topic will be discussed in section 5.3 of this chapter.

The results and trends presented in this section are unique to the geometry, input parameters, and setpoints used for this experiment. While the qualitative trends provide insight into the natural convection in enclosed, staggered horizontal cylinder bundles, the reader should exercise caution before quantitatively applying these to bundles with different enclosure temperatures, different size rods, different rod powers, or different system pressures.

5.3 Full Array Heat Transfer Correlations

This section presents the dimensionless Nusselt-Rayleigh number correlations for the entire rod array. All of the correlations are of the form recommended by Morgan for natural convection from single horizontal cylinders, where $Nu = C(Ra)^n$ [Morgan, 1975]. Since both helium and nitrogen have Prandtl numbers close to that of air (helium ranges from 0.678 to 0.680, nitrogen ranges from 0.704 to 0.716), no explicit dependence on Prandtl number is needed for these correlations. Three bundle correlations are presented. The first correlation defines the Nusselt and Rayleigh numbers using the bundle average temperature difference, ΔT_{bund}. The second correlation uses the Nusselt and Rayleigh numbers based on the maximum rod temperature difference, ΔT_{max}. The third full array correlation again uses the Nusselt number based on ΔT_{bund}, but uses the Rayleigh number based on the total convective heat rate, Q'_{conv} (eqn. 2.27). Next, the full array results are compared to the results for Canaan's aligned array. Finally, the results are compared to convection results for forced convection over aligned and staggered tube banks and to results from other natural convection studies of staggered tube arrays.

5.3.1 Correlation 1: Based on Average Temperature Difference, ΔT_{bund}

Figure 5.7 presents the Nusselt-Rayleigh number data calculated using equation 2.21 for the Nusselt number and equation 2.24 for the Rayleigh number. The data seem split into two separate regimes, one in which the Nusselt number increases very slowly with Rayleigh number, and another in which the Nusselt number increases much more rapidly. The two regimes were fit according to the equation:

$$Nu_{bund} = 10.4\ (Ra_{bund})^{0.019} \qquad 3.2*10^4 < Ra_{bund} < 1.0*10^6$$
$$Nu_{bund} = 0.140\ (Ra_{bund})^{0.322} \qquad 1.4*10^6 < Ra_{bund} < 1.9*10^8$$
$$Ra_{critical} = \text{approx. } 1.2*10^6 \qquad (5.1)$$

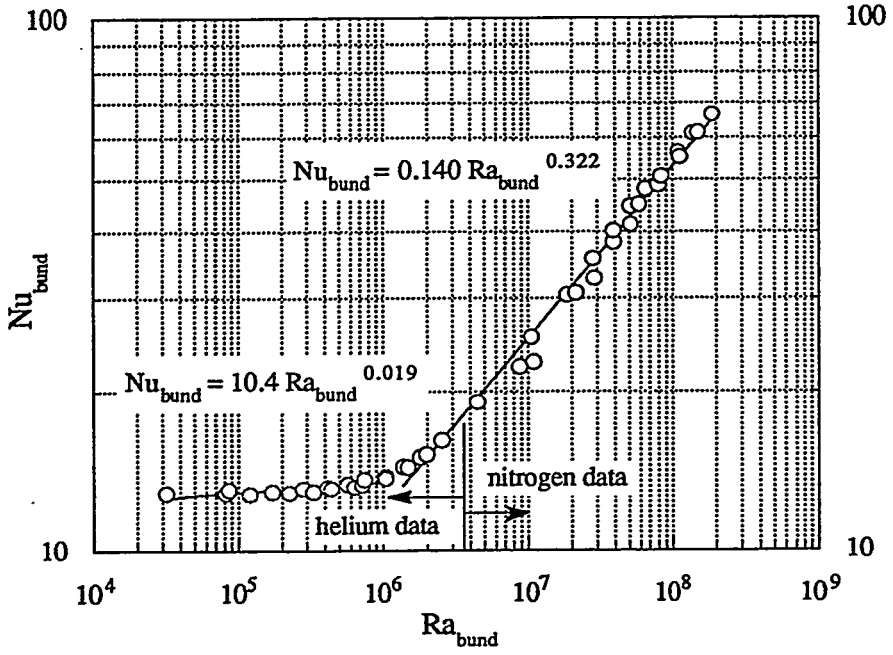

Figure 5.7 Full array Nusselt vs. Rayleigh numbers, where Nu and Ra are functions of the mean bundle temperature difference, ΔT_{bund}.

The two-regime trend of the data is similar to the pattern of the Rayleigh-Benard conduction / convection problem. In the Rayleigh-Benard problem, heat being transferred from a hot lower flat plate to a cooler upper plate occurs only by conduction at small Rayleigh numbers. For conduction, the Nusselt number is constant as the temperature difference between the plates (which is proportional to the Rayleigh number) is increased. However, once a critical Rayleigh number is reached, buoyant forces overcome viscous fluid forces and fluid motion occurs. From this point on, the Nusselt number increases monotonically as Rayleigh number is increased [Koschmeider, 1993]. While this enclosed staggered tube bundle experiment has a much different geometry and boundary conditions than two horizontal flat plates, the heat transfer behavior is similar.

Notice that the slope of the first regime is not exactly zero, but is slightly positive. This indicates that heat transfer in the lower Rayleigh number regime is not pure conduction, but has a slight amount of fluid flow and convection occurring. Also, notice that in the convective regime, the Nusselt number increases with Rayleigh number to the power of about 1/3. This is consistent with the correlation of Globe and Dropkin [1959] for Rayleigh-Benard type convection of a fluid within a rectangular cavity with a hot bottom plate, a cool top plate, and insulated side walls. Their correlation is given as

$$Nu_{avg} = 0.069 Ra^{1/3} Pr^{0.074} \qquad (5.2)$$

Thus, the comparison of this experiment to the Rayleigh-Benard convection problem seems valid.

It has been observed that for turbulent natural convection, the Nusselt number is proportional to the characteristic temperature difference, ΔT, raised to the power of 1/3 [Bejan, 1984]. For the above correlation (eqn. 5.1), the defined Rayleigh number, Ra_{bund}, is proportional to the bundle-averaged temperature difference, ΔT_{bund} (see eqn. 2.24). Since the correlation's Rayleigh number exponent is 0.322, which is very close to 1/3, this gives evidence that the convection within the rod bundle is turbulent for Rayleigh numbers above the critical value.

The transition to the turbulent convection regime is not at the same Rayleigh number as the division between the helium and nitrogen data. The fact that the nitrogen and helium data do not overlap is simply a coincidence. If a helium backfill were used with much higher vessel pressures or higher rod input powers, then the helium data would overlap into the nitrogen data. Similarly, if the nitrogen backfill were used with very low rod powers and / or vessel pressures, then the nitrogen data would overlap into the upper end of the helium data. It just so happens that the Rayleigh number for the 1 W / rod, 0 psig, nitrogen case is a bit higher than the Rayleigh number for the 5 W / rod, 60 psig, helium case.

5.3.2 Correlation 2: Based on Maximum Rod Temperature Difference, ΔT_{max}

Figure 5.8 presents the Nusselt-Rayleigh number data for the 42 experimental state points, correlated using the maximum rod temperature difference, ΔT_{max}, instead of the average rod temperature difference. The definitions of Nu_{max} and Ra_{max} are given in equations 2.22 and 2.25, respectively. Notice that the characteristic temperature difference used is the maximum rod temperature difference, but that the fluid properties are still based upon the mean bundle film temperature, $T_{f,bund} = (T_C + T_{bund}) / 2$. The data were correlated with the following equation:

$$Nu_{max} = 6.36\ (Ra_{max})^{0.018} \qquad 5.3*10^4 < Ra_{max} < 1.7*10^6$$
$$Nu_{max} = 0.038\ (Ra_{max})^{0.366} \qquad 2.3*10^6 < Ra_{max} < 2.6*10^8$$
$$Ra_{critical} = \text{approx. } 2.0*10^6 \qquad (5.3)$$

The data of Figure 5.8 show the same trends as the data based on the mean bundle film temperature. There is a two-regime division which is characterized by a critical Rayleigh number. The first regime Nusselt number has a weak dependence on Rayleigh number, suggesting heat transfer dominated by conduction. The second regime has a stronger dependence on Rayleigh number, which suggests heat transfer dominated by convection.

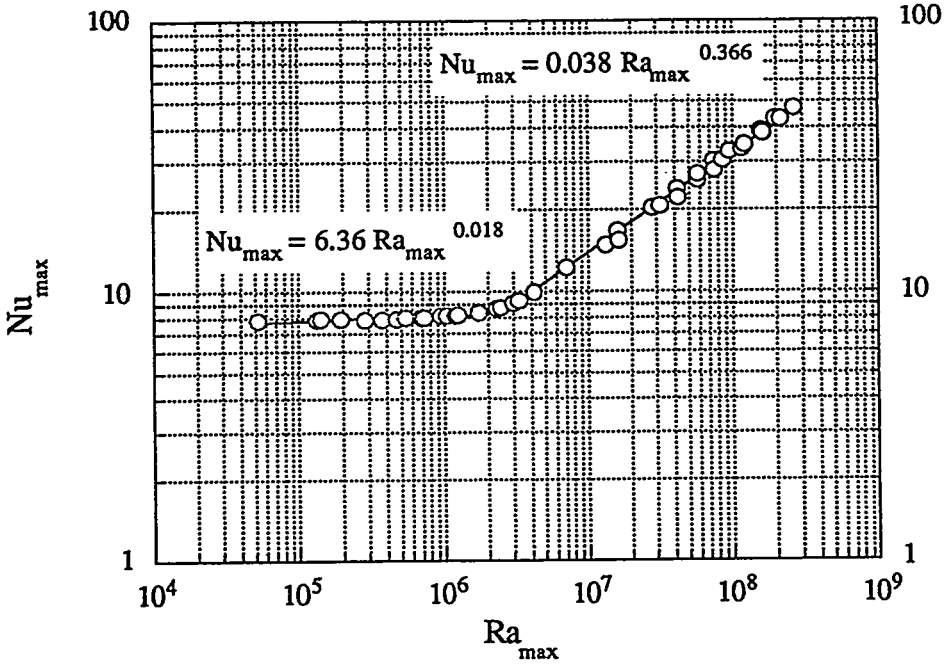

Figure 5.8 Nusselt-Rayleigh number data for the staggered array, where Nu and Ra are functions of the maximum rod temperature difference, ΔT_{max}.

Notice that the slope of the convection regime data in correlation 1 is steeper than the slope of the data in correlation 2. This is because the first correlation is based on the bundle average temperature difference, while the second is based on the maximum rod temperature difference. If the ratio between the two temperature differences were constant over all of the state points, then the slopes of the two correlations should be very close to each other. However, as shown in Figure 5.9, the ratio of ΔT_{max} to ΔT_{bund} varies between 1.7 and 1.4. This variation in temperature ratio is the cause of the change of the shapes of the Nusselt-Rayleigh number curves between correlations 1 and 2.

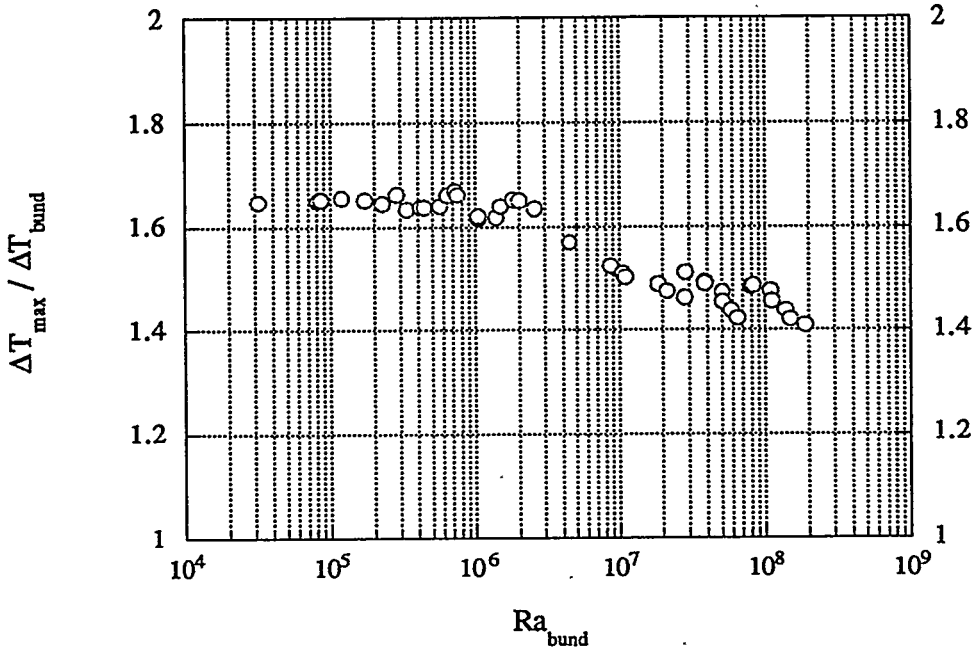

Figure 5.9 Ratio of maximum rod temperature difference to bundle average temperature difference.

The fact that the two temperature differences do not vary in exactly the same way indicates the importance of selecting the proper characteristic temperature difference for natural convection correlations. It is important to select a temperature difference that is a good physical representation of the driving force for heat transfer. In this case, the bundle average temperature difference, ΔT_{bund}, is probably a better characteristic temperature difference for heat transfer from the entire bundle to the CuBE surface. However, the correlation based on ΔT_{max} is useful because it gives information about the maximum rod temperature in the bundle, which is often useful in heat transfer calculations and design. Often, the critical factor in a cooling application is keeping a certain component or material under a critical maximum temperature. Thus, the type of correlation used depends

upon whether one is interested in the overall heat transfer behavior or in the maximum temperature.

5.3.3 Correlation 3: Based on Total Convective Heat Rate Per Unit Length, Q'_{conv}

Figure 5.10 presents the Nusselt-Rayleigh number data using the definitions of Nusselt and Rayleigh number from equations 2.21 and 2.27, respectively. The Nusselt number is based on the bundle-averaged rod temperature. In this data, the Nusselt numbers are the same as the Nusselt numbers from correlation 1; however, the Rayleigh numbers based on total convective heat rate are larger than the Rayleigh numbers based on ΔT_{bund}. Thus, the curve is shifted to the right on the Rayleigh number axis. The data in Figure 5.10 was correlated using the following equation:

$$Nu_{bund} = 9.93\ (Ra_{Q'})^{0.019} \qquad 4.1*10^5 < Ra_{Q'} < 1.4*10^7$$
$$Nu_{bund} = 0.224\ (Ra_{Q'})^{0.244} \qquad 2.0*10^7 < Ra_{Q'} < 1.2*10^{10}$$
$$Ra_{critical} = \text{approx. } 1.7*10^7 \qquad (5.4)$$

Figure 5.11 gives a plot of all three sets of data, and Table 5.1 gives a summary of the full array convection correlations. The percent error reported for each correlation is the maximum data point deviation from the best-fit equation. First, the Nusselt number is calculated from each Rayleigh number by using the $Nu = C\,Ra^{n}$ equations. The percent error for each data point is calculated by comparing the calculated value of Nu to the actual data point. The maximum percent error is the one reported below. Notice that this is the correlation error only. Recall from Chapter 4 that the data itself has experimental uncertainty associated with it of approximately 4 percent error for full array Rayleigh numbers and about 2 percent error for full array Nusselt numbers.

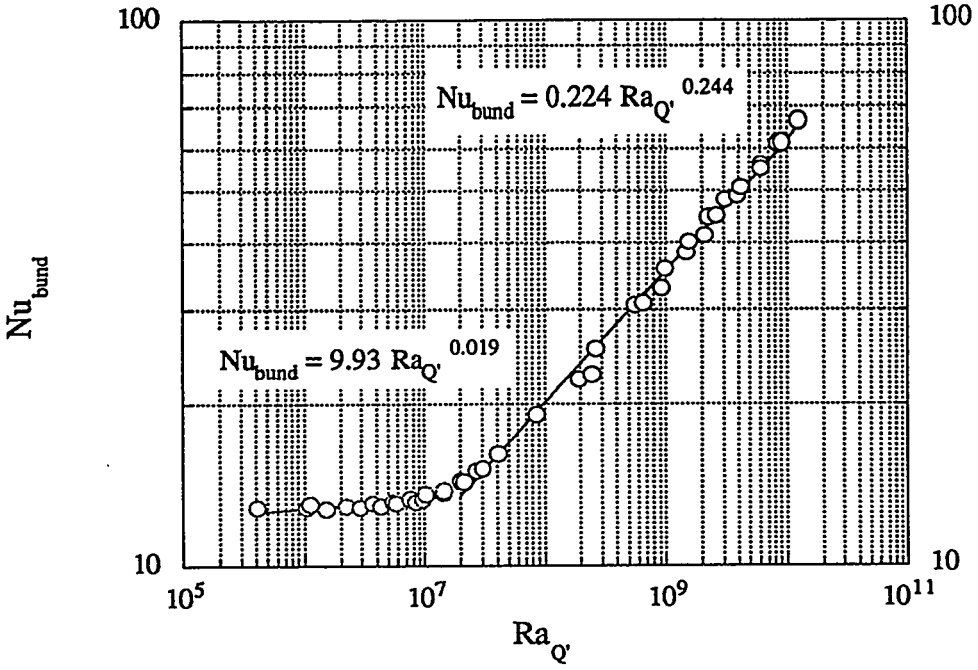

Figure 5.10 Nusselt-Rayleigh number data for the staggered array based on linear convective heat rate, Q'_{conv}.

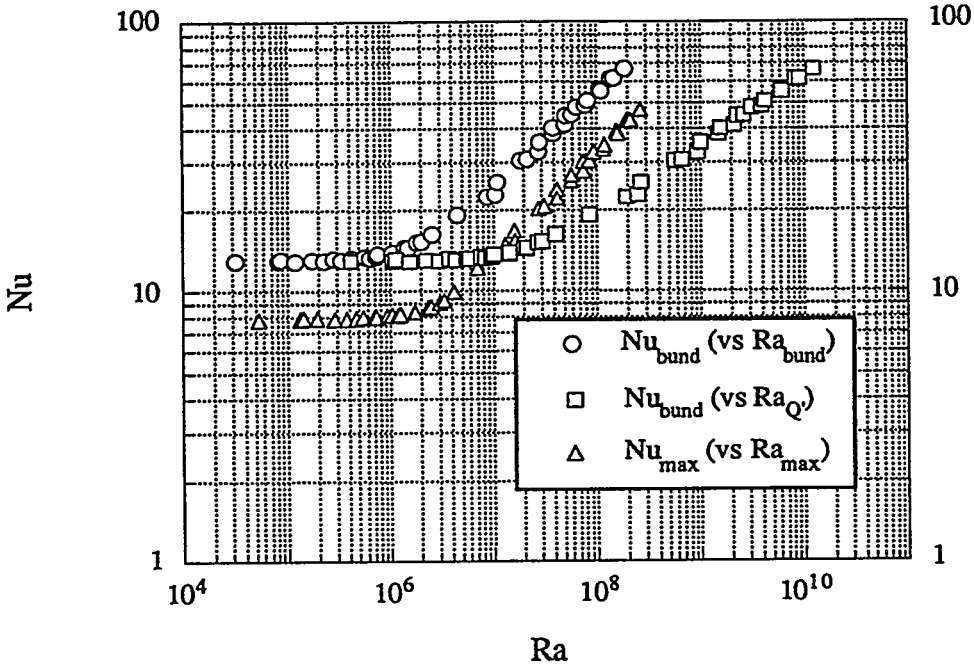

Figure 5.11 Full array Nusselt-Rayleigh number data for the staggered array, using all three calculation methods.

Table 5.1 Summary of Full Array Convection Coefficients

Correlation	Range	Critical Rayleigh number	Maximum percent error*
$Nu_{bund} = 10.4\ (Ra_{bund})^{0.019}$	$3.2*10^4 < Ra_{bund} < 1.0*10^6$	$1.2*10^6$	14
$Nu_{bund} = 0.140\ (Ra_{bund})^{0.322}$	$1.4*10^6 < Ra_{bund} < 1.9*10^8$		
$Nu_{max} = 6.36\ (Ra_{max})^{0.018}$	$5.3*10^4 < Ra_{max} < 1.7*10^6$	$2.0*10^6$	11
$Nu_{max} = 0.038\ (Ra_{max})^{0.366}$	$2.3*10^6 < Ra_{max} < 2.6*10^8$		
$Nu_{bund} = 9.93\ (Ra_{Q'})^{0.019}$	$4.1*10^5 < Ra_{Q'} < 1.4*10^7$	$1.7*10^7$	9
$Nu_{bund} = 0.224\ (Ra_{Q'})^{0.244}$	$2.0*10^7 < Ra_{Q'} < 1.2*10^{10}$		

* defined as the maximum deviation between any Nusselt number data point and the correlation.

5.3.4 Comparison of Full Array Results for the Staggered and Aligned Rod Bundles

Figure 5.12 shows the full array Nusselt-Rayleigh number correlation for Canaan's aligned rod bundle. The data, like the staggered array data, fall into two distinct regimes corresponding to a conduction and a convection regime. Canaan's aligned array data were correlated with the equation [Canaan, 1995]:

$$Nu_{bund} = 11.6\ (Ra_{bund})^{0.022} \qquad 3.0*10^4 < Ra_{bund} < 2.7*10^6$$
$$Nu_{bund} = 0.137\ (Ra_{bund})^{0.321} \qquad 2.7*10^6 < Ra_{bund} < 2.0*10^8$$
$$Ra_{critical} = \text{approx. } 1.2*10^6 \qquad (5.5)$$

The Rayleigh number exponent of about 0.32 in the second regime is, like the staggered array, very close to 1/3. This result indicates the presence of turbulent

flow within the bundle at higher Rayleigh numbers. However, while the results of the staggered and aligned arrays are quite similar, there are some important differences between the two rod configurations.

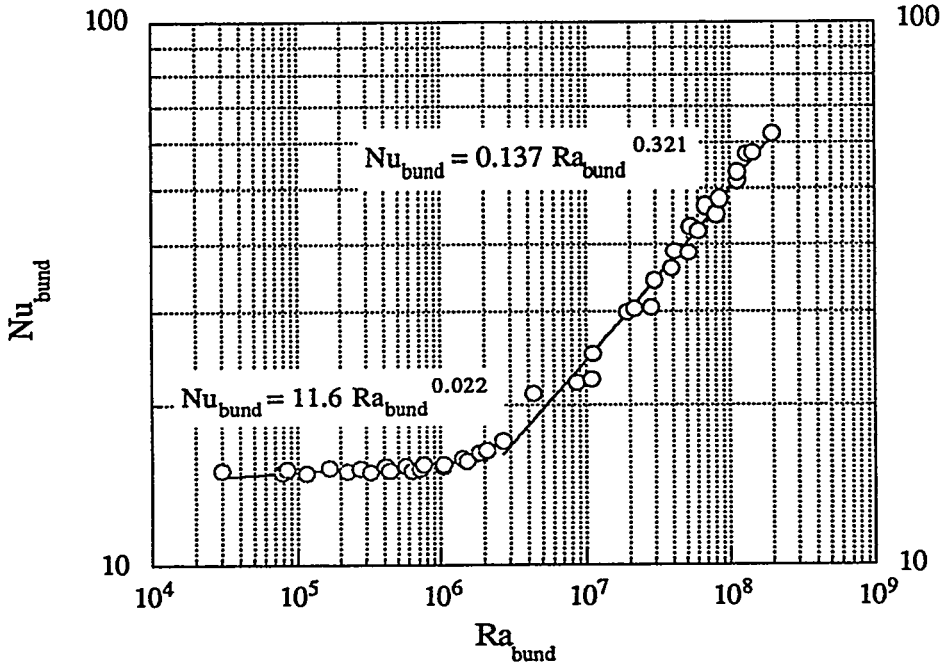

Figure 5.12 Nusselt-Rayleigh number correlations for aligned tube bundle. [Canaan, 1995].

Figure 5.13 shows the Nusselt-Rayleigh number results for both the aligned and staggered arrays. There is a noticeable difference between the Nusselt numbers for the aligned and staggered arrays, particularly for the conduction regime data. In the conduction regime, the staggered array has a lower Nusselt number than the aligned array. In the lower end convection regime, the staggered array has a slightly lower Nusselt number than the aligned array. However, the slope of the staggered array data in the convection regime is steeper than the aligned array data.

Thus, at higher Rayleigh numbers, the Nusselt number for the staggered array overtakes and becomes slightly greater than the aligned array Nusselt number.

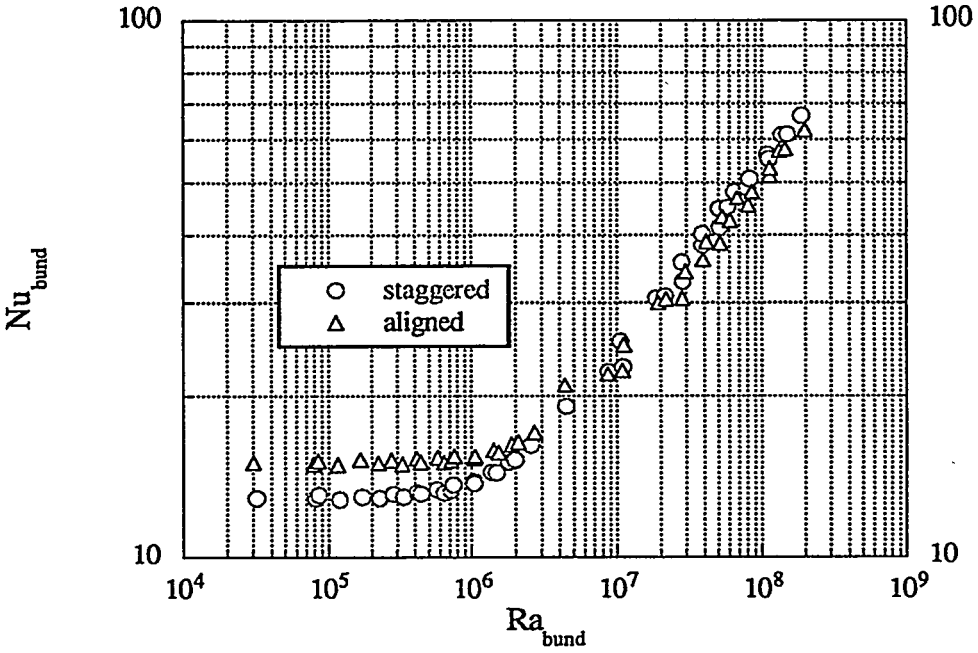

Figure 5.13 Nusselt-Rayleigh number data for both staggered and aligned bundles.

The results of Figure 5.13 are a bit surprising, because it indicates that, for most of the lower Rayleigh number range, an aligned tube bundle has a higher convection coefficient than a staggered tube bundle. The results of Choi and Cha [1990] indicate that a staggered heated tube array has a Nusselt number that is about 7 to 15 percent higher than an aligned array, depending on the rod spacing to diameter ratio. Their results were for an non-enclosed tube bundle. Warrington and Weaver [1984] also reported slightly higher Nusselt numbers for an enclosed staggered tube array versus an aligned array. Why then, are the heat transfer coefficients lower for the staggered array in this experiment?

Recall that the dominant heat transfer mechanism in the Rayleigh number regime where the aligned Nu values are greater than the staggered Nu values is conduction, not convection. In conduction, the only factors that affect the heat transfer behavior of the system are the geometry of the system and the thermal conductivities of the system pieces. The heater rods have a higher thermal conductivity than the backfill fluid. Since the aligned array has 4 more rods than the staggered array, the aligned array has a higher effective thermal conductivity for heat flow through the bundle. Also, in addition to having more rods within the enclosure, the aligned configuration may provide a better conduction path to the cool walls than the staggered configuration. This is because the aligned array has a greater number of rods on the sides that are the minimum distance from the cooled wall. This possibility is considered further in sub-section 5.3.7, which looks at a numerical conduction comparison between Canaan's aligned array and the current staggered array.

5.3.5 Comparison of Full Array Results to Forced Convection in Cylinder Banks

It was mentioned above that it was an unexpected result for the aligned array Nusselt number to be higher than the staggered array Nusselt number, for a given Rayleigh number. This is because most quoted results for convection across cylinder banks give higher average heat transfer coefficients for staggered arrays. In forced convection, these increased heat transfer coefficients for staggered tube arrays result from the increased turbulence and mixing created by the fluid flow around the alternating rows of cylinders. Conversely, an aligned array has "preferred flow channels" that reduce the total surface area of rods that are exposed to vigorous flow. Figure 5.14 gives a diagram of this behavior.

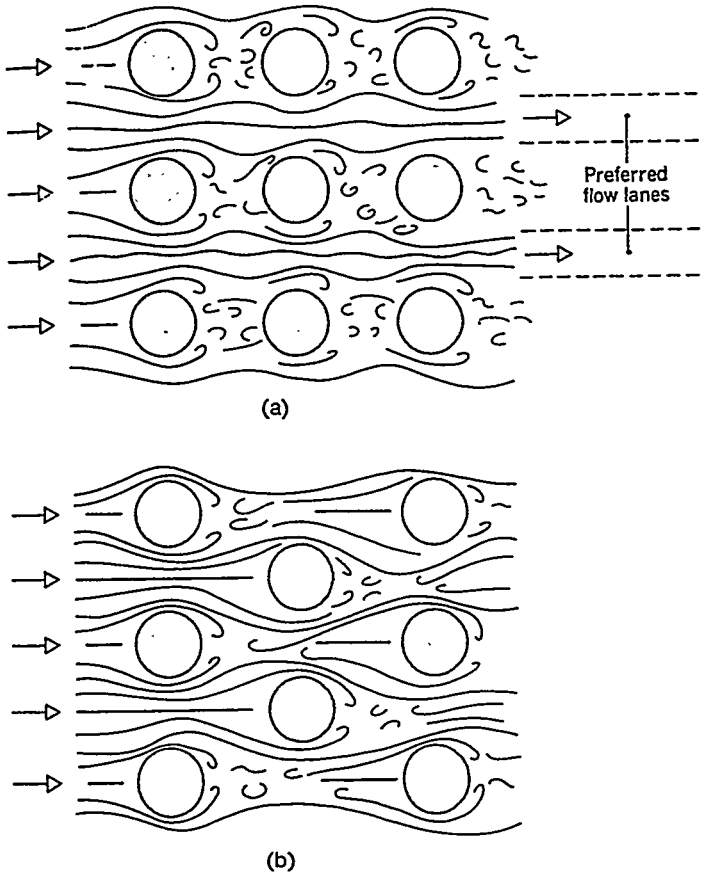

Figure 5.14 Diagram of forced convection flow for a) an aligned tube bank and b) a staggered tube bank. [Incropera and DeWitt, 1990].

Incropera and DeWitt [1990] give heat transfer correlations for forced convection across both aligned and staggered tube banks. They are of the form $Nu = C\,Re_D^n$, where Re_D is the Reynolds number based on the maximum flow velocity around the tubes and the individual tube diameter, D. The constants C and n are tabulated for various rod pitch to diameter ratios. It is interesting to compare the Nusselt-Reynolds number trends for forced convection across the aligned and staggered geometries to the Nusselt-Rayleigh number trends for this experiment. For Canaan's aligned array, the P/D ratio was 1.33. For the staggered array of this experiment, the distance between rods on a row was 1.33 times the rod diameter, and the distance between rows was also 1.33 times the rod diameter. Since the C and n values were only tabulated for P/D values of 1.25 and 1.5, linear

interpolation was used to find the C and n values for forced convection. For a Prandtl number of 0.7, these correlations are:

$$\begin{aligned} &\text{aligned array:} && Nu_{avg} = 0.328\ Re_D{}^{0.597} \\ &\text{staggered array:} && Nu_{avg} = 0.496\ Re_D{}^{0.559} \\ &2{,}000 < Re_D < 40{,}000 && \end{aligned} \tag{5.6}$$

These correlations are plotted below in Figure 5.15. It is clear that the Nusselt number for the staggered array is higher than for the aligned array, particularly at lower Reynolds numbers. At higher Reynolds numbers, the flow is so fully turbulent that the geometric differences in the rod locations are not as important in determining the Nusselt number.

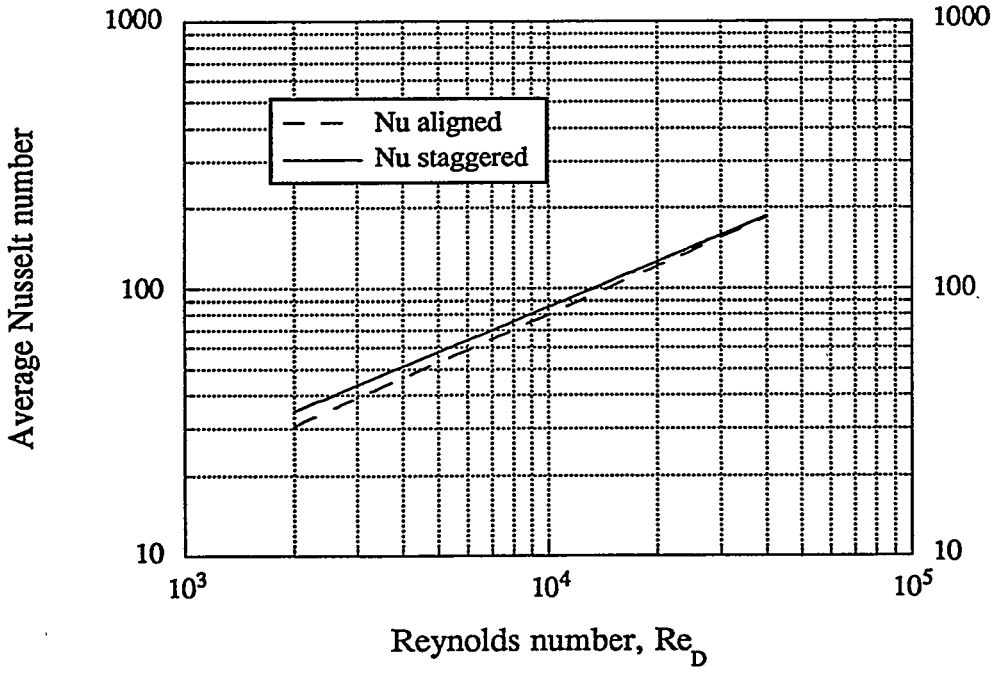

Figure 5.15 Nusselt vs. Reynolds number for forced convection across aligned and staggered tube banks [Incropera & DeWitt, 1990].

5.3.6 Comparison of Full Array Results to Other Experiments on Natural Convection in Cylinder Banks

It is generally expected that natural convection in a staggered array will have higher full array Nusselt numbers than in an aligned array. However, unlike forced convection, it is not because the staggered array mixes the flow better. Rather, augmentation of the heat transfer in a staggered array occurs because the buoyant plumes from each rod can travel up farther before impinging on the bottom of the next rod than in an aligned array. This extra room to form a plume allows an increased plume velocity that increases the heat transfer coefficients for each rod. However, if the rod bundle is enclosed, the formation of these buoyant plumes is generally inhibited, and flow tends to circulate throughout the spaces in the rod bundle rather than rising upward from each rod. Thus, an enclosed rod bundle ought to have a smaller difference in heat transfer between an aligned and a staggered array than a non-enclosed bundle. This question is investigated in this sub-section by considering other experiments in natural convection in aligned versus staggered rod bundles.

5.3.6.1 Comparison of Results to Non-Enclosed Tube Bundles

In 1976, Tilman presented full array convection coefficients for a 4x4 aligned array and a 14-rod staggered array of heated cylinders in air at atmospheric pressure. No radiation correction was made, and the bank of tubes was not enclosed, but open to room temperature air. Also, it is not clear exactly what shape of staggered array was used. He calculates full array Nusselt and Rayleigh numbers using a characteristic length based on the rod pitch-to-diameter ratio, the rod center-to-center spacing, the bundle-averaged temperature difference, and the total rod power. Tilman's correlations, for Rayleigh numbers of 10^2 to 10^6, were

$$Nu_{bund,staggered} = 0.067\ (Ra)^{0.5}$$
$$Nu_{bund,aligned} = 0.057\ (Ra)^{0.5} \qquad (5.7)$$

Thus, Tilman asserts that the Nusselt number for the staggered array is always greater than that of the aligned array by a factor of (0.067 / 0.057), or about 1.17. Notice that Tilman's Rayleigh number exponent is high, at about 0.5. Since he did not subtract out radiation heat transfer, it is counted as convection, which tends to inflate the Nusselt number dependence on Rayleigh number [Canaan, 1995].

In 1990, Choi and Cha published results from a flow visualization study of natural convection in a non-enclosed, horizontally-oriented tube bundle. The results were presented for two different rod pitch-to-diameter ratios, 2.0 and 4.0. Their rectangular tube bundle consisted of hollow copper tubes through which a DC current was passed to heat the rods. As shown in Figure 5.16, the rectangular bundle could be rotated to produce an aligned or a staggered array. Notice that the staggered array produced by rotating an aligned array is different than one produced by shifting every other row over by 1/2 rod pitch. A Mach-Zehnder interferometer was used to photograph constant temperature contour lines throughout the bundle. Some sample interferograms from their experiments are shown in Figure 5.17. Notice the well-defined buoyant plumes from each rod. The local, circumferential angle-dependent Nusselt number was computed by using the pictures to compute the temperature gradient at a distance of 1/2-rod diameter from the rod surface. They also computed rod surface averaged Nusselt numbers, which is the type of individual rod Nusselt number calculated in the current and the Canaan experiment.

While Choi and Cha did not compute a full array Nusselt number, they do report that for a P/D ratio of 4, that the Nusselt number for a particular individual rod is, on average, 7 to 9 percent higher in a staggered array than in an aligned array. For a tighter spacing with a P/D ratio of 2, the individual Nusselt numbers were about 14 to 18 percent higher in a staggered array. Thus, they concluded that a smaller P/D ratio increases the difference in average heat transfer between an aligned and a staggered array. However, it is not likely that this difference continues to increase as the P/D ratio approaches unity, since there is very little convection between rods at all for very low P/D ratios.

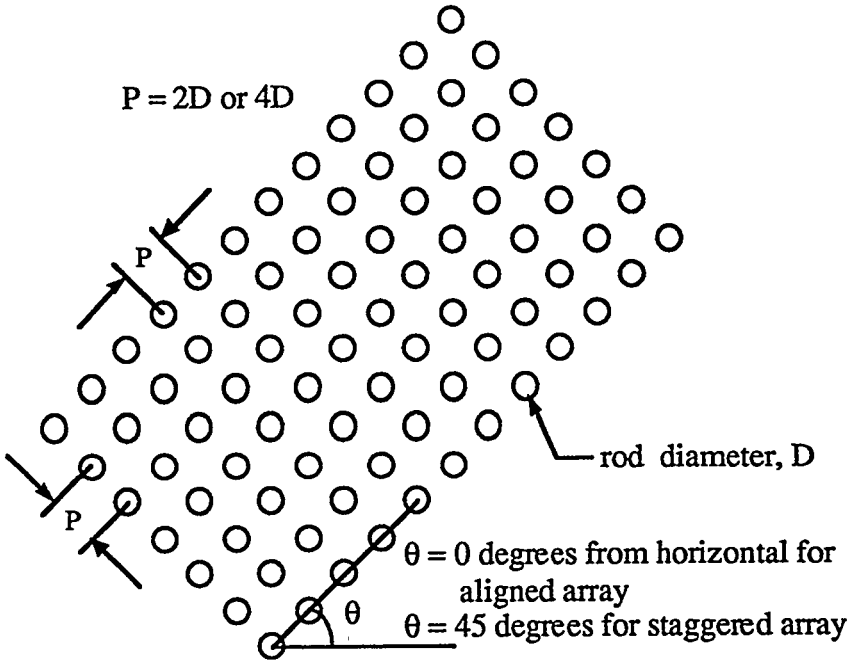

Figure 5.16 Diagram of Choi and Cha's rod bundle, viewed from the end. [Choi and Cha, 1990].

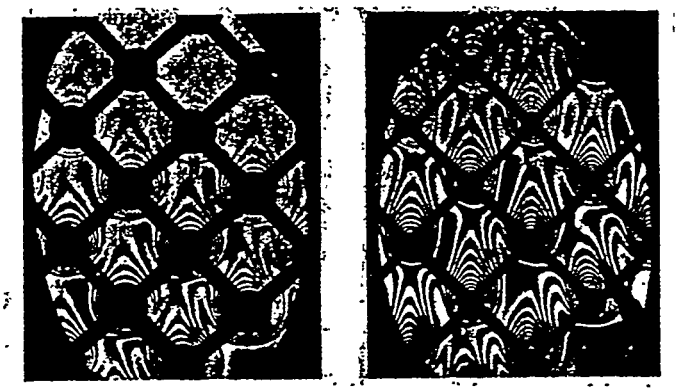

Figure 5.17 Interferograms from Choi and Cha's non-enclosed rod bundle. θ = 45 degrees from horizontal.

The main differences between the UT experiment and Choi and Cha's experiment are the enclosure (or lack thereof), the difference in rod P/D ratios, and the difference in the staggered array shapes. The enclosure of the UT experiment probably limited the plume formation that could cause a staggered array to have higher Nusselt numbers. However, there was more than one significant difference between the two experiments, and none of these differences were investigated independently of one another. Thus, it is difficult to say just from comparing these two experiments what the major factor is in determining the difference in natural convection heat transfer between an aligned and a staggered array.

5.3.6.2 Comparison of UT Results to Another Enclosed Tube Bundle

The experiments of Warrington and Weaver are geometrically more like the current UT experiment than were Choi and Cha's. Their experiments, like the UT experiments, had a water-cooled enclosure, and their staggered array was the same shape as the UT staggered array. They investigate 4x4 and 3x3 aligned cylinder arrays and 14- and 8-cylinder staggered arrays enclosed in a cubical, water-cooled enclosure filled with various fluids at atmospheric pressure. They also used a tighter rod spacing, with P/D ratios of 1.45 and 1.83 (recall that the P/D ratio for the UT experiments was 1.33). They reported that "the enclosure *reduced* the expected *increase* in both the average and the local heat transfer coefficients caused by changing the inner body [the cylinder bundle] from an in-line arrangement to a staggered arrangement of comparable spacing" (emphasis added). Unfortunately, they did not run an experiment without an enclosure with which their results could be compared.

Warrington and Weaver had an unusual result compared to the convection regime of the UT array results. The Rayleigh number range for their full array correlations ranged from about 10^5 to 10^8. For a Rayleigh number of 10^5 and an air backfill, their correlations give a staggered array Nusselt number that is about 11 percent higher than the aligned array Nusselt number. At a higher Rayleigh number (about 10^8), the Nusselt numbers are about the same for the staggered and aligned arrays. Recall that for the UT arrays in the convection regime, the slope of the

staggered array Nusselt number was steeper than the aligned Nusselt number. However, the slope of Warrington and Weaver's staggered array Nusselt number was less steep than the aligned array slope, which is the opposite of the trend displayed by the UT arrays. This source of this discrepancy in Nusselt number trends is not known; however, it is possible that the short length of Warrington and Weaver's rod bundle could be causing some three-dimensional flow effects that would not be seen in the UT arrays.

The main conclusion of the comparison of aligned vs. staggered full array heat transfer for these different experiments is that having an enclosure surrounding the rod bundle should decrease the difference in convective heat transfer between an aligned and a staggered array. Furthermore, since the enclosure for the UT experiments was closer to the rod bundle than it was in the Warrington and Weaver experiment, the UT experiment ought to have the smallest difference in Nusselt numbers between an aligned and a staggered array. However, since the Nusselt numbers for the aligned array are 12 to 17 percent *higher* than the staggered array (for low Rayleigh numbers), it is likely some other physical effect is causing the difference in Nusselt numbers in the UT experiments. The following section discusses this topic.

5.3.7 FIDAP Numerical Conduction Simulation

Recall that in section 5.3.4 it was noted that the regime in which the UT staggered Nusselt numbers were lower than the aligned Nusselt numbers was the low Rayleigh numbers, where conduction is the dominant heat transfer mechanism. Thus, a conduction analysis could provide answers to why the aligned array has better heat transfer in this regime.

To better understand and quantify the differences in conduction between the two geometries, a numerical conduction simulation was performed using FIDAP, a commercial fluid dynamics and heat transfer code from Fluid Dynamics International. To model the staggered and aligned configurations, symmetry was assumed about the vertical centerline of each bundle, so only half of the bundle was

modeled. The symmetry boundary was specified to be a zero heat flux boundary, i.e., the temperature gradients at this boundary were defined to be zero. The gas was modeled as a solid with the same thermal conductivity as helium, at a temperature of about 300K. Modeling the gas as a solid limited the heat transfer to pure conduction. Since the rods are practically isothermal, the rods themselves were not modeled, and the experimentally measured rod temperatures served as 32 boundary conditions. The CuBE was also specified as a constant temperature boundary, set to the experimentally measured inner wall temperature. For this simulation, the rod and CuBE temperatures used for each configuration were those from the 1 W / rod, 0 psig, helium case. For both arrays, this state point corresponded to the lowest Rayleigh number, and therefore this case was most like pure conduction.

FIDAP uses finite-elements to analyze fluid dynamics and heat transfer problems. The first step in creating this conduction model was to mesh the helium and the rod and enclosure boundaries. Figures 5.18 and 5.19 show the mesh used for these two configurations. The user specifies the number of nodes along the boundaries, and then FIDAP automatically generates the mesh elements needed to fill the geometry. Once the mesh is created, then boundary conditions are defined. For this problem, the boundary conditions were 1) the temperature of the isothermal enclosure, 2) the 32 individual isothermal rod surface temperatures, and 3) the zero-flux condition at the symmetry boundary.

Figures 5.20 through 5.23 show the resulting temperature profiles from FIDAP's solution of this problem. Figures 5.20 and 5.21 show filled color contour plots of the temperature distribution, and Figures 5.22 and 5.23 show monochromatic contour line plots to show the shape of the temperature curves. Notice that the temperature contours are shifted slightly upward, which indicates slight convection effects. However, this is not because convection was included in the FIDAP model, but because the experimental rod temperatures, which were slightly shifted upward due to convection, were used as boundary conditions. Notice the similarities in wall temperatures and maximum rod temperatures between the two configurations. The wall temperatures differ by only 0.03K, and the maximum rod temperatures differ by only about 0.2K. Thus, the maximum rod

temperature difference is quite similar. However, there is a significant difference in the total heat transferred to the CuBE wall.

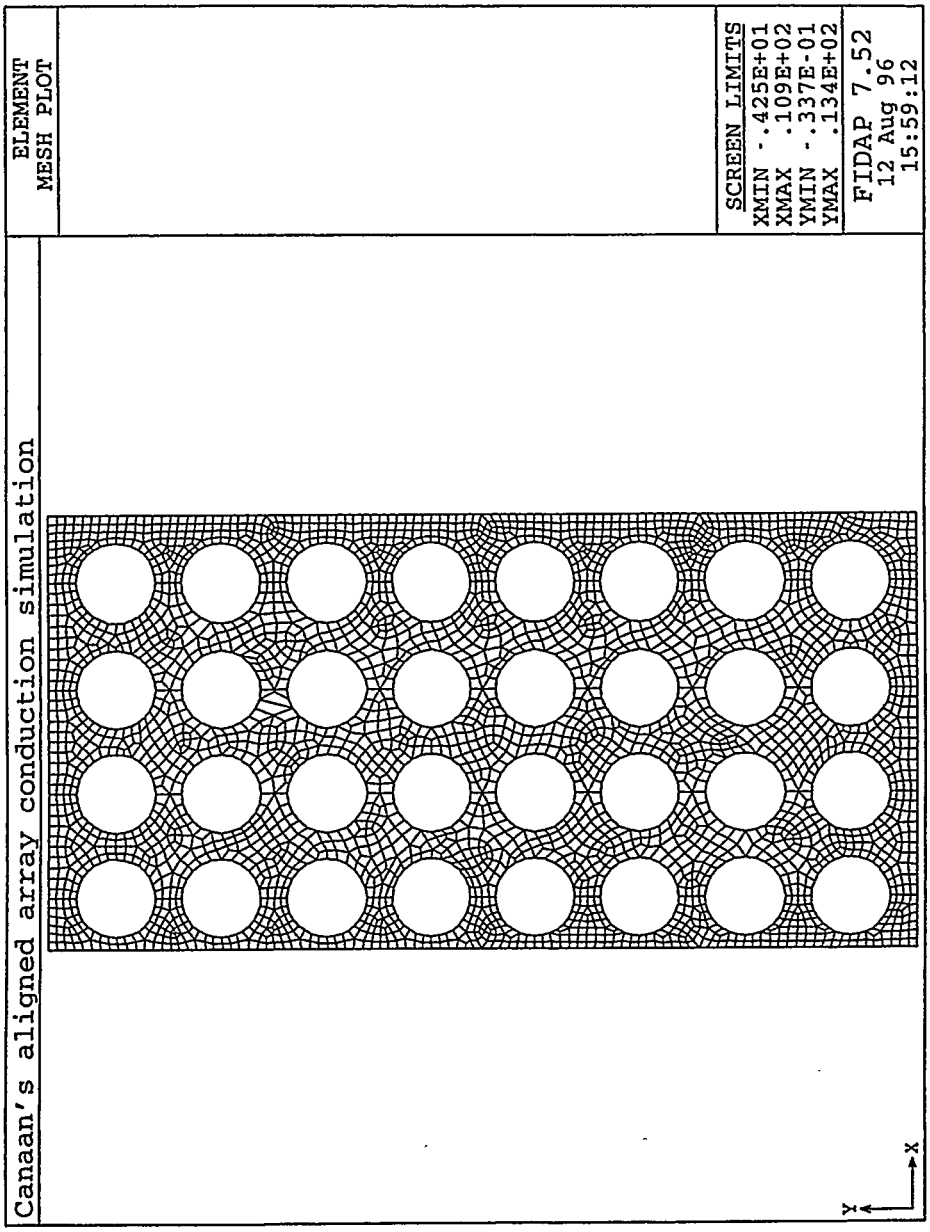

Figure 5.18 Finite element mesh used for conduction analysis of Canaan's aligned array.

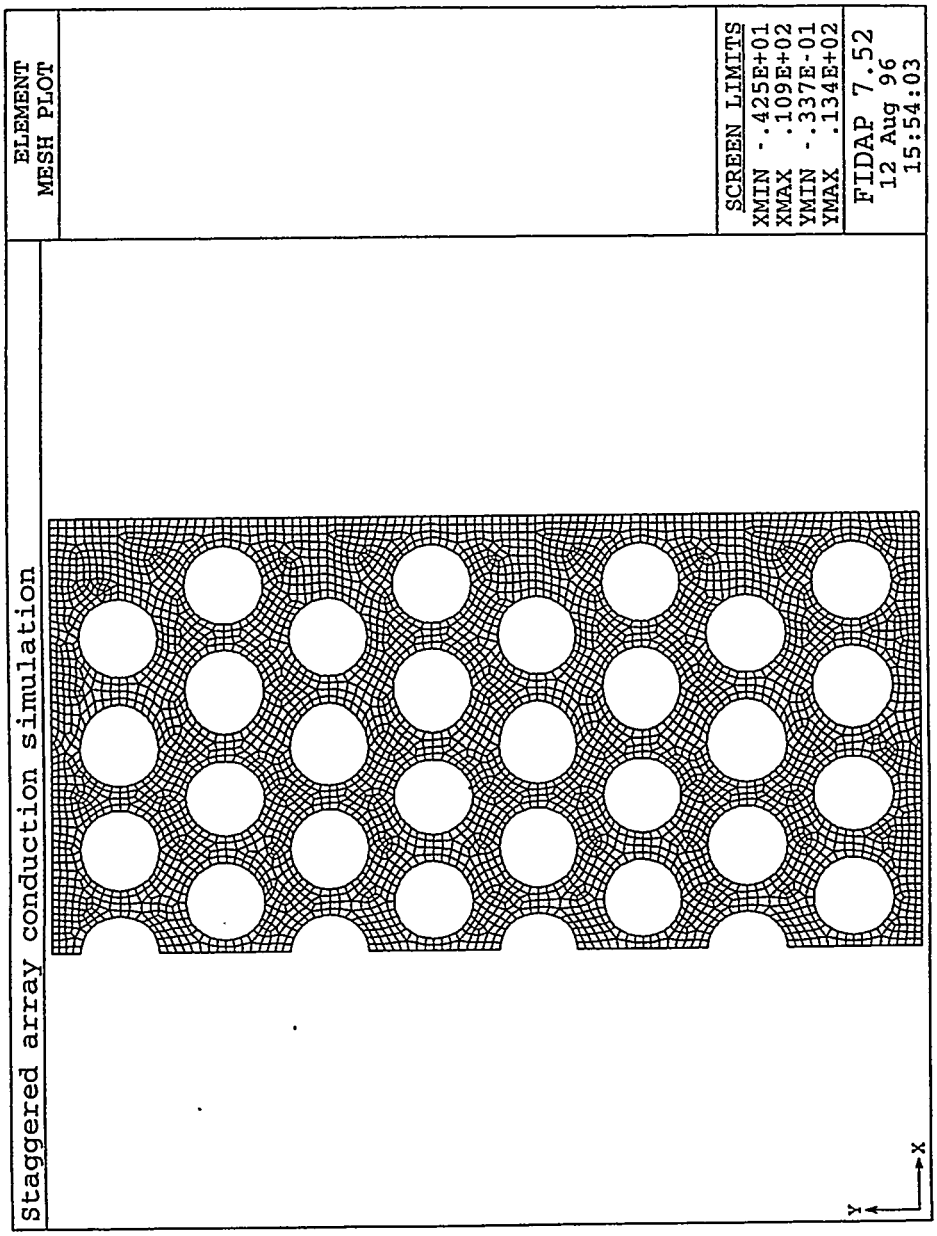

Figure 5.19 Finite element mesh used for conduction analysis of staggered array.

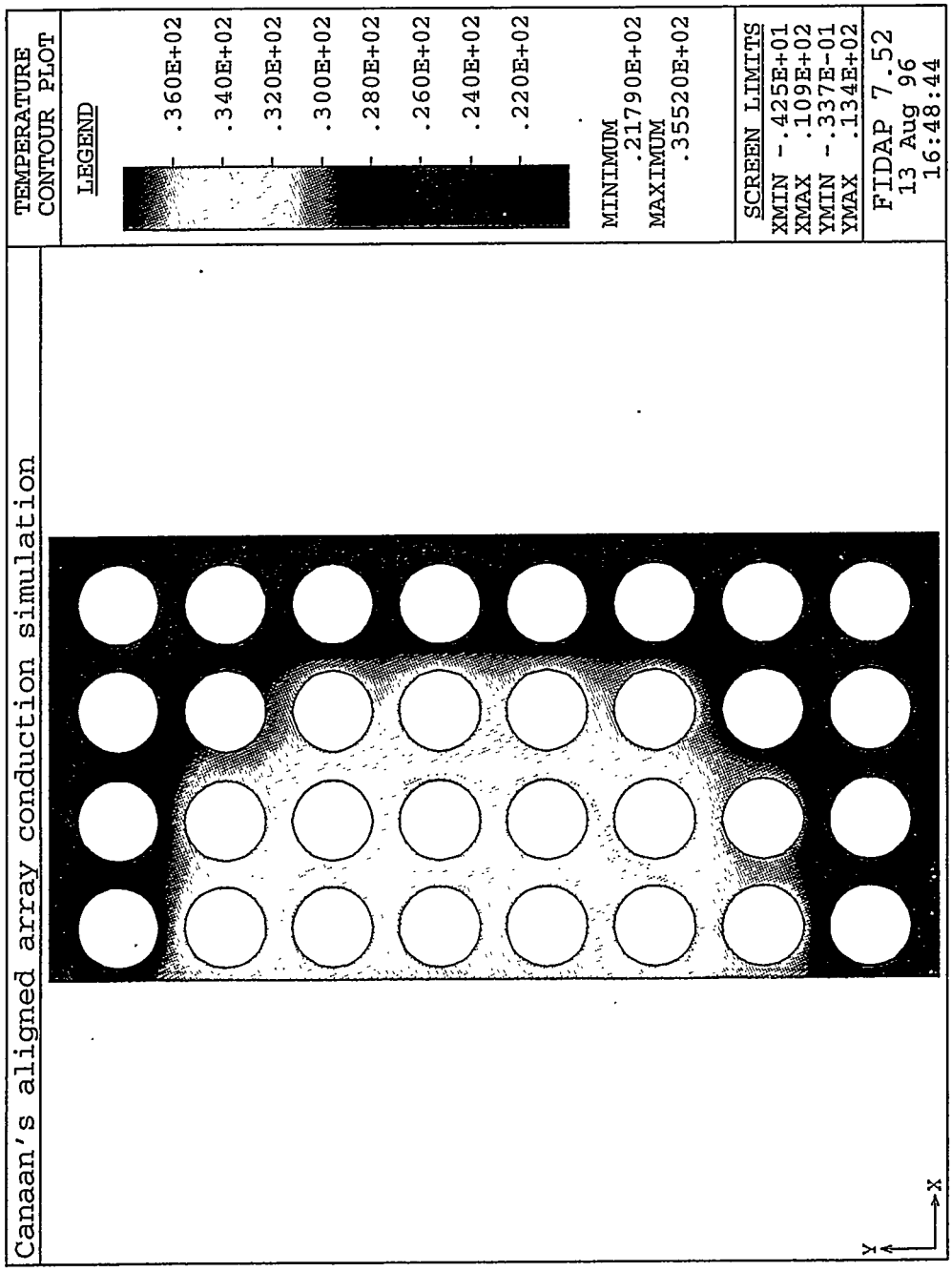

Figure 5.20 Color temperature contours for Canaan's aligned array conduction simulation.

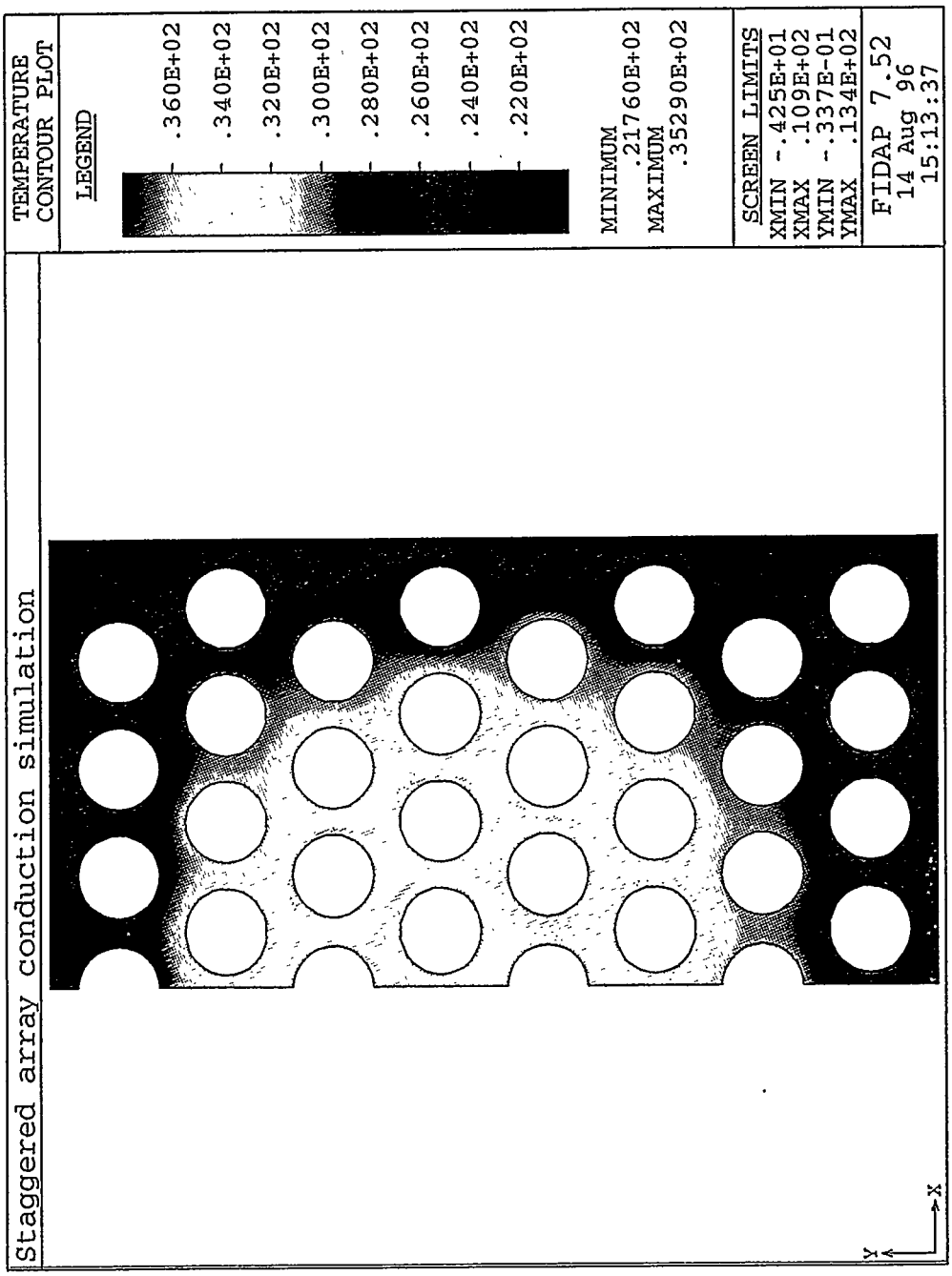

Figure 5.21 Color temperature contours for the staggered array conduction simulation.

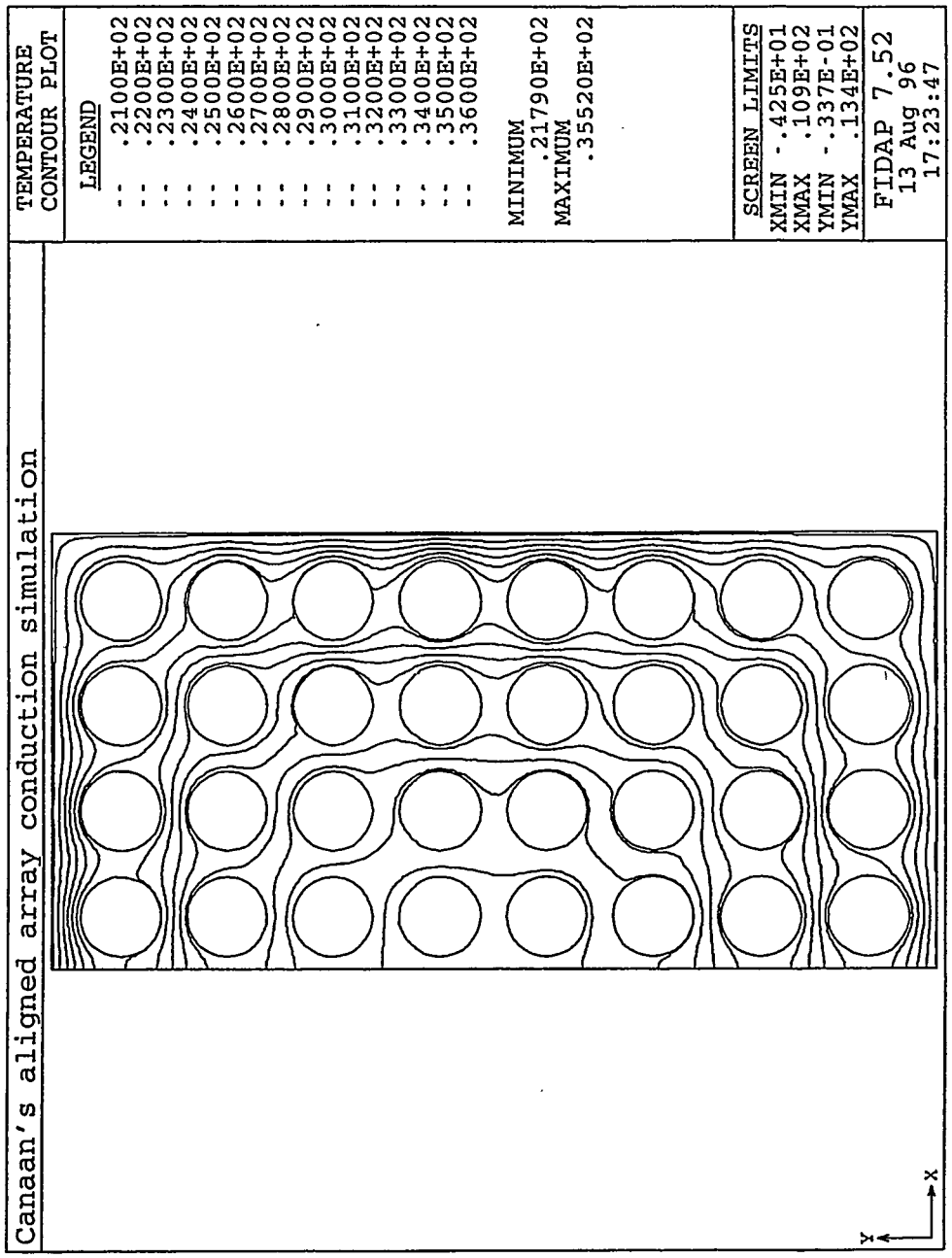

Figure 5.22 Temperature contours for Canaan's aligned array conduction simulation.

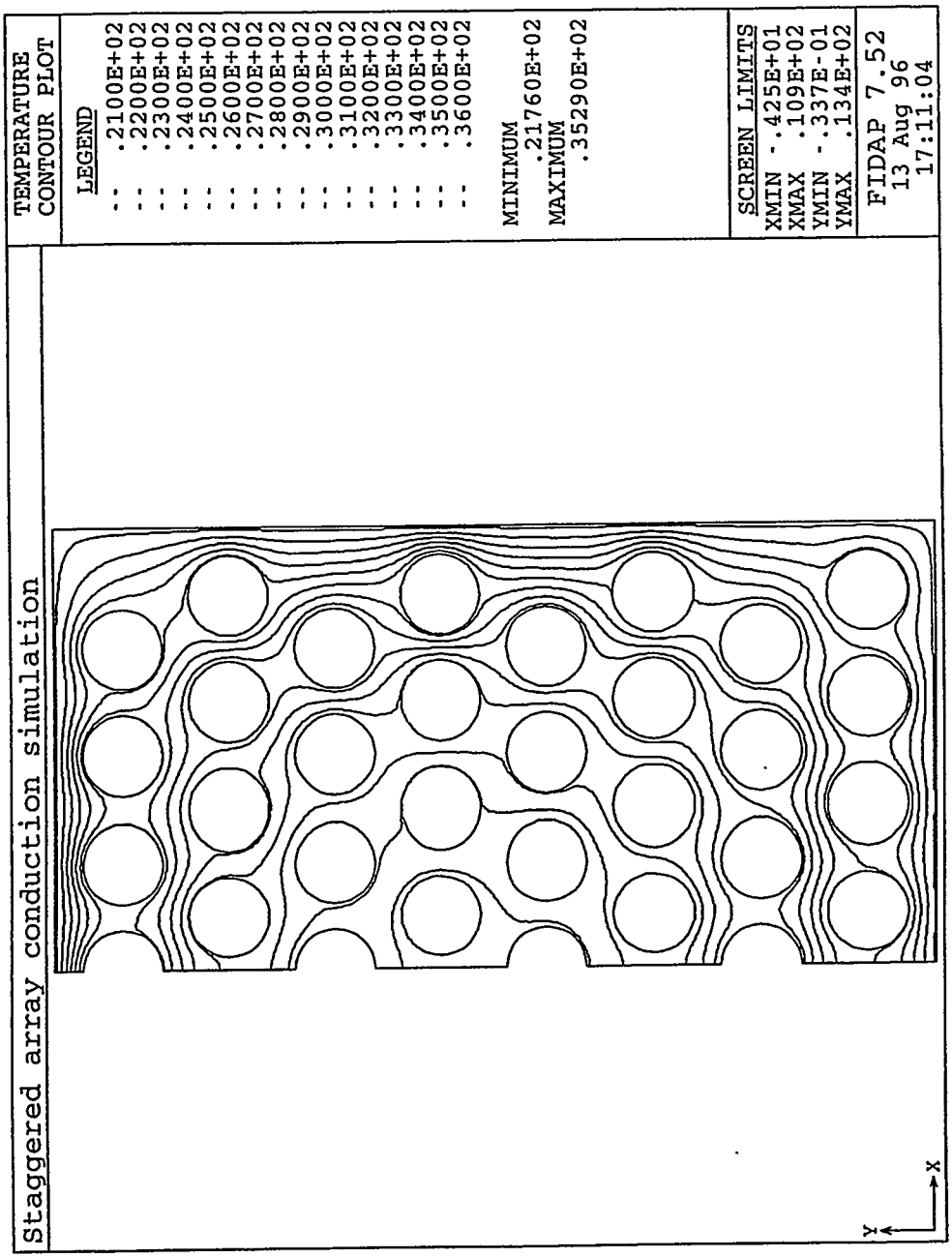

Figure 5.23 Temperature contours for the staggered array conduction simulation.

The main difference between the two solutions is the temperature *gradient* at the side CuBE wall. For the aligned array, there are 8 rods close to the wall that cause the temperature gradient to be sharper than in the staggered array, where there are only 4 rods close to the wall. Thus, in the staggered array, the overall heat flux, which is proportional to the temperature gradient, is lower than in the aligned array. Thus, in the conduction regime, the aligned array transfers heat to the CuBE better because it has more rods very close to the cooled wall than does the staggered array.

To quantify this difference, Nusselt numbers were calculated for these conduction experiments, using the same definitions of Nusselt number as for the full array correlations of section 5.3.1. This Nusselt number is given by

$$Nu_{cond} = \frac{Q'_{cond}}{4\Delta T_{bund} k} \qquad (5.8)$$

where k is the thermal conductivity of the helium (0.152 W/m-K), Q'_{cond} is the total heat flow to the CuBE wall calculated by FIDAP, and ΔT_{bund} is the average temperature of the rods minus the CuBE temperature. Table 5.2 summarizes the results of the Nusselt number calculations, and compares these Nusselt numbers to the experimental Nusselt number values for the aligned and staggered arrays. Table 5.2 also gives the ratio of aligned to staggered Nusselt number for both the simulation and the experimental data.

Table 5.2 Comparison of Conduction Simulation Nusselt Numbers to Experimental Nusselt Numbers

Aligned array Nu, FIDAP simulation	13.2
Staggered array Nu, FIDAP simulation	11.3
Aligned array Nu, experiment	15.1
Staggered array Nu, experiment	12.9
$Nu_{aligned} / Nu_{stagg}$, FIDAP	1.17
$Nu_{aligned} / Nu_{stagg}$, experiment	1.17

For the same rod temperature distribution, the pure conduction simulation Nusselt numbers are about 88 percent of the experimental Nusselt numbers. Since the experimental data actually had a small amount of convection and was not pure conduction, one would expect the experimental Nusselt numbers to be a bit higher than those from the pure conduction simulation. More importantly, the FIDAP numerical conduction simulations yield the *same ratio* of Nusselt numbers between the aligned and staggered arrays as the experiments do. These results support the hypothesis that it is the conduction effects based on the difference in geometry between the UT aligned and staggered arrays that causes the aligned Nusselt number to be higher in the low Rayleigh number regime. While a more detailed numerical study that included a mesh-independence analysis is necessary to fully support this hypothesis, the results of this simple analysis seem reasonable in explaining this unusual Nusselt number behavior.

This section has considered the full array heat transfer behavior of the current experiment and has compared the results to other full array results from convection in aligned and staggered arrays. The following section considers the heat transfer behavior of each individual rod.

5.4 Individual Rod Heat Transfer Correlations

This section presents the Nusselt-Rayleigh number data and correlations for the 32 instrumented rods of the staggered rod bundle. First, the data and correlations for all of the rods will be presented graphically, followed by a tabulation of the correlations for the individual rods. The next sub-section discusses trends in the results. The next sub-section compares the staggered array results to selected rod results for Canaan's aligned array, and the final sub-section compares the UT staggered results to Choi and Cha's individual rod results from their staggered array experiment. While Warrington and Weaver's experiment was more

similar to the UT experiment, they did not calculate individual rod Nusselt numbers.

5.4.1 Individual Rod Nusselt-Rayleigh Number Results -- Figures and Tables

Recall that Figure 5.4 gives a diagram of the positions of each instrumented rod within the array. Notice that all of the rods denoted as being in "column A" or "column D" are not a true column, since all of the rods are not directly above each other. Figures 5.24 through 5.69 give the Nusselt-Rayleigh number data for columns A through D, then for rows 8 through 1. That is, for each column, the data is presented from the bottom row to the top row. Next, Tables 5.3 through 5.6 present the Nusselt-Rayleigh number correlations for each rod. These results are discussed in sub-section 5.4.2. For some rods, it was not clear how best to divide up the data into different regimes. In those cases, more than one correlation is presented.

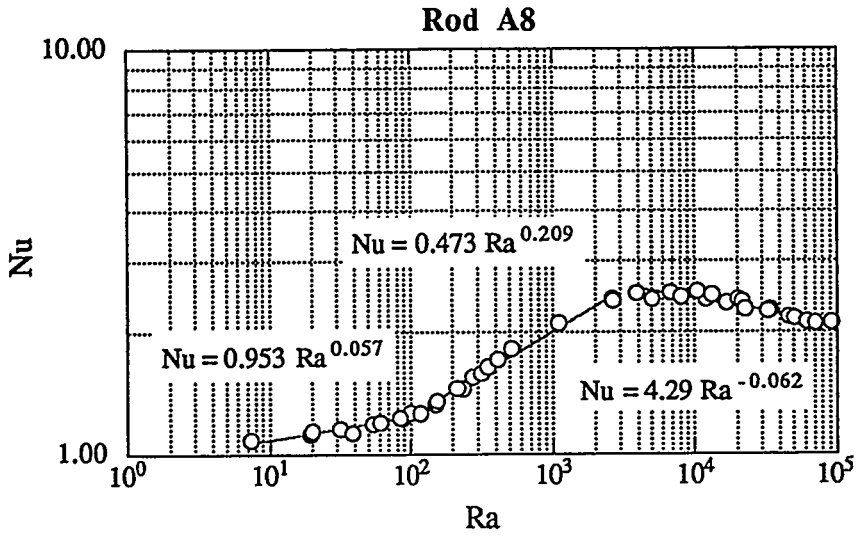

Figure 5.24 Nusselt number for rod A8.

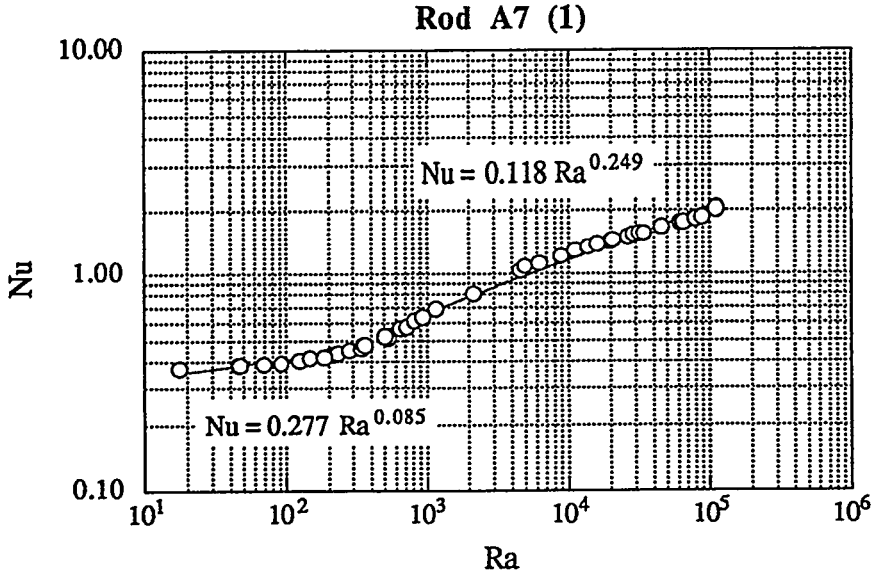

Figure 5.25 Nusselt number for rod A7, correlation 1.

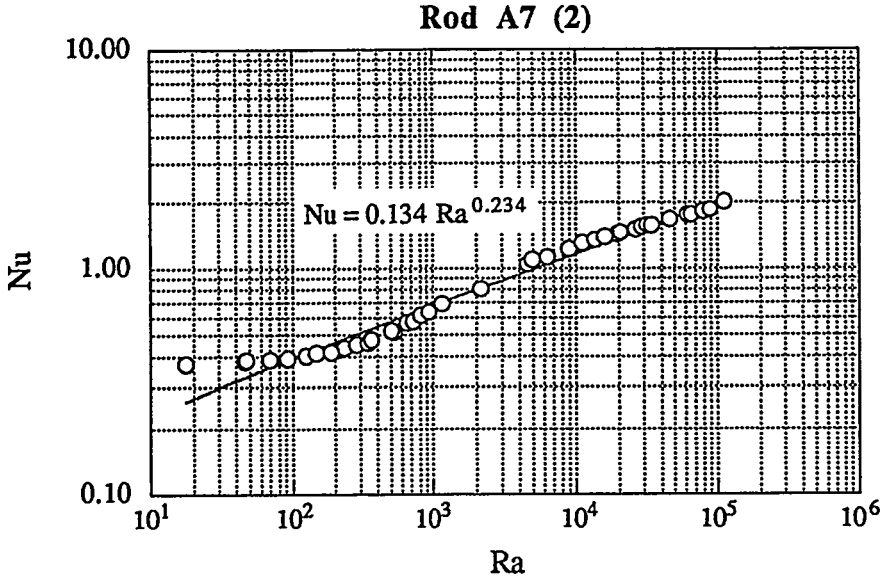

Figure 5.26 Nusselt number for rod A7, correlation 2.

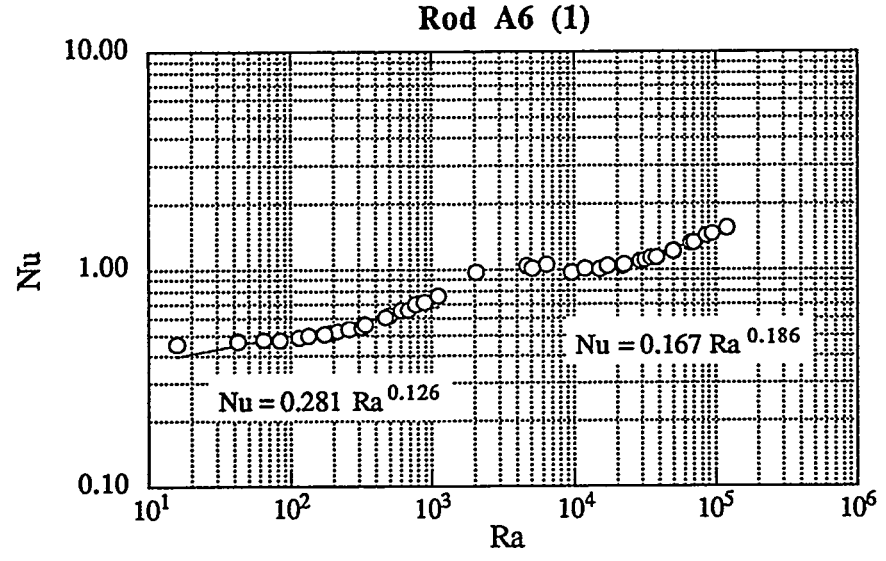

Figure 5.27 Nusselt number for rod A6, correlation 1.

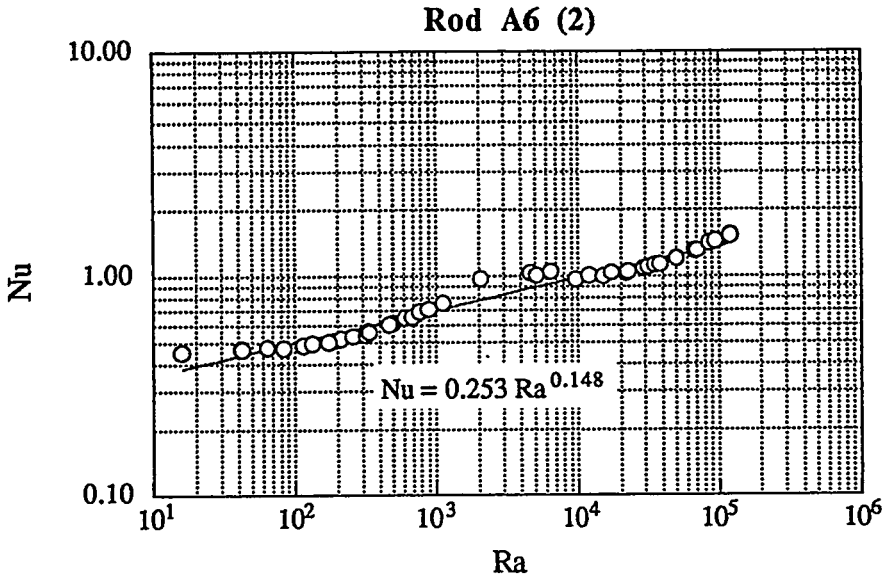

Figure 5.28 Nusselt number for rod A6, correlation 2.

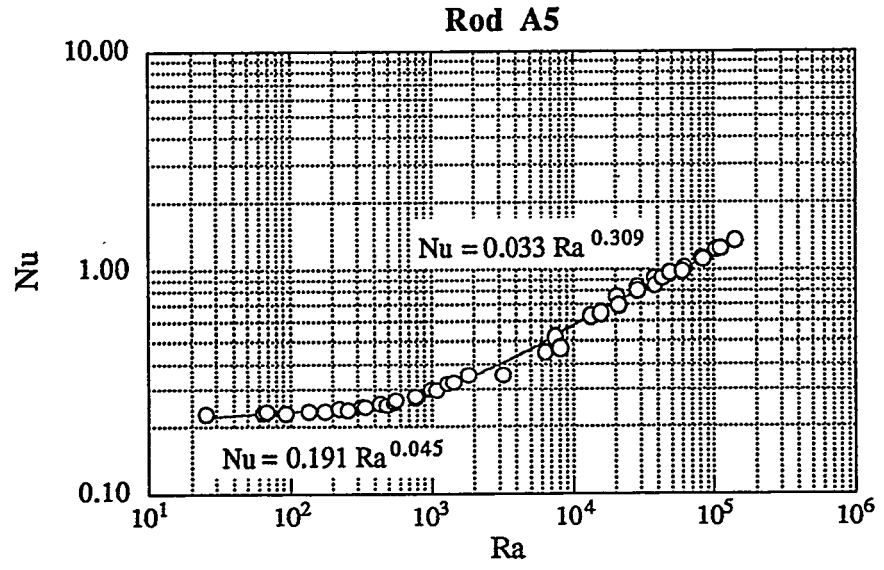

Figure 5.29 Nusselt number for rod A5.

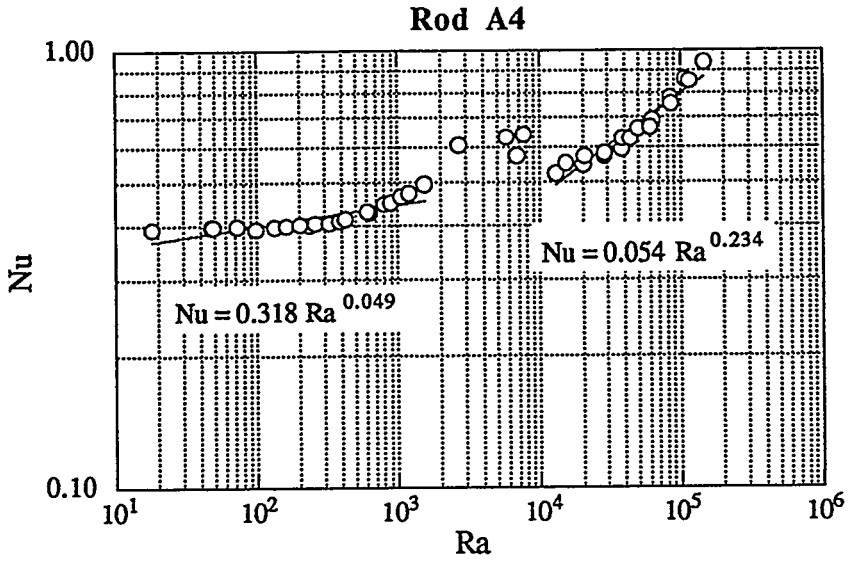

Figure 5.30 Nusselt number for rod A4.

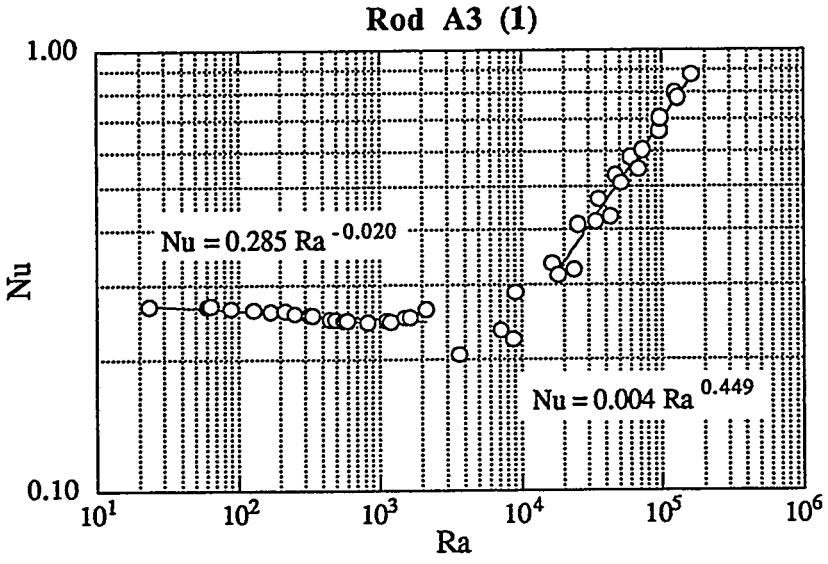

Figure 5.31 Nusselt number for rod A3, correlation 1.

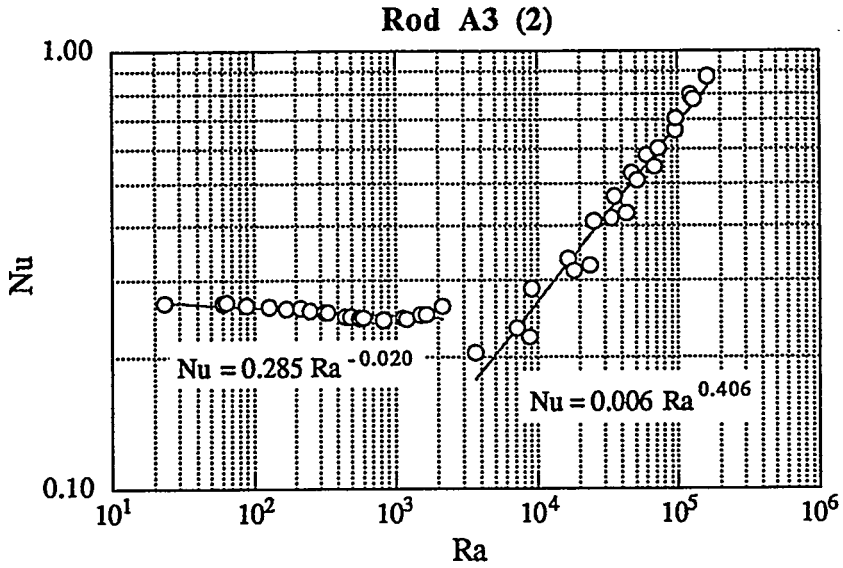

Figure 5.32 Nusselt number for rod A3, correlation 2.

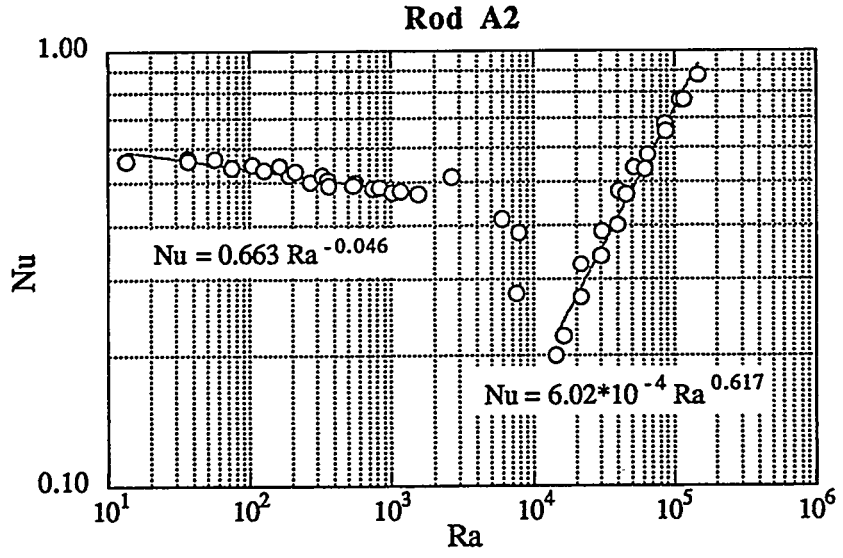

Figure 5.33 Nusselt number for rod A2.

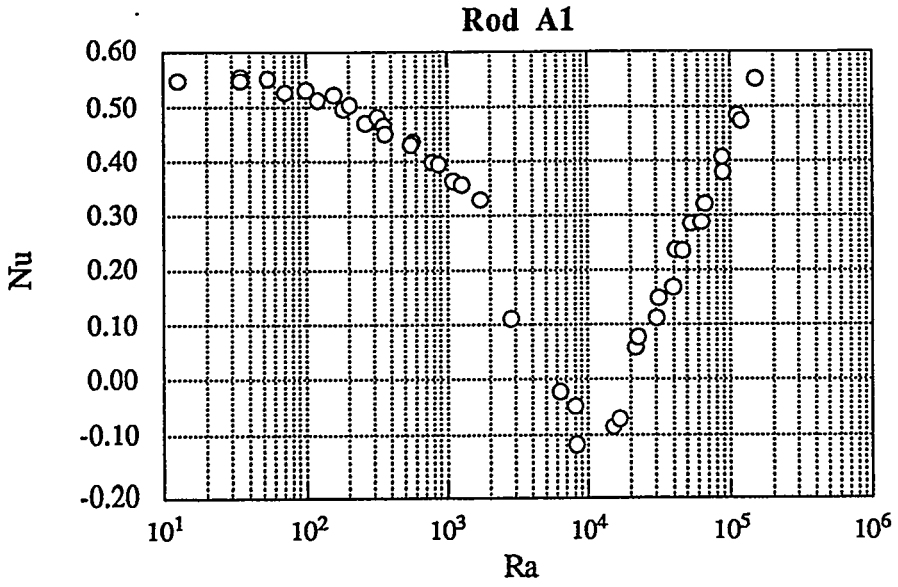

Figure 5.34 Nusselt number for rod A1, showing negative values.

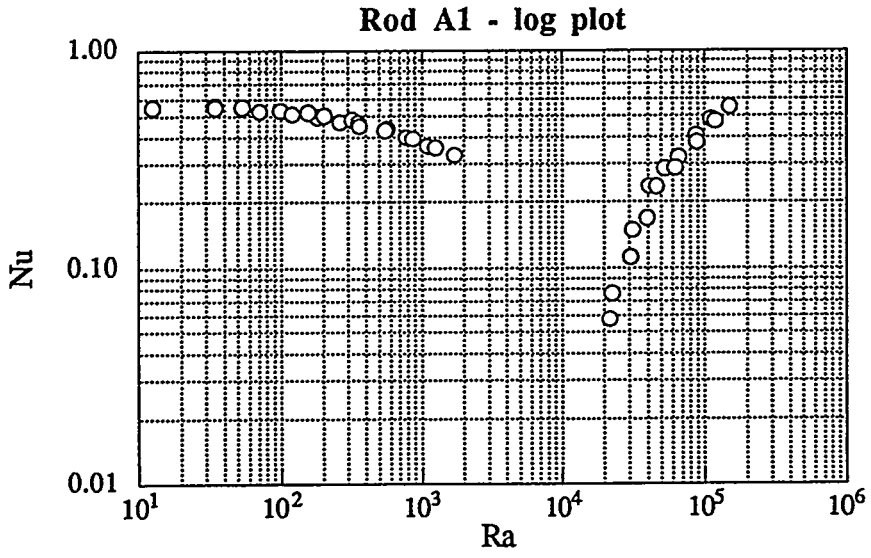

Figure 5.35 Nusselt number for rod A1, without negative values.

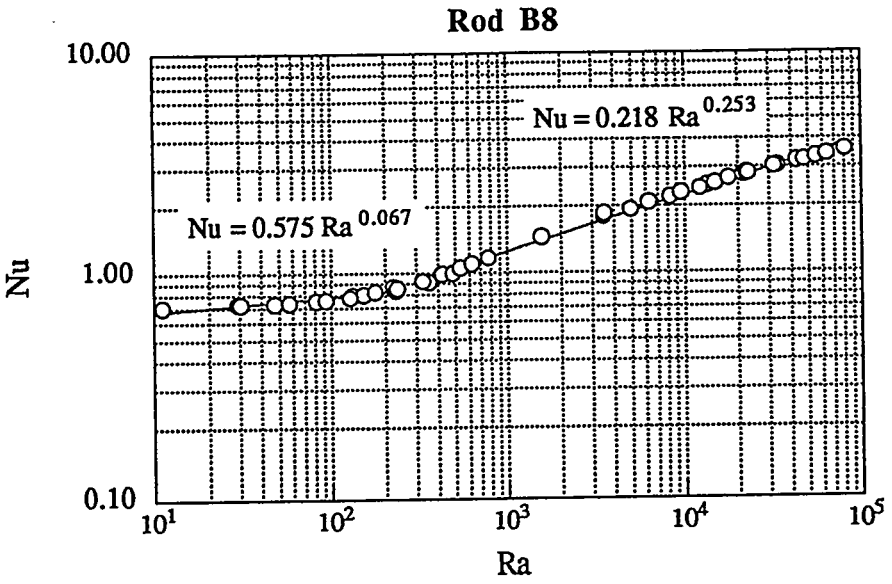

Figure 5.36 Nusselt number for rod B8.

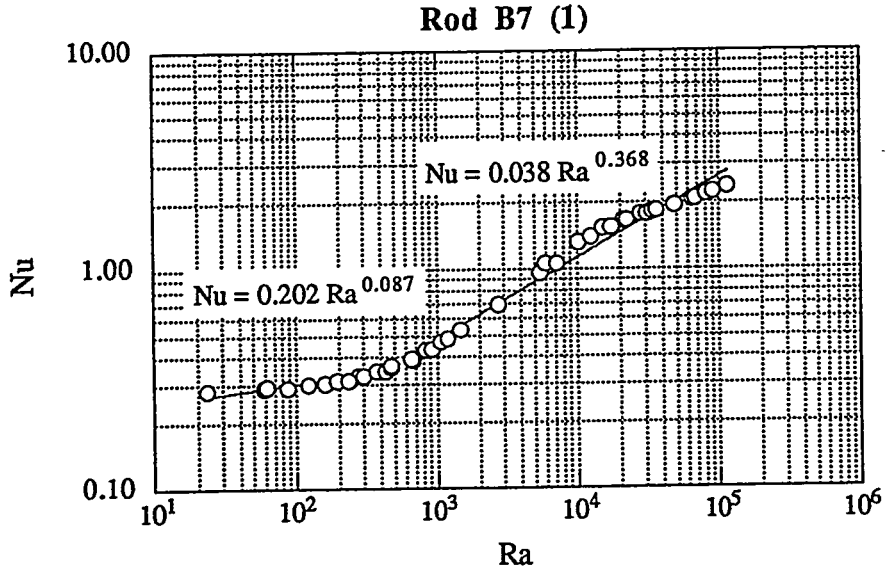

Figure 5.37 Nusselt number for rod B7, correlation 1.

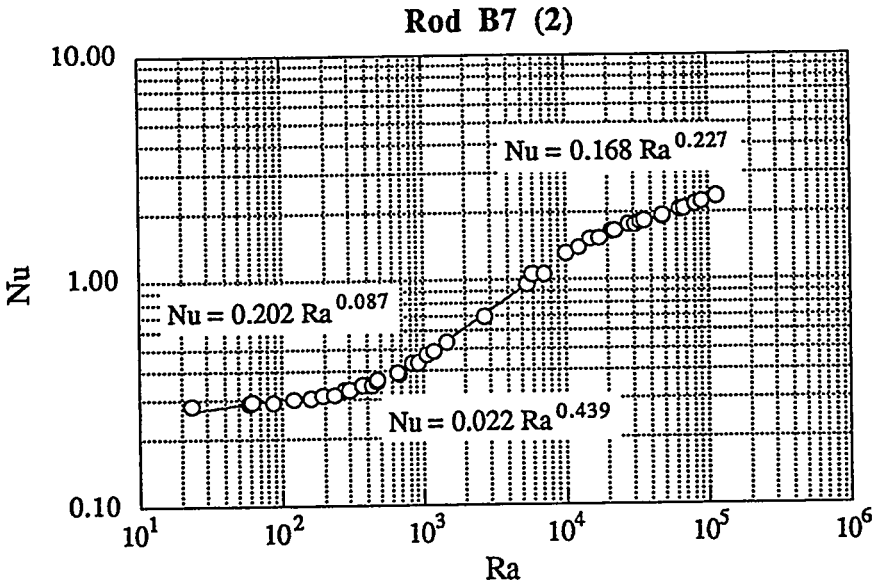

Figure 5.38 Nusselt number for rod B7, correlation 2.

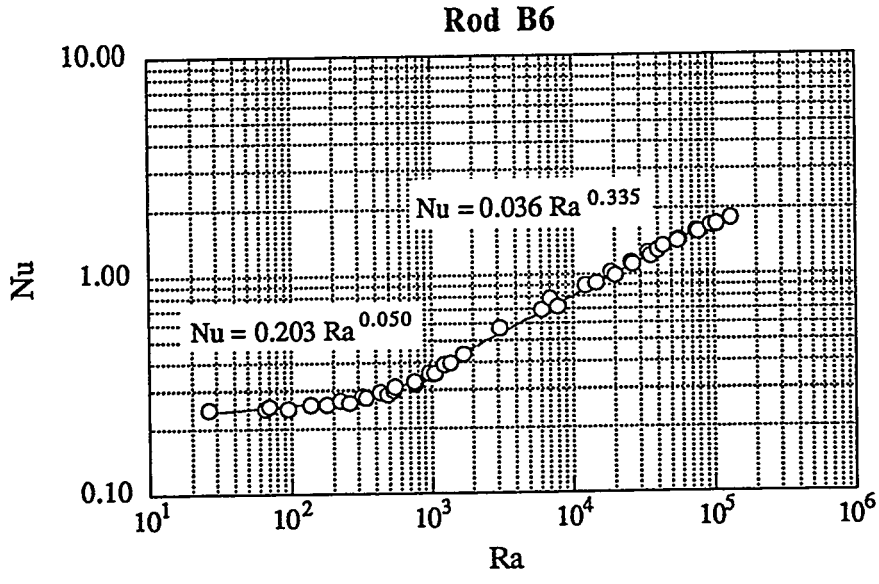

Figure 5.39 Nusselt number for rod B6.

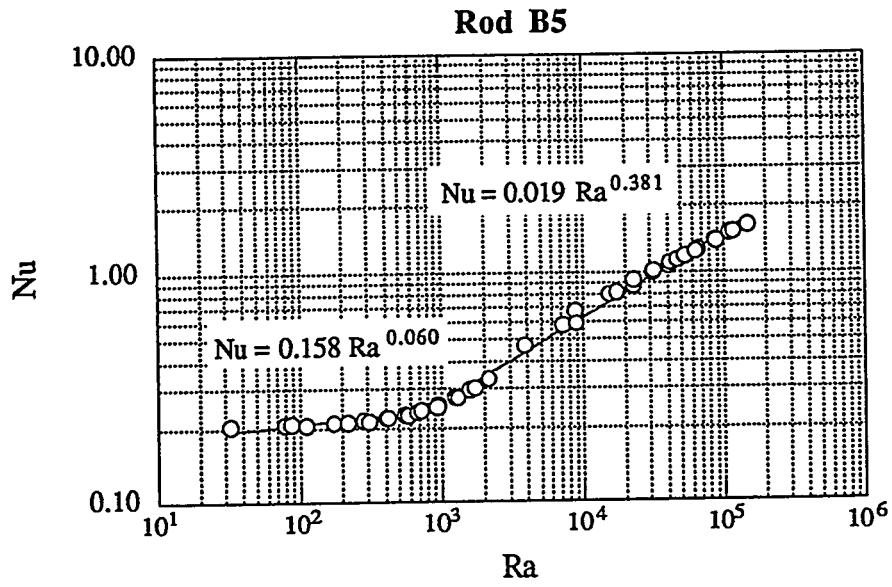

Figure 5.40 Nusselt number for rod B5.

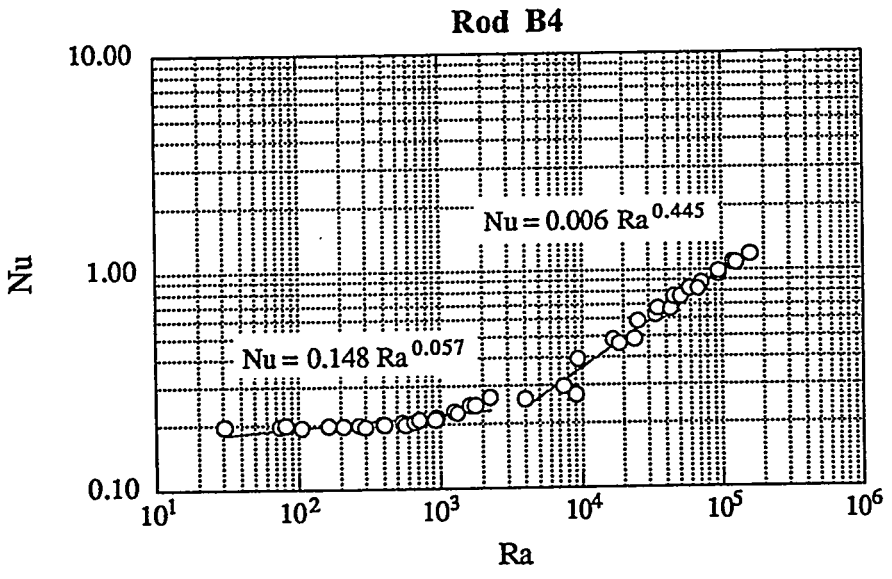

Figure 5.41 Nusselt number for rod B4.

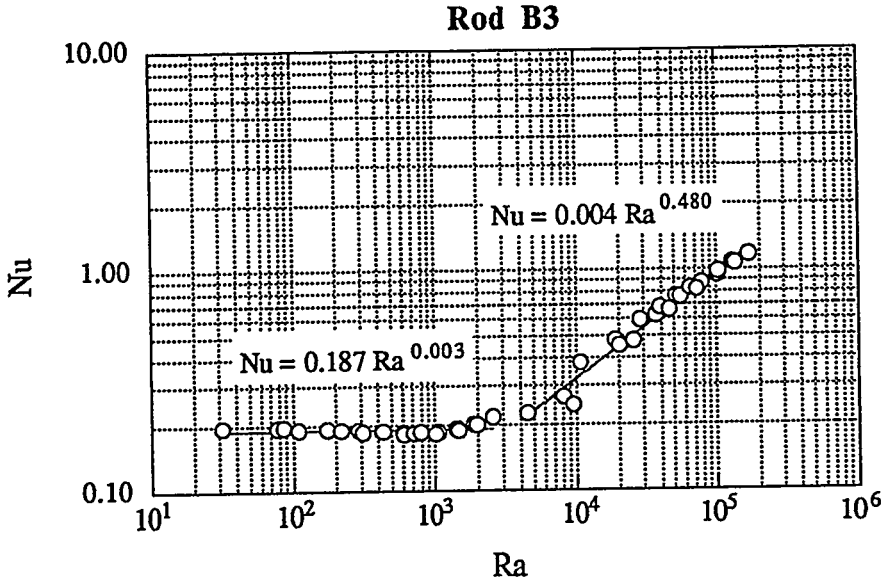

Figure 5.42 Nusselt number for rod B3.

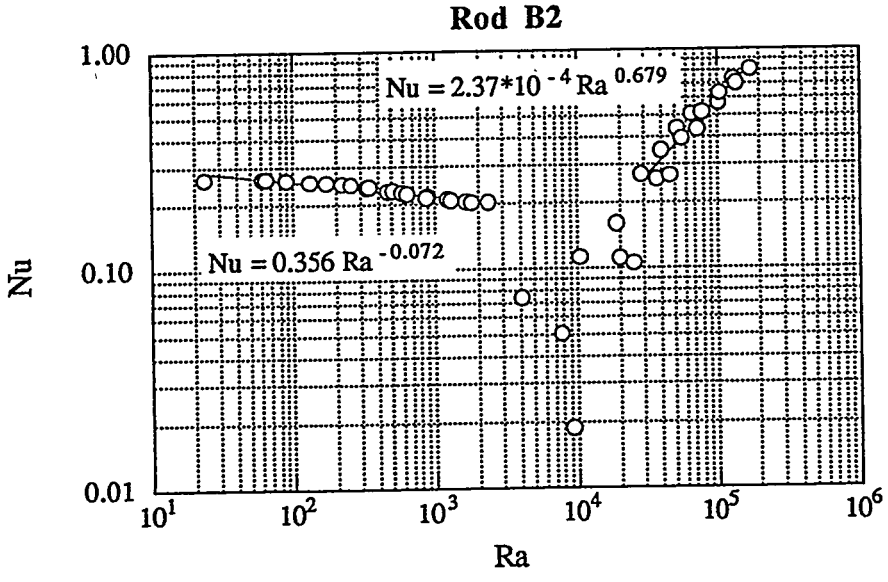

Figure 5.43 Nusselt number for rod B2.

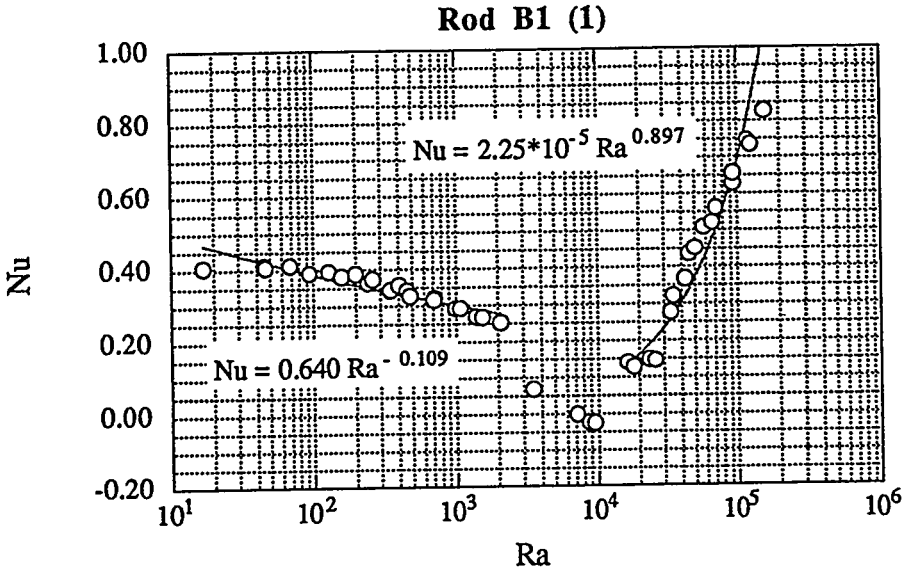

Figure 5.44 Nusselt number for rod B1, correlation 1, including negative values.

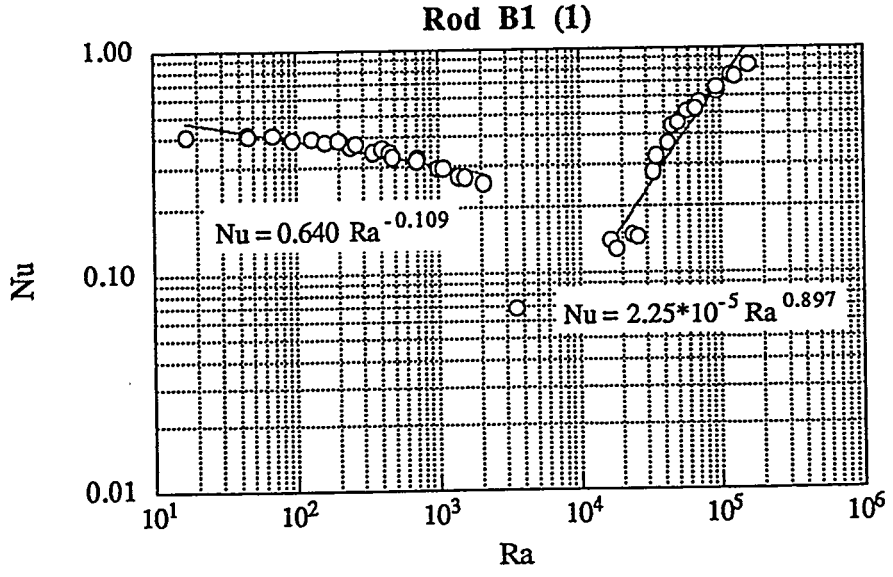

Figure 5.45 Nusselt number for rod B1, correlation 1, log plot.

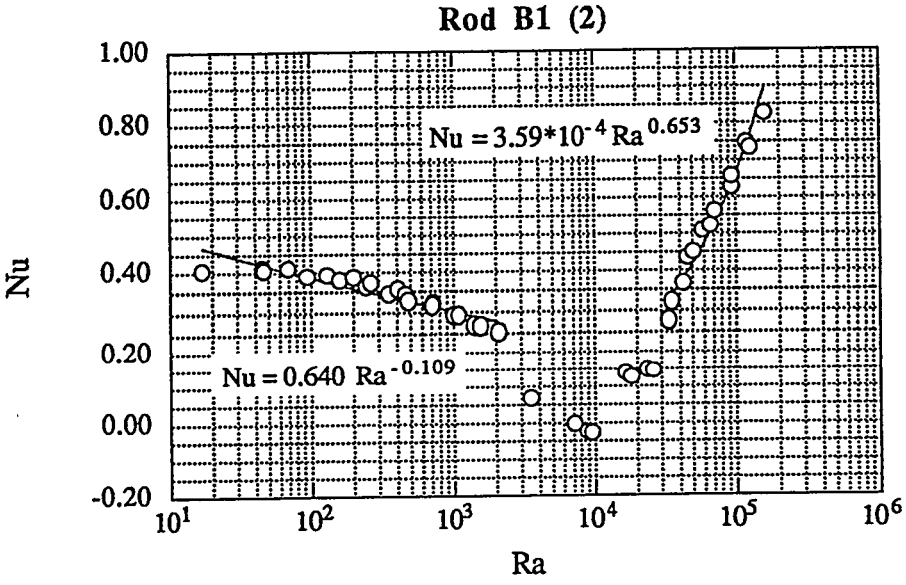

Figure 5.46 Nusselt number for rod B1, correlation 2.

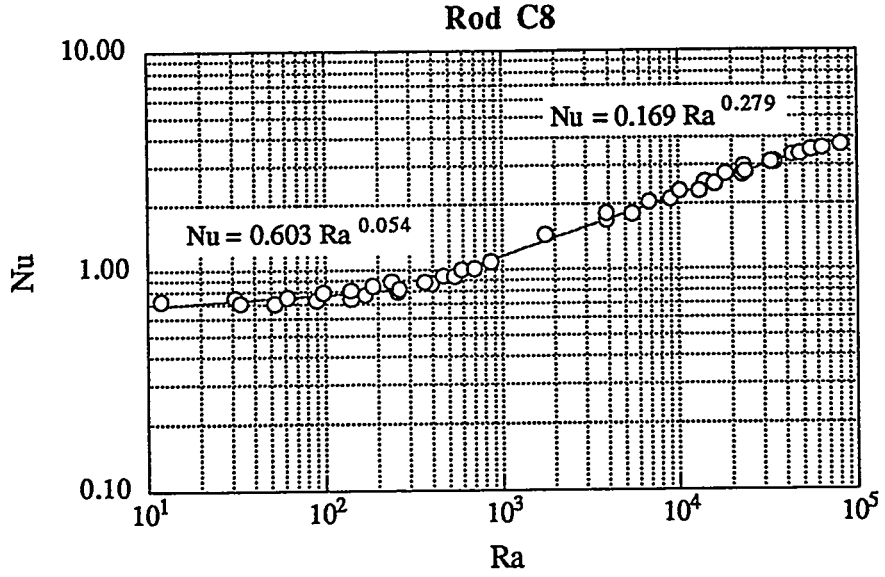

Figure 5.47 Nusselt number for rod C8.

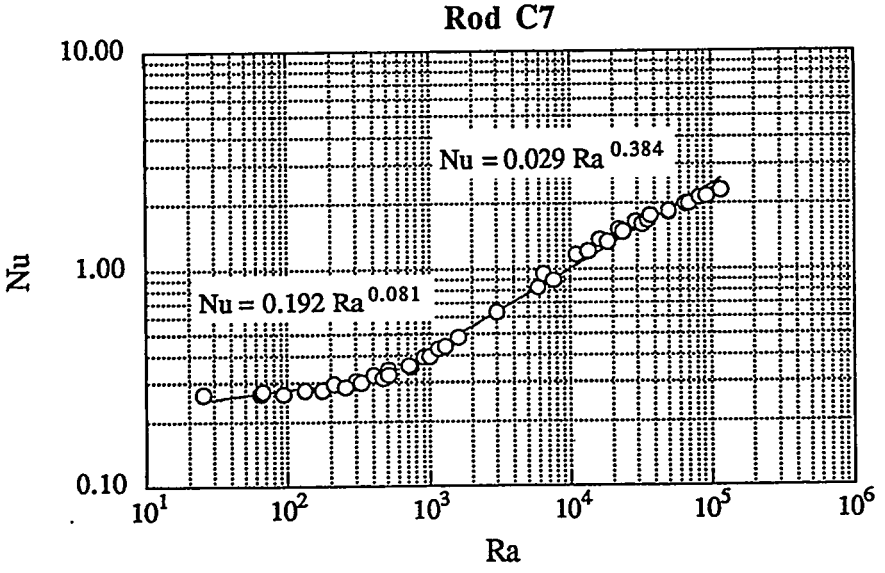

Figure 5.48 Nusselt number for rod C7.

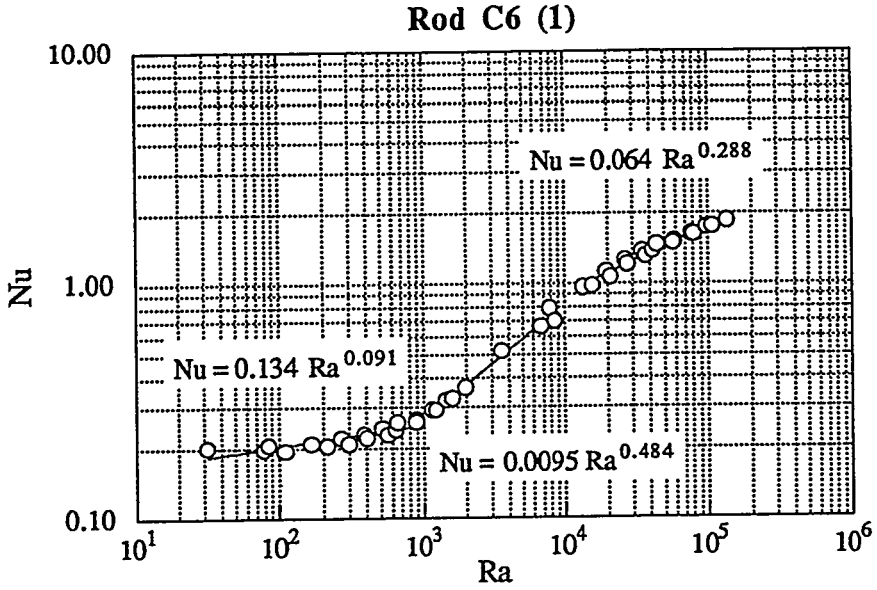

Figure 5.49 Nusselt number for rod C6, correlation 1.

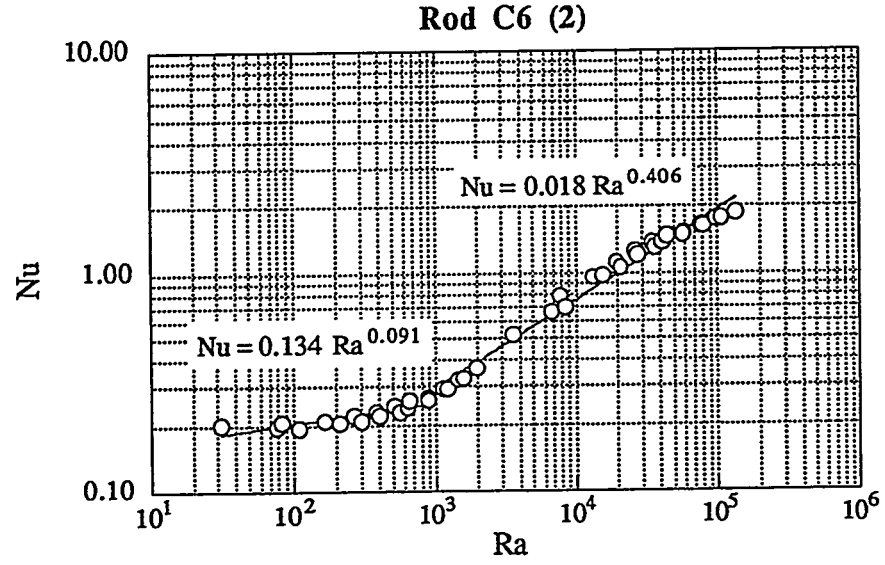

Figure 5.50 Nusselt number for rod C6, correlation 2.

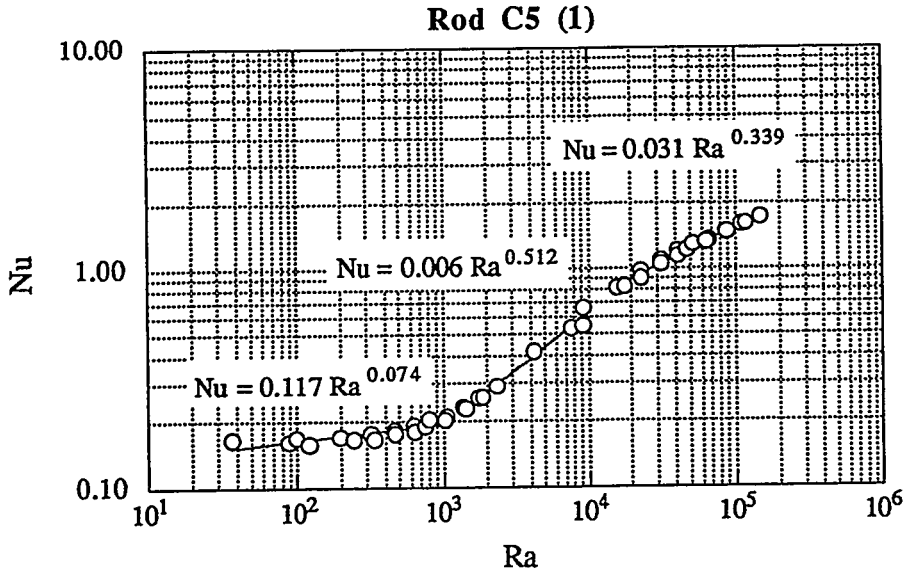

Figure 5.51 Nusselt number for rod C5, correlation 1.

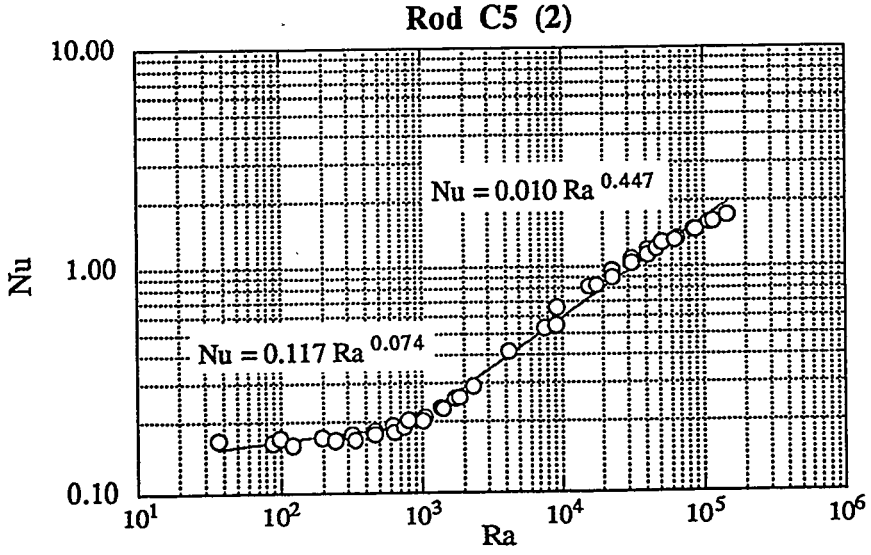

Figure 5.52 Nusselt number for rod C5, correlation 2.

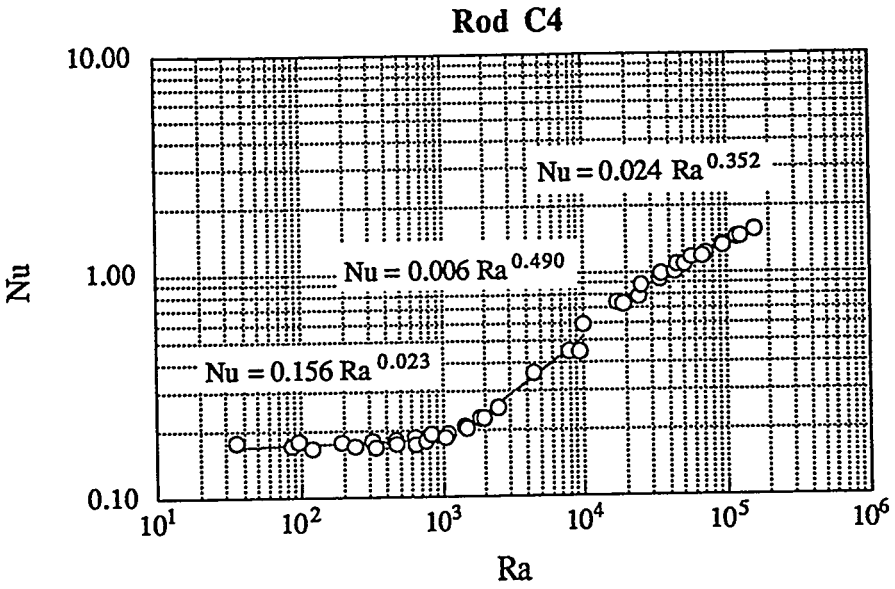

Figure 5.53 Nusselt number for rod C4.

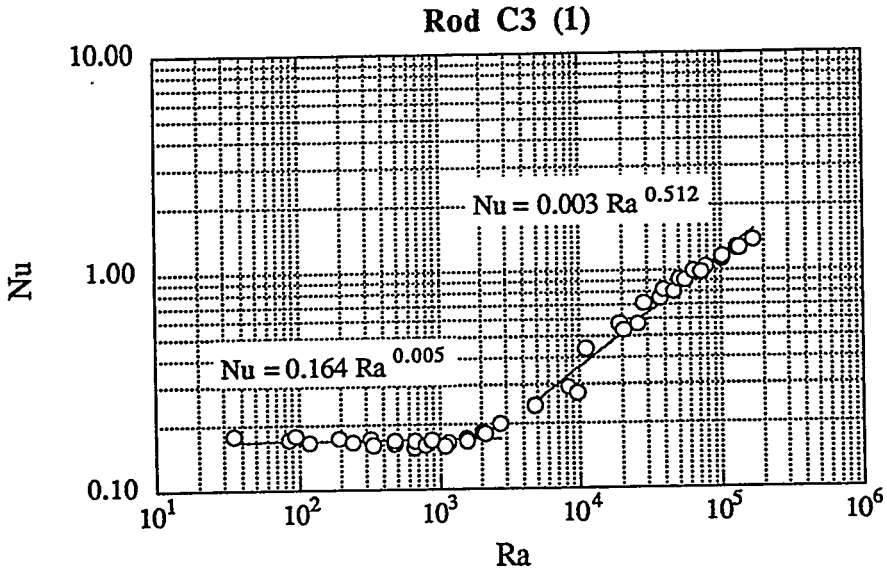

Figure 5.54 Nusselt number for rod C3, correlation 1.

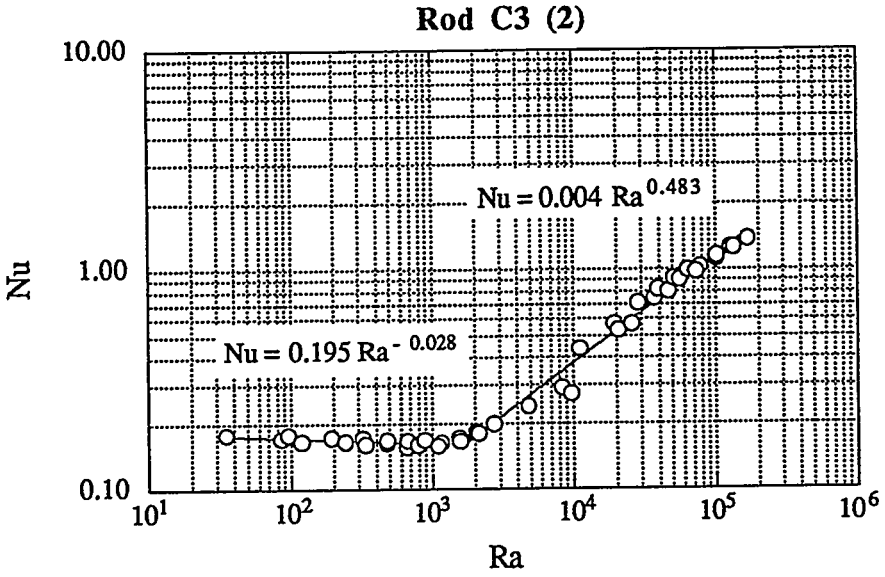

Figure 5.55 Nusselt number for rod C3, correlation 2.

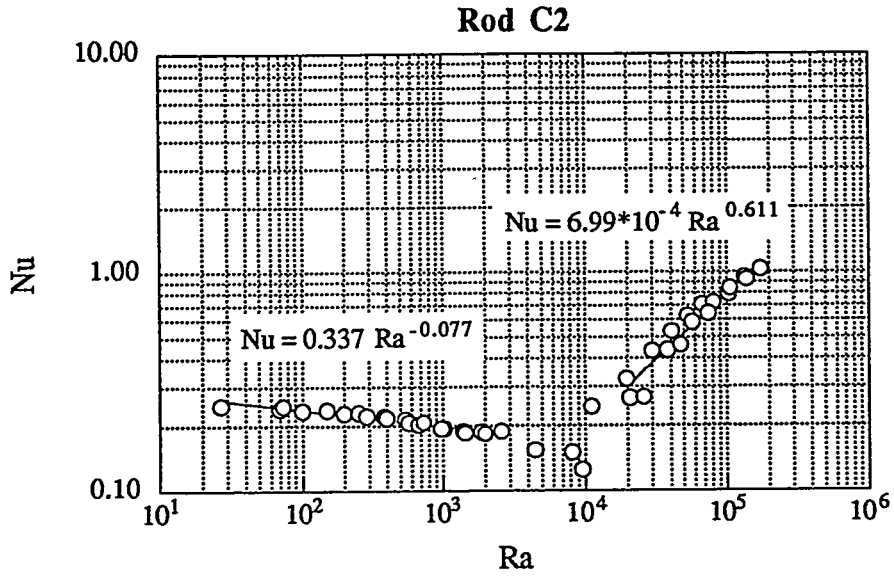

Figure 5.56 Nusselt number for rod C2.

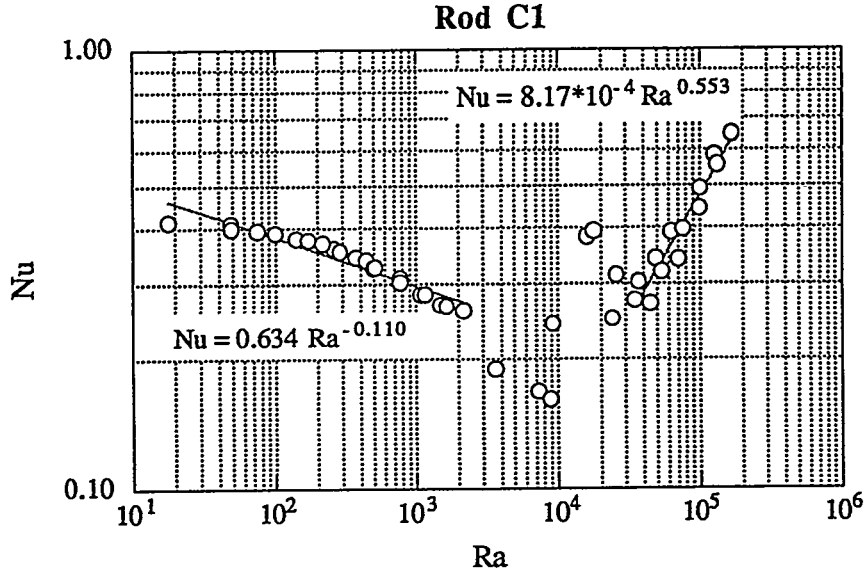

Figure 5.57 Nusselt number for rod C1.

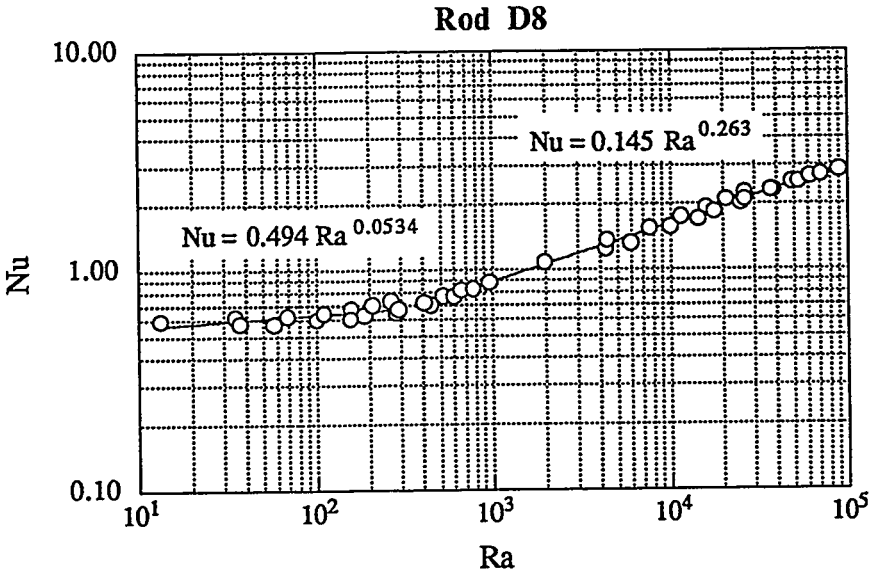

Figure 5.58 Nusselt number for rod D8.

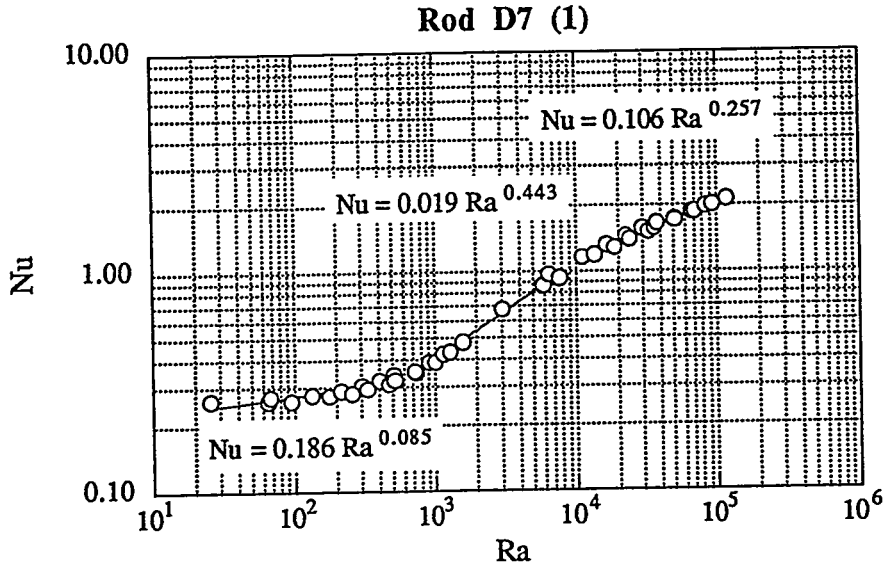

Figure 5.59 Nusselt number for rod D7, correlation 1.

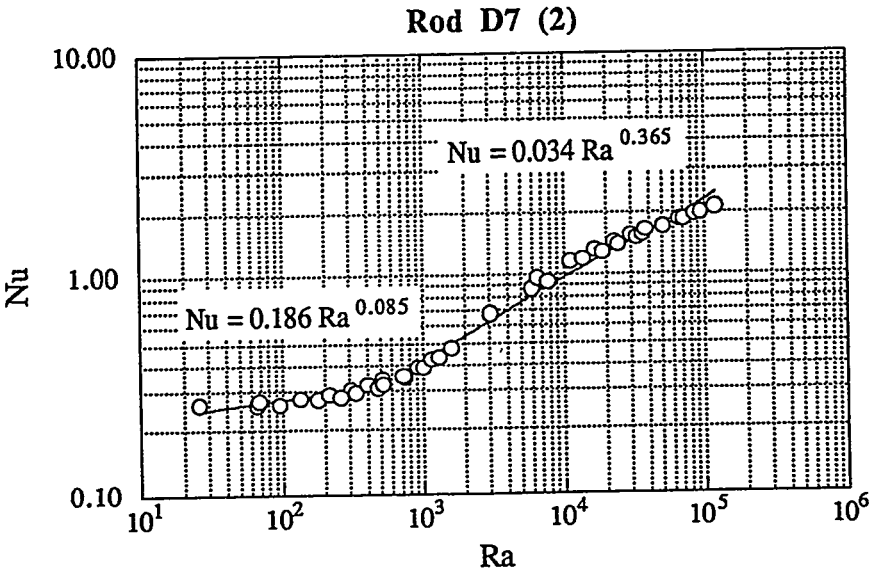

Figure 5.60 Nusselt number for rod D7, correlation 2.

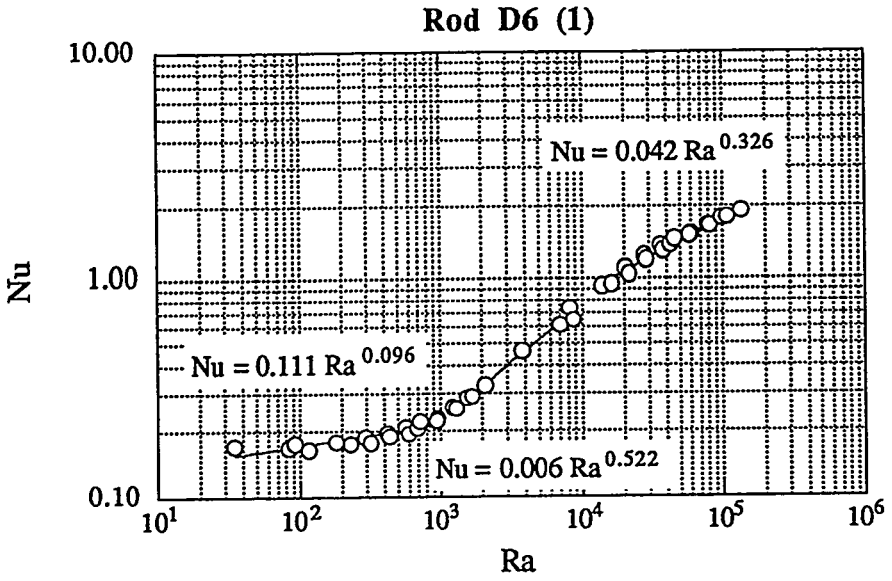

Figure 5.61 Nusselt number for rod D6, correlation 1.

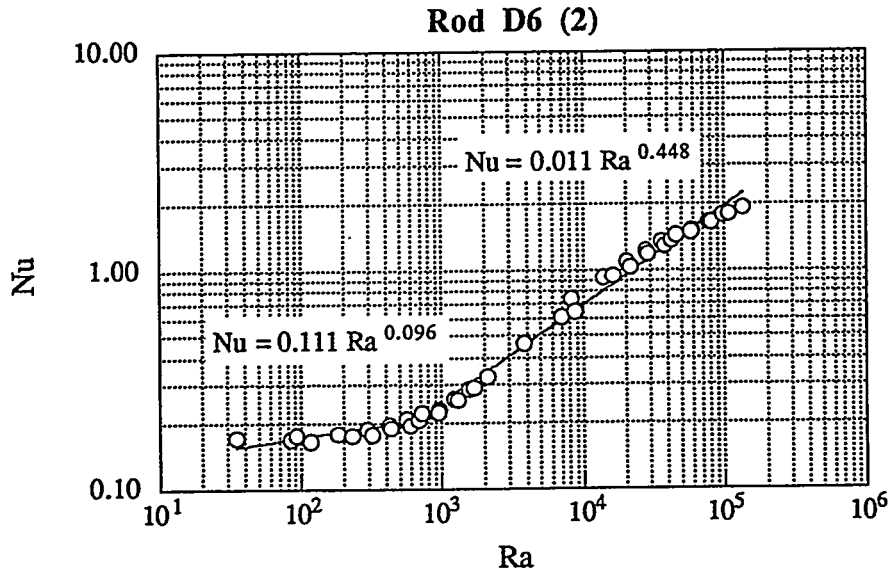

Figure 5.62 Nusselt number for rod D6, correlation 2.

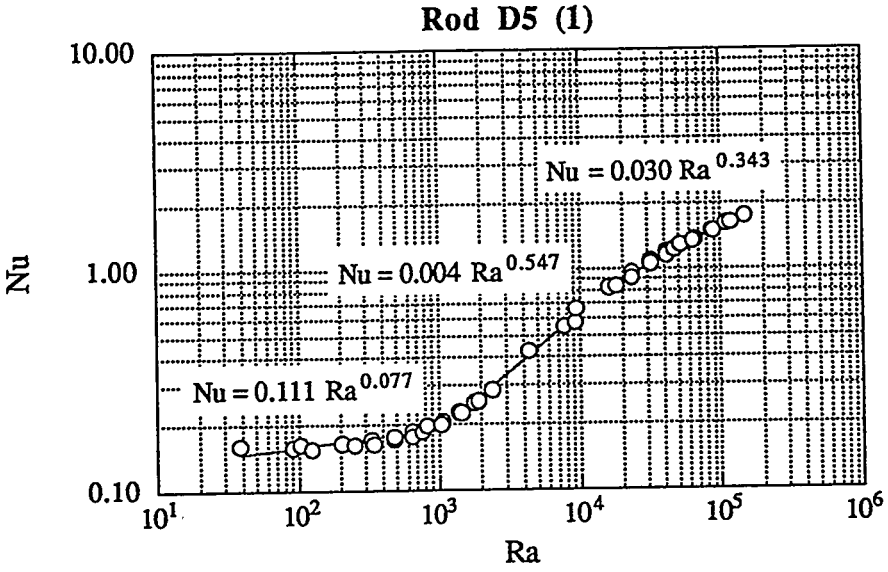

Figure 5.63 Nusselt number for rod D5, correlation 1.

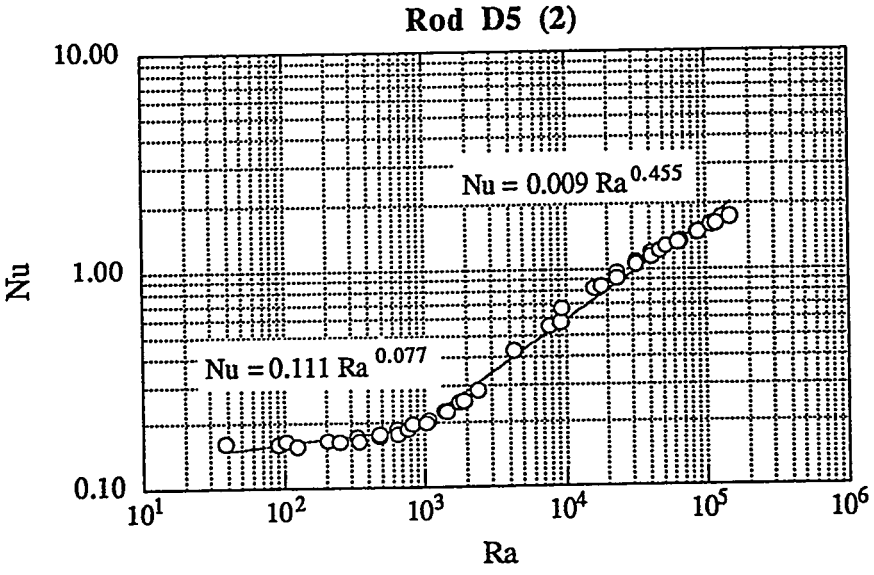

Figure 5.64 Nusselt number for rod D5, correlation 2.

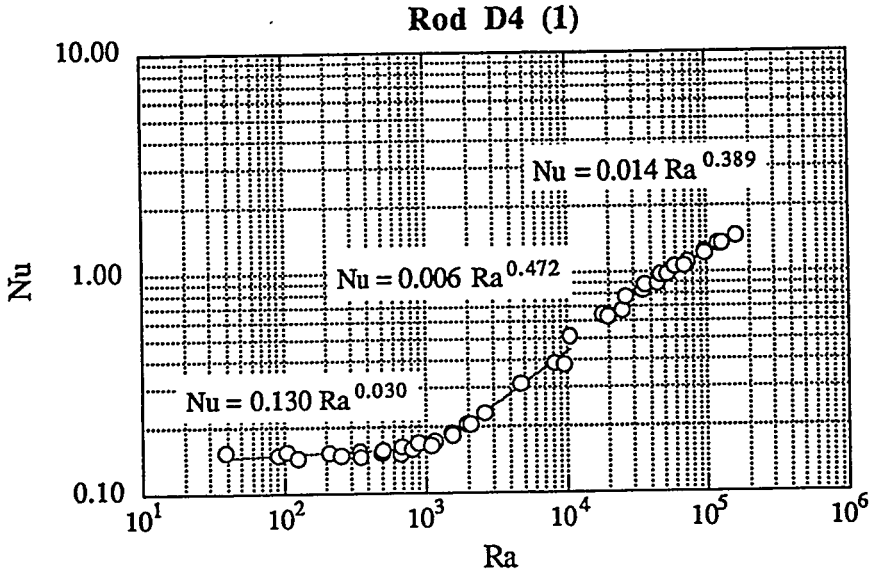

Figure 5.65 Nusselt number for rod D4, correlation 1.

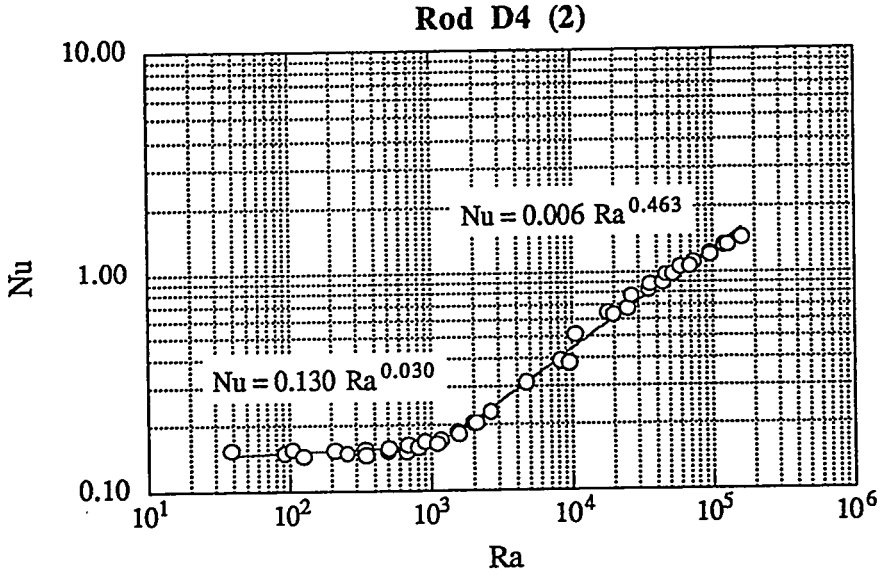

Figure 5.66 Nusselt number for rod D4, correlation 2.

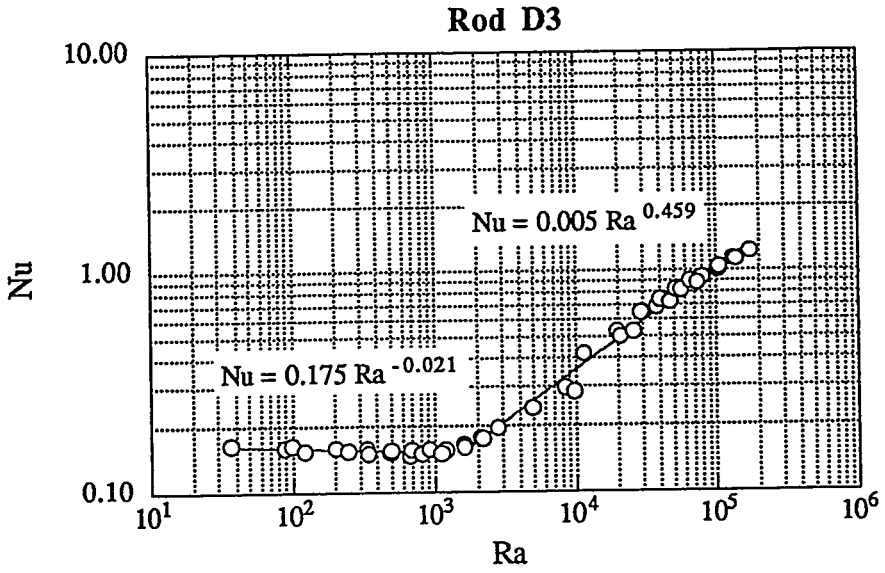

Figure 5.67 Nusselt number for rod D3.

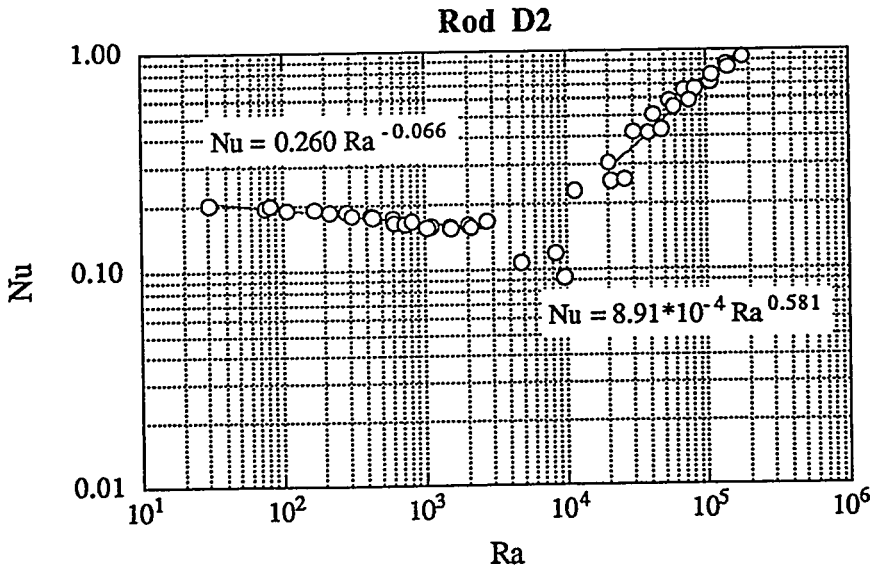

Figure 5.68 Nusselt number for rod D2.

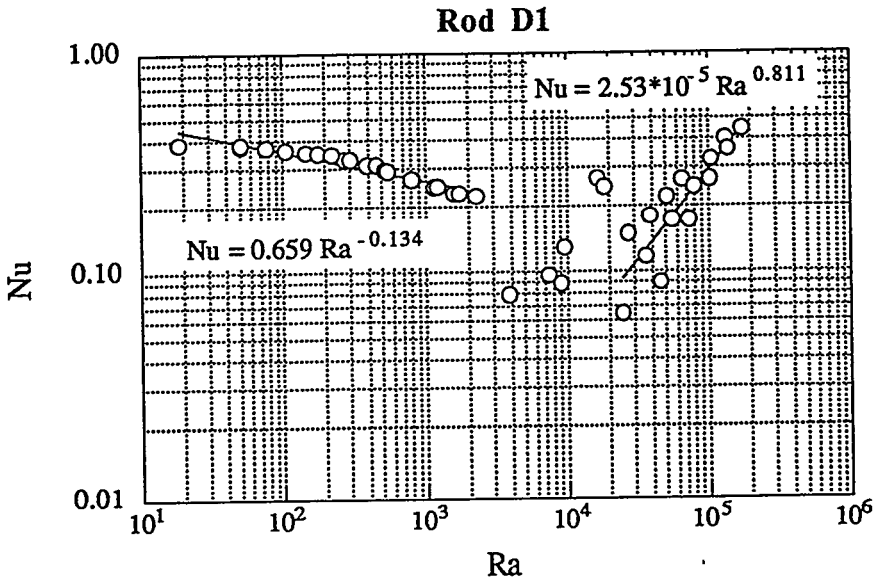

Figure 5.69 Nusselt number for rod D1.

Table 5.3 Individual Rod Correlations for Column A

$Nu = C (Ra)^n$

Rod ID	C and n values C	n	Rayleigh number range
A1	not correlated		--
A2	0.663	-0.046	13 - 1600
	6.02 e -4	0.617	14,000 - 1.5 e5
A3 (1)	0.285	-0.020	23 - 2100
	0.004	0.449	17,000 - 1.6 e5
A3 (2)	0.285	-0.020	23 - 2100
	0.006	0.406	3700 - 1.6 e5
A4	0.318	0.049	18 - 1500
	0.054	0.234	13,000 - 1.5 e5
A5	0.191	0.045	26 - 570
	0.033	0.309	780 - 1.4 e5
A6 (1)	0.281	0.126	16 - 1100
	0.167	0.186	9600 - 1.2 e5
A6 (2)	0.253	0.148	16 - 1.2 e5
A7 (1)	0.277	0.085	18 - 360
	0.118	0.249	500 - 1.1 e5
A7 (2)	0.134	0.234	18 - 1.1 e5
A8	0.953	0.057	54 - 120
	0.473	0.209	150 - 2700
	4.29	-0.062	3900 - 92,000

Table 5.5 Individual Rod Correlations for Column C
$Nu = C (Ra)^{n}$

Rod ID	C and n values C	n	Rayleigh number range
C1	0.634	-0.110	18 - 2200
	8.17e -4	0.553	35,000 - 1.7 e5
C2	0.337	-0.077	27 - 2600
	6.99e -4	0.611	20,000 - 1.8 e5
C3 (1)	0.164	0.005	35 - 2700
	0.003	0.512	4800 - 1.7 e5
C3 (2)	0.195	-0.028	35 - 1200
	0.004	0.483	1600 - 1.7 e5
C4	0.156	0.023	36 - 1100
	0.006	0.490	1400 - 10,000
	0.024	0.352	17,000 - 1.6 e5
C5 (1)	0.117	0.074	37 - 1100
	0.006	0.512	1400 - 9300
	0.031	0.339	16,000 - 1.5 e5
C5 (2)	0.117	0.074	37 - 1100
	0.010	0.447	1400 - 1.5 e5
C6 (1)	0.134	0.091	32 - 890
	0.0095	0.484	1100 - 8500
	0.064	0.288	13,000 - 1.4 e5
C6 (2)	0.134	0.091	32 - 890
	0.018	0.406	1100 - 1.4 e5
C7	0.192	0.081	25 - 520
	0.029	0.384	720 - 1.2 e5
C8	0.603	0.054	19 - 260
	0.169	0.279	360 - 81,000

Table 5.4 Individual Rod Correlations for Column B
$Nu = C (Ra)^n$

Rod ID	C and n values C	n	Rayleigh number range
B1 (1)	0.640	-0.109	17 - 2100
	2.25 e -5	0.897	16,000 - 1.6 e5
B1 (2)	0.640	-0.109	17 - 2100
	3.59 e -4	0.653	34,000 - 1.6 e5
B2	0.356	-0.072	24 - 2400
	2.37 e -4	0.679	29,000 - 1.7 e5
B3	0.187	0.003	32 - 2600
	0.004	0.480	4500 - 1.7 e5
B4	0.148	0.057	30 - 2300
	0.006	0.445	4000 - 1.6 e5
B5	0.158	0.060	26 - 340
	0.019	0.381	430 - 1.3 e5
B6	0.203	0.050	26 - 340
	0.036	0.335	430 - 1.3 e5
B7 (1)	0.202	0.087	23 - 470
	0.038	0.368	660 - 1.1 e5
B7 (2)	0.202	0.087	23 - 470
	0.022	0.439	660 - 7200
	0.168	0.227	10,000 - 1.1 e5
B8	0.575	0.067	11 - 240
	0.218	0.253	330 - 81,000

Table 5.6 Individual Rod Correlations for Column D

$Nu = C (Ra)^{n}$

Rod ID	C and n values C	n	Rayleigh number range
D1	0.659	-0.134	19 - 2300
	2.53e -5	0.811	25,000 - 1.8 e5
D2	0.260	-0.066	30 - 2800
	8.91e -4	0.581	20,000 - 1.8 e5
D3	0.175	-0.021	37 - 1200
	0.005	0.459	1600 - 1.7 e5
D4 (1)	0.130	0.030	39 - 1200
	0.006	0.472	1500 - 11,000
	0.014	0.389	18,000 - 1.6 e5
D4 (2)	0.130	0.030	39 - 1200
	0.006	0.463	1500 - 1.6 e5
D5 (1)	0.111	0.077	38 - 110
	0.004	0.547	140 - 9400
	0.030	0.343	16,000 - 1.5 e5
D5 (2)	0.111	0.077	38 - 110
	0.009	0.455	140 - 1.5 e5
D6 (1)	0.111	0.096	35 - 960
	0.006	0.522	1200 - 8700
	0.042	0.326	14,000 - 1.4 e5
D6 (2)	0.111	0.096	35 - 960
	0.011	0.448	1200 - 1.4 e5
D7 (1)	0.186	0.085	26 - 520
	0.019	0.443	720 - 7700
	0.106	0.257	11,000 - 1.2 e5
D7 (2)	0.186	0.085	26 - 520
	0.034	0.365	720 - 1.2 e5
D8	0.494	0.053	13 - 290
	0.145	0.263	410 - 90,000

5.4.2 Discussion of Individual Rod Results

The data sets for each rod were correlated using the Morgan form, $Nu = C(Ra)^n$. There are several interesting trends in the data to be noticed. However, two important points need to be made in order to avoid confusion about trends in the data.

First, recall that these Nusselt numbers are circumferentially rod-averaged Nusselt numbers. Since temperature and heat flux were not measured as functions of circumferential angle, this local Nusselt number cannot be calculated.

Second, it very important to keep in mind the definition of Nusselt and Rayleigh number for these individual rods--in particular, the definition of the characteristic temperature difference, ΔT. For most typical experimental heat transfer calculations, the characteristic temperature difference is defined as the difference between the surface temperature of the body and the local temperature of the fluid flowing over or around the body. In this experiment, this local fluid temperature would correspond to some average temperature of the fluid surrounding each rod. However, since each of these local fluid temperatures is very difficult to measure accurately, the enclosure temperature, T_C, was used as the temperature of the heat sink. Also, as Canaan points out in his dissertation, these correlations are not useful unless they are presented in terms of known or easily measurable parameters. The individual local fluid temperatures are difficult to measure, the enclosure temperature is not. However, what this means is that the trends in the Nusselt numbers with increasing Rayleigh number do not necessarily follow actual trends in convective heat transfer for a particular rod. This effect will be shown for particular rods in the next few paragraphs of discussion.

There are three general areas into which the trends of the individual rod data can be grouped. The first group consists of the rods from columns B through D, and from rows 4 through 8. These rods loosely define the rods in the lower-middle of the bundle. The second group is columns B through D, and rows 1 through 3. The final group is the column A rods, which display some interesting trends in the upper and lower corners.

The group 1 rods display similar behavior to the trends of the full array results. That is, they display a conduction and a convection regime, reminiscent of the Rayleigh-Benard problem. As one goes up within the array, that is, from row 8 to row 4, the Nusselt number decreases. This is because—for tightly packed cylinder arrays—the fluid rising from a heated rod tends not only to increase the temperature of the fluid surrounding the upper rod, but also causes a thickening of the boundary layer of the upper rod, which decreases the convective heat transfer from the upper rod.

Also, notice that there is a large drop in Nusselt number from row 8 to row 7, but less of a drop from row 7 to 6, and even less from row 6 to 5. This is because row 8 is not preheated by any rods, while row 7 is preheated by row 8. Row 6 is preheated by rows 7 *and* 8, but this difference is not as drastic of a change as going from row 8 to row 7. The drop in Nusselt number for individual rods as one goes up within the rod bundle will be compared to a similar effect seen in Choi and Cha's experiment in sub-section 5.4.4.

Sparrow and Niethammer describe the "preheating" effect in a 1981 report. Their experiment investigated the natural convection trends in two heated horizontal cylinders placed one on top of the other. The cylinders were given the same heat input and the vertical spacing of the upper rod was varied. For very small vertical spacings ($P/D < 2$), they report that the upper cylinder Nusselt number is significantly lower than the lower cylinder. However, as the spacing is increased, the Nusselt number for the upper rod increases and actually becomes larger than the lower cylinder. This is because of the relationship of two competing effects. The first effect is the preheating of the ambient fluid around the upper rod by the plume of the lower rod. The second is the increased flow velocity around the upper rod caused by the flow from the lower rod. At small separation distances, the lower rod plume has no space for the heat to dissipate and the Nusselt number of the upper rod is decreased. However, at higher separation distances, the heat from the lower plume dissipates and the increased flow velocity on the upper rod increases its Nusselt number. It is as if the upper cylinder is subjected to forced convection. However, since the rods are closely packed in the UT staggered array ($P/D = 1.32$),

the upper rods Nusselt numbers are only decreased. The qualitative flow patterns described by Sparrow and Niethammer as diagrammed below in Figure 5.70.

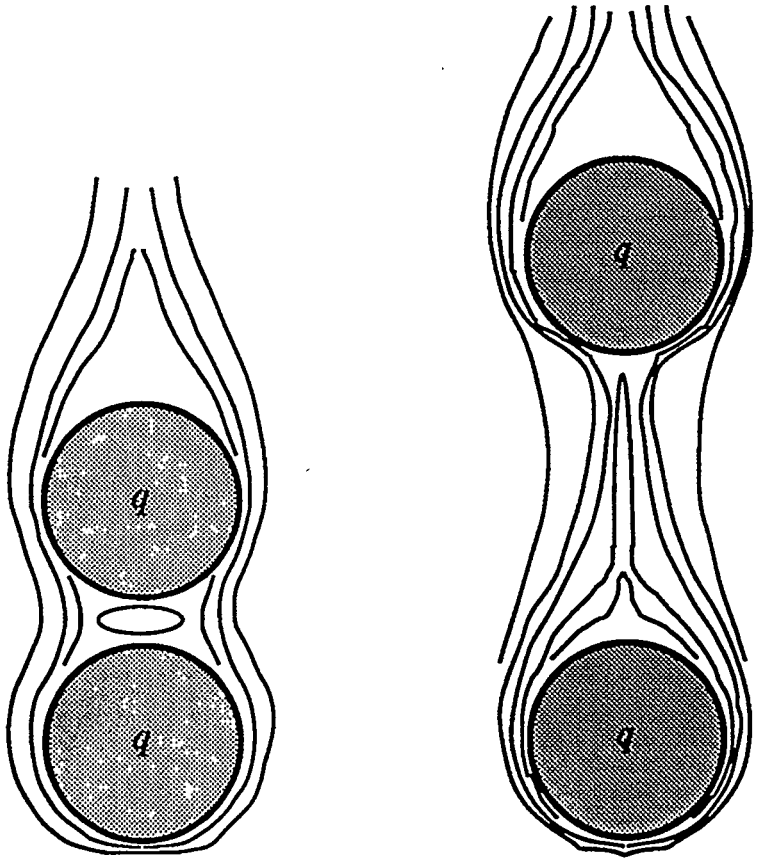

Figure 5.70 Different flow patterns for two heated cylinders of different vertical spacing.

The preheating effect continues in the second group of rods--rows 3, 2, and 1 and columns B, C, and D. However, the continuous decrease of Nusselt number for rows 8 through 1 of a given column only occurs in the *convective* regime. In the conduction regime, these upper rows are closer to the cooled CuBE ceiling, which causes steeper temperature gradients around rows 1 and 2 than in rows 3 through 5. This is expected, because in pure conduction the temperature gradients

(which are proportional to the Nusselt number) are greatest for those rods closest to the CuBE wall, whether the rods are on the top or the bottom of the array. This effect can be further noted by comparing the Nusselt numbers for a given row, moving across from row A to row D, in the conduction regime. In these plots, Nusselt number drops as one moves away from the cooled side walls of the CuBE. This effect can be seen qualitatively by recalling Figures 5.21 and 5.23, which show the temperature contours from the FIDAP conduction simulation. The temperature gradients, and thus the resulting conduction-regime Nusselt numbers, are higher nearest to the CuBE wall.

There is another surprising result seen in the data from the upper 3 rows. Notice that in these rows, the Nusselt number *decreases* with increasing Rayleigh number in the lower regime, then jumps back up as Ra increases further. Also, notice that the Nusselt number is mostly less than 1.0. Physically, Nu = 1.0 corresponds to pure conduction; thus, a Nusselt number less than 1.0 should not exist. Also, since a zero slope of Nu with increasing Ra indicates pure conduction, it should also not be physically possible to obtain a negative Nusselt number slope. Thus, how can this experimental data be correct? The answer lies in the definition of the Nusselt and Rayleigh numbers, as mentioned above. It is in these upper row rods that these definitions cause the most unusual trends.

The defined Nusselt and Rayleigh numbers for each rod are based on the temperature difference between the rod surface and the enclosure surface, $T_r - T_c$. The more traditional definition of the characteristic temperature difference is $T_r - T_\infty$, where T_∞ is the temperature of the local fluid surrounding the rod. As the rod power and vessel pressure is increased, strengthening the buoyant flow within the rod bundle, the hottest fluid and the maximum rod surface temperature shifts upward from the center of the array to rows 2 and 3. Thus, the rods on rows 1, 2, and 3 increase in temperature relative to the CuBE. Since the defined Rayleigh number is proportional to $T_r - T_c$, the Rayleigh number increases. However, the more traditional Rayleigh number based on $T_r - T_\infty$ actually *decreases* due to the local increase in T_∞ around these upper row rods. Thus, what appears to be a decreasing Nusselt number with increasing Rayleigh number is in fact a decreasing Nusselt number with decreasing Rayleigh number, using the more traditional

Rayleigh number definition. Also, the fact that some Nusselt numbers are less than 1.0 is because the Nusselt number is proportional to $(T_r - T_c)^{-1}$, which is much larger in magnitude than $T_r - T_\infty$. If the Nusselt number were based on $T_r - T_\infty$, these Nusselt numbers would likely be greater than 1.0. Recall that this thesis used the non-traditional characteristic temperature difference $T_r - T_c$ because of the difficulty in measuring a local T_∞ for each rod.

Another very unusual trend is observed for rods A1 and B1. These two rods not only show decreasing Nusselt number, they even have a few negative Nusselt numbers in the lower end of the convection regime. This seems to imply that somehow heat is flowing in the same direction as the temperature gradient rather than the opposite direction, which is physically impossible. The explanation is that in this particular flow regime, the surfaces of rods A1 and B1 are hotter than the CuBE wall, thus $(T_r - T_c)$ is positive. However, the average local fluid temperature around these two rods is actually hotter than the rod surfaces, thus $(T_r - T_\infty)$ is negative. This means that heat is actually being transferred from the fluid to the rod and that the thermal radiation away from the rod is greater than the total power input to the rod, even though the rod has internal heat generation. If one defined a Nusselt number based on $T_r - T_\infty$, this Nusselt number would be positive. However, because of the definition of ΔT used in this thesis, negative Nusselt numbers are possible.

The column A rods display unusual trends at the upper and lower corners of the bundle; that is, at rods A1 and A8. The negative Nusselt number behavior of rod A1 was mentioned above. The final trend to be noted is the unusual behavior of rod A8. Notice that the Nusselt number for rod A8 seems to transition from a conduction to a convection regime at mid-range Rayleigh numbers, but then as the Rayleigh number increases further, the Nusselt number levels off and even drops back down again. Also, as shown in Figure 5.71, the Nusselt number for rod A8 is lower than that for rod B8 in the convection regime. One would expect A8 to always be the coldest rod in the array, and at lower Rayleigh numbers, it is. However, at higher Rayleigh numbers, B8 becomes the coldest rod. Canaan has also observed this behavior between rods A8 and B8, and he speculates that it is caused by changes in the fluid flow pattern above a certain Rayleigh number that

might cool B8 more effectively than A8. For example, if at high Rayleigh numbers the cool downward flow along the sides of the CuBE "rounded the corner" and impinged more forcefully on rod B8 than on rod A8, this could make the ΔT for rod B8 lower than that of A8. Since Nu is proportional to $1/\Delta T$, this would imply that B8 would have a lower Nusselt number. Canaan is currently engaged in numerical flow simulation to characterize the flow patterns within the bundle which predicate this behavior. Hopefully, his numerical research can shed some light on this phenomenon.

However, in order to give the reader a qualitative feel for the flow patterns occurring within the staggered array, a FIDAP natural convection simulation was run for the lowest Rayleigh number case of helium at 1W / rod and 0 psig pressure. At higher Rayleigh numbers, the flow is turbulent and would require a more sophisticated model. This simulation used the same mesh as for the conduction simulation, shown in Figure 5.19. In this case, the helium was modeled as a laminar fluid. Zero velocity was specified at the rod and CuBE surfaces, and the x-direction velocity was set to zero at the symmetry boundary. The results of the simulation are presented in Figures 5.72 and 5.73. The temperature contours for this simulation are almost identical to the conduction case, and are not shown here. Figure 5.72 shows the fluid velocity vectors, and Figure 5.73 shows the streamlines of the flow. No buoyant plumes form from the individual rods, and all of the fluid motion is in sort of a half-cylindrical roll pattern that circulates down the sides of the CuBE and then back upward through the spaces between the cylinders. The maximum fluid velocity occurs in the downward flow on the sides. This flow solution was not subjected to a mesh-independence study and had a relatively large convergence criterion, thus the actual velocity values likely have a high uncertainty. However, this should give the reader a good feel for the general flow pattern of the fluid within the enclosure.

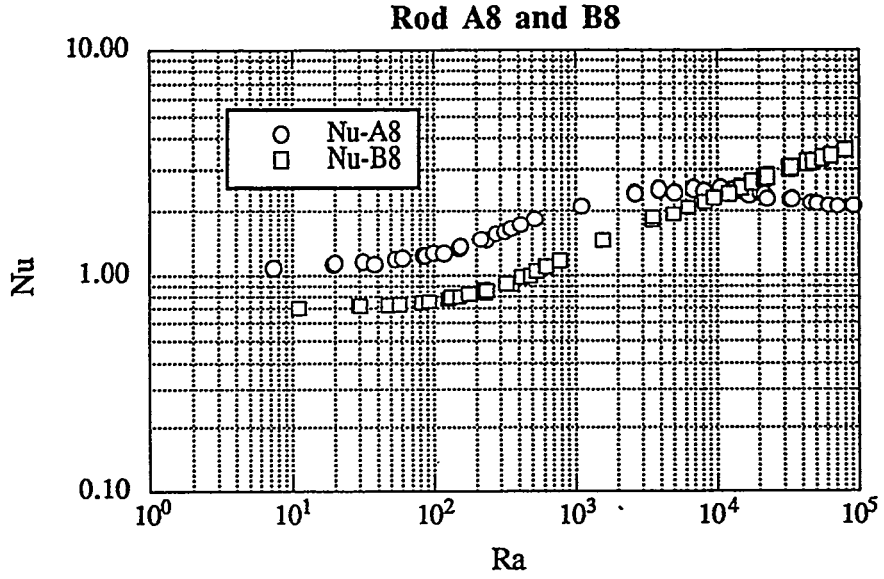

Figure 5.71 Comparison of Nusselt numbers for rods A8 and B8.

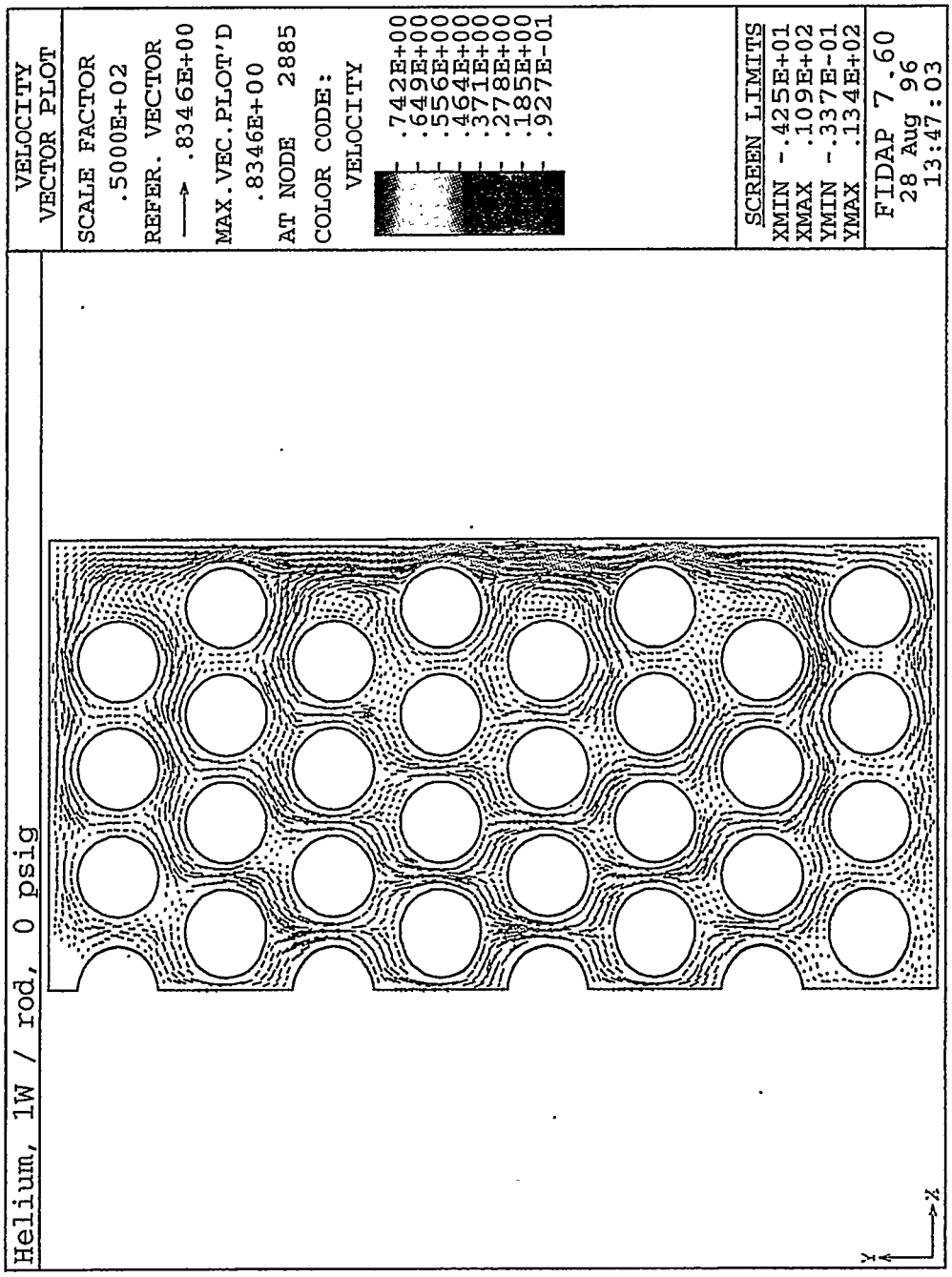

Figure 5.72 Flow velocity vectors from FIDAP laminar natural convection simulation, Ra_{bund} = 32,000.

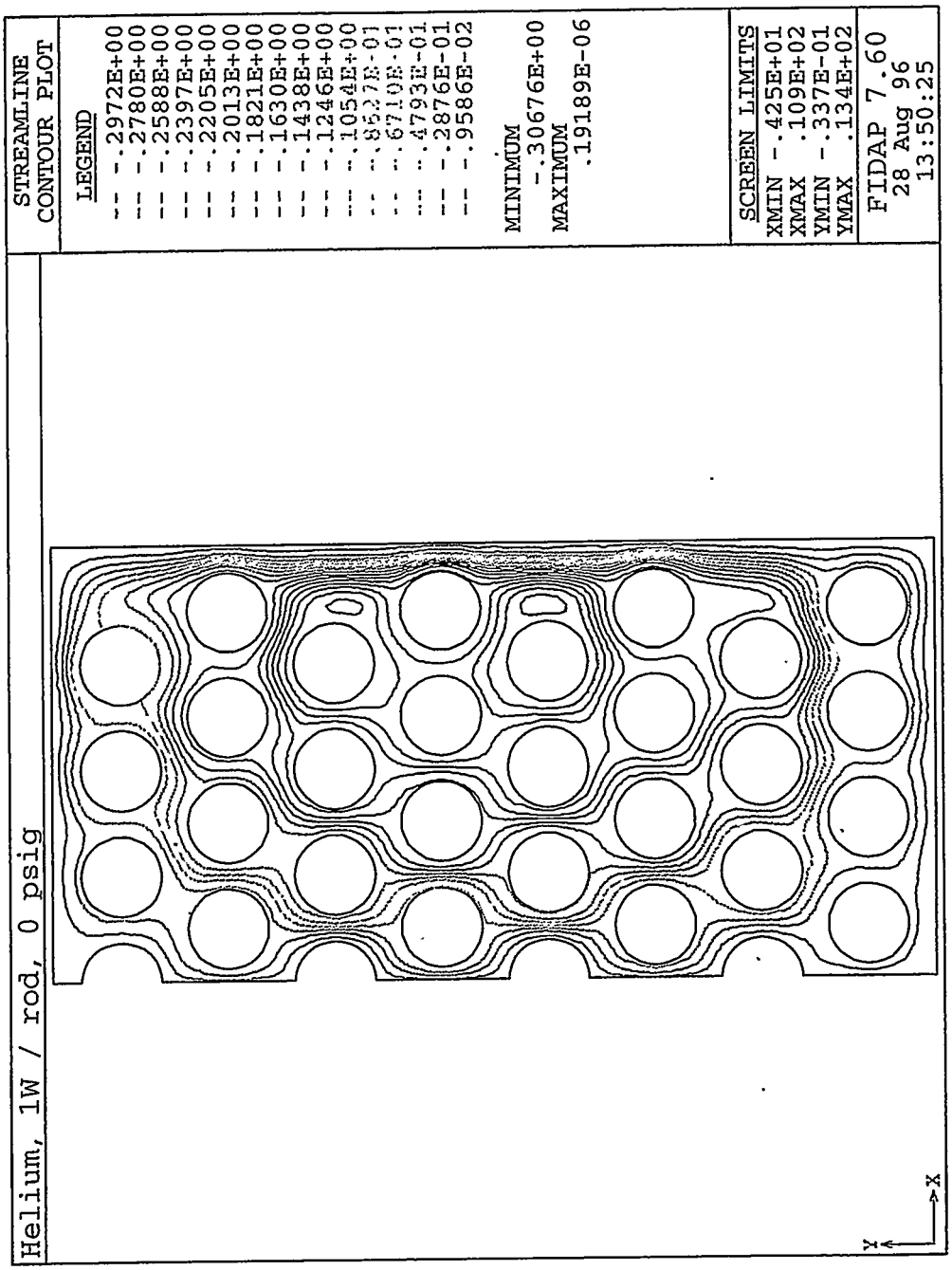

Figure 5.73 Streamlines from FIDAP simulation, $Ra_{bund} = 32{,}000$.

5.4.3 Comparison of Individual Rod Results to Canaan's Aligned Array Results

Since the UT staggered and Canaan aligned array experiments were performed in exactly the same manner, with the only difference being the change in position of roughly half of the heater rods, it is appropriate to compare the individual rod heat transfer results of each geometry. It was found that the column B through D rods had very similar characteristics, while the most notable contrasts in behavior occurred in the column A rods. Figure 5.74 gives a comparison of the geometry and rod position identities for the aligned and staggered arrays.

In the column C and D rods, the trends and the quantitative values of the Nusselt numbers are very similar. In fact, the only notable difference between the behavior of these rods for the aligned and staggered arrays is for the top row rods, rods C1 and D1. For these two rods, the conduction regime Nusselt numbers are almost identical, but the convection regime Nusselt numbers are noticeably higher for the staggered array. Figure 5.75 compares the Nusselt numbers of the aligned and staggered arrays for rod C1. Since these rods are the same distance from the cool CuBE ceiling, one would expect the conduction regime Nusselt numbers to be the same. The higher Nusselt numbers for the staggered array in the convection regime indicate that the fluid flows more strongly around C1 and D1 in the staggered array.

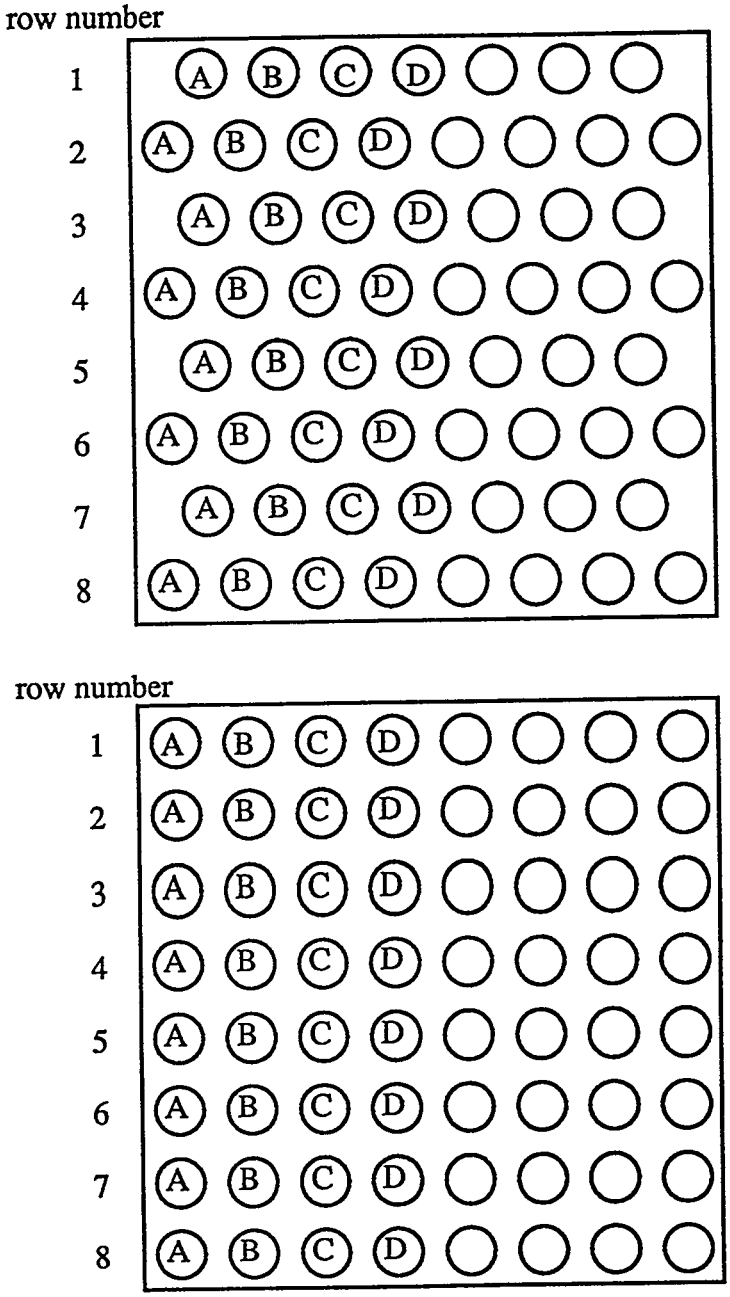

Figure 5.74 Diagram of rod positions for the UT aligned and staggered arrays.

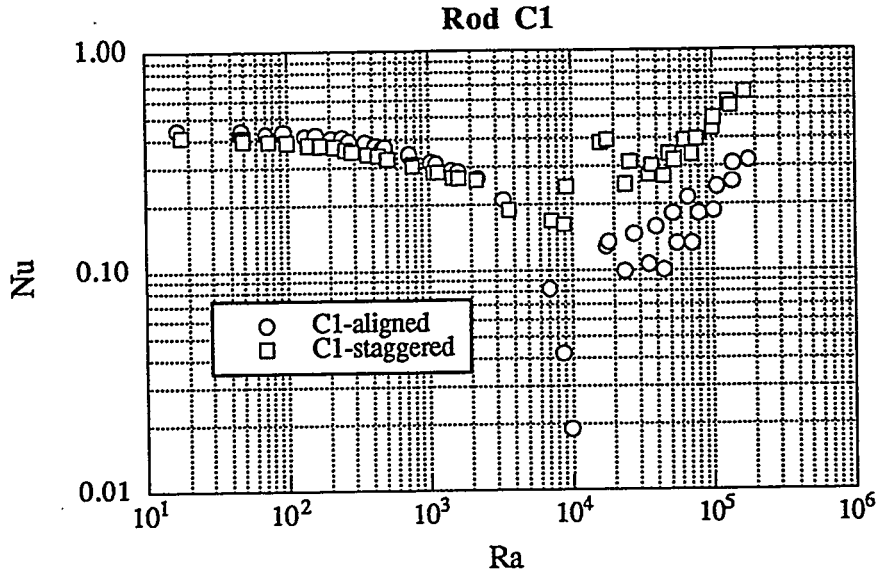

Figure 5.75 Aligned and staggered array Nusselt numbers for rod C1.

In column B, the main contrast between aligned and staggered array results is for the rods on odd-numbered rows. It is these rows where the rods are closer to the CuBE wall in the aligned array. On these odd-numbered rows, the conduction regime Nusselt number is higher for the aligned array. This is expected, since the column B, odd-numbered row rods are closer to the CuBE wall in the aligned array. However, in the conduction regime, the Nusselt numbers are about the same. For the even-numbered rows, there is no significant difference between the Nusselt numbers of each rod in the aligned and staggered arrays.

The most significant differences occur in the column A rods. For the even-numbered rows, the conduction regime Nusselt numbers are the about the same between the two arrays, while the convection regime Nusselt numbers are higher in the staggered array rods. Since rods A8, 6, 4, and 2 are the same distance from the wall in both arrays, the similarity in conduction regime Nusselt numbers is expected. As the flow in the arrays becomes stronger, the staggered array rods are cooled more effectively. Figure 5.76 compares a representative rod, A6, for each array.

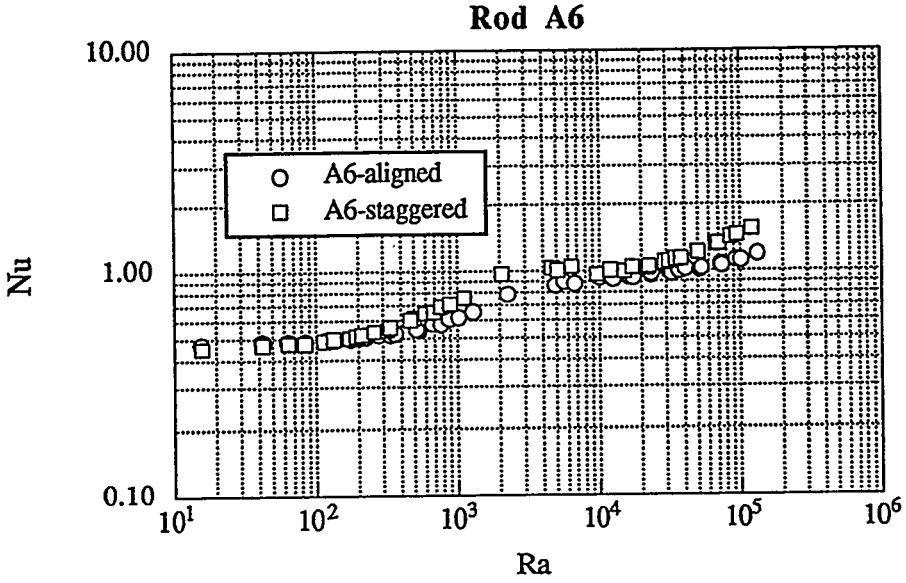

Figure 5.76 Aligned and staggered array Nusselt numbers for rod A6.

For the odd-numbered rows of column A, the aligned array has a higher conduction regime Nusselt number. This is because rods A7, 5, 3, and 1 are much farther from the cooled wall in the staggered array. Then, as the flow velocities increase, these rods are cooled more effectively in the staggered configuration. Figure 5.77 shows the Nusselt numbers of a representative rod, A7. There is a slight exception for rod A1. In this rod the convection regime Nusselt number is about the same for the staggered and aligned arrays. Figure 5.78 shows the aligned and staggered array Nusselt numbers for rod A1.

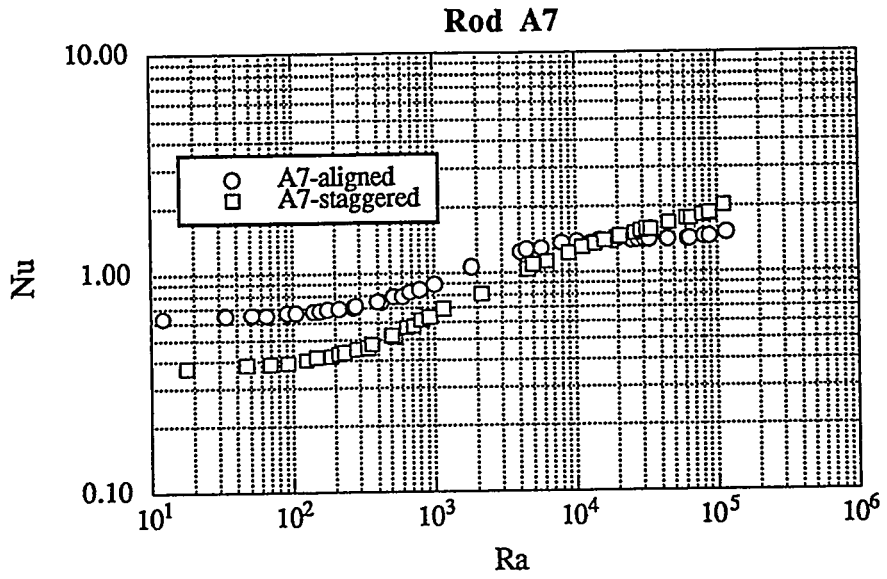

Figure 5.77 Aligned and staggered array Nusselt numbers for rod A7.

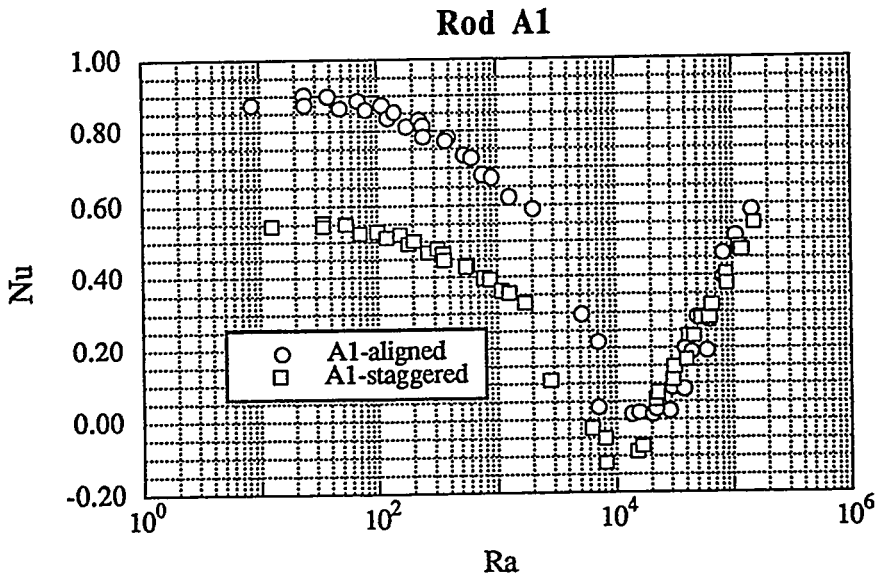

Figure 5.78 Aligned and staggered array Nusselt numbers for rod A1.

5.4.4 Comparison of Individual Rod Results to Choi and Cha's Individual Rod Results

In their 1990 flow visualization of heated, staggered tube arrays, Choi and Cha calculated individual rod Nusselt numbers for a single column of rods near the middle of the array. They compared the Nusselt numbers for each of the rods in the column to the bottom rod of the column, in order to determine the effect of preheating on each rod. They identified the bottom rod as rod 1, then numbered each subsequently higher rod as number 2, 3, 4, and 5. Their geometry and rod numbering system is shown in Figure 5.79. They calculated a Nusselt number trend for rods 1 through 5 by first calculating the Nusselt number for each rod, then dividing it by the Nusselt number for rod 1. This data is shown in Figure 5.80 for a rod pitch to diameter ratio of 2.0. Notice that as rod number increases, the preheating from rods below decreases the effectiveness of heat transfer from the rod.

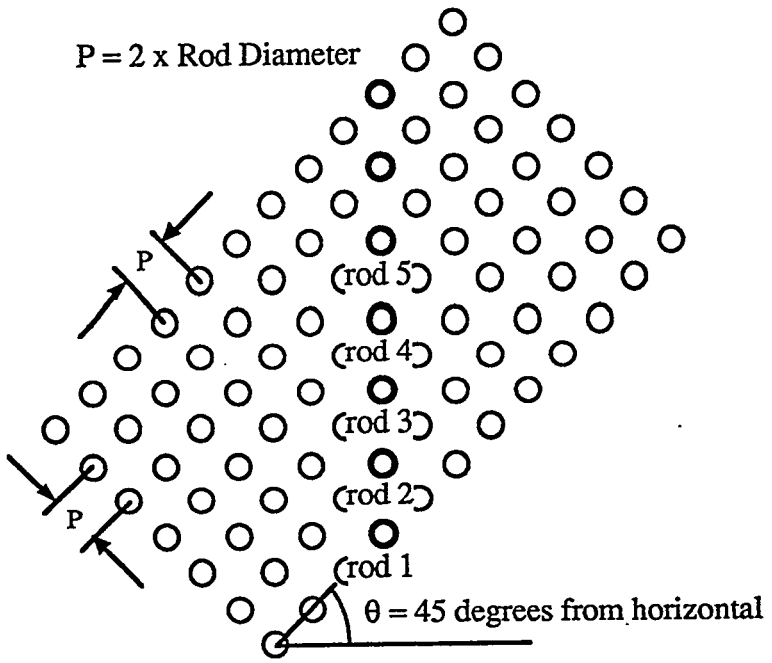

Figure 5.79 Diagram of rod positions and rod numbering within Choi and Cha's staggered array.

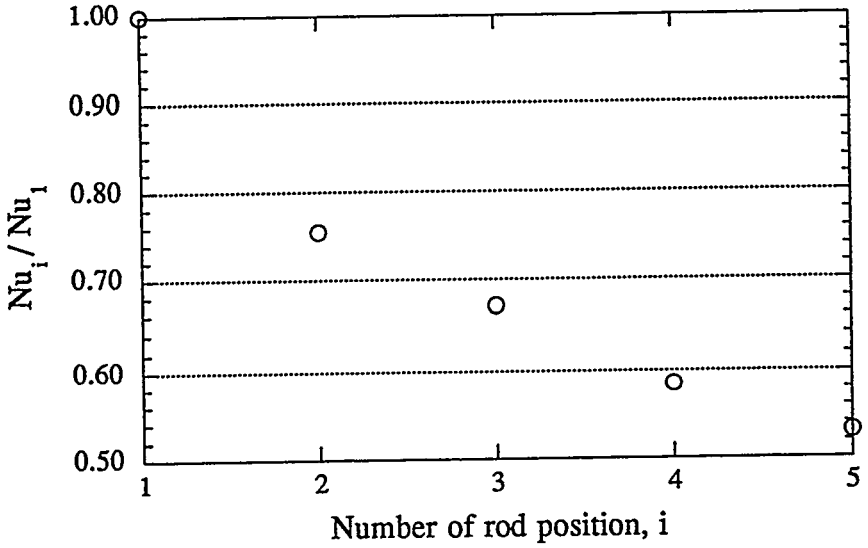

Figure 5.80 Normalized Nusselt number for rods of a single column within Choi and Cha's staggered array. P/D = 2.0.

To compare this data to the UT staggered array, consider Figure 5.81, which shows a plot of the Nusselt number for rods D8, D6, D4, and D2. Figure 5.82 shows a plot of the Nusselt number for rods D7, D5, D3, and D1. These rods are closest to the middle of the array and show the trends of a column of rods where the rods are directly above one another. Rods D8, D6, D4, and D2 form a vertical column, as do rods D7, 5, 3, and 1. In the *convection* regime, moving up from the bottom to the top rod, the Nusselt number decreases. Thus, the preheating effect is seen in both the Choi and Cha and UT staggered arrays.

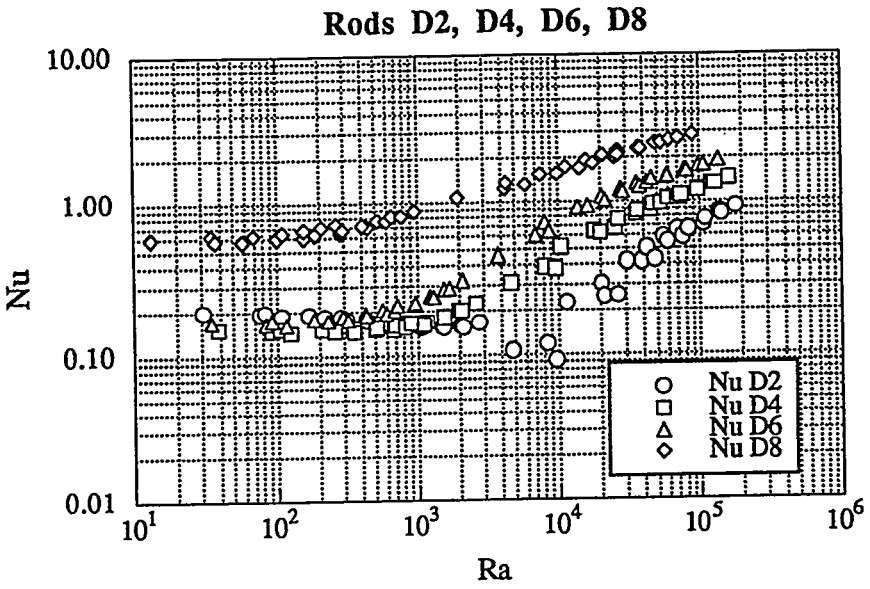

Figure 5.81 Nusselt numbers for rods D8, D6, D4, and D2.

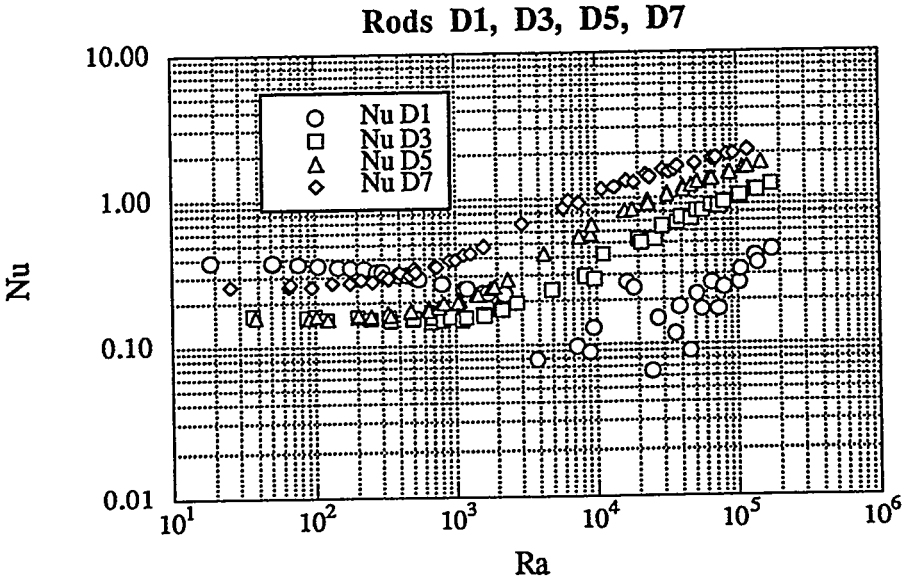

Figure 5.82 Nusselt numbers for rods D7, D5, D3, and D1.

To quantitatively compare these trends to Choi and Cha's results, the same normalized Nusselt number trend was calculated for the column D odd numbered rods and for the column D even numbered rods. Using a Rayleigh number of 50,000, which is in the mid-to-upper convection regime for most of the rods, the rod correlations were used to calculate Nusselt numbers. For the odd numbered rods, rod D7 was considered to be the bottom rod (numbered as rod 1), and rods D5, D3, and D1 were numbered as rods 2, 3, and 4, according to Choi and Cha's convention. For the even numbered rods, rod D8 was the bottom rod, and rods D6, D4, and D2 were labeled as rods 2, 3, and 4. The final comparison of these trends is shown in Figure 5.83.

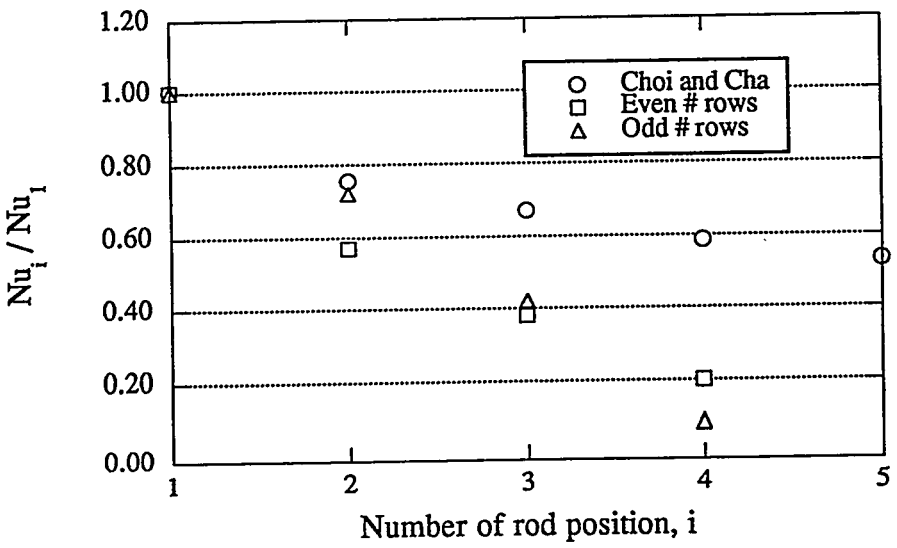

Figure 5.83 Comparison of normalized Nusselt number trends for the UT staggered and Choi and Cha staggered arrays.

The main result from this comparison is that as one moves from the bottom rod toward the top of the array, the Nusselt number drops off much more rapidly for the UT staggered array than for the Choi and Cha array. There are two main reasons for this difference.

First, the Choi and Cha array is not enclosed. This allows the plumes of each rod to form much more freely than in an enclosure. If the plumes of lower rods can develop freely, then they can increase the flow velocity around the upper rods, which tends to increase the Nusselt number of the upper rods. However, a competing effect is that the lower rods cause hotter air to flow past the upper rods, which effectively reduces the temperature difference between the rod surface and the local ambient fluid. For the rod spacings of the Choi and Cha and the UT experiments, the results of Sparrow and Niethammer state that this preheating effect is stronger, and thus the overall tendency is for the Nusselt numbers of the upper rods to be reduced. In the UT staggered array, the enclosure impedes upward moving fluid from increasing its velocity as it flows around the upper rods. Thus, while the same two competing effects seen in the Choi and Cha array also exist within the UT rod array, the preheating effect dominates in the UT array. This is the reason why the Nusselt numbers decrease so much more in the UT staggered array than in the Choi and Cha array.

Second, there is a major difference between the spacing of rods in the two staggered array configurations, as seen in Figure 5.84. In the Choi and Cha array, constructed by rotating a square array, the vertical distance between rods of a column is the square root of 2 times 2 rod diameters, or about 2.8 diameters. The horizontal distance between two rods on the same row is also 2.8 diameters. By contrast, the UT staggered array has a vertical distance of 2.64 diameters between rods directly above each other, but only a distance of 1.32 diameters between rods on the same row. To impinge on the rod directly above it, fluid from a heated rod must pass through a gap between the two rods diagonally above the heated rod to get to the rod directly above it. In the UT staggered array, this gap is much smaller than in the Choi and Cha array.

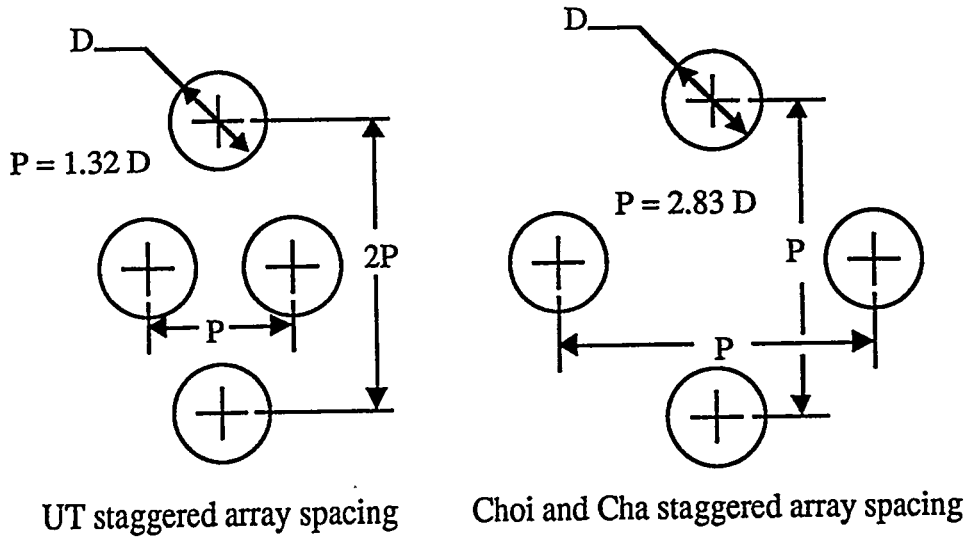

Figure 5.84 Difference between UT staggered array spacing and Choi and Cha's staggered array spacing.

This means that the UT staggered array has two independent differences between itself and the Choi and Cha array that cause upward buoyant flow to be hindered more in the UT array--the enclosure and the tighter rod spacing. Since hindering the flow prevents the cooling effect of forcing flow past the upper rods, but does not hinder the preheating effect of the lower rods on the upper rods, it is expected that the ratio $Nu_{upper\ rods} / Nu_{bottom\ rod}$ would be much lower in the UT staggered array.

5.5 SUMMARY

This chapter has presented and discussed the results of the UT experimental investigation of heat transfer in an enclosed, staggered array of heated, horizontally-oriented cylinders. The most important results from this experiment are summarized below.

Important general trends for the rod bundle

- For a given rod power and pressure state point, both the average and the maximum rod temperature difference are higher for a nitrogen than for a helium backfill. This is due to helium's higher thermal conductivity.

- For a constant rod power, increasing the pressure of the backfill gas increases the overall full array Rayleigh number. This decreases both the maximum rod surface temperature and the average rod surface temperature, relative to the CuBE temperature. This change in temperature is much larger for the nitrogen backfill than for the helium backfill. This is attributed to the fact that most of the helium data lies in a conduction regime, while most of the nitrogen data lies in a convection regime.

- For a constant backfill gas pressure, increasing the rod power increases both the maximum and average rod surface temperatures, relative to the CuBE temperature.

- For a given rod power, increasing the system pressure decreases the percent of total heat transferred by radiation. This change is much larger for the nitrogen backfill. For a given system pressure, increasing the rod power increases the percent radiation. In general, the percentage of total heat transferred by radiation is about 14 to 16 percent for the helium backfill, and is about 23 to 46 percent for the nitrogen backfill. However, these percentages are dependent upon the specific temperature ranges of this

experiment, and might not be the same for, say, a much hotter enclosure temperature.

- The location of the hottest rod in the bundle shifts upward from row 4 to row 3, and then again to row 2, as the full array Rayleigh number is increased.

Important results from the full array heat transfer correlations

- The full array correlations exhibit a two-regime behavior that is similar to the Rayleigh-Benard problem. These two regimes are characterized by a conduction regime, in which the Nusselt number increases slightly with increasing Rayleigh number, and a convection regime, in which the Nusselt number increases more dramatically with increasing Rayleigh number. The conduction regime is comprised mostly of helium backfill data, while the convection regime is comprised mostly of nitrogen backfill data.

- The slope of the Nusselt number curve in the convection regime suggests that flow is turbulent within the bundle.

- The Nusselt numbers for the UT staggered array are lower than Canaan's aligned array Nusselt numbers in the conduction regime. However, the Nusselt number increases more sharply for the staggered array in the convection regime, and the staggered array Nusselt number becomes greater than the aligned array Nusselt number at high Rayleigh numbers.

- As supported by a FIDAP numerical conduction simulation, the reason for the staggered array having lower Nusselt numbers than the aligned array at low Rayleigh numbers is because the aligned array has several more rods in the array that lie very close to the cooled side wall of the enclosure. This effect increases the temperature gradients at the side wall, and more effectively transfers heat from these rods to the wall.

- One cannot automatically assume that a staggered array has higher overall heat transfer coefficients than an aligned array for natural convection within an enclosure. Depending on the flow regime, the rod spacing, and the proximity of the enclosure to the rod bundle, it is possible for an aligned array to have more effective heat transfer.

- The nature of natural convection within an enclosed rod bundle is fundamentally different from natural convection within a non-enclosed rod bundle. The enclosure limits formation of buoyant plumes from each rod. Also, the flow behavior for natural convection within an enclosed rod bundle is much different from forced convection through a rod bundle.

Important results from the individual rod heat transfer correlations

- Rods in the lower-middle of the array tend to display the same two-regime heat transfer behavior as seen in the full array results.

- For the convection regime, rods in the upper part of the array have lower Nusselt numbers than rods in the lower part. This is because the lower rods tend to preheat the fluid that surrounds the upper row rods. This effect, coupled with the author's definition of the characteristic temperature difference, ΔT, causes some unusual Nusselt number trends for the upper row rods. Most upper row rods show a Nusselt number that decreases with increasing Rayleigh number in some regimes, and some rods (A1 and B1) even exhibit negative Nusselt numbers in a particular regime. However, these effects do not actually indicate local flow conditions, but rather describe the behavior of the rod temperature relative to the CuBE temperature.

- The bottom corner rod (A8), surprisingly, was not the coldest rod in the array at higher Rayleigh numbers. Instead, rod B8 had the lowest temperature in the convection regime. It is speculated that this effect is caused by a change in the array flow pattern at higher Rayleigh numbers that

causes the downward-moving cool fluid to drive inward and "cut the corner," thus impinging more forcefully on rod B8.

- Comparing the UT staggered array results to Canaan's aligned array shows many similarities in the Nusselt number behavior of individual rods. In general, rods that are in the same position in both arrays demonstrate very similar behavior. Rods that are slightly closer to the cooled wall yield slightly higher Nusselt numbers in the conduction regime. In the convection regime, individual rods in the staggered array tend to have slightly higher Nusselt numbers than in the aligned array.

- The decrease in Nusselt number for the UT staggered array in the conduction regime from the bottom row to the top row is much greater than the similar decrease for rods in the Choi and Cha staggered array. This is attributed to Choi and Cha's lack of a cooled enclosure around the rod bundle and a wider rod spacing within Choi and Cha's array.

Chapter 6 -- Conclusions and Recommendations

This thesis has presented the results of an experimental investigation of natural convection heat transfer for a staggered array of heated cylinders, oriented horizontally within a rectangular enclosure. While applications of this research include electronic component cooling and immersion heat exchangers, the main purpose of this research was to extend the knowledge of heat transfer within enclosed bundles of spent nuclear fuel rods sealed within a shipping or storage container. This research extends Canaan's investigation of an *aligned* array of heated cylinders that simulate a spent BWR fuel assembly.

The heated rod array was comprised of tubular stainless steel heater rods with a resistance heating element running along the center of each rod. A rectangular, water-cooled copper box supported the rods and provided an isothermal heat sink. The rod ends were insulated to minimize axial temperature variations and allow a two-dimensional heat transfer analysis of the rod bundle. Detailed spatial characterization of the rod bundle was obtained by measuring the rod surface temperature with embedded thermocouples placed within the cladding of each rod. Thorough thermal characterization of the staggered rod array was performed by filling the array with two different backfill gases, nitrogen and helium, and by varying the pressure within the array ~~from 0 to 60 psig~~. The heater rod power input was about the same for each rod, and was varied between 1 and 5 watts per rod.

Nusselt and Rayleigh numbers were calculated both for each individual rod in the array and for the full array. Calculation of these dimensionless numbers required the calculation of the net radiative heat rate from each rod, so that the convection correlations would be based only on the convective heat rate from the rods. The radiative power from each rod was calculated using a finite-element formulation that solved the radiative transport equation (assuming diffuse-gray surfaces and non-participating media) for small, discretized elements on each rod. The radiative heat rate was then subtracted from the rod power input to obtain the

convective power. The results were presented in piecewise correlations of the form $Nu = C(Ra)^n$, where C and n are constants.

6.1 CONCLUSIONS

The results of this analysis showed several trends. These trends were grouped into three types: general temperature and heat transfer trends, full array Nusselt and Rayleigh number trends, and individual rod Nusselt and Rayleigh numbers trends.

In general, increasing the system pressure at constant rod input power reduced the maximum rod temperature and the bundle-averaged temperature. The decrease in temperature was more dramatic for the nitrogen backfill than for the helium backfill. For a given system pressure, increasing the rod input power increased both the maximum and the average rod temperature. For a given rod power and pressure state point, the nitrogen backfill always had a higher maximum and average rod temperature than the helium backfill. This is because helium has a higher thermal conductivity, which reduces the resistance to heat flow from the rods to the cooled enclosure wall.

For a given rod power, increasing the system pressure decreased the percentage of total heat transferred by radiation, thus increasing the heat transferred by convection. This percentage radiation decrease was more dramatic for the nitrogen backfill than for the helium backfill. Also, the percentage of total heat transferred by radiation was much higher for the nitrogen cases than for the helium cases. For the nitrogen cases, the percent radiation varied between 23 and 46 percent, whereas this value was between 14 and 16 percent for the helium cases. These percentages are only valid for the range of enclosure temperatures measured for this experiment, and cannot be applied to higher enclosure temperatures.

The location of the rod with the highest temperature shifted upward from the fourth row to the second row of rods as the system Rayleigh number was increased. This is due to the increased buoyancy forces that occur within the rod bundle when the rod power and the system pressure is increased.

For the full array, the Nusselt-Rayleigh number results showed a definite two-regime trend within the bundle, characterized by a conduction regime, which consisted mostly of helium data, and a convection regime, which consisted mostly of the nitrogen data. This two-regime trend is reminiscent of the results of the Rayleigh-Benard convection problem. The dependence of Nusselt number on ΔT to the one-third power suggested that the flow in the convection regime was turbulent.

In the conduction regime, the staggered array had a lower bundle Nusselt number than Canaan's aligned array. A numerical conduction simulation showed that this result was due to the aligned array having a less resistant conduction path to the cooled side walls of the enclosure than did the staggered array. In the convection regime, the staggered array had a slightly higher bundle Nusselt number, probably due to the staggered array's increased space for each rod to form its buoyant plume.

In most experiments on non-enclosed rod bundles, the staggered array always has a higher bundle Nusselt number than the aligned array. However, one cannot assume that this is the case for an enclosed array. The flow regime of the fluid and the geometry of the conduction path between the rods and the enclosure must be considered before the effectiveness of heat transfer for an aligned versus a staggered array is compared.

Natural convection in a staggered rod bundle within an enclosure is fundamentally different from natural convection within a non-enclosed staggered rod bundle. The enclosure limits formation of buoyant plumes from each rod, while in an open rod bundle, buoyant plumes can more easily form from each rod. Also, the flow behavior for natural convection within an enclosed rod bundle is much different from forced convection flow through a rod bundle.

For the individual rods, the rods in the upper half of the array are warmed by the upward-moving plumes from rods lower in the array. Thus, rods higher up in the array tend to have lower Nusselt numbers than rods in the lower half of the array. Also, the lower-row rods with higher Nusselt numbers tend to display a two-regime conduction / convection trend that is similar to the two-regime trend seen in the full array Nusselt-Rayleigh data.

A couple of top row rods actually had negative Nusselt numbers in some Rayleigh number regimes. This is because the Nusselt number's characteristic temperature difference was defined between the rod surface and the wall temperature, not between the rod surface and the fluid immediately surrounding the rod. This means that these rods with negative Nusselt numbers actually had local fluid surrounding them that was hotter than the rod surface, yet the rod surface was still hotter than the CuBE wall. This means that, for those particular rods, the radiative power away from the rod surfaces was greater than the power input to those rods.

The rod in the lower corner (A8) was, surprisingly, not always the coldest rod in the array. For higher Rayleigh numbers, the bottom row rod next to the corner rod (B8) was the coldest rod. This effect is most likely caused by the downward flow of cooled fluid along the enclosure side wall "rounding the corner" and impinging more forcefully on the inner rod than on the corner rod.

6.2 Recommendations For Future Work

The effect of the enclosure position on the bundle heat transfer behavior should be quantified. Given a specific rod bundle, a series of experiments could be conducted, varying the enclosure distance from the bundle. A study of this type could quantify a threshold distance beyond which the rod bundle behaves as if it were not enclosed.

The effect of varying the pitch-to-diameter ratio of the rods within the enclosure could be investigated. By studying the heat transfer within enclosed rod bundles of various numbers and spacings of rods, perhaps a new length scale could be found that collapses all of the rod bundle correlations into a more universal correlation. Since a few studies have already been done on rod bundles with fewer rods than the UT rod arrays, perhaps more studies could be performed on rod bundles with greater numbers of rods. For example, an experimental investigation of a 17x17 array would allow the characterization of a typical PWR spent fuel assembly.

A numerical study should be performed to investigate the flow patterns within the rod bundle. This study could use experimentally measured temperatures as input boundary conditions, so that radiation would not need to be modeled within the array. However, the model should include the ability to handle turbulent flow in the higher Rayleigh number regimes. Alternatively, a more complex numerical study could "go all out" and model both convection with turbulence and radiation between the surfaces. This code could model many more complex geometries without the expense of building new rod bundles and enclosures. This code could also be benchmarked by comparing the results for a known geometry (say, the geometry of this thesis) to the code results.

Flow visualization studies should be performed on the enclosed rod bundle. Some techniques that should be considered are photographic techniques such as Mach-Zehnder interferometry, laser Doppler velocimetry, or particle image velocimetry. It would be a challenge to perform flow visualization at above or below atmospheric pressure, because either a transparent window is needed on the pressure vessel or the flow visualization equipment must fit inside of the pressure vessel. Even then, it is still difficult to effectively see into the array, because the support plates or grids used to support the rods would obstruct the view. However, higher rod powers could be used at atmospheric pressure to obtain the higher Rayleigh number data at atmospheric pressure.

Appendix -- RADERA II Code Listing

This appendix contains the listing of the FORTRAN code used to calculate net radiative heat transfer rate of each of the 60 rods of the UT staggered array experiment, given the geometry of the rods, the rod and enclosure surface temperatures, and the rod and enclosure surface emissivities.

RADERA II uses the following input files:

"sysmem.blk" This file contains the anticipated memory requirements and array variable dimensioning commands. An example of this small file is given below.

```
parameter (maxnd= 1681, maxelm= 840, maxbc= 33, maxsrf= 64)
parameter (maxnz= maxnd*maxnd)
```

"shdw.dat" This file (see example on following pages) contains the location of the center of each rod in the array, as well as each rod's radius.

"in" This file (see example on following pages) contains the all of the rod and wall temperature data, as well as the surface emissivity data. The size of the enclosure, as well as the number of elements that the rods and the walls are divided up into are also specified.

RADERA II produces the following output files:

"run"	This file is a run-time message file that contains iteration and solution convergence information.
"view.dat"	This is the view, or configuration factor file. If a flag within the input file "in" is set to zero, then this file is created when the code runs. If the flag in the input file is set to 1, then this file is read as a previously created file. Much of the running time of the entire code goes into creating this file.
"out"	This file (see example on following pages) contains the calculated net radiative heat rate for each rod, presented in W/cm. This file also calculates the heat balance error for the particular case.

Example listings of the "shdw.dat" and the input and output files are presented for the case of a nitrogen backfill, 5 W / rod power setting, at a vessel pressure of 60 psig. The RADERA II code listing follows these three example files.

Sample file "shdw.dat"

```
Triangular pitch array, RADERAII input
c  number of rods
    32
c    x position     y position     rod radius
     1  C
  0.8100000d+00  1.0330000d+00  0.6135000d+00
     2  C
  2.4300000d+00  1.0330000d+00  0.6135000d+00
     3  C
  4.0500000d+00  1.0330000d+00  0.6135000d+00
     4  C
  5.6700000d+00  1.0330000d+00  0.6135000d+00
     5  C
  0.0000000d+00  2.6530000d+00  0.6135000d+00
     6  C
  1.6200000d+00  2.6530000d+00  0.6135000d+00
     7  C
  3.2400000d+00  2.6530000d+00  0.6135000d+00
     8  C
  4.8600000d+00  2.6530000d+00  0.6135000d+00
     9  C
  0.8100000d+00  4.2730000d+00  0.6135000d+00
    10  C
  2.4300000d+00  4.2730000d+00  0.6135000d+00
    11  C
  4.0500000d+00  4.2730000d+00  0.6135000d+00
    12  C
  5.6700000d+00  4.2730000d+00  0.6135000d+00
    13  C
  0.0000000d+00  5.8930000d+00  0.6135000d+00
    14  C
  1.6200000d+00  5.8930000d+00  0.6135000d+00
    15  C
  3.2400000d+00  5.8930000d+00  0.6135000d+00
    16  C
  4.8600000d+00  5.8930000d+00  0.6135000d+00
    17  C
  0.8100000d+00  7.5130000d+00  0.6135000d+00
    18  C
  2.4300000d+00  7.5130000d+00  0.6135000d+00
    19  C
  4.0500000d+00  7.5130000d+00  0.6135000d+00
    20  C
  5.6700000d+00  7.5130000d+00  0.6135000d+00
    21  C
  0.0000000d+00  9.1330000d+00  0.6135000d+00
    22  C
  1.6200000d+00  9.1330000d+00  0.6135000d+00
    23  C
  3.2400000d+00  9.1330000d+00  0.6135000d+00
```

```
 24  C
4.8600000d+00  9.1330000d+00  0.6135000d+00
 25  C
0.8100000d+00  1.0753000d+01  0.6135000d+00
 26  C
2.4300000d+00  1.0753000d+01  0.6135000d+00
 27  C
4.0500000d+00  1.0753000d+01  0.6135000d+00
 28  C
5.6700000d+00  1.0753000d+01  0.6135000d+00
 29  C
0.0000000d+00  1.2373000d+01  0.6135000d+00
 30  C
1.6200000d+00  1.2373000d+01  0.6135000d+00
 31  C
3.2400000d+00  1.2373000d+01  0.6135000d+00
 32  C
4.8600000d+00  1.2373000d+01  0.6135000d+00
```

Sample input file "in" for nitrogen, 5W / rod, 60 psig case

```
  Input file from Eric Triplett's staggered assembly

 8.0000000d-01  Uniform surface emissivity
 5.6700000d-12  Stefan-Boltzmann constant [w/cm^2K^4]

            1  Shape factor file flag

           20  Number of elements per rod (must be even)
          200  Number of elements on walls (must be even)
13.406000d+00  Height of enclosure (cm)

           33  Number of isothermal surfaces
43.680000d+00  rod 1 (left to right, bottom to top in deg. C)
41.330000d+00  rod 2
41.140000d+00  rod 3
44.430000d+00  rod 4
52.730000d+00  rod 5
52.300000d+00  rod 6
51.380000d+00  rod 7
50.410000d+00  rod 8
58.600000d+00  rod 9
58.640000d+00  rod 10
57.270000d+00  rod 11
53.260000d+00  rod 12
63.380000d+00  rod 13
63.560000d+00  rod 14
63.800000d+00  rod 15
60.930000d+00  rod 16
68.990000d+00  rod 17
67.470000d+00  rod 18
68.460000d+00  rod 19
62.300000d+00  rod 20
74.240000d+00  rod 21
72.500000d+00  rod 22
73.060000d+00  rod 23
69.580000d+00  rod 24
77.850000d+00  rod 25
75.130000d+00  rod 26
73.690000d+00  rod 27
63.160000d+00  rod 28
75.230000d+00  rod 29
71.930000d+00  rod 30
67.880000d+00  rod 31
64.620000d+00  rod 32
22.120000d+00  Assembly walls
```

Sample output file "out" for nitrogen, 5W / rod, 60 psig case

```
Net radiative heat rate, qnet=     0.41583439518434
estimated error=    -0.13762944908109 (% of qnet)
```

Surface	T	Heat Rate
1	43.68	0.70558E-02
2	41.33	0.29728E-02
3	41.14	0.54448E-02
4	44.43	0.22605E-01
5	52.73	0.20729E-02
6	52.30	0.38852E-02
7	51.38	0.40011E-02
8	50.41	0.14113E-01
9	58.60	0.17136E-02
10	58.64	0.35631E-02
11	57.27	0.86485E-02
12	53.26	0.20948E-01
13	63.38	-0.57813E-04
14	63.56	0.10024E-02
15	63.80	0.51080E-02
16	60.93	0.17023E-01
17	68.99	0.24131E-02
18	67.47	0.10826E-04
19	68.46	0.15067E-01
20	62.30	0.29059E-01
21	74.24	0.29187E-02
22	72.50	0.18059E-02
23	73.06	0.97607E-02
24	69.58	0.25761E-01
25	77.85	0.16409E-01
26	75.13	0.13110E-01
27	73.69	0.25563E-01
28	63.16	0.31063E-01
29	75.23	0.20353E-01
30	71.93	0.33177E-01
31	67.88	0.28326E-01
32	64.62	0.40593E-01
33	22.12	-0.41606E+00

```
c=======================================================================
c=======================================================================

                        program RADERAII

c=======================================================================
c=======================================================================

c     The RADERA II program calculates the radiative exchange within an
c     array of isothermal rods enclosed by an isothermal, square
c     enclosure.  The number, position, and radius of each of the rods
c     is specified on input.

c     The RADERA II program makes the following assumptions:
c           1)    The enclosure is symmetric about the vertical mid-plane
c           2)    All the surfaces, including the wall, have the
c                 same emissivity
c           3)    The emissivity is constant
c           4)    All surfaces are gray and diffuse

c     The RADERA II program includes an internal mesh generator which
c     paves the rods and walls with second order (three node) bar elements.
c     The mesh generator ensures that all elements are constructed according
c     to the appropriate righ hand rule but it does not insure that the
c     rods are contained within the enclosure.

c     IT IS THE USERS RESPONSIBILITY TO INSURE THAT THE INPUT IS
c     CONSISTENT AND THAT ALL OF THE RODS ACTUALLY FIT WITHIN THE
c     CONFINES OF THE ENCLOSURE WALL!

c     REQUIRED FILES:

c     the RADERA II program requires three (3) additional data files
c     in order to operate correctly:

c     sysmem.blk - Contains the FORTRAN parameter statement which
c                  sets the memory allocation.

c     shdw.dat - Contains the number, centerpoint, and radius of each
c                of the rods in the enclosure.  It is only necessary to
c                specify the rods in the right hand side of the array.  The
c                left hand side is constructed from symmetry (see
c                assumption 1).

c     in - Contains the mesh generation data, emissivity, Stefan-
c               Boltzmann constant, and the temperatures of each of the
c               rods in the array and the wall temperature.

c               THE WALL TEMPERATURE IS ALWAYS SPECIFIED LAST!

c               THE ROD TEMPERATURES MUST BE SPECIFIED IN THE SAME ORDER
c               AS IN THE shdw.dat FILE!
c
c=======================================================================
```

```
c     memory allocation

c     maxelm - Maximum number of elements
c     maxnd - maximum number of nodes
c     maxbc - maximum number of surfaces
c     maxsrf - Maximum number of potentially shadowing surfaces
c     maxnz - Maximum number of nonzero configuration factors
c             maxnd**2

c     common storage

c     /GLint/ - Gauss Legendre integration rule

c     xint(3) - master element coordinate of integration point i
c     w(3) - Integration weight for point i
c     Nl - Number of integration points

c     /head/ - Character neutral file tile info
c       title*80 - Neutral file title
c       date*12 - date neutral file was created
c       time*8 - Time neutral file was created
c       vers*12 - PATRAN version number used to create neutral file
c       srftp(maxsrf)*1 - Shadowing surface type, circle - 'c',
c                         line - 'l'

c     /icntrl/ - Integer control parameters

c     itp4 - Runtime message file (run)
c     itp5 - not used
c     itp6 - emissivity and temperature input file (in.dat)
c     itp7 - Shape factor storage file (view.dat)
c     itp8 - not used
c     itp9 - Integrated surface heat flux file (out)
c     itp10 - Shadow surface data file (shdw.dat)
c     iparam(20) - Integer control parameters
c       i= 1 - Shape factor storage file flag

c     /mesh/ - Finite element mesh information

c     Ne(maxelm) - Number of nodes in element i
c     inde(maxelm, 3) - Node numbers in element i
c     Nnd - Number of nodes
c     Nelem - Number of elements
c     Nbc - Number of isothermal surfaces
c     Nsrf - Number of potentially shadowing surfaces
c     Nnzr - The number of nonzero viewfactors which are stored
c     ide(maxelm) - PATRAN id number for element i
c     idn(maxnd) - PATRAN id number for node i
c     idbc(maxelm) - Boundary condition applied to element i
c     jcoef(maxnz, 2) - Index pointers for viewfactor storage

c     /mtrl/ - Material properties

c     emsvty - Uniform emissivity
c     sb - Stefan Boltzmann constant

c     /rmesh/ - Real mesh information
```

```
c     xnd(maxnd, 2) - x,y coordinates of node i
c     T(maxbc) - Temperature of each surface
c     Tn(maxnd) - Nodal temperatures
c     srfdat(maxsrf, 4) - Shadowing surface data

c     /shpfac/ - Shape factors

c     Ex(maxnz), Ey(maxnz) - x, y coordinate emission configuration
c                            factors
c     Rxx(maxnz), Rxy(maxnz), Ryx(maxnz), Ryy(maxnz) - Reflection
c                            tensor

c     /solu/ - Principal solution
c       qr(maxnd, 2) - Incident radiative flux vector components at
c                      node i
c       qout(maxbc) - Net integrated radiative heat flux leaving
c                     each surface
c       err - Estimated percent error in total integrated heat flux
c       qnet - Net heat flux

c     /work/ - workspace
c       wi(maxnd) - Workspace vectors

c
```

```
      implicit double precision (a-h, o-z)
      include 'sysmem.blk'
      character title*80, date*12, time*8, vers*12, srftp(maxsrf)*1

      common /head/ title, date, time, vers, srftp
      common /icntrl/ itp4, itp5, itp6, itp7, itp8, itp9, itp10,
     #                iparam(20)
      common /mesh/ Ne(maxelm), inde(maxelm, 3), Nnd, Nelem, Nbc,
     #              ide(maxelm), idn(maxnd), idbc(maxelm), Nsrf,
     #              Nnzr, jcoef(maxnz, 2), ner, new
      common /rmesh/ xnd(maxnd, 2), T(maxbc), Tn(maxnd),
     #               srfdat(maxsrf, 4), tol, hwall
      common /mtrl/ emsvty, sb
      common /GLint/ xint(8), w(8), Nl
      common /shpfac/ Ex(maxnz), Ey(maxnz), Rxx(maxnz), Rxy(maxnz),
     #                Ryx(maxnz), Ryy(maxnz)
      common /solu/ qr(maxnd, 2), qout(maxbc), err, qnet
      common /work/ w1(maxnd), w2(maxnd)

      dimension xc(2)

c     Initialize memory

      call init

c     Read emissivity and temperature data

      write (itp4, *) 'Reading temperatures and emissivity'
      call rprob
```

```
c     read shadow surface data

      write (itp4, *) 'Reading shadow surface description'
      call rshdw

c     set up mesh

      call mshwl (itp4, new, hwall, nnd, nelem,
     #            ne, inde, xnd)

c     set boundary condition flag

      do 10 i= 1, nelem
 10     idbc(i)= Nbc

c     mesh the rods in the right side of the enclosure

      do 20 i= 1, nsrf
        xc(1)= srfdat(i, 1)
        xc(2)= srfdat(i, 2)
        r= srfdat(i, 3)
        call mshrd (itp4, xc, r, ner, xnd, ne, inde, nnd,
     #              nelem, i, idbc)

 20   continue

c     reflect shadowing surfaces to left side of array

      nnr= 0
      do 30 isrf= 1, nsrf

c       don't reflect rods on the centerline

        if (srfdat(isrf, 1).ne.0.000d+00) then
          nnr= nnr+1
          srfdat(nsrf+nnr, 1)= -srfdat(isrf, 1)
          srfdat(nsrf+nnr, 2)= srfdat(isrf, 2)
          srfdat(nsrf+nnr, 3)= srfdat(isrf, 3)
        end if

 30   continue
      nsrf= nsrf + nnr

c     set node and element id numbers

      do 40 i= 1, nnd
 40     idn(i)= i
      do 50 i= 1, nelem
 50     ide(i)= i
```

```
c     Evaluate shape factors

      if (iparam(1).ne.1) then

        write (itp4, *) 'Calculating shape factors'
        call config

        call store

      else

        write (itp4, *) 'Reading shape factors'
        call store

      end if

c     Evaluate incident radiative flux at each node

      write (itp4, *) 'Evaluating incident radiative flux'
      call proc

c     Integrate net radiative flux leaving each rod

      write (itp4, *) 'Integrating net radiative heat flux'
      call post

c     write results

      write (itp4, *) 'Printing results'
      call wres

      write (itp4, *) 'Execution complete'
      write (itp4, *) 'Have a nice day'

      stop
      end
```

```
c ============================================================

      subroutine config

c ============================================================

c     Calculates the configuration factors for direct surface
c     emission and surface reflaction between each node in the
c     mesh

c ============================================================
```

```
      implicit double precision (a-h, o-z)

      include 'sysmem.blk'

      common /mesh/ Ne(maxelm), inde(maxelm, 3), Nnd, Nelem, Nbc,
     #              ide(maxelm), idn(maxnd), idbc(maxelm), Nsrf,
     #              Nnzr, jcoef(maxnz, 2), ner, new
      common /shpfac/ Ex(maxnz), Ey(maxnz), Rxx(maxnz), Rxy(maxnz),
     #                Ryx(maxnz), Ryy(maxnz)

      dimension esinte(3, 2), esintr(3, 2, 2)

      Nnzr= 0

c     Loop through each node in the mesh

      do 30 i= 1, Nnd

c       set pointer for Nnzr(i)

        Nnzri= Nnzr + 1

c       loop through each element in the mesh

        do 30 j= 1, Nelem

c         calculate elemental contribution

          call sint (j, i, esinte, esintr, istore)

c         assemble elemental contribution if contribution is not 0

          if (istore.eq.1) then

            do 20 jn= 1, Ne(j)

c             find correct storage location

              ifndk= 0

              do 10 k= Nnzri, Nnzr

                if ((jcoef(k, 1).eq.i) .and.
     #              (jcoef(k, 2).eq.inde(j, jn))) then

                  ifndk= 1

                  Ex(k)= Ex(k) + esinte(jn, 1)
                  Ey(k)= Ey(k) + esinte(jn, 2)
                  Rxx(k)= Rxx(k) + esintr(jn, 1, 1)
                  Rxy(k)= Rxy(k) + esintr(jn, 1, 2)
                  Ryx(k)= Ryx(k) + esintr(jn, 2, 1)
                  Ryy(k)= Ryy(k) + esintr(jn, 2, 2)

                end if

 10           continue
```

```
c             if this is a new interaction, make a new location

              if (ifndk.eq.0) then

                Nnzr= Nnzr + 1
                jcoef(Nnzr, 1)= i
                jcoef(Nnzr, 2)= inde(j, jn)

                Ex(Nnzr)= esinte(jn, 1)
                Ey(Nnzr)= esinte(jn, 2)
                Rxx(Nnzr)= esintr(jn, 1, 1)
                Rxy(Nnzr)= esintr(jn, 1, 2)
                Ryx(Nnzr)= esintr(jn, 2, 1)
                Ryy(Nnzr)= esintr(jn, 2, 2)

              end if

 20         continue

          end if

 30   continue

      return
      end

c ==========================================================

      subroutine init

c ==========================================================

c     Initializes memory and Gauss integration and opens data files

c ==========================================================

      implicit double precision (a-h, o-z)

      include 'sysmem.blk'

      character title*80, date*12, time*8, vers*12, srftp(maxsrf)*1

c
      common /head/ title, date, time, vers, srftp
      common /icntrl/ itp4, itp5, itp6, itp7, itp8, itp9, itp10,
     #                iparam(20)
      common /mesh/ Ne(maxelm), inde(maxelm, 3), Nnd, Nelem, Nbc,
     #              ide(maxelm), idn(maxnd), idbc(maxelm), Nsrf,
     #              Nnzr, jcoef(maxnz, 2), ner, new
      common /rmesh/ xnd(maxnd, 2), T(maxbc), Tn(maxnd),
     #               srfdat(maxsrf, 4), tol, hwall
      common /mtrl/ emsvty, sb
      common /GLint/ xint(8), w(8), Nl
```

```
      common /shpfac/ Ex(maxnz), Ey(maxnz), Rxx(maxnz), Rxy(maxnz),
     #                Ryx(maxnz), Ryy(maxnz)
      common /solu/ qr(maxnd, 2), qout(maxbc), err, qnet

      itp4= 10
      itp5= 11
      itp6= 12
      itp7= 13
      itp8= 14
      itp9= 15
      itp10= 16

      open (unit= itp4, file= 'run', status= 'unknown')

      write (itp4, *) 'Initializing storage'

      xint(1)= -0.9602899
      xint(2)= -0.7966665
      xint(3)= -0.5255324
      xint(4)= -0.1834346
      xint(5)= -xint(4)
      xint(6)= -xint(3)
      xint(7)= -xint(2)
      xint(8)= -xint(1)

      w(1)= 0.1012285
      w(2)= 0.2223810
      w(3)= 0.3137066
      w(4)= 0.3626838
      w(5)= w(4)
      w(6)= w(3)
      w(7)= w(2)
      w(8)= w(1)

      Nl= 8

      do 10 i= 1, maxelm
        Ne(i)= 0
        inde(i, 1)= 0
        inde(i, 2)= 0
        inde(i, 3)= 0
        ide(i)= 0
        idbc(i)= 0
10    continue

      do 20 i= 1, maxnd
        idn(i)= 0
        Tn(i)= 0.0000d+00
        xnd(i, 1)= 0.000000d+00
        xnd(i, 2)= 0.000000d+00
        qr(i, 1)= 0.00000d+00
        qr(i, 2)= 0.00000d+00
20    continue

      do 30 i= 1, maxbc
        qout(i)= 0.0000d+00
30      T(i)= 0.00000d+00
```

```
      return
      end
```

```
c
=======================================================================

      subroutine mshrd (itp, xc, r, ner, xnd, ne, inde, nnd, nelem,
     #                  ibc, idbc)

c
=======================================================================

c     Paves a rod with center xc, and radius r with bar/3 elements

c
=======================================================================

      implicit double precision (a-h, o-z)

      include 'sysmem.blk'

      dimension xc(2), xnd(maxnd, 2), inde(maxelm, 3), ne(maxelm),
     #          idbc(maxelm)

c     if rod is on line of symmetry go to mshhrd

      if (xc(1).eq.0.000d+00) then
        call mshhrd (itp, xc(2), r, ner, xnd, ne, inde, nnd, nelem,
     #               ibc, idbc)
        return
      end if

c     write error message if r<xc(1)

      if (xc(1).lt.r) go to 901

c     pave rod

      nnr= 2*ner
      pi= dacos(-1.000d+00)
      dtheta= 2.0*pi/nnr

c     set node positions

      do 10 in= 1, nnr
        nnd= nnd + 1
        xnd(nnd, 1)= xc(1) + r*dcos((pi/2.0) - dtheta*(in-1))
        xnd(nnd, 2)= xc(2) + r*dsin((pi/2.0) - dtheta*(in-1))
 10   continue
```

```
c     set element connectivity

      do 20 ie= 1, ner - 1
        nelem= nelem + 1
        idbc(nelem)= ibc
        ne(nelem)= 3
        inde(nelem, 1)= nnd - nnr + (ie-1)*2 + 1
        inde(nelem, 2)= inde(nelem, 1) + 2
        inde(nelem, 3)= inde(nelem, 1) + 1
 20   continue

c     tie in last element

      nelem= nelem + 1
      idbc(nelem)= ibc
      ne(nelem)= 3
      inde(nelem, 1)= inde(nelem-1, 2)
      inde(nelem, 2)= inde(nelem-ner+1, 1)
      inde(nelem, 3)= inde(nelem, 1) + 1

      return

 901  write (itp, *) ' '
      write (itp, *) '=====>  FATAL ERROR IN MESH GENERATOR <====='
      write (itp, *) 'rod too close to centerline'
      write (itp, *) 'rods can only intersect centerline'
      write (itp, *) 'if they are bisected by the centerline'
      write (itp, *) 'e.g. xc= 0'
      write (itp, *) 'move the rod at (x, y)= ',xc(1), xc(2)
      write (itp, *) 'with radius r= ', r
      write (itp, *) ' '
      write (itp, *) '   =====> EXECUTION TERMINATED'
      stop


      end




c ==========================================================

      subroutine mshhrd (itp, yc, r, ner, xnd, ne, inde, nnd, nelem,
     #                   ibc, idbc)

c ==========================================================

c     Paves half rod with center at (0, yc) and radius r with bar/3 elements

c ==========================================================

      implicit double precision (a-h, o-z)
```

```
      include 'sysmem.blk'

      dimension xnd(maxnd, 2), inde(maxelm, 3), ne(maxelm),
     #          idbc(maxelm)

      pi= dacos(-1.000d+00)

      nnr= ner + 1
      dtheta= pi/(nnr-1)

c     set up nodes
      do 10 in= 1, nnr
        nnd= nnd + 1
        xnd(nnd, 1)= r*cos((pi/2.0) - dtheta*(in-1))
        xnd(nnd, 2)= yc + r*sin((pi/2.0) - dtheta*(in-1))
 10   continue

c     set up nodal connectivity

      do 20 ie= 1, ner/2
        nelem= nelem + 1
        idbc(nelem)= ibc
        ne(nelem)= 3
        inde(nelem, 1)= nnd - nnr + (ie-1)*2 + 1
        inde(nelem, 2)= inde(nelem, 1) + 2
        inde(nelem, 3)= inde(nelem, 1) + 1
 20   continue

      return
      end
```

```
c
=======================================================================

      subroutine mshwl (itp, nw, H, nnd, nelem, ne, inde, xnd)

c
=======================================================================

c     This subroutine paves the walls of the enclosure with a uniform
c     grid of bar/3 elements

c     H - The height of the enclosure
c     nw - Number of elements on all walls (bottom, side, top inclusive)

c
=======================================================================

      implicit double precision (a-h, o-z)
```

```
      include 'sysmem.blk'

      dimension ne(maxelm), inde(maxelm, 3), xnd(maxnd, 2)

      dx= H/nw
      pi= dacos(-1.000d+00)

c     set nodes - lower wall

      do 10 i= 1, (nw/2)+1
        nnd= nnd+1
        xnd(nnd, 2)= 0.00000000d+00
        xnd(nnd, 1)= (i-1)*dx
        xnd(nnd, 1)= H*dsin(pi*xnd(nnd, 1)/H)/2.00
 10   continue

c     - side wall

      do 20 i= 1, nw
        nnd= nnd + 1
        xnd(nnd, 1)= H/2.00000d+00
        xnd(nnd, 2)= i*dx
        xnd(nnd, 2)= H*(1.00-dcos(pi*xnd(nnd, 2)/H))/2.00
 20   continue

c     - top wall

      do 30 i= 1, nw/2
        nnd= nnd+1
        xnd(nnd, 2)= H
        xnd(nnd, 1)= (H/2.0000d+00) - i*dx
        xnd(nnd, 1)= H*dsin(pi*xnd(nnd, 1)/H)/2.00
 30   continue

c     Set element connectivity

      do 40 i= 1, nw
        nelem= nelem+1
        ne(nelem)= 3
        inde(nelem, 1)= nnd - (2*nw+1) + 2*(i-1) + 1
        inde(nelem, 2)= inde(nelem, 1)+2
        inde(nelem, 3)= inde(nelem, 1)+1
 40   continue

      return
      end


c
=======================================================================

      subroutine norm (itp, dpsi, xj, Ne, n)

c
=======================================================================
```

```
c     Calculates the outward directed norm at a given location on the
c     side of the element.  The location is implied by the value of the
c     derivatives of the master element basis functions corresponding
c     to the side.  The side of the element is specified by the coordinates of
c     the nodes which lie on the side (listed in CCW fasion).

c     dpsi(3) - The derivative of the master element basis
c                  functions, i, corresponding to the side element (in)
c     xj(3, 2) - The coordinates, j, of the nodes, i, specifying the side
c                element (in)
c     Ne - The number of nodes in the side element (in)
c     n(3) - The coordinates, i, of the outward directed normal (out)

c
=============================================================

      implicit double precision (a-h, o-z)

      dimension dpsi(3), xj(3, 2), dxdx(2)
      double precision n(2)

c     Initialize gradient map

      do 10 i= 1, 2
        n(i)= 0.00d+00
 10     dxdx(i)= 0.000d+00

c     calculate gradients in global coordinates

      do 20 i= 1, Ne
        do 20 j= 1, 2
 20       dxdx(j)= dxdx(j) + xj(i, j)*dpsi(i)

c     Evaluate elements of the norm vector

      n(1)= dxdx(2)
      n(2)= -dxdx(1)

c     divide by ||norm||

      h= dsqrt( n(1)*n(1) + n(2)*n(2) )

      if (h.eq.0.00d+00) then
        write (itp, *) '*** error in subroutine norm ***'
        write (itp, *) '||n||= h= 0'
        write (itp, *) 'check for inconsistent node specification'
        write (itp, *) 'node locations:'
        do 30 i= 1, Ne
 30       write (itp, *) i, (xj(i, j), j= 1, 2)
        stop
      else
        n(1)= n(1)/h
        n(2)= n(2)/h
      end if

      return
      end
```

```
c
=======================================================================

      subroutine obstrc (xi, xj, xc, r, iflg, tol)

c
=======================================================================

c     determines if the line i-j and the circle (xc, r) have any
c     intersections and if an intersection lies between i and j

c
=======================================================================

      implicit double precision (a-h, o-z)

      dimension xi(2), xj(2), xc(2)

      iflg= 0
      tol= 0.001

c     find the distance between i and j

      dij= dsqrt ((xj(1)-xi(1))**2 + (xj(2)-xi(2))**2)
      if (dij.eq.0.00000d+00) go to 900

c     find equation of line Lij

      A= xj(2) - xi(2)
      B= xi(1) - xj(1)
      C= xi(2)*(xj(1)-xi(1)) - xi(1)*(xj(2)-xi(2))

c     find distance between rod center and line Lij

      dcij= dabs ((A*xc(1) + B*xc(2) + C)/dij)

c     circle xc,r can only intersect Lij if dcij<r

      if (dcij.gt.r) return

c     check to make sure intersection is between i and j

      dcj= dsqrt ((xc(1)-xj(1))**2 + (xc(2)-xj(2))**2)
      dci= dsqrt ((xc(1)-xi(1))**2 + (xc(2)-xi(2))**2)

      d1= dsqrt(dcj**2 - dcij**2)
      d2= dsqrt(dci**2 - dcij**2)

c     rod can only obstruct if d1+d2=dij

      if ((d1+d2).gt.(dij+tol)) return
```

```
c     if we get this far then the rod must obstruct Lij

      iflg= 1
      return

 900  write (*, *) '=====>  WARNING: SUBROUTINE OBSTRC  <====='
      write (*, *) 'point i and j are the same point'
      write (*, *) '(xi, yi)= ',xi(1), xi(2)
      write (*, *) '(xj, yj)= ',xj(1), xj(2)
      write (*, *) '=====> EXECUTION CONTINUES'
      write (*, *) ' '

      return
      end




c
c=======================================================================

      subroutine obstrl (xi, xj, xa, xb, iflg, tol)

c
c=======================================================================

c     determines if the intersection of i-j and a-b lies between
c     the points i, j, a, and b

c
c=======================================================================

      implicit double precision (a-h, o-z)

      dimension xi(2), xj(2), xa(2), xb(2), xint(2)
      double precision mij, mab

      iflg= 0
      big= 1.000d+10

c     calculate slopes

      mij= (xj(2) - xi(2)) / (xj(1) - xi(1))
      mab= (xb(2) - xa(2)) / (xb(1) - xa(1))
      if (xj(1).eq.xi(1)) mij= big
      if (xb(1).eq.xa(1)) mab= big

c     calculate intersection

      xint(1)= (xa(2) - xi(2) + mij*xi(1) - mab*xa(1)) / (mij - mab)
      xint(2)= mij*(xint(1) - xi(1)) + xi(2)
```

```
c     calculate distances

      dij= dsqrt((xi(1)-xj(1))**2 + (xi(2)-xj(2))**2)
      dab= dsqrt((xa(1)-xb(1))**2 + (xa(2)-xb(2))**2)
      dsi= dsqrt((xint(1)-xi(1))**2 + (xint(2)-xi(2))**2)
      dsj= dsqrt((xint(1)-xj(1))**2 + (xint(2)-xj(2))**2)
      dsa= dsqrt((xint(1)-xa(1))**2 + (xint(2)-xa(2))**2)
      dsb= dsqrt((xint(1)-xb(1))**2 + (xint(2)-xb(2))**2)

c     check for intersection between i, j and a, b

      if ((dsi.lt.(dij-tol)) .and. (dsj.lt.(dij-tol)) .and.
     #    (dsa.lt.(dab-tol)) .and. (dsb.lt.(dab-tol))) iflg= 1

      return
      end




c
=======================================================================

      subroutine post

c
=======================================================================

c     Integrates net radiative heat flux leaving each of the
c     isothermal surfaces

c
=======================================================================

      implicit double precision (a-h, o-z)

      include 'sysmem.blk'

      common /mesh/ Ne(maxelm), inde(maxelm, 3), Nnd, Nelem, Nbc,
     #              ide(maxelm), idn(maxnd), idbc(maxelm), Nsrf,
     #              Nnzr, jcoef(maxnz, 2), ner, new
      common /rmesh/ xnd(maxnd, 2), T(maxbc), Tn(maxnd),
     #               srfdat(maxsrf, 4), tol, hwall
      common /mtrl/ emsvty, sb
      common /GLint/ xint(8), w(8), Nl
      common /solu/ qr(maxnd, 2), qout(maxbc), err, qnet

      dimension psi(3), dpsi(3), xj(3, 2), rn(2)

c     loop through all of the elements in the mesh

      do 40 ie= 1, Nelem

c       initialize integral

        sum= 0.0000d+00
```

```
c       store the node locations

        do 10 in= 1, Ne(ie)
            do 10 j= 1, 2
 10           xj(in, j)= xnd(inde(ie, in), j)

c       loop through each integration point

        do 30 L= 1, Nl

c         Evaluate basis functions, Jacobian, and normal

          call shape (itp4, Ne(ie), xint(L), psi, dpsi)
          call srfjcb (Ne(ie), xj, dpsi, Rj)
          call norm (itp4, dpsi, xj, Ne(ie), rn)

c         evaluate net radiation out of surface at L

          qe= 0.0000d+00
          do 20 j= 1, Ne(ie)
            qe= qe + psi(j)*emsvty*(sb*(Tn(inde(ie, j))**4) -
     #               qr(inde(ie, j), 1)*rn(1) -
     #               qr(inde(ie, j), 2)*rn(2))
 20         continue

c         assemble integral

          sum= sum + qe*Rj*w(L)

 30     continue

c       add element contribution onto appropriate surface

        qout(idbc(ie))= qout(idbc(ie)) + sum

 40   continue

c     determine the net radiative transfer and error
c     Remember, the integration was only done over half of the
c     domain

      qpos= 0.00000d+00
      qneg= 0.0000d+00

      do 50 i= 1, Nbc
        if (qout(i).ge.0.000d+00) then
          qpos= qpos + qout(i)
        else if (qout(i).le.0.000d+00) then
          qneg= qneg - qout(i)
        end if
 50   continue

      qnet= (qpos + qneg) /2.0000d+00
      err= 100.0*(qpos - qneg) / qnet
```

```
      return
      end

c
=======================================================================

      subroutine proc

c
=======================================================================

c     Iterates to find the incident radiative heat flux at each
c     node

c
=======================================================================

      implicit double precision (a-h, o-z)

      include 'sysmem.blk'

      common /icntrl/ itp4, itp5, itp6, itp7, itp8, itp9, itp10,
     #                iparam(20)
      common /mesh/ Ne(maxelm), inde(maxelm, 3), Nnd, Nelem, Nbc,
     #              ide(maxelm), idn(maxnd), idbc(maxelm), Nsrf,
     #              Nnzr, jcoef(maxnz, 2), ner, new
      common /rmesh/ xnd(maxnd, 2), T(maxbc), Tn(maxnd),
     #               srfdat(maxsrf, 4), tol, hwall
      common /mtrl/ emsvty, sb
      common /shpfac/ Ex(maxnz), Ey(maxnz), Rxx(maxnz), Rxy(maxnz),
     #                Ryx(maxnz), Ryy(maxnz)
      common /solu/ qr(maxnd, 2), qout(maxbc), err, qnet
      common /work/ w1(maxnd), w2(maxnd)

c     set nodal temperatures

      do 10 i= 1, Nelem
        do 10 j= 1, Ne(i)
          Tn(inde(i, j))= T(idbc(i))
 10   continue

c     initialize iteration

      small= 1.0000d-10
      dqmax= small
      maxit= 100
      iter= 0
```

```
c     Begin Picard iteration

      do while ((dqmax.ge.small) .and. (iter.lt.maxit))
        iter= iter + 1
        dqmax= 0.000d+00

        do 20 i= 1, Nnd
          w1(i)= 0.0000d+00
 20       w2(i)= 0.0000d+00

c       loop through each node in the mesh

        do 30 k= 1, Nnzr

          w1(jcoef(k, 1))= w1(jcoef(k, 1)) -
     #      (1.00-emsvty)*(qr(jcoef(k, 2), 1)*Rxx(k) +
     #                     qr(jcoef(k, 2), 2)*Rxy(k)) -
     #      emsvty*sb*(Tn(jcoef(k, 2))**4)*Ex(k)
          w2(jcoef(k, 1))= w2(jcoef(k, 1)) -
     #      (1.00-emsvty)*(qr(jcoef(k, 2), 1)*Ryx(k) +
     #                     qr(jcoef(k, 2), 2)*Ryy(k)) -
     #      emsvty*sb*(Tn(jcoef(k, 2))**4)*Ey(k)


 30     continue

c       evaluate change in solution and update

        do 40 i= 1, Nnd
          dq= dsqrt((qr(i, 1) - w1(i))**2 + (qr(i, 2) - w2(i))**2)
          if (dq.gt.dqmax) dqmax= dq
          qr(i, 1)= w1(i)
          qr(i, 2)= w2(i)
 40     continue

c       print convergence information

        write (itp4, *) '     ',iter, dqmax
        write (*, *) '     ',iter, dqmax

      end do

      return
      end
```

c

```
      subroutine rprob

c
=======================================================================

c     Reads problem description file including surface temperatures
c     and emissivities

c
=======================================================================

      implicit double precision (a-h, o-z)

      include 'sysmem.blk'

      common /icntrl/ itp4, itp5, itp6, itp7, itp8, itp9, itp10,
     #                iparam(20)
      common /mesh/ Ne(maxelm), inde(maxelm, 3), Nnd, Nelem, Nbc,
     #              ide(maxelm), idn(maxnd), idbc(maxelm), Nsrf,
     #              Nnzr, jcoef(maxnz, 2), ner, new
      common /rmesh/ xnd(maxnd, 2), T(maxbc), Tn(maxnd),
     #               srfdat(maxsrf, 4), tol, hwall
      common /mtrl/ emsvty, sb

c     open file

      open (unit= itp6, file= 'in', status= 'old')

c     Skip over header

      read (itp6, *)
      read (itp6, *)
      read (itp6, *)

c     read emissivity and Stefan-Boltzmann number

      read (itp6, 1) emsvty
      read (itp6, 1) sb
      read (itp6, *)

c     read shape factor file flag

      read (itp6, 2) iparam(1)
      read (itp6, *)

c     read mesh data

      read (itp6, 2) ner
      read (itp6, 2) new
      read (itp6, 1) hwall
      read (itp6, *)


c     read the number of surfaces

      read (itp6, 2) Nbc
```

```
c     read surface temperatures

      do 10 i= 1, Nbc
        read (itp6, 1) T(i)

c       convert temperatures to Kelvin

        T(i)= T(i) + 273.15

 10   continue

      close (unit= itp6, status= 'keep')

 1    format (d14.7)
 2    format (i14)

      return
      end
c
```

```
      subroutine rshdw

c     ================================================================

c     Reads the shadow surface data file

c     ================================================================

      implicit double precision (a-h, o-z)

      include 'sysmem.blk'

      character title*80, date*12, time*8, vers*12, srftp(maxsrf)*1

      common /head/ title, date, time, vers, srftp
      common /icntrl/ itp4, itp5, itp6, itp7, itp8, itp9, itp10,
     #                iparam(20)
      common /mesh/ Ne(maxelm), inde(maxelm, 3), Nnd, Nelem, Nbc,
     #              ide(maxelm), idn(maxnd), idbc(maxelm), Nsrf,
     #              Nnzr, jcoef(maxnz, 2), ner, new
      common /rmesh/ xnd(maxnd, 2), T(maxbc), Tn(maxnd),
     #               srfdat(maxsrf, 4), tol, hwall

      open (unit= itp10, file= 'shdw.dat', status= 'old')

c     skip header

      read (itp10, *)
      read (itp10, *)

c     read number of surfaces in the right hand side

      read (itp10, 1) Nsrf
      read (itp10, *)
```

```
c     read all surface data

      do 10 i= 1, Nsrf
        read (itp10, 2) srftp(i)
        read (itp10, 3) (srfdat(i, j), j= 1, 4)
 10   continue

      close (unit= itp10, status= 'keep')

 1    format (i5)
 2    format (7x, a1)
 3    format (4(1x, d14.7))

      return
      end

c ==========================================================

      subroutine shadow (xi, xj, ishdw)

c ==========================================================

c     Determines if the line segment i-j is intersected by any of
c     the potentially shadowing surfaces

c     xi(2) - Cartesian coordinates of node i (in)
c     xj(2) - Cartesian coordinates of integration point j (in)

c     ishdw - Flag indicating obstruction (out)
c             ishdw= 1 - true, ishdw= 0 - false

c     Block Memory:
c       /shdsrf/ Ne, inde, Nelem
c       /rmesh/ xnd

c ==========================================================

      implicit double precision (a-h, o-z)

      include 'sysmem.blk'

      character title*80, date*12, time*8, vers*12, srftp(maxsrf)*1

      common /head/ title, date, time, vers, srftp
      common /mesh/ Ne(maxelm), inde(maxelm, 3), Nnd, Nelem, Nbc,
     #              ide(maxelm), idn(maxnd), idbc(maxelm), Nsrf,
     #              Nnzr, jcoef(maxnz, 2), ner, new
      common /rmesh/ xnd(maxnd, 2), T(maxbc), Tn(maxnd),
     #               srfdat(maxsrf, 4), tol, hwall

      dimension xi(2), xj(2), xa(2)

      ishdw= 0
```

```
c     compare i-j to each surface

      do 10 isrf= 1, Nsrf

        xa(1)= srfdat(isrf, 1)
        xa(2)= srfdat(isrf, 2)

        call obstrc (xi, xj, xa, srfdat(isrf, 3), ishdw, tol)

        if (ishdw.eq.1) return
 10   continue
      return
      end

C=======================================================================

      SUBROUTINE SHAPE (ITP, NE, X, PSI, DPSI)

C=======================================================================
C
C     Evaluates elemental basis functions and derivatives on master
C     element  (rod elements only)
C
C          ITP       Error file unit number for error print out (I/input)
C          NE        Number of nodes in element (I/input)
C          X         Coordinates of point P where basis functions are
C                    evaluated (R/input)
C
C          PSI(I)    Basis functions evaluated at point P, I= 1, 9
C                    (R/output)
C          DPSI(I)   Derivative of basis functions evaluated at point P,
C                    I= 1, 9 (R/M/output)
C
C=======================================================================

      IMPLICIT DOUBLE PRECISION (A-H, O-Z)

      DIMENSION PSI(3), DPSI(3)

C     Initialize memory

      DO 10 J= 1, 3
        DPSI(J)= 0.000000d+00
        PSI(J)= 0.0000000d+00
 10   CONTINUE

c     set element basis functions

      IF (NE.EQ.3) THEN

C       Set ROD/3 basis functions

        PSI(1)= 0.5 * X * (X - 1.0)
        PSI(2)= 0.5 * X * (X + 1.0)
        PSI(3)= 1.0 - X * X
```

```
        DPSI(1)= 0.5 * (2.0 * X - 1.0)
        DPSI(2)= 0.5 * (2.0 * X + 1.0)
        DPSI(3)= -2.0 * X

        RETURN

      ELSE IF (NE.EQ.2) THEN

C       Set ROD/2 basis functions

        PSI(1)= 0.5 * (1.0 - X)
        PSI(2)= 0.5 * (1.0 + X)

        DPSI(1)= -0.5
        DPSI(2)= 0.5

        RETURN

      ELSE

C     This element is not included in element library

        WRITE (ITP, *) '*** Fatal Error in SHAPE ***'
        WRITE (ITP, *) 'Element with ',NE,' nodes and ISHPE= ',
     #                  ISHPE, ' is not in library'
        WRITE (ITP, *) 'Translator execution is terminated by SHAPE'
        STOP

      END IF

      END


c
=======================================================================

      subroutine sint (je, in, esinte, esintr, istore)

c
=======================================================================

c     Calculates the elemental contribution to the reflection and
c     direct emission operators.  Includes mirroring, assuming a mirror
c     plane at x= 0.

c     in - Global node number of interest (in)
c     je - Element over which integration is performed (in)

c     esinte(4, 3) - The x, y, z, component, j, of the surface
c                    emission integral contributing source term at
c                    node i  (out)
c     esintr(4, 3, 3) - The x, y, z component, j, of the reflection
c                       contributing to the k component of the
c                       radiation flux vector at node i
c     istore - Flag indicating elemental contribution is shadowed
c              or otherwise obstructed, istore= 0 - do not store
c              istore= 1 - store elemental contribution
```

```
c     dot - Inner product of rn and roh (data)
c     dpsi(9, 3) - jth derivative of the ith master element basis
c                  function evaluated at an integration point (data)
c     h - |ri-ro| (data)
c     imirr - Flag indicating if current integration point has been
c             mirrored (data)
c     Last - Last element to cause a shadow (data)
c     Nl - Number of integration points (data)
c     pi - What do you think it is? (data)
c     psi(9) - ith master element basis function evaluated at a given
c              integration point (data)
c     ri(3) - (x, y, z) coordinates of the node i (in)
c     Rj - The Jacobian for this surface element at an integration point (data)
c     rn(3) - Outward directed unit normal to the mesh at a given integration
c             point (data)
c     ro(3) - (x, y, z) global coordinates of a given integration point (data)
c     roh(3) - Unit vector (ri-ro)/|ri-ro| (data)
c     w(27) - Integration weight corresponding to point i (data)
c     x - Optical distance from ri to ro (data)
c     xint(27, 3) - (x, y, z) coordinates, j, of integration
c                   point i (data)
c     xj(9, 3) - The global coordinates, j, of each node, i, in the
c                boundary element (data)

c     Block Common:
c       /icntrl/ itp4
c       /mesh/ Nd
c       /mtrl/ prop, emsvty

c     Dependencies:
c       setint, shape, map, norm, srfjcb, Sn

c
```

```
      implicit double precision (a-h, o-z)

      include 'sysmem.blk'

      common /icntrl/ itp4, itp5, itp6, itp7, itp8, itp9, itp10,
     #                iparam(20)
      common /mesh/ Ne(maxelm), inde(maxelm, 3), Nnd, Nelem, Nbc,
     #              ide(maxelm), idn(maxnd), idbc(maxelm), Nsrf,
     #              Nnzr, jcoef(maxnz, 2), ner, new
      common /rmesh/ xnd(maxnd, 2), T(maxbc), Tn(maxnd),
     #               srfdat(maxsrf, 4), tol, hwall
      common /GLint/ xint(8), w(8), Nl


      dimension esinte(3, 2), esintr(3, 2, 2), psi(3), dpsi(3),
     #          xj(3, 2), ro(2), rn(2), roh(2), ri(2)

c     initialize

      pi= dacos(-1.000d+00)
      Last= 1
```

```
      ishdw= 0
      istore= 0

      ri(1)= xnd(in, 1)
      ri(2)= xnd(in, 2)

      do 5 i= 1, Ne(je)
        do 5 j= 1, 2
 5        xj(i, j)= xnd(inde(je, i), j)

c     initialize boundary integral

      do 10 i= 1, 3
        do 10 j= 1, 2
          esinte(i, j)= 0.00d+00
          do 10 k= 1, 2
 10         esintr(i, j, k)= 0.000d+00

c     loop through each integration point, L

      do 50 L= 1, Nl
        imirr= 0

c       evaluate basis functions, Jacobian, and normal at L

        call shape (itp4, Ne(je), xint(L), psi, dpsi)
        call srfjcb (Ne(je), xj, dpsi, Rj)
        call norm (itp4, dpsi, xj, Ne(je), rn)

c       map integration point L onto global coordinates

        ro(1)= 0.0000d+00
        ro(2)= 0.0000d+00
        do 11 i= 1, Ne(je)
          ro(1)= ro(1) + xj(i, 1)*psi(i)
 11       ro(2)= ro(2) + xj(i, 2)*psi(i)

c       evaluate unit vector ri-ro, return error if |ri-ro|=0

 15     roh(1)= ri(1) - ro(1)
        roh(2)= ri(2) - ro(2)
        h= dsqrt (roh(1)*roh(1) + roh(2)*roh(2))

        if (h.eq.0.000d+00) go to 99

        roh(1)= roh(1) / h
        roh(2)= roh(2) / h

c       evaluate inner product of rn*roh

        dot= rn(1)*roh(1) + rn(2)*roh(2)

c       calculate shape factor only if element "faces" ri

        if (dot.ge.0.000d+00) go to 45
```

```
c       Is i shadowed from j?

        call shadow (ri, ro, ishdw)

        if (ishdw.eq.0) then

          istore= 1

c         evaluate boundary integral

          do 40 j= 1, 2
            do 40 i= 1, Ne(je)

              esinte(i, j)= esinte(i, j) + psi(i)*dot*roh(j)*
     #                                     Rj*w(L) / (2.000*h)
              esintr(i, j, 2)= esintr(i, j, 2) + psi(i)*dot*
     #                         roh(j)*rn(2)*Rj*w(L) / (2.000*h)

c           Don't neglect to mirror the reflection shape factor

            if (imirr.eq.0) then
              esintr(i, j, 1)= esintr(i, j, 1) + psi(i)*dot*
     #                         roh(j)*rn(1)*Rj*w(L) / (2.000*h)
            else
              esintr(i, j, 1)= esintr(i, j, 1) - psi(i)*dot*
     #                         roh(j)*rn(1)*Rj*w(L) / (2.000*h)
            end if

 40         continue

        end if

c       Evaluate contribution of mirror image

 45     if (imirr.eq.0) then
          ro(1)= -ro(1)
          rn(1)= -rn(1)
          imirr= 1
          go to 15
        end if
 50   continue

      return

 99   write (itp4, *) '*** error in SINT ***'
      write (itp4, *) 'h= 0'
      write (itp4, *) 'i= ',in
      write (itp4, *) 'je= ',je
      write (itp4, *) 'L= ',L
      write (itp4, *) 'ri= ',(ri(i), i= 1, 2)
      write (itp4, *) 'ro= ',(ro(i), i= 1, 2)
      write (itp4, *) 'execution is terminated'
      stop

      end
```

```
c
=======================================================================

      subroutine srfjcb (Ne, xyz, dpsi, Rj)

c
=======================================================================

c     Evaluates the Jacobian for surface integration

c     dpsi(3) - The (x, y, z) derivatives, j, of each basis
c                  function, i, in the element of interest (in)
c     Ne - Number of nodes in the element of interest (in)
c     xyz(3, 2) - The (x, y, z) coordinates, j, of each node, i, in
c                 the element of interest (in)
c     Rj - The surface Jacobian (out)

c
=======================================================================

      implicit double precision (a-h, o-z)

      dimension xyz(3, 2), dpsi(3)

c     initialize transformation gradients

      dxdu= 0.000d+00
      dydu= 0.000d+00

c     calculate the tranformation derivatives

      do 10 i= 1, Ne
        dxdu= dxdu + xyz(i, 1)*dpsi(i)
 10     dydu= dydu + xyz(i, 2)*dpsi(i)

c     calculate surface Jacobian

      Rj= dsqrt( dxdu**2 + dydu**2 )

      return
      end




c
=======================================================================

      subroutine store
```

```
c
c=======================================================================

c     Reads or writes the configuration factors to/from an
c     external file

c
c=======================================================================

      implicit double precision (a-h, o-z)

      include 'sysmem.blk'

      character title*80, date*12, time*8, vers*12, srftp(maxsrf)*1

      common /head/ title, date, time, vers, srftp
      common /icntrl/ itp4, itp5, itp6, itp7, itp8, itp9, itp10,
     #                iparam(20)
      common /mesh/ Ne(maxelm), inde(maxelm, 3), Nnd, Nelem, Nbc,
     #              ide(maxelm), idn(maxnd), idbc(maxelm), Nsrf,
     #              Nnzr, jcoef(maxnz, 2), ner, new
      common /shpfac/ Ex(maxnz), Ey(maxnz), Rxx(maxnz), Rxy(maxnz),
     #                Ryx(maxnz), Ryy(maxnz)

      if (iparam(1).eq.1) go to 30

c     write shape factors to a file

      open (unit= itp7, file= 'view.dat', status= 'unknown')

      write (itp7, *) title
      write (itp7, *) ' '
      write (itp7, 3) Nnd, Nelem, Nnzr

c     write index pointers

      write (itp7, *) ' '
      write (itp7, *) '******************'
      write (itp7, *) 'jcoef'
      write (itp7, *) '******************'
      write (itp7, *) ' '

      write (itp7, 1) (jcoef(i, 1), i= 1, Nnzr)
      write (itp7, 1) (jcoef(i, 2), i= 1, Nnzr)

c     write emission shape factor

      write (itp7, *) ' '
      write (itp7, *) '******************'
      write (itp7, *) 'Ex'
      write (itp7, *) '******************'
      write (itp7, *) ' '

      write (itp7, 2) (Ex(i), i= 1, Nnzr)

      write (itp7, *) ' '
      write (itp7, *) '******************'
```

```
      write (itp7, *) 'Ey'
      write (itp7, *) '******************'
      write (itp7, *) ' '

      write (itp7, 2) (Ey(i), i= 1, Nnzr)

c     write reflection shape factor

      write (itp7, *) ' '
      write (itp7, *) '******************'
      write (itp7, *) 'Rxx'
      write (itp7, *) '******************'
      write (itp7, *) ' '

      write (itp7, 2) (Rxx(i), i= 1, Nnzr)

      write (itp7, *) ' '
      write (itp7, *) '******************'
      write (itp7, *) 'Rxy'
      write (itp7, *) '******************'
      write (itp7, *) ' '

      write (itp7, 2) (Rxy(i), i= 1, Nnzr)

      write (itp7, *) ' '
      write (itp7, *) '******************'
      write (itp7, *) 'Ryx'
      write (itp7, *) '******************'
      write (itp7, *) ' '

      write (itp7, 2) (Ryx(i), i= 1, Nnzr)

      write (itp7, *) ' '
      write (itp7, *) '******************'
      write (itp7, *) 'Rxx'
      write (itp7, *) '******************'
      write (itp7, *) ' '

      write (itp7, 2) (Ryy(i), i= 1, Nnzr)

      close (unit= itp7, status= 'keep')

      return

c     read shape factor data

 30   open (unit= itp7, file= 'view.dat', status= 'old')

      read (itp7, *)
      read (itp7, *)
      read (itp7, 3) n1, n2, Nnzr

c     trap errors

      if ((n1.ne.Nnd) .or. (n2.ne.Nelem)) go to 99
```

```
c     read index counters

      read (itp7, *)
      read (itp7, *)
      read (itp7, *)
      read (itp7, *)
      read (itp7, *)

      read (itp7, 1) (jcoef(i, 1), i= 1, Nnzr)
      read (itp7, 1) (jcoef(i, 2), i= 1, Nnzr)

c     read emission shape factor data

      read (itp7, *)
      read (itp7, *)
      read (itp7, *)
      read (itp7, *)
      read (itp7, *)

      read (itp7, 2) (Ex(i), i= 1, Nnzr)

      read (itp7, *)
      read (itp7, *)
      read (itp7, *)
      read (itp7, *)
      read (itp7, *)

      read (itp7, 2) (Ey(i), i= 1, Nnzr)

c     read reflection shape factor data

      read (itp7, *)
      read (itp7, *)
      read (itp7, *)
      read (itp7, *)
      read (itp7, *)

      read (itp7, 2) (Rxx(i), i= 1, Nnzr)

      read (itp7, *)
      read (itp7, *)
      read (itp7, *)
      read (itp7, *)
      read (itp7, *)

      read (itp7, 2) (Rxy(i), i= 1, Nnzr)

      read (itp7, *)
      read (itp7, *)
      read (itp7, *)
      read (itp7, *)
      read (itp7, *)

      read (itp7, 2) (Ryx(i), i= 1, Nnzr)

      read (itp7, *)
      read (itp7, *)
```

```
      read (itp7, *)
      read (itp7, *)
      read (itp7, *)

      read (itp7, 2) (Ryy(i), i= 1, Nnzr)

      close (unit= itp7, status= 'keep')

      return

 1    format (16i5)
 2    format (6(d12.5))
 3    format (3i20)

 99   write (itp4, *) '*** Fatal error in STORE ***'
      write (itp4, *) 'view.dat is not compatible with mesh'
      write (itp4, *) 'check to make sure the files are correct'
      write (itp4, *) 'or set shape factor file flag to 0'
      write (itp4, *) 'execution terminated'
      stop

      end



c
c=======================================================================

      subroutine wres

c
c=======================================================================

c     prints results to external files

c
c=======================================================================


      implicit double precision (a-h, o-z)

      include 'sysmem.blk'

      character title*80, date*12, time*8, vers*12, srftp(maxsrf)*1

      common /head/ title, date, time, vers, srftp
      common /icntrl/ itp4, itp5, itp6, itp7, itp8, itp9, itp10,
     #                iparam(20)
      common /mesh/ Ne(maxelm), inde(maxelm, 3), Nnd, Nelem, Nbc,
     #              ide(maxelm), idn(maxnd), idbc(maxelm), Nsrf,
     #              Nnzr, jcoef(maxnz, 2), ner, new
      common /rmesh/ xnd(maxnd, 2), T(maxbc), Tn(maxnd),
     #               srfdat(maxsrf, 4), tol, hwall
      common /solu/ qr(maxnd, 2), qout(maxbc), err, qnet
```

```
c     open data files

      open (unit= itp8, file= 'qres', status= 'unknown')
      open (unit= itp9, file= 'out', status= 'unknown')

c     make PATRAN results file

      write (itp8, 1) title
      write (itp8, 2) Nnd, 0, 0.0, 0, 4
      write (itp8, 3) date, time
      write (itp8, 4) vers

c     print flux vectors and nodal locations

      do 10 i= 1, Nnd
 10     write (itp8, 5) idn(i), qr(i, 1), qr(i, 2), xnd(i, 1),
     #                   xnd(i, 2)

c     print integrated heat flux table

      write (itp9, *)
      write (itp9, 1) title
      write (itp9, *)
      write (itp9, *) 'Net radiative heat rate, qnet= ',qnet
      write (itp9, *) 'estimated error= ',err, ' (% of qnet)'
      write (itp9, *) ' '
      write (itp9, 6)

      do 20 i= 1, Nbc

c       convert temperatures to centigrade scale

        T(i)= T(i) - 273.15

 20     write (itp9, 7) i, T(i), qout(i)

      close (unit= itp8, status= 'keep')
      close (unit= itp9, status= 'keep')

 1    format (a80)
 2    format (2i9, e15.6, 2i9)
 3    format ('Neutral file created: ',a8, 2x, a12)
 4    format ('PATRAN version: ',a12)
 5    format (i8, (5e13.7))
 6    format (1x, 'Surface', 7x, 'T', 4x, 'Heat Rate')
 7    format (1x, i7, 1x, f7.2, 1x, e12.5)

      return
      end
```

Bibliography

1. Aliaga, D.A., *Experimental Measurement of Local Heat Transfer Coefficients over Discrete Roughened Plates Using Infrared Thermography*, Ph.D. Dissertation, The University of Texas at Austin, Austin, TX, 1992.

2. Babcock and Wilcox, *Preliminary Design Report B&W BR-100 100-Ton Rail/Barge Spent Fuel Shipping Cask*, DOE/ID/12701-1, Washington, D.C., 1990.

3. Bejan, A., *Convection Heat Transfer*, John Wiley and Sons, New York, New York, 1984.

4. Burns, S.P., RADERA II (RADiation in Enclosed Rod Arrays, ver. II) numerical radiation code, Sandia National Laboratories, 1995.

5. Butler, J.B., *A Numerical Study of Natural Convection Heat Transfer in a Horizontal Spent Nuclear Fuel Rod Array*, M.S. Thesis, The University of Texas at Austin, Austin, TX, 1994.

6. Canaan, R.E., *Natural Convection Heat Transfer Within Horizontal Spent Nuclear Fuel Assemblies*, Ph.D. Dissertation, The University of Texas at Austin, Austin, TX, 1995.

7. Choi, K.J., and Cha, S., "Plume-Rise Effect on Natural Convection Heat Transfer in Staggered Arrays of Circular Heating Elements," *American Institute of Aeronautics and Astronautics (AIAA) Journal of Thermophysics and Heat Transfer*, vol. 4, no. 2, pp. 228-232, 1990.

8. Eckert, E.R.G., and Soehngen, E., "Studies on Heat Transfer in Laminar Free Convection with the Zehnder-Mach Interferometer," Technical Report no. 5745, United States Air Force, Air Material Command, Dayton, Ohio, 1948.

9. Globe, S., and Dropkin, D., "Natural Convection Heat Transfer in Liquids Confined Between Two Horizontal Plates," *Journal of Heat Transfer*, vol. 81C, p. 24, 1959.

10. Incropera, F.P., and DeWitt, D.P., *Fundamentals of Heat and Mass Transfer*, 3rd ed., John Wiley and Sons, New York, New York, 1990.

11. Koschmieder, E.L., *Benard Cells and Taylor Vortices*, Cambridge University Press, New York, New York, 1993.

12. Longenbough, R.S., and Sanchez, L.C., and Mahoney, A.R., "Thermal Response of a Small Scale Cask-Like Test Article to Three Different High Temperature Environments," DOT/FRA/ORD -90/01, Appendix B, February 1990.

13. Moffatt, R.J., "Describing the Uncertainties in Experimental Results," *Experimental Thermal and Fluid Science*, 1:3-17, pp.257-271, 1988.

14. Morgan, V.T., "The Overall Convective Heat Transfer from Smooth Circular Cylinders," in T.F. Irvine and J.P. Hartnett, Eds., *Advances in Heat Transfer*, vol. 11, Academic Press, New York, New York, pp. 199-264, 1975.

15. Reid, R.C., Prausnitz, J.M., and Poling, B.E., *The Properties of Gases and Liquids*, 4th ed., McGraw-Hill, New York, New York, 1987.

16. Siegel, R., and Howell, J.R., *Thermal Radiation Heat Transfer*, 3rd ed., Hemisphere Publishing Corp., Washington, D.C., 1992.

17. Sparrow, E.M., and Niethammer, J.E., "Effect of Vertical Separation Distance and Cylinder-to-Cylinder Temperature Imbalance on Natural Convection for a Pair of Horizontal Cylinders," ASME Journal of Heat Transfer, vol. 103, pp. 638-644, 1981.

18. Tillman, E.S., "Natural Convection Heat Transfer from Horizontal Tube Bundles," ASME paper 76-HT-35, New York, New York, 1976.

19. Todreas, N.E., and Kazimi, M.S., *Nuclear Systems I: Thermal Hydraulic Fundamentals*, Hemisphere Publishing Corp., Washington, D.C., 1990.

20. Vargaftik, N.B., *Tables of Thermophysical Properties of Liquids and Gases*, 2nd ed., Hemisphere Publishing Corp., New York, New York, 1975.

21. Wade, W.R., and Slemp, W.S., "Measurements of Total Emittance of Several Refractory Oxides, Cermets, and Ceramics for Temperatures from 600°F to 2000°F," NASA Technical Note D-998, March 1962.

22. Warrington, R.O., and Weaver, R.A., "Natural Convection Between Arrays of Horizontal Cylinders and Their Enclosure," *Heat Transfer in Enclosures*, ASME HTD-39, Winter Annual Meeting of the American Society of Mechanical Engineers, December 1984, New Orleans, Louisiana, pp. 99-102.

Vita

Christopher Eric Triplett was b[redacted], the son of Donna Day Triplett and John Richard Triplett. After graduating from Dripping Springs High School, Dripping Springs, Texas, in June of 1989, he entered The University of Texas at Austin in September of 1989. In May of 1994, he graduated with a Bachelor of Science in Mechanical Engineering with highest honors. While an undergraduate at UT Austin, he worked internships for Texas Eastman Chemical Company in Longview, Texas, and for the Lower Colorado River Authority in Austin, Texas. In September of 1994, he entered The Graduate School at The University of Texas at Austin to pursue an MS in Mechanical Engineering. While studying at The Graduate School, he worked an internship for Sandia National Laboratories in Albuquerque, New Mexico, and in 1995, he received a Department of Energy fellowship to support his research.

Permanent Address: P.O. Box 163042
Austin, Texas 78716

This thesis was typed by the author.